

On the identification, characterization and investigation of phase dependent coupling in neuronal networks

Roemer van der Meij

ON THE IDENTIFICATION,
CHARACTERIZATION AND INVESTIGATION
OF PHASE DEPENDENT COUPLING IN
NEURONAL NETWORKS

Roemer van der Meij

Ph.D. Thesis

Donders Institute for Brain, Cognition, and Behaviour

Radboud University Nijmegen

© 2015 Roemer van der Meij

ISBN 978-94-6284-017-1

Cover design by Roemer van der Meij

Printed by Ipkamp Drukkers, Enschede

On the identification, characterization and investigation of phase dependent coupling in neuronal networks

Proefschrift

ter verkrijging van de graad van doctor
aan de Radboud Universiteit Nijmegen
op gezag van de rector magnificus prof. dr. Th.L.M. Engelen,
volgens besluit van het college van decanen
in het openbaar te verdedigen op dinsdag 2 juni 2015
om 10.30 uur precies

door

Roemer van der Meij

geboren op 5 december 1984
te Groningen

Promotor

Prof. dr. Markus Ullsperger

Co-promotor

Dr. Eric Maris

Manuscriptcommissie

Prof. dr. Ole Jensen

Prof. dr. Stefano Panzeri (Università degli Studi di Trento, Italië)

Prof. dr. Andreas Daffertshofer (VU)

De productie van dit proefschrift was gesponsord door CTF MEG™.

On the identification, characterization and investigation of phase dependent coupling in neuronal networks

Doctoral Thesis

to obtain the degree of doctor
from Radboud University Nijmegen
on the authority of the Rector Magnificus Prof. dr. Th.L.M. Engelen,
according to the decision of the Council of Deans
to be defended in public on Tuesday, June 2, 2015
at 10.30 hours

by

Roemer van der Meij

born on December 5, 1984
in Groningen, The Netherlands

Supervisor

Prof. dr. Markus Ullsperger

Co-Supervisor

Dr. Eric Maris

Manuscript Committee

Prof. dr. Ole Jensen

Prof. dr. Stefano Panzeri (Università degli Studi di Trento, Italy)

Prof. dr. Andreas Daffertshofer (VU University Amsterdam, the Netherlands)

The production of this dissertation was sponsored by CTF MEG™.

Table of Contents

Chapter 1	General introduction	8
Chapter 2	Phase-amplitude coupling in human ECoG is spatially distributed and phase diverse	22
Chapter 3	Uncovering phase-coupled oscillatory networks	50
Chapter 4	Rhythmic components in extracranial brain signals reveal multifaceted task modulations of overlapping phase-coupled oscillatory networks	98
Chapter 5	General summary	148
Appendix		156
	Bibliography	158
	Nederlandse samenvatting	164
	Acknowledgements	170
	Publication list	176
	About the author	178
	Donders series	180

Chapter 1

General introduction

In our constantly changing environment, our brain needs to be able to flexibly and quickly route information through its neuronal networks. This requires connections to be rapidly formed and dissolved between populations of neurons that need to interact. The brain's anatomical connections however, cannot change at this required speed. Connections formed by the coupling of oscillatory neuronal activity on the other hand, *can* change at the necessary time scales. Moreover, as will be explained in the following, this coupling is likely to be implicated in the effective communication between populations. Therefore, the coupling of neuronal oscillations could be the key building block for the routing of information through the brain.

This thesis concerns the identification, characterization and investigation of neuronal networks formed by the coupling of neuronal oscillations. In this thesis I present and use new decomposition techniques that are capable of uncovering these networks from electrophysiological data, and that allow for analyses of their properties. With these techniques, we can overcome the tremendous challenge of revealing these networks in the absence of *a priori* hypotheses on their location and the involved frequencies.

In this introductory chapter, I first introduce what neuronal oscillations are, and how they are generated. I describe how oscillations can be coupled, and how this coupling can be used for the selective communication between neuronal populations. Then, I describe how the coupling of oscillations in neuronal networks can be investigated, and I illustrate the benefits of using decomposition techniques for this purpose. Finally, I describe the decomposition techniques I developed and used in this thesis, and present an outline of each of the chapters that follow.

1. INTRODUCING NEURONAL OSCILLATIONS

Neuronal oscillations are a ubiquitous feature of brain activity ([Buzsaki and Draguhn, 2004](#)). Oscillations are observed as rhythms in electrical measurements, such as the electroencephalogram (EEG; see Fig 1). Oscillations originate from the rhythmic synchronization of synaptic input and reflect the aggregate activity of many neurons. Synaptic input refers to the signals from sending neurons that arrive at a receiving neuron. A neuron sends its signal - called an action potential or spike – when its *membrane potential* reaches a threshold. A neuron actively keeps its membrane potential away from this threshold, at its

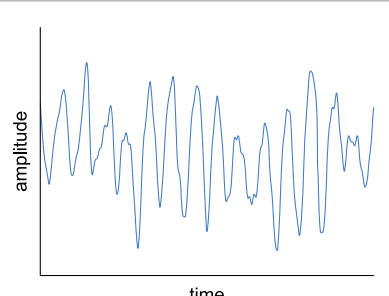


Figure 1. Example of neuronal oscillations in an EEG recording.

so-called resting potential. However, when a spike from a sending neuron arrives at a receiving neuron, it pushes the membrane potential of that neuron towards its threshold. This push lasts very shortly, and is denoted as the post-synaptic potential. When many spikes arrive quickly after each other, their post-synaptic potentials are combined. These combined potentials can then be sufficient to push the receiving neuron's membrane potential over its threshold, causing it to spike itself.

Because the membrane potential determines whether incoming spikes generate outgoing spikes, it reflects the *excitability* of a neuron. When input arrives at a neuron rhythmically, its membrane potential oscillates. If this occurs simultaneously at a sufficient number of neurons, their summed membrane potential oscillations are visible as an oscillation in the measured signal, e.g. the EEG. Oscillations thus reflect synchronized fluctuations of the combined membrane potentials of post-synaptic neurons. Because membrane potentials reflects a neuron's excitability, *neuronal oscillations reflect rhythmic fluctuations of excitability* (Bishop, 1933).

Neuronal oscillations occur at many frequencies, and oscillations at multiple frequencies are often jointly present in recordings. The frequency of oscillations is often denoted in terms of *frequency bands*. Traditional bands are delta (1-4 Hz), theta (4-8 Hz), alpha (8-14 Hz), beta (14-30 Hz), and gamma (30-80 Hz). Oscillations at different frequencies have been suggested to have different functional roles (see e.g. Fries, 2009; Jensen and Mazaheri, 2010; Lisman and Jensen, 2013), and are implicated in many cognitive functions (Wang, 2010; Cannon et al., 2014). Additionally, the size of the neuronal populations that are involved differs between oscillations in different frequency bands, with slower oscillations involving larger populations than faster ones (von Stein and Sarnthein, 2000; Buzsaki and Draguhn, 2004).

Oscillations at different frequencies can also interact. An example of this is *phase-amplitude coupling* (PAC; Chrobak and Buzsaki, 1998). PAC reflects the coupling of the amplitude (strength of a rhythm) of a fast oscillation, to the phase (position in an oscillatory cycle) of a slower oscillation. Because of their difference in frequency, multiple cycles of the fast oscillation fit in a single cycle of the slow oscillation. PAC involves that, at a particular phase of the slow oscillation, the amplitude of the fast oscillation is much higher than at the other phases of the slow oscillation. This type of coupling is likely to be implicated in neuronal communication, as I will argue in the next two sections.

Neuronal oscillations can be recorded with different techniques, which differ in the spatial specificity of the recorded signals. Measurements taken on the outside of the skull, such as EEG or magnetoencephalography (MEG), are distant, and reflect the aggregate activity of many neurons. Electrocorticography (ECoG) is EEG recorded directly from the brain's surface and reflects the aggregate activity of a

smaller number of neurons. Such recordings are invasive, and are therefore only obtained as part of the pre-surgical diagnosis of patients, such as those suffering from pharmacologically untreatable epilepsy. There are also recordings that are even more invasive, such as those obtained from arrays of micro-electrodes that are inserted into the brain. These arrays record activity directly adjacent to neurons, and they reflect the aggregate activity of an even smaller number of neurons. These recordings are only common in animal studies.

2. SELECTIVE NEURONAL COMMUNICATION BY PHASE COUPLING OF NEURONAL OSCILLATIONS

Neuronal oscillations are thought to be important for the communication between neuronal populations. Neuronal populations can oscillate together, which means that the difference in their phase is consistent over time (see Fig 2). This is called *phase coupling*, which is short for *phase-phase coupling*, a term in line with phase-amplitude coupling. Phase coupling between populations is of interest, because it could be used for selective communication between neuronal populations (Fries, 2005). The phase of a neuron's oscillating membrane potential reflects its excitability, and therefore influences the probability of spiking output, and the efficacy of incoming spikes. That is, when spikes arrive at a phase of peak excitability of the receiving neuron, then these incoming spikes will have a high probability to cause the receiving neuron to spike as well.

On the other hand, if spikes arrive at a phase of lowest excitability, then these incoming spikes will less likely result in spiking output. When the membrane potentials of two neurons are strongly phase-coupled (i.e. their phase differences over time are very consistent; Fig 2A), then their rhythmically occurring windows of peak excitability can co-occur, allowing for effective communication. If, on the other hand, their membrane potentials are not phase-coupled, then their windows of communication will not rhythmically co-occur (Fig 2B), and effective communication is unlikely. This principle can be extended to multiple neuronal populations,

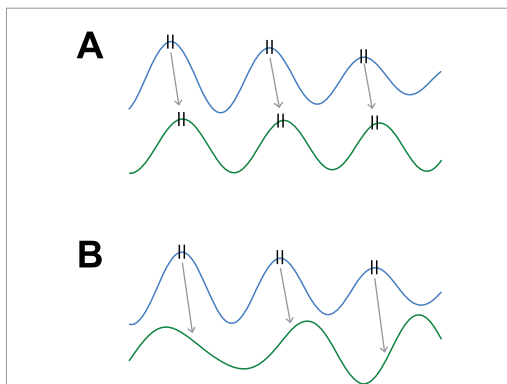


Figure 2. Strength of phase coupling of oscillations between populations can be used for selective communication. **A**, schematic oscillations of two neuronal populations that are strongly phase-coupled. Spikes (black lines) from the sending population reach the receiving population at a phase of peak excitability, and result spiking output. Effective communication is achieved. **B**, schematic oscillations of two neuronal populations that are weakly phase-coupled. Spikes do not arrive at a phase of peak excitability, and do not result in spiking output. Effective communication is not achieved.

where populations that are strongly phase-coupled can effectively communicate, whereas those that are weakly coupled cannot.

PAC is another form of coupling that could implement selective communication between neuronal populations (Canolty and Knight, 2010). PAC involves phase coupling between a slow oscillation and the amplitudes of a faster oscillation. The phase at which the amplitude of the faster oscillation is highest, is denoted as *the preferred coupling phase*. When PAC occurs between populations, it requires that the slow oscillations of both populations are phase-coupled. If so, then the amplitude of the fast oscillation of each population can be phase-coupled to the slow oscillations of both populations (see Fig 3). As such, the slow oscillation can coordinate when the epochs of high amplitudes of the fast oscillation occur at both populations. If the epochs of strong fast oscillations are aligned between populations, communication could be achieved according to two scenarios. The first scenario involves phase coupling (or phase-phase coupling in line with PAC) of the fast oscillations between populations, which could allow for effective communication using the mechanism described in the previous paragraph. In the second scenario, the high amplitude of the fast oscillations only reflects an increase of neuronal activity in both populations (e.g. increased spike rate), and effective communication is achieved by some other (unknown) mechanism. In both scenarios, phase coupling of the slow oscillations determines whether populations communicate. If there is strong phase coupling of the slow oscillation between populations, then the windows of communication can be shared between populations (Fig 3A). If there is weak phase coupling of the slow oscillation, then these windows cannot be shared (Fig 3B). As such, PAC could implement selective

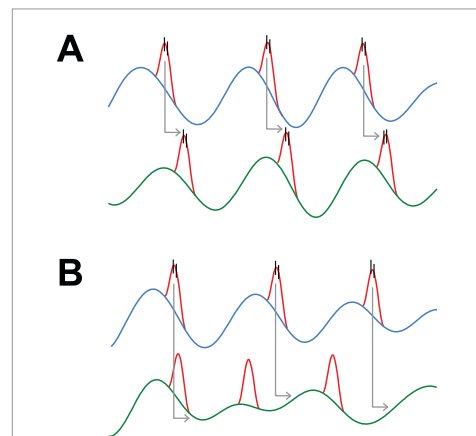


Figure 3. Strength of phase coupling of slow oscillations in PAC can be used for selective communication. **A**, schematic of PAC between two neuronal populations, whose slow oscillations are strongly phase-coupled. This allows both populations to have simultaneously strong fast oscillations, which could allow them to share their windows of communication. If the fast oscillations are phase-coupled, spikes (black lines) arrive at the receiving population at peak excitability, and result in spiking output. In another scenario, the fast oscillations only reflect increased neuronal activity, and communication is achieved by some other mechanism. This scenario is not pictured. **B**, schematic of PAC between two populations, whose slow oscillations are weakly phase-coupled. Strong fast oscillations at both populations cannot be aligned. Spikes do not arrive at peak excitability, and do not result in spiking output.

communication between populations by coordinating whether populations share their windows of communication. Although it has a potential role in selective neuronal communication, investigations of between-population PAC are scarce.

3. CONSISTENT PHASE DIFFERENCES AS A MECHANISM FOR SELECTIVE NEURONAL COMMUNICATION

When two populations are strongly phase-coupled, their phase difference is consistent over time, and this can allow for effective communication between them. This consistent phase difference reflects the temporal offset between the oscillations of the two populations (see Fig 4). Populations can be strongly phase-coupled at different temporal offsets. That is, they can be coupled at different consistent phase differences. Importantly, the consistent phase difference at which this coupling occurs, determines whether or not the windows of communication between populations are temporally aligned. As such, when phase coupling is strong, the phase difference between populations can be used as a mechanism for selective communication between populations ([Womelsdorf et al., 2007](#)). In this scenario, there is an optimal phase difference, and a non-optimal phase difference. At the optimal phase difference, two populations share their windows of communication (i.e. they are temporally aligned). Spikes arrive at excitability peaks (Fig 4A), and effective communication can be achieved. At the (opposite) non-optimal phase difference, they do not share their windows of communication. In this case, spikes arrive at excitability troughs (lowest excitability; Fig 4B), and effective communication cannot be achieved. What the optimal and non-optimal phase differences are, depends on the time it takes for a spike of the sending population to reach the receiving population. Because of this, the optimal phase difference can be anywhere between 0 to 360° for a given pair of populations, and the non-optimal phase difference is its opposite (i.e. the optimal phase shifted by 180°). In this scenario, selective communication between multiple

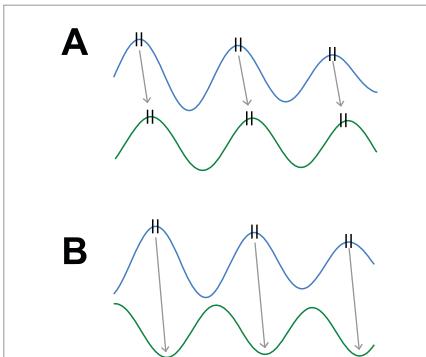
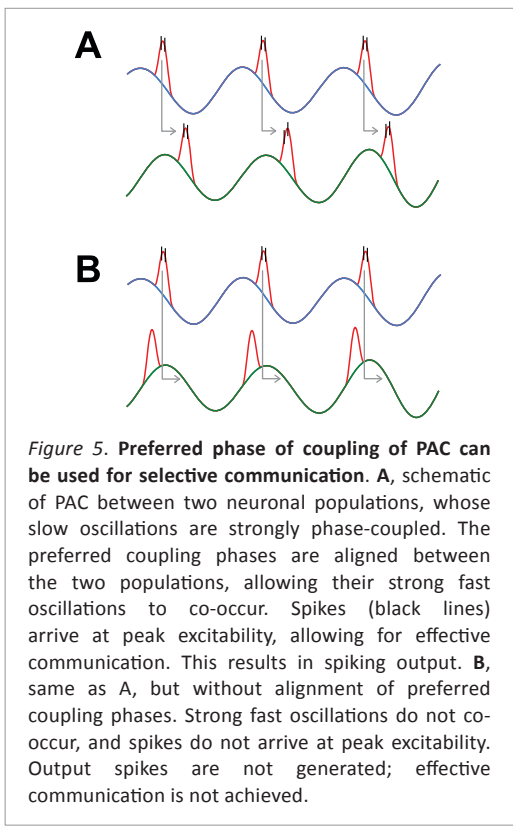


Figure 4. Consistent phase difference of phase coupling between oscillations can be used for selective communication. A, schematic oscillations of two neuronal populations that are strongly phase-coupled at an optimal phase difference. Spikes (black lines) from the sending population reach the receiving population at the optimal phase of excitability, resulting in spiking output. Effective communication is achieved. B, schematic oscillations of two neuronal populations that are strongly phase-coupled at a non-optimal phase difference. Spikes now arrive at the phase of lowest excitability, and are unlikely to influence the receiving population. This does not result in spiking output.



strongly phase-coupled populations can be implemented by having optimal phase differences between populations that should communicate, and by having non-optimal phase differences between those populations that should not.

In another scenario, the preferred coupling phase of PAC can be used as a selection variable to implement the selective communication between populations (see Fig 5). In this scenario, the slow oscillations of multiple populations are strongly phase-coupled, and these populations have strong fast oscillations at different preferred coupling phases of their slow oscillation. Importantly, the occurrence of these strong fast oscillations can be temporally aligned. That is, their preferred

coupling phases can be aligned. If this is the case, then effective communication can be achieved by phase coupling of the fast oscillation (Fig 5A), or by some other (unknown) mechanism. Conversely, populations can also have strong fast oscillations that are not temporally aligned. That is, they have non-aligned preferred coupling phases, such that their strong fast oscillations do not temporally overlap, and effective communication cannot be achieved (Fig 5B). In this scenario, the preferred coupling phase of PAC implements selective communication by aligning preferred coupling phases between populations that should communicate, and by not aligning them between populations that should not. As such, the slow oscillation of PAC can be used to coordinate which populations can communicate when. This scenario allows for multiple communication ‘channels’ to be used for the selective communication between pairs of populations (one channel per pair), with the number of channels depending on the cycle length of the fast oscillation compared to that of the slow oscillation.

4. INVESTIGATING COUPLING IN NEURONAL NETWORKS USING PAIR-WISE MEASURES

The two forms of coupling introduced above, phase coupling and phase-amplitude coupling (PAC), can be used to form temporary connections between multiple neuronal populations. These populations form temporary networks, and their between-population phase coupling strength and phase differences can determine which populations communicate with each other ([Canolty and Knight, 2010](#); [Miller et al., 2012a](#); [Siegel et al., 2012](#)).

Coupling in neuronal networks is usually investigated using *pair-wise measures*, which quantify the coupling strength between pairs of electrodes, for each frequency. Such measures typically quantify coupling strength by a single coefficient for a pair of electrodes, such as the coherence coefficient ([Mormann et al., 2000](#)) or the phase-locking value ([Lachaux et al., 1999](#)). This quantification can then be compared to that of other electrode-pairs, to investigate which electrodes are coupled to each other at which frequency. Here, it is important to distinguish between the situation in which there are *a priori* hypotheses about which electrodes and frequencies show network activity, and the situation in which there are no such hypotheses. In the former situation, networks can be revealed by what is called the *seed-based approach*. Such an investigation involves choosing a seed electrode and frequency, and then quantifying pair-wise coupling strength with all other electrodes. The network is then revealed by choosing a seed electrode and frequency which are central to the network, and then quantifying coupling strength between this electrode and all other electrodes (see e.g. [Miller et al., 2012b](#)).

If however, there are no *a priori* hypotheses about which electrodes and frequencies show relevant network activity, then investigating coupling using a seed-based approach is a tremendous challenge. To illustrate this, consider the number of recording electrodes in typical situations. ECoG recordings in epilepsy patients can easily involve over 100 electrodes (e.g. [Burke et al., 2013](#)), micro-electrode arrays used in e.g. monkey recordings can exceed 200 electrodes (e.g. [Canolty et al., 2012a](#)), and a typical MEG helmet contains around 300 sensors (e.g. [van Ede et al., 2012](#)). Furthermore, recent major EU and US funding initiatives demonstrate that, in the next decade, mass-electrode arrays for intracranial recordings will become much more common, easily reaching up to several 1000s of electrodes. If one combines this with the need for an investigation at multiple frequencies, and a comparison between multiple experimental conditions or time-windows, then a seed-based approach to revealing networks easily requires the visualization of several 1000s of pair-wise interactions. This combinatorial explosion makes the seed-based approach unfeasible. This is a data analysis problem, and it requires techniques that are able to extract revealing patterns from coupling measures.

In addition to the prohibitively large number of pair-wise interactions that have

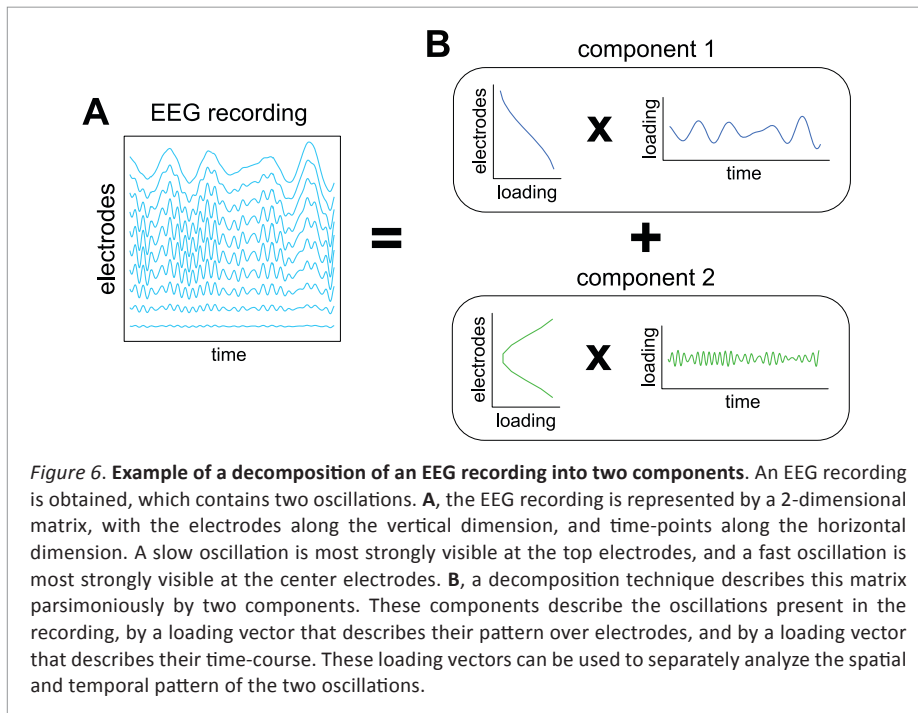
to be investigated, there are also the problems induced by the fact that a single electrode can measure activity from multiple neuronal populations. This is more strongly the case when the distance between neurons and the electrode is large, such as for EEG/MEG, as compared to when it is small, such as for intracranial micro-electrodes. This leads to spatial overlap in the coupling patterns of networks at the level of the electrodes. If one then quantifies the coupling from one electrode to all other electrodes, it can be unclear from which network the observed coupling patterns originate. Investigating networks with overlapping coupling patterns at the electrode-level requires a technique that is capable of separating them.

5. INTRODUCING DECOMPOSITION TECHNIQUES

In this thesis I have developed and used decomposition techniques to investigate coupling in neuronal networks. These mathematical techniques are capable of extracting coupling patterns from electrophysiological data, and separating the patterns from multiple overlapping networks. The developed decomposition techniques uncover these coupling patterns by using the systematic variability in coupling measures over (1) electrodes, (2) frequencies, and (3) trials of an experiment. Importantly, these coupling patterns are more straightforward to interpret than the original data, and are more suitable for analyses. By extracting and analyzing these patterns, a prohibitive amount of seed-based investigations can be avoided.

To illustrate a decomposition, consider the following example (see Fig 6). In part of an EEG experiment we obtain measurements from multiple EEG electrodes over the course of a few seconds. The numbers representing these recordings are arranged in a 2-dimensional matrix (Fig 6A), where one of the dimensions corresponds to the EEG electrodes (vertical in Fig 6A), and the other to the time-points (horizontal in Fig 6A). Two distinct oscillations are present in this recording, a slow one and a fast one. Whereas the slow oscillation is strongest at the electrodes at the top, the fast oscillation is strongest at the middle electrodes. Analyzing these two oscillations separately is difficult, because they overlap in space (electrodes) and in time (time-points). A decomposition technique uses the variability over the two dimensions (space and time), to separate these oscillations into what are called *components*. Each of the components describes one of the oscillations, by two 1-dimensional *loading vectors* (Fig 6B). One of the loading vectors describes the pattern over electrodes (the spatial pattern), and the other describes its time-course (the temporal pattern). The spatial loading vector quantifies how strongly each electrode reflects, or loads, the time-course, and vice versa, the temporal loading vector quantifies how strongly each time-point reflects the spatial pattern. Importantly, because the components describe the spatial and temporal patterns of the oscillations separately, they are easier to interpret and analyze than the original

matrix. The components are also a parsimonious description of the original matrix, because they describe the same patterns with fewer numbers.



6. INVESTIGATING COUPLING IN NEURONAL NETWORKS USING DECOMPOSITION TECHNIQUES

In this thesis, I present new decomposition techniques that can reveal networks that are formed by phase coupling, also denoted as phase-coupled oscillatory networks, and networks formed by PAC. These techniques identify networks by making use of the systematic variability in high dimensional arrays of coupling measures. This high dimensionality is advantageous, because each dimension provides additional information with which networks can be identified, and separated from other networks.

To identify *phase-coupled oscillatory networks*, I analyzed 4-dimensional arrays of phase coupling measures, involving the dimensions space (1) by space (2) by frequency (3) by trial (4). The first two dimensions of this array, describe which electrodes are coupled to each other. The third dimension describes at which frequency this coupling occurs, and the fourth dimension at which trials of an experiment this occurs. To identify *PAC networks*, I analyzed 4-dimensional arrays of PAC measures, involving the dimensions space (1) by space (2) by frequency (3) by

frequency (4). The first two dimensions describe which electrode provides the high frequency amplitudes involved in the coupling, and which electrode provides the low frequency phase. The last two dimensions describe which frequency provides the amplitude involved in the coupling, and which frequency provides the phase.

The techniques for extracting phase-coupled oscillatory networks and PAC networks both extract components, and each component represents a network. These components can reveal interesting properties of these networks, because they allow for separately investigating patterns over space, frequency, and trials. The spatial patterns of the components are described by *spatial maps* (loading vectors for the various spatial dimensions). These spatial maps describe which electrodes are coupled to each other by a single number per electrode, which straightforwardly reveals which electrodes are part of a network. In the case of PAC, there are two spatial maps per component, which separately describe the electrodes that provide phase information and those that provide amplitude information for the coupling. The coupling frequencies of components from both techniques are described by *frequency profiles* (loading vectors for the frequency dimensions). These frequency profiles describe which frequencies are involved in the network, also by a single number per frequency. For the PAC networks there are two frequency profiles, and they describe which amplitude-providing frequencies and which phase-providing frequencies are involved in the network. Finally, in the case of phase-coupled oscillatory networks, there are also *trial profiles*. These profiles quantify the strength of a network in each trial of an experiment. Importantly, they can be conveniently used to analyze the dependence of network activity on experimental conditions.

7. OVERVIEW OF THE THESIS

In the three chapters that follow, the decomposition techniques are described and used to investigate networks formed by coupling and their properties. In doing so, I make use of two kinds of recording techniques. The first is ECoG, which are intracranial grid recordings directly from the surface of the brain. These recordings were obtained from epilepsy patients. ECoG allows for recording spatially specific neuronal activity simultaneously from many brain regions, which makes it highly suitable for revealing distributed neuronal networks formed by the coupling of oscillations. I used ECoG to investigate PAC networks, and to demonstrate our technique for extracting phase-coupled oscillatory networks. The second recording technique is MEG, which measures the magnetic fields produced by electrical brain activity using sensors surrounding the head. These recordings were obtained from healthy participants. MEG en EEG recordings are much more common than ECoG recordings, but they suffer strongly from spatial overlap at the sensor/electrode-level of neuronal activity produced by different populations. I used MEG to demonstrate

that our technique for extracting phase-coupled oscillatory networks is capable of separating such overlapping activity. Below follows an outline of each of the three chapters.

In **chapter 2**, I investigate PAC networks in ECoG recordings using the decomposition technique for extracting PAC networks as described above. Extracted PAC networks are shown to be widely spatially distributed, and involve diverse frequencies. Additionally, PAC had strong diversity in its preferred coupling phases. Using the decomposition technique, I show that this diversity originates from the phase-providing oscillations. This is interesting, because it reveals temporal characteristics of the extracted PAC networks: high amplitudes of the fast oscillations occurred closely together in time. These temporal characteristics, together with the spatial distribution, phase diversity, and frequency diversity of PAC networks, could make PAC a flexible mechanism for the selective communication in neuronal networks.

In **chapter 3**, I present the decomposition technique that is capable of extracting phase-coupled oscillatory networks, which is denoted as SPACE. This technique uses a plausible model of a neurobiological rhythm: a spatially distributed oscillation which involves multiple frequencies with frequency-specific between-electrode phase differences. Because of this, it is capable of characterizing networks in a neurobiologically informative way. I validate the technique by extracting example networks from ECoG recordings. These example networks show that it is capable of uncovering networks with interesting patterns of between-electrode phase differences that vary as a function of frequency, such as travelling waves. Using simulations, I show that the technique can recover networks in the context of neurobiologically realistic noise.

In **chapter 4**, I demonstrate the usefulness of SPACE for analyzing extracranial brain signals, such as EEG or MEG. I do this by investigating the spatial and frequency diversity of neuronal activity in MEG recordings, as well as its task modulations using the trial profiles. Phase-coupled oscillatory networks, and other activity patterns, are uncovered in MEG recordings. These patterns of neuronal activity strongly overlapped, which highlights the capability of the technique to separate and characterize neuronal activity on the basis of its patterns of between-sensor phase coupling. Using the trial profiles, a multifaceted task modulation of the strength of these activity patterns is revealed.

Chapter 2

Phase-amplitude coupling
in human ECoG is spatially
distributed and phase
diverse

ABSTRACT

Spatially distributed phase-amplitude coupling (PAC) is a possible mechanism for selectively routing information through neuronal networks. If so, two key properties determine its selectivity and flexibility, phase diversity over space and frequency diversity. To investigate these issues we analyzed 42 human electrocorticographic (ECoG) recordings from 27 patients performing a working memory task. We demonstrate that (1) spatially distributed PAC occurred at distances over 10 cm, (2) involved diverse preferred coupling phases, and (3) involved diverse frequencies. Using a novel technique (N-way decomposition based on the PARAFAC model), we demonstrate that (4) these diverse phases originated mainly from the phase-providing oscillations. With these properties, PAC can be the backbone of a mechanism that is able to separate spatially distributed networks operating in parallel.

Adapted from:

van der Meij R, Kahana M, Maris E (2012). *Phase-amplitude coupling in human electrocorticography is spatially distributed and phase diverse*. Journal of Neuroscience.

INTRODUCTION

In a fast-changing complex environment, it is essential that the brain can selectively route information through multiple networks operating in parallel. Oscillatory coupling provides the temporal and spatial dynamics necessary to implement this. Oscillations reflect rhythmic modulations of neuronal excitability, affecting the efficacy of incoming EPSPs and the probability of spike output. It has been proposed that coherently oscillating networks create selective windows of communication between neuronal groups by synchronizing their periods of maximum excitability (Fries, 2005). We investigated spatially distributed phase-amplitude coupling (PAC), a phenomenon that may emerge in spatially distributed oscillating networks. We observed two key properties, phase diversity and frequency diversity, that allow spatially distributed PAC to flexibly and selectively route information through distributed neuronal networks.

PAC describes the coupling between the phase of a slow oscillation and the amplitude of a fast oscillation, with the highest amplitude occurring at the so-called preferred coupling phase (Jensen and Colgin, 2007; Lakatos et al., 2008; Canolty and Knight, 2010). PAC has been observed in multiple species, including rats (Chrobak and Buzsaki, 1998; Sirota et al., 2008; Tort et al., 2008), monkeys (Lakatos et al., 2005; Lakatos et al., 2008), and humans (Schack et al., 2002; Bruns and Eckhorn, 2004; Mormann et al., 2005; Canolty et al., 2006; Cohen, 2008; Osipova et al., 2008; Miller et al., 2010b; Voytek et al., 2010; Maris et al., 2011). A recent study has shown that PAC in human ECoG is widely spatially distributed (Maris et al., 2011), which is a key requirement for routing information through distributed networks. Using a novel decomposition technique, this study showed that amplitude- and phase-providing oscillations occurred at broadly distributed sites. However, the decomposition only allowed for diversity over space in the preferred coupling phases of the amplitude-providing oscillations, and not of the phase-providing oscillations. Selective routing of information could greatly benefit from phase diversity in the phase-providing oscillation, as its phase could be used to select neuronal populations for interactions. Such phase diversity has not been shown so far. Frequency diversity is another key property determining the flexibility of PAC in selective routing of information. Although theta-gamma PAC dominates the literature, recent reports (He et al., 2010; Miller et al., 2010b; Maris et al., 2011) have shown that PAC occurs at many different frequencies.

We analyzed ECoG recordings from 27 patients to investigate the phase diversity and frequency diversity in spatially distributed PAC. We show that PAC occurred over distances that exceed 10 cm, that there was strong phase diversity, and that it involved diverse frequencies. Using a modified version of N-way decomposition

based on the PARAFAC model ([Maris et al., 2011](#)), we were able to show that spatially distributed phase-providing oscillations were the main source of phase diversity. These oscillations showed large and consistent phase diversity over space. In contrast, the amplitude-providing oscillations showed bursts that were much more synchronized. This phase and frequency diversity are two important attributes that determine how flexibly and selectively spatially distributed PAC can route information through distributed networks operating in parallel.

MATERIALS AND METHODS

SUBJECTS

27 patients (12 female, 15 male) with pharmaco-resistant epilepsy were implanted with subdural grid, strip and depth-electrodes prior to resective surgery. Patients were selected from a large pool of datasets if they had more than 15 electrodes and more than 70 trials per recording session after artifact rejection. Informed consent was obtained from the patients or their guardians if they were underage. The research protocol was approved by the appropriate institutional review boards at the Hospital at the University of Pennsylvania (Philadelphia, PA), Children's Hospital (Philadelphia, PA), University Clinic (Freiburg, Germany), Children's Hospital (Boston, MA), and Brigham and Women's Hospital (Boston, MA). Some of the datasets have been analyzed before, but the analyses presented here are novel (see e.g. [Rizzuto et al., 2003](#); [Raghavachari et al., 2006](#); [Jacobs and Kahana, 2009](#); [van Vugt et al., 2010](#)) or complementary ([Maris et al., 2011](#)).

EXPERIMENTAL PARADIGM

Recordings were obtained from patients performing a Sternberg working memory task ([Sternberg, 1966](#)). Patients were presented with a series of letters (from 1 to 6) on a computer screen that they had to remember. At the beginning of each trial a fixation cross was presented, followed by 700ms of letter presentation, and then by 275-350ms (uniformly distributed) of blank screen. The last letter was followed by a retention interval of 425-575ms (uniformly distributed), after which a probe letter was presented. Patients had to indicate by key press whether the probe letter was part of the previous letter series. After the key press, visual feedback was given and the patient could initiate the next trial by another key press. The main purpose of our study was to characterize fundamental properties of PAC (spatial distribution, phase diversity, and frequency diversity), and therefore we did not investigate any behavioral contrasts (e.g. correct vs incorrect) or stimulus type contrasts (e.g.

number of letters). We only analyzed the period between the fixation cross and the onset of the probe letter, during which patients were actively engaged.

RECORDINGS AND PREPROCESSING

Electrophysiological recordings were obtained from subdural grid, strip and depth-electrodes. Recordings were sampled at 256 to 1024 Hz, depending on the hospital, and were referenced to a common average reference. Note: using a nearest neighbor bipolar referencing scheme did not substantially change the electrode pairs that showed strong PAC, nor the level of diversity in the preferred coupling phases. Only recordings from grid and strip electrodes were analyzed. Artifact rejection was performed by visual inspection. All trials and/or electrodes contaminated by epileptiform activity were removed. To remove power line noise, we band-stop filtered the data with 1 Hz windows at 50 and 60 Hz (depending on continent) and at other frequencies containing line noise. All recordings were band-pass filtered between 0.01 and 100 Hz. All filters were 4th order Butterworth.

Electrode locations were determined by first co-registering a postoperative computed tomography scan with a higher resolution preoperative magnetic resonance image. All patients' brains were normalized to Talairach space ([Talairach and Tournoux, 1988](#)) and coordinates were subsequently computed. All preprocessing and the first step of our spectral analyses were performed using the FieldTrip open source MATLAB toolbox ([Oostenveld et al., 2011](#)) developed at the Donders Institute for Brain, Cognition and Behaviour (<http://www.ru.nl/neuroimaging/fieldtrip>).

AMPLITUDE-WEIGHTED PHASE-LOCKING FACTOR

To quantify PAC, we calculated amplitude-weighted phase-locking factors (wPLFs). These coefficients were calculated using the output of a time-resolved spectral analysis. This spectral analysis was performed by convolving the data with complex-valued wavelets, one for every frequency of interest. All wavelets were obtained from an element-wise multiplication of a three-cycle complex exponential and a Hanning taper of equal length. For every given sampling rate, we only used frequencies for which the corresponding wavelet has an integer number of samples per cycle. Under this constraint, we selected frequencies between 2 and 67 Hz in steps of approximately 1 Hz. This resulted in one complex-valued time-series per trial per frequency bin, called the wavelet transform, describing the time-varying amplitudes and phases.

A wPLF is a complex-valued number representing the relation averaged over time between the phase of one oscillation (obtained from electrode k at frequency m) and the amplitude of another (obtained from electrode j at frequency l).

Thus, a wPLF is indexed by an electrode pair (indices k and j) and a frequency pair (indices m and l). A wPLF is normalized, with magnitude ranging from 0 to 1. The magnitude of a wPLF measures the consistency, over trials, of the phase of the phase-providing oscillation at which amplitude increases of the amplitude-providing oscillations occur. The angle of a wPLF indicates this phase, called the preferred coupling phase. A wPLF is amplitude-weighted because trials with high amplitudes in one oscillation have a bigger influence than trials with low amplitudes.

The calculation of the wPLFs can be expressed as follows:

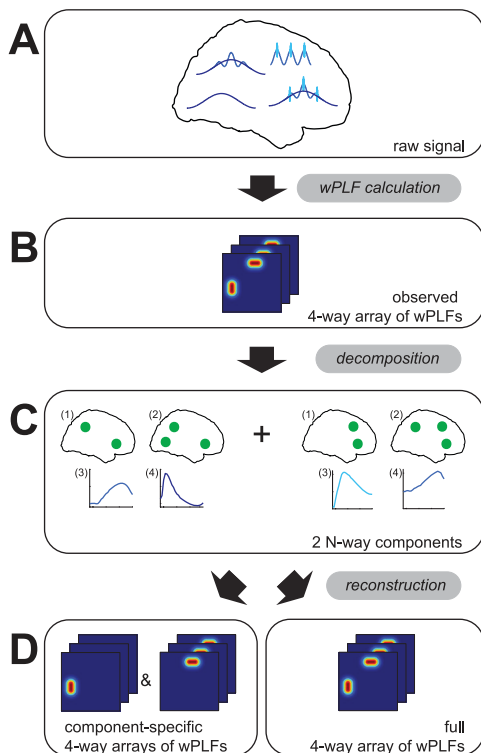
$$\text{wPLF}_{jklm} : \frac{\langle A(x_j, f_l), W(x_k, f_m) \rangle}{\|A(x_j, f_l)\| \cdot \|W(x_k, f_m)\|}$$

in which $A(x_j, f_l)$ denotes the mean-centered absolute-value of the wavelet transform at frequency l of the raw signal x of electrode j , $W(x_k, f_m)$ denotes the wavelet transform at frequency m of the raw signal x of electrode k , $\langle \cdot, \cdot \rangle$ denotes the inner-product and $\| \cdot \|$ denotes the norm. wPLFs were computed for all possible electrode and frequency pairs. Thus, each electrode in the dataset provides amplitude and phase information for PAC with all other electrodes, and for all estimated frequencies. This results in one 4-way array of wPLFs for each dataset. The dimensions correspond to (1) amplitude-providing electrodes (of size J), (2) phase-providing electrodes (of size K), (3) amplitude-providing frequencies (of size L) and (4) phase-providing frequencies (of size M). We show a schematic of the construction of this 4-way array in Figure 1A and 1B.

SELECTING SIGNIFICANT WPLFs

As a part of the analysis of the 4-way arrays of wPLFs, statistically significant wPLFs were selected. Statistical significance was assessed by comparing every wPLF to a dataset-specific reference distribution obtained under the null hypothesis that the time-varying amplitudes and phases are uncorrelated. Reference distributions were created by randomly pairing the amplitudes of one trial with the phases of another trial. This was repeated 50 times for each dataset, providing 50 random wPLFs for each electrode pair and frequency pair. A normal probability density function was then estimated for every wPLF, using the mean and standard deviation of the magnitude of these 50 random wPLFs. wPLFs were selected if their magnitude surpassed the 99th percentile of this estimated probability density function. Apart from this selection based on a statistical threshold, we also removed all wPLFs where the phase-providing frequency is higher than or equal to the amplitude-providing frequency.

Figure 1. Schematic representation of analyses. The data flow in our analyses is illustrated by a schematic decomposition and reconstruction of two different PAC patterns, one between a slow and a medium fast rhythm, and one between the medium fast and a very fast rhythm. These two PAC patterns have a different spatial distribution. After calculating a 4-way array of wPLFs, the two PAC patterns are separated in two different components using our N-way decomposition. The two patterns can then be reconstructed individually into two 4-way arrays of wPLFs, or jointly into one 4-way array of wPLFs. For the purpose of simplicity, we have left out phase information in this schematic. Phase information is crucial throughout our analyses, and is important for separating PAC patterns. **A**, PAC at 4 electrodes involving 3 oscillations. Not all oscillations are present at each location. **B**, 4-way array of wPLFs obtained from the raw data in A. The dimensions of this 4-way array are (1) amplitude-providing electrodes, (2) phase-providing electrodes, (3) amplitude-providing frequencies, and (4) phase-providing frequencies. **C**, Decomposition of the 4-way array of wPLFs in B into two components. Each component describes one PAC pattern, and each consists of an (1) amplitude-providing spatial map, a (2) phase-providing spatial map, an (3) amplitude-providing frequency profile, and a (4) phase-providing frequency profile. **D**, Reconstruction of 4-way arrays of wPLFs based on the decomposition in C. On the left, we show the component-specific reconstruction, where each component is used to create one 4-way array of wPLFs, which is determined by only one PAC pattern. On the right, we show the full reconstruction, resulting in a 4-way array of wPLFs describing both PAC patterns. For details, see Materials and Methods. PAC = phase-amplitude coupling; wPLF = weighted phase-locking factor.



EVALUATING THE RELIABILITY OF PREFERRED COUPLING PHASES

To evaluate the reliability of the preferred coupling phase of our significant wPLFs, we used a split-half procedure. This involved a random split of the trials of each dataset in two partitions, followed by constructing a 4-way array of wPLFs for both partitions. In this way, we obtained two independent estimates of every wPLF. The more the preferred coupling phase is influenced by random noise, the larger the phase difference will be between the two estimates. Based on these split-half wPLFs, we calculated a split-half reliability coefficient:

$$\text{split-half reliability: } \left| \frac{1}{J} \sum_{j=1}^J \exp(i\theta_{1j} - \theta_{2j}) \right|$$

In this formula, we first take the difference between the preferred coupling phase of the wPLFs of the first partition θ_{1j} and of the second partition θ_{2j} . We do this for all J significant wPLFs, as determined above (using the 4-way array of wPLFs based on all trials). These phase differences are then expressed as unit-magnitude complex numbers and averaged over all significant wPLFs (indexed by j). The split-half reliability coefficient is then attained by taking the absolute value of the resulting complex number, also known as the mean resultant vector of phase differences. Such a coefficient was calculated for each dataset.

N-WAY DECOMPOSITION BASED ON THE PARAFAC MODEL

We use N-way decomposition to refer to the decomposition of an N-way array with more than 2 dimensions. Unlike 2-way decompositions, such as principal and independent component analysis, N-way decomposition has not been used extensively in neuroscience (for exceptions see [Beckmann and Smith, 2005](#); [Morup et al., 2006](#)). N-way decomposition decomposes an N-way array into several components, each consisting of N loading vectors, one corresponding to each dimension of the original array. Every component describes one aspect of the array, and the original array can be reconstructed from its components. There are multiple models for decomposing an N-way array, but here we will only describe and use the most parsimonious decomposition, which is based on the PARAFAC model ([Harshman, 1970](#)) (PARAllel FACtor analysis), also known as CANDECOMP ([Carroll and Chang, 1970](#)) (CANonical DECOMPosition). This decomposition can be derived from a few plausible assumptions about the spatio-spectral characteristics of the sources that are involved in PAC ([Maris et al., 2011](#)). Crucially, for N-way arrays with more than two dimensions ($N > 2$), N-way decomposition based on the PARAFAC model is unique up to scaling and permutation, which are two transformations that do not affect the interpretation of the components. The N-way PARAFAC algorithm we used (see below) will be implemented in the FieldTrip open source MATLAB toolbox ([Oostenveld et al., 2011](#)) developed at the Donders Institute for Brain, Cognition and Behaviour (<http://www.ru.nl/neuroimaging/fieldtrip>).

N-WAY DECOMPOSITION OF 4-WAY ARRAYS OF WPLFS INTO TWO COMPLEX-VALUED SPATIAL MAPS AND TWO FREQUENCY PROFILES

We used N-way decomposition based on the PARAFAC model to decompose each 4-way array of wPLFs into one or more components. We show this schematically in Figure 1C. Each component consists of 4 loading vectors, one for each dimension. Because the first two dimensions of a 4-way array of wPLFs correspond to amplitude- and phase-providing electrodes, the corresponding loading vectors in

a component describe spatial locations. We denote these two loading vectors as amplitude-providing and phase-providing spatial maps. Further, because the last two dimensions of a 4-way array of wPLFs correspond to amplitude- and phase-providing frequencies, we denote these as amplitude- and phase-providing frequency profiles. Each component thus describes a PAC pattern that is characterized by an amplitude- and phase-providing spatial map, and an amplitude- and phase-providing frequency profile.

The decomposition of a single wPLF can be expressed in a formula involving element-wise multiplication:

$$\text{wPLF}_{jklm} = \sum_{f=1}^F a_{jf} b_{kf} c_{lf} d_{mf}$$

A wPLF_{jklm} is described as the sum, over components f , of the product of the loadings $a_{jf} b_{kf} c_{lf}$ and d_{mf} . These loadings are organized in the loading matrices A, B, C and D respectively. Matrices A and B contain as columns the amplitude- and phase-providing spatial maps, and matrices C and D contain as columns the amplitude-and phase-providing frequency profiles. The spatial maps A and B are complex-valued, whereas frequency profiles C and D are real-valued. This differs from the previous approach (Maris et al., 2011), where only the amplitude-providing spatial map (A) was complex-valued, reflecting the assumption that there are no between-electrode phase differences in the phase-providing oscillation over electrodes (except for phase differences of exactly $+/-\pi$, which are translated into loadings that have different signs). For our current approach, investigating phase diversity in PAC, it is essential that the phase-providing spatial map B is complex-valued as well.

DECOMPOSITION OF PREFERRED COUPLING PHASES IN PAC INTO RELATIVE PHASES IN TWO SPATIAL MAPS

Our N-way decomposition decomposes all preferred coupling phases in spatially distributed PAC into two complex-valued spatial maps. As such, phase diversity in PAC is fully explained by the phase relations *within* the two spatial maps. Phase diversity in the phase-providing spatial map reflects consistent phase differences of the phase-providing oscillation over electrodes. Phase diversity in the amplitude-providing spatial map reflects time delays between amplitude increases of the amplitude-providing oscillation. The exact time delay depends on the cycle length of the phase-providing oscillation. In Figure 2, we show a schematic of this decomposition. This schematic shows PAC between 5 electrodes (Fig. 2A), and their decomposition into an amplitude-providing (Fig. 2B) and a phase-providing spatial map (Fig. 2C). The phase relations within the amplitude-providing spatial map

reflect between-electrode time delays between bursts of the amplitude-providing oscillations (Fig. 2B). The phase relations within the phase-providing spatial map reflect the between-electrode phase differences in the phase-providing oscillations (2C). Note, we cannot distinguish between (1) the case where every cycle of the phase-providing oscillation shows a burst of the amplitude-providing oscillation (first row of table in 2A) and (2) the case where only some cycles show such a burst (second row of table in 2A).

INDETERMINACIES OF THE PARAFAC MODEL

The spatial maps and frequency profiles can only be determined up to scaling and permutation. Because of permutation indeterminacy, the order of components is irrelevant. And because of scaling indeterminacy, any loading vector of the same component can be multiplied with any number, as long as another loading vector of the same component is multiplied with the inverse of this number. Moreover, because the two spatial maps are complex-valued, there is phase indeterminacy. If one spatial map is multiplied with $\exp(-i\theta)$ and the other is multiplied with $\exp(i\theta)$, then all phases are shifted by θ , yet the decomposition remains exactly the same. Note that this does not affect the phase *differences* within a component. Because of the above, the components in our decomposition are sorted by explained variance, all loading vectors are normalized to have a norm of 1, and all spatial maps have an average magnitude-weighted phase of 0. This means that absolute phases inside a spatial map cannot be interpreted. To stress that, within a component, only between-electrode phase *differences* can be interpreted, the phase of the spatial maps will be denoted as relative phases. Analogously, the magnitude of each electrode in a spatial map, and the value of each frequency in the frequency profiles can only be interpreted relative to the other electrodes in the map and the other frequencies in the profile respectively.

RECONSTRUCTING 4-WAY ARRAYS OF WPLFs AND EVALUATING THEIR ACCURACY

Using the extracted components, we can reconstruct each 4-way array of wPLFs. We computed reconstructions based on all components to evaluate the accuracy of the N-way decomposition for every dataset. We also computed reconstructions based on a single component to select significant electrodes in a spatial map. We show both reconstructions schematically in Figure 1D. The reconstruction of wPLF x_{jklm} is denoted by \hat{x}_{jklm} and, when based on all components, it is calculated as follows:

$$\hat{x}_{jklm} = \sum_{f=1}^F a_{jf} b_{kf} c_{lf} d_{mf}$$

Thus, the wPLF at amplitude- and phase-providing electrodes j and k and

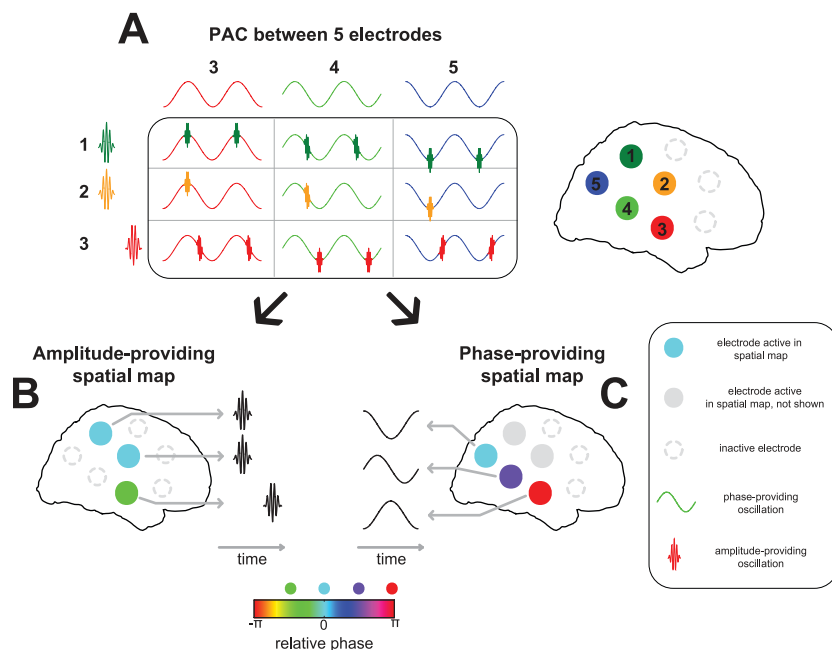


Figure 2. Preferred coupling phases in spatially distributed PAC are decomposed into relative phases in amplitude- and phase-providing spatial maps. Phase diversity of PAC is fully explained by the two complex-valued spatial maps (i.e., phase variability over space). **A**, Schematic representation of PAC between 5 electrodes. **B**, Schematic amplitude-providing spatial map with three electrodes that show amplitude bursts. Color indicates the relative phase of the electrodes. The third electrode has a phase shift of $\pi/2$ relative to the other electrodes. This reflects a time-offset of the corresponding amplitude-providing oscillation, given by the phase-offset and the cycle length of the phase-providing oscillation in **C**. **C**, Same as **B**, but for the phase-providing spatial map. The phase-providing oscillations have a phase offset equal to their relative phases. Note, we cannot distinguish between the case where every cycle of the phase-providing oscillation has a burst of the amplitude-providing oscillation (first row of table) and the case where only some cycles of the phase-providing oscillation have a burst (second row of table). PAC = phase-amplitude coupling; wPLF = weighted phase-locking factor.

at amplitude- and phase-providing frequencies l and m can be reconstructed by taking the product $a_{jl}b_{kf}c_{lf}d_{mf}$ and summing over the components. When based on a single component f , x_{jklm} is equal to the product $a_{jf}b_{kf}c_{lf}d_{mf}$.

We evaluated the accuracy of reconstructed wPLFs (based on all components) by a coefficient comparing the reconstructed wPLFs to the observed wPLFs. This coefficient was calculated as follows:

$$\text{reconstruction accuracy: } \frac{\langle \overline{\text{vec}(X)}, \text{vec}(\hat{X}) \rangle}{\|X\| \cdot \|\hat{X}\|}$$

We took the inner product \langle , \rangle of the complex conjugate of the vectorized 4-way

array of observed wPLFs $\overline{\text{vec}(X)}$ and the vectorized 4-way array of reconstructed wPLFs $\text{vec}(\widehat{X})$. This inner product is then normalized by the product of the vector norms, and the absolute value is taken. This number ranges from 0 to 1. It can be interpreted as a generalized cosine of the angle between two complex-valued vectors.

REPORTING ON THE RESULTS OF THE N-WAY DECOMPOSITION

To report the decomposition results we selected electrodes on the basis of component-specific reconstructed wPLFs. This selection is necessary because we are interested in the phases of the two types of spatial maps, and these phases can only be reliably estimated for electrodes that are involved in the component. We performed our electrode selection by first reconstructing a 4-way array of wPLFs on the basis of a single component (see Materials and Methods). Next, this array of reconstructed wPLFs was compared to the reference distribution from the same dataset (see *Selecting significant wPLFs*). When more than one component was extracted from an array of wPLFs, the same reference distribution was used multiple times. An electrode in the amplitude-providing spatial map was selected if any of the reconstructed wPLFs that have this electrode as the amplitude-providing electrode exceeded the 99th percentile of the reference distribution. The same criterion was applied to the phase-providing spatial maps.

We report on phase differences within each spatial map by computing the difference between pairs of selected electrodes. Amongst others, we show phase differences occurring between 0 and +/- π . To demonstrate that these phase differences are reliable (i.e. reflecting true phase differences between 0 and +/- π) we calculated the split-half reliability of our decomposition results. This involved randomly splitting the trials of each dataset, and calculating two 4-way arrays of wPLFs, one for each of the two sets of trials. We then decomposed both arrays into the same number of components and computed the phase differences between pairs of selected electrodes (see above). In addition to this selection based on statistical significance, we selected electrode pairs with phase differences in the intervals from $-2\pi/3$ to $-\pi/3$ and from $\pi/3$ to $2\pi/3$. For these electrode pairs, we calculated the following split-half reliability coefficient:

$$\text{split-half reliability: } \left| \frac{1}{J} \sum_{j=1}^J \exp(i\theta_{1j} - \theta_{2j}) \right|$$

In this formula, we first take the difference between the two independent estimates of the phase difference for electrode pair j , one obtained from the first (θ_{1j}) and the other from the second partition (θ_{2j}). We do this for all J selected electrode

pairs. All phase differences are then expressed as unit-magnitude complex numbers and averaged, producing a mean resultant vector. The split-half reliability coefficient is then obtained by taking the magnitude of this mean resultant vector.

AN ALTERNATING LEAST-SQUARES ALGORITHM FOR N-WAY DECOMPOSITION OF A 4-WAY ARRAY OF WPLFs

N-way decomposition according to the PARAFAC model can be performed using an alternating least-squares (ALS) algorithm that has been implemented for real-valued arrays (Bro, 1998) and for complex-valued arrays (Sidiropoulos et al., 2000). The algorithm for complex-valued arrays produces only complex-valued components. In contrast, in our application, we decompose a complex-valued array into components that consist of two complex-valued spatial maps and two real-valued frequency profiles. We now describe the algorithm and how we adapted it for complex-valued arrays for our application.

The ALS algorithm is an iterative algorithm with, per iteration, as many steps as the number of different loading matrices. In our case, in every stage of an iteration, a loading matrix' least squares estimate is calculated, while keeping the other loading matrices constant. The algorithm continues until an iteration does not provide an increase in fit over and above the previous iteration. All loading matrices are initialized by random starting values, which are orthogonal over components. The algorithm can converge to a suboptimal solution, which is a local minimum of the least-squares objective function that we want to minimize. This is undesirable but can be controlled for by running the algorithm many times with random starting values. If the algorithm converges multiple times to the same solution using different random starting values, and this solution also achieves the smallest objective function value, then it is assumed to have converged to the global minimum. It is crucial to detect and discard degenerate models, which occur when component pairs are nearly identical but negatively correlated (Bro, 1998). To perform an N-way decomposition based on the PARAFAC model it is also necessary to estimate the number of components, or the so-called rank of the array. We determined this rank using a split-half procedure, identical to the procedure in Maris et al. (2011).

To describe our ALS algorithm, it is convenient to make use of the Khatri-Rao product $| \otimes |$, which is defined as follows:

$$A| \otimes |B = \left[a_1 \otimes b_1 \ a_2 \otimes b_2 \dots a_F \otimes b_F \right]$$

This applies to any matrix A and B with an equal number of columns. The Khatri-Rao product is defined as the concatenation of the Kronecker tensor products \otimes of column 1 to F of A and B . Using the Khatri-Rao product, we can express the 4-way PARAFAC model as follows:

$$X^{J \cdot KLM} = A(D| \otimes |C| \otimes |B)^T + E^{J \cdot KLM}$$

In this formula, $X^{J \cdot KLM}$ denotes a 2-way array that is obtained by unfolding the 4-way array X along its last three dimensions. The formula expresses that $X^{J \cdot KLM}$ is the sum of a model term $A(D| \otimes |C| \otimes |B)^T$ and an error term $E^{J \cdot KLM}$. The model term is a function of the loading matrices A, B, C and D with dimensions $J \times F$, $K \times F$, $L \times F$ and $M \times F$, respectively. F , the number of columns in each loading matrix, denotes the number of components being extracted. In our application, $J = K$ (the number of electrodes), and $L = M$ (the number of frequencies). The error term $E^{J \cdot KLM}$ is necessary to express the fact that the observed wPLFs may differ from the model wPLFs (which are determined by the loadings) as a result of sampling error.

Each least squares estimate is calculated using the following equation. Because of the symmetry between the four loading matrices, we only present the estimation equations for one loading matrix, which we denote by A . A single iteration of the algorithm estimates all loading matrices once, and then determines the fit. By keeping the loading matrices B , C and D fixed, the least squares estimation for loading matrix A is the following:

$$A = X^{I \cdot JKL} \cdot \overline{Z} \cdot \overline{(Z^* Z)^+},$$

where $Z = (D| \otimes |C| \otimes |B)$, \overline{Z} denotes the complex conjugate of Z , Z^* denotes the complex conjugate transpose of Z and $+$ denotes the Moore-Penrose pseudoinverse. The least-squares estimate of a real-valued loading matrix (matrix C and D) is obtained by replacing Z and X by the real-valued matrices $Z = [Re(Z) Im(Z)]$, which is the row-wise concatenation of $Re(Z)$ and $Im(Z)$ (the real and the imaginary parts of Z) and $X = [Re(X) Im(X)]$, which is the column-wise concatenation of $Re(X)$ and $Im(X)$.

RESULTS

We analyzed PAC in human ECoG recordings from 42 datasets obtained from 27 patients performing a working memory task (see Materials and Methods). We investigated the phase diversity of spatially distributed PAC by means of weighted phase-locking factors (wPLFs). These wPLFs are complex-valued association measures, quantifying coupling between the phase of one oscillation and the amplitude of another, averaged over time (see Materials and Methods). Our wPLF is a correlational and not a causal measure. To reflect this, we use the causally neutral terms “phase-providing” and “amplitude-providing” to denote the first and respectively the second oscillation. wPLFs were computed for all amplitude- and

phase-providing electrodes and frequencies. This results in a 4-way array of wPLFs. As an example, we show one slice of such a 4-way array (Fig. 3A), containing the wPLFs for all frequency pairs and a single electrode pair. For this electrode pair, the strongest coupling is between the phase of a theta oscillation (center frequency 6 Hz) and the amplitude of a beta/low-gamma oscillation (center frequency 23 Hz). The preferred coupling phase is π , which corresponds to the trough of the theta oscillation.

We used two approaches to investigate phase diversity in spatially distributed PAC, one based on selecting significant wPLFs from the 4-way arrays (one array for every dataset), and the other based on a decomposition of each of these arrays. We first report on the results obtained by selecting significant wPLFs, showing that PAC

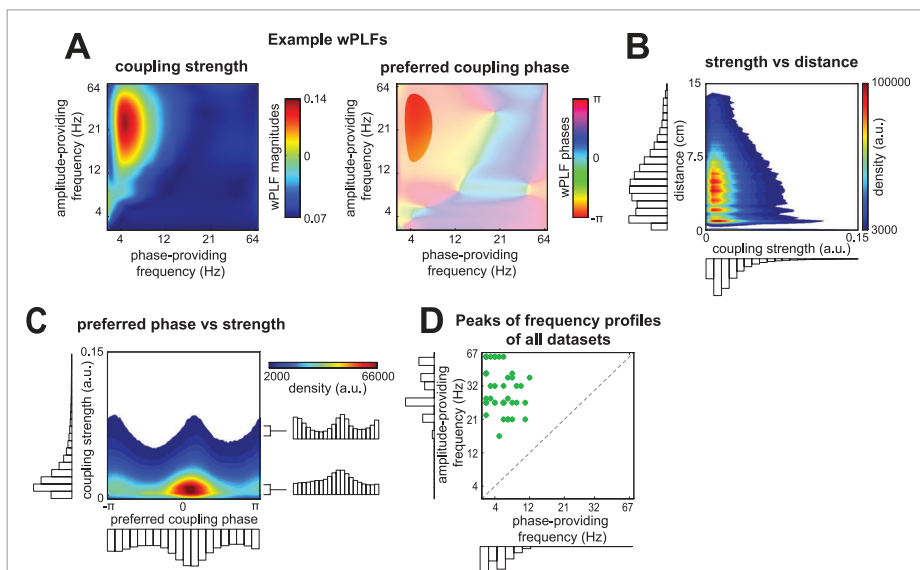


Figure 3. PAC occurred over long distances, has diverse preferred coupling phases and involved many frequencies. **A.** Example wPLFs for one electrode pair. For this electrode pair, the strongest coupling is between the phase of a theta oscillation (\sim 3-8 Hz) and the amplitude of a beta/gamma oscillation (\sim 18-42 Hz). The preferred coupling phase is π , which corresponds to the trough of the theta oscillation. Color bar codes reflect wPLF magnitude and phase. **B.** Density of the significant wPLFs from all datasets as a function of their strength and the distance between the amplitude- and phase-providing electrodes. The majority of PAC occurs at distances around \sim 6 cm and can go up to \sim 14 cm. Color bar code reflects the density of wPLFs at each XY-coordinate. **C.** Density of the significant wPLFs as a function of their preferred coupling phase and their strength. PAC occurs with diverse preferred coupling phase, with most preferred phases around the peak of the phase-providing oscillation (angle = 0). However, especially for the wPLFs that show a strong coupling, preferred phases also cluster at the trough (angle = $+\text{-} \pi$). Color bar code same as in B. **D.** Scatter plot of the peaks of the frequency profiles obtained from the significant wPLFs (see Materials and Methods). The peak phase-providing frequencies show a substantial spread, ranging from delta to alpha, and so do the amplitude-providing frequencies, ranging from beta to gamma. PAC = phase-amplitude coupling; wPLF = weighted phase-locking factor.

occurred over long distances with substantial phase diversity. Next, we report on the decomposition results, showing that this phase diversity originated mainly from the spatially distributed phase-providing oscillations.

PAC OCCURRED OVER LONG DISTANCES, INVOLVED DIVERSE PREFERRED COUPLING PHASES, AND INVOLVED MANY FREQUENCIES

We selected statistically significant wPLFs from each of the 42 datasets. Significance was assessed by comparing every wPLF to a reference distribution obtained under the null hypothesis of independence of phases and amplitudes (see Materials and Methods). wPLFs were selected if their magnitude exceeded the 99th percentile of this distribution. On average, 15.7% (SD = 9.0%) of the wPLFs were selected from each of the 42 datasets. These were combined into one large data array used for all analyses on significant wPLFs. The contribution of each of the 42 datasets to this data array was on average 2.4% (SD = 2.3%), and the contribution of each of the 27 patients was on average 3.7% (SD = 3.5%).

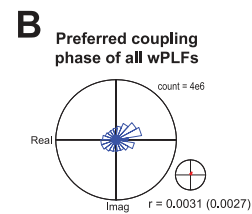
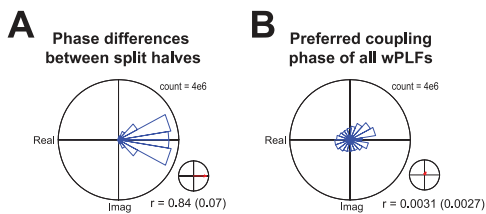
To investigate the spatial extent of the observed PAC we computed the Euclidian distance (using Talairach-coordinates) between all electrode pairs involved in the significant wPLFs. We constructed the density of wPLFs as a function of their strength (horizontal axis) and the distance between electrodes within a pair (vertical axis) (Fig. 3B). We observed that (1) PAC occurred predominantly at distances around 6 cm, (2) PAC occurred at distances as large as 14 cm and (3) PAC strength decreased with distance.

Next, we investigated the diversity in preferred coupling phases. We constructed the density of significant wPLFs as a function of their phase and their strength (Fig. 3C). We make the following three observations: (1) PAC occurred with diverse preferred coupling phases, (2) for weak coupling, phases were clustered around the peak of the phase-providing oscillation (phase = 0), and (3) for strong coupling, phases were clustered both around the peak and the trough (phase = +/- π). The observed diversity in preferred coupling phase is not produced by sampling error resulting from unreliable phase estimates (see Fig. 4).

We obtained peaks of frequency profiles of the amplitude- and phase-providing frequencies of the significant wPLFs for each dataset by counting the significant wPLFs in the three other dimensions. We constructed a scatter plot (Fig. 3D) and observed that PAC involved many frequencies. The peak phase-providing frequencies showed a substantial spread ranging from delta (2 Hz or lower) to alpha (12 Hz), and so do the amplitude-providing frequencies, ranging from alpha (15 Hz) to gamma (67 Hz or higher).

From our analysis of significant wPLFs we conclude that PAC (1) occurred over

Figure 4. Diversity in preferred coupling phase is produced by reliable phase estimates. To estimate the reliability of our phase estimates we randomly partitioned the trials of each dataset into two sets. A 4-way array of wPLFs was then calculated for each of the two sets of trials. **A**, Histogram of phase differences between wPLFs of the first and the second set of trials for all datasets. The majority of phase differences are very close to 0, indicating that the preferred coupling phases are highly similar in the two sets of trials. The reliability coefficient, calculated on these phase differences (see Materials and Methods), was on average 0.84 (SD = 0.07). **B**, For comparison with the reliability results in A, we show the same information for the preferred coupling phase of the wPLFs, instead of their between-set phase differences. The phase histogram shows diversity in preferred coupling phase (same information as in 3C). We calculated the same coefficient as in A, but now applied to the preferred coupling phase (instead of the between-set phase differences) and found that it was on average 0.0031 (SD = 0.0027). The difference with the average reliability coefficient shows that our phase estimates are highly reliable. wPLF = weighted phase-locking factor.



long distances, (2) showed substantial diversity in preferred coupling phases and (3) involved many frequencies. However, analyzing significant wPLFs does not inform us about the spatial distribution of PAC, nor about the origin of the phase diversity. More specifically, we do not know (1) whether the observed long-distance PAC is generated by multiple small spatially separated sources or by one very large source, (2) whether the phase diversity is due to phase differences within a source or between sources, nor (3) how the spatial distribution of the phase-providing electrodes is related to that of the amplitude-providing electrodes. To investigate these issues we decomposed each 4-way array of wPLFs into sets of two spatial maps and two frequency profiles. Importantly, these spatial maps provide information about the spatial distribution of PAC and the origin of the phase diversity.

N-WAY DECOMPOSITION REVEALS THE SPATIAL DISTRIBUTION OF PAC IN SETS OF TWO SPATIAL MAPS AND TWO FREQUENCY PROFILES

To analyze the spatial distribution and phase diversity of PAC we used N-way decomposition based on the PARAFAC model (see Materials and Methods). This method has been used previously (Maris et al., 2011) but in a version that was unable to reveal the phase diversity that we identified (see Materials and Methods). Each 4-way array of wPLFs was decomposed into one or more components. Every component characterizes one PAC pattern, and consists of an amplitude- and a phase-providing spatial map and an amplitude- and a phase-providing frequency profile. Because a dataset may involve multiple PAC patterns, the decomposition can extract multiple components. To illustrate the decomposition, we show an example component of a representative subject (Fig. 5). The spatial maps are shown as grids on a template brain (Fig. 5A and 5B; not all ECoG grids are shown), and the

frequency content is shown in the frequency profiles (Fig. 5C). With respect to the example component, we observed that: (1) both the amplitude- (Fig. 5A) and the phase-providing spatial map (Fig. 5B) had a wide spatial distribution over cortex, (2) the phase-providing spatial map had a wider spatial distribution than the amplitude-providing spatial map, and (3) there was more phase diversity in the phase- than in the amplitude-providing map (Fig. 5A). These observations are representative for all 42 datasets. Note, the phase-providing spatial map in the example component shows a spatial structure similar to that of travelling waves. This was the case for 42 out of 85 components.

The example component (Fig. 5A, 5B and 5C) reflects the main pattern in the original 4-way array of wPLFs. To show this, we selected two electrode pairs that share the same amplitude-providing electrode (electrode 43) but have different phase-providing electrodes (electrode 29 and 57). We show the wPLFs for both pairs, for all frequency pairs (Fig. 5D). The frequencies that exhibit strong coupling closely match the frequency profiles from the decomposition (Fig. 5C). Moreover, the phase difference between the two electrode pairs closely match the phase differences in the phase-providing spatial map (Fig. 5B). (Note, in contrast to between-electrode phase *differences*, absolute phases cannot be interpreted; see Materials and Methods). It is important to note that relative phases in amplitude- and phase-providing spatial maps reflect different properties of spatially distributed PAC (Fig. 2; see Materials and Methods). From the 42 datasets we extracted 85 components, explaining on average 50.7% (SD = 20.1%) of the variance of significant wPLFs. We evaluated the accuracy of the reconstruction of all preferred coupling phases. For the phases of all significant wPLFs, we compared their reconstructed and their corresponding observed values. All magnitudes were set to 1. For every dataset, we calculated a coefficient that quantified reconstruction accuracy (see Materials and Methods), which ranges from 0 to 1. This coefficient of reconstruction was on average 0.70 (SD = 0.15), indicating that the observed wPLFs can be accurately reconstructed from the decompositions.

We now show two sets of aggregated results obtained from all components. First, we investigated the spatial extent of the spatial maps. We constructed a scatter plot of the mean between-electrode Euclidian distance of each spatial map per component (Fig. 6A). We selected electrodes in each spatial map by comparing the component-specific reconstructed wPLFs to the 99th percentile of the reference distribution used to select significant wPLFs (see Materials and Methods). The mean distance was on average higher for the phase- than for the amplitude-providing spatial maps (paired samples t-test; $t(84) = -5.56$, $p < 1e-6$). This shows that our PAC was not generated by distributed sharp-edged waveforms, as both maps would be equally large. This issue has been discussed elsewhere ([Maris et al., 2011](#)).

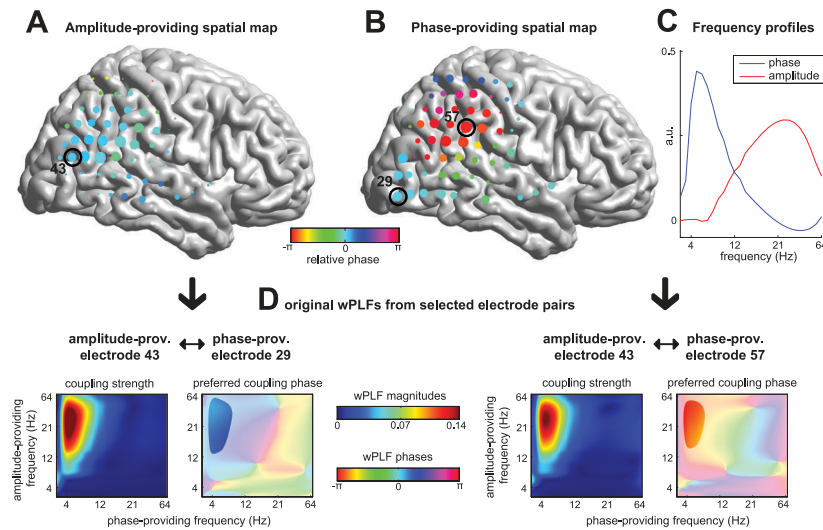


Figure 5. N-way decomposition reveals the spatial distribution in PAC in sets of two spatial maps and two frequency profiles. Each 4-way array of wPLFs from each dataset was decomposed into one or more components, each component being a set of two spatial maps and two frequency profiles. The diversity in the preferred coupling phase is explained by the two complex-valued spatial maps, namely by their phase diversity across space. **A, B, C,** Example component from a representative subject. **A,** Amplitude-providing spatial map. **B,** Phase-providing spatial map. Both the amplitude- and phase-providing spatial map are widely distributed over the cortex, but the phase-providing spatial map is wider and shows more phase diversity. The size of the markers indicates the contribution of each electrode to the spatial map, the color indicates the relative phase of the electrodes. **C,** Amplitude- and phase-providing frequency profiles. These profiles show that the example component involves a coupling between the phase of a theta oscillation and the amplitude of a beta/gamma oscillation. **D,** wPLFs (for all frequency pairs) of two selected electrode pairs. The frequency pairs for which there is strong coupling closely match the frequency profiles in C and the difference between the preferred coupling phases closely match the corresponding phase difference in the phase-providing spatial map. PAC = phase-amplitude coupling; wPLF = weighted phase-locking factor.

Second, we investigated the frequency profiles of the amplitude- and phase-providing oscillations of all components. We constructed a scatter plot of the peaks of the amplitude- and phase-providing frequency profiles (Fig. 6B). Peaks of the phase-providing frequency profiles were spread out, ranging from delta (~2 Hz) to alpha (~16 Hz). Peaks of amplitude-providing frequency profiles were spread out even more, ranging from theta (~5 Hz) to gamma (~67 Hz or higher). Note the difference with Figure 3D. The peak frequencies determined from the decomposition (Fig. 6B) showed a much larger spread than to those from the 4-way array of wPLFs (Fig. 3D). This most likely results from the fact that each 4-way array of wPLFs carries several PAC patterns.

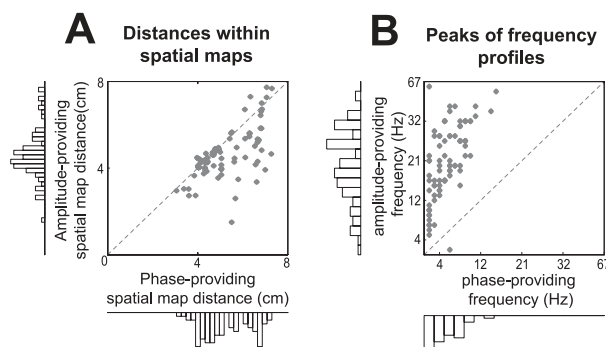


Figure 6. Spatial extent of spatial maps and frequency profiles. **A,** Mean distance within components in phase-providing spatial maps (horizontal axis) plotted against the mean distance in amplitude-providing spatial maps (vertical axis). The mean distance within components was on average higher for the phase-providing than for the amplitude-providing spatial maps (paired samples t-test; $t(84) = -5.56$, $p < 1e-6$). **B,** Scatter plot of the peaks of the phase-providing frequencies (horizontal axis) versus the peaks of the amplitude-providing frequencies (vertical axis). There is a substantial spread of the peaks of the phase-providing frequency profiles, ranging from delta to alpha, and those of the amplitude-providing frequency profiles, ranging from theta to gamma. Note the difference with respect to Figure 3D, and see Results section for a possible explanation. For selection of electrodes see Materials and Methods.

PHASE-PROVIDING AND AMPLITUDE-PROVIDING SPATIAL MAPS SHOW DIFFERENT PHASE CONFIGURATIONS

To investigate the phase configuration within both types of spatial maps, we calculated the phase differences for all possible pairs of electrodes selected from a spatial map (Fig. 7). As before, we selected electrodes based on the component-specific reconstructed wPLFs (see Materials and Methods). To show the aggregate phase diversity in both spatial maps, we show the density of electrode pairs as a function of their strength and their phase difference (Fig. 7A and 7B). We observe (1) that both amplitude- and phase-providing spatial maps showed phase differences clustered around 0, (2) that phase-providing spatial maps also showed phase differences clustered around $+/- \pi$, and (3) that both maps showed phase differences between 0 and $+/- \pi$. This indicates that the amplitude-providing spatial maps mainly showed synchronous phase configurations. On the other hand, the phase-providing spatial maps also showed so-called anti-phasic configurations, with two groups of electrodes having small *within* group, but large *between* group phase differences. Importantly, both maps showed phase differences between 0 and $+/- \pi$. Modulation of phase relations across the complete circle (not limited to synchrony/anti-phase) may have important consequences for the computational mechanism that PAC reflects. More specifically, if PAC reflects selective routing of information by modulating excitability of neuronal groups, then phase determines its flexibility.

From this perspective, it is crucial to establish that the observed phase differences between 0 and $+/-\pi$ are not estimation errors, but true phase differences. To demonstrate this, we evaluated the split-half reliability of these phase differences. For each dataset we randomly partitioned trials in two sets, and calculated 4-way arrays of wPLFs for both. We then decomposed each array into the same number of components and computed phase differences as above. We show the split-half reliability as the density of between-electrode phase differences from the first set of trials plotted against those of the second set (Fig. 7C and 7D). We observe that all phase differences were highly similar between the two sets of trials, and this

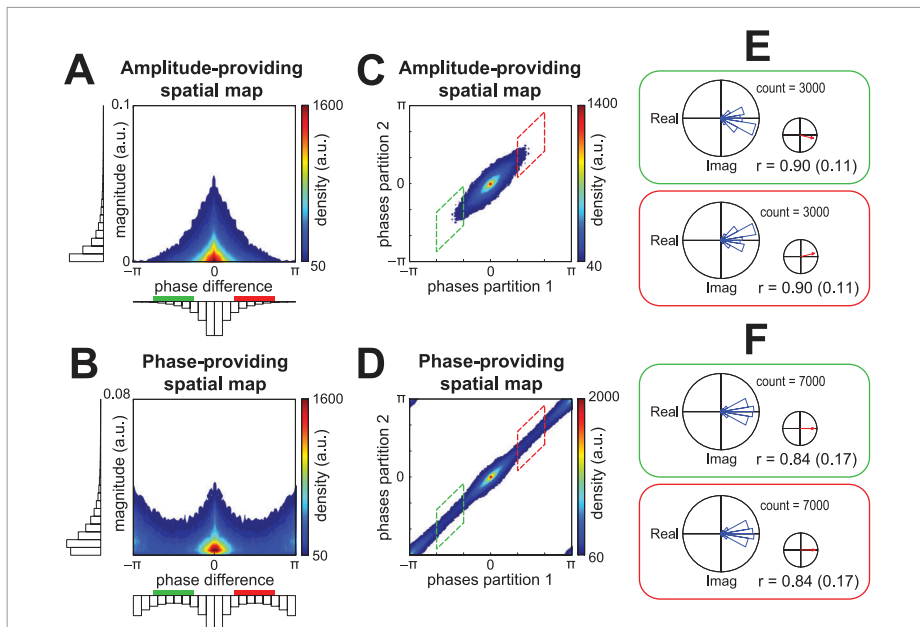


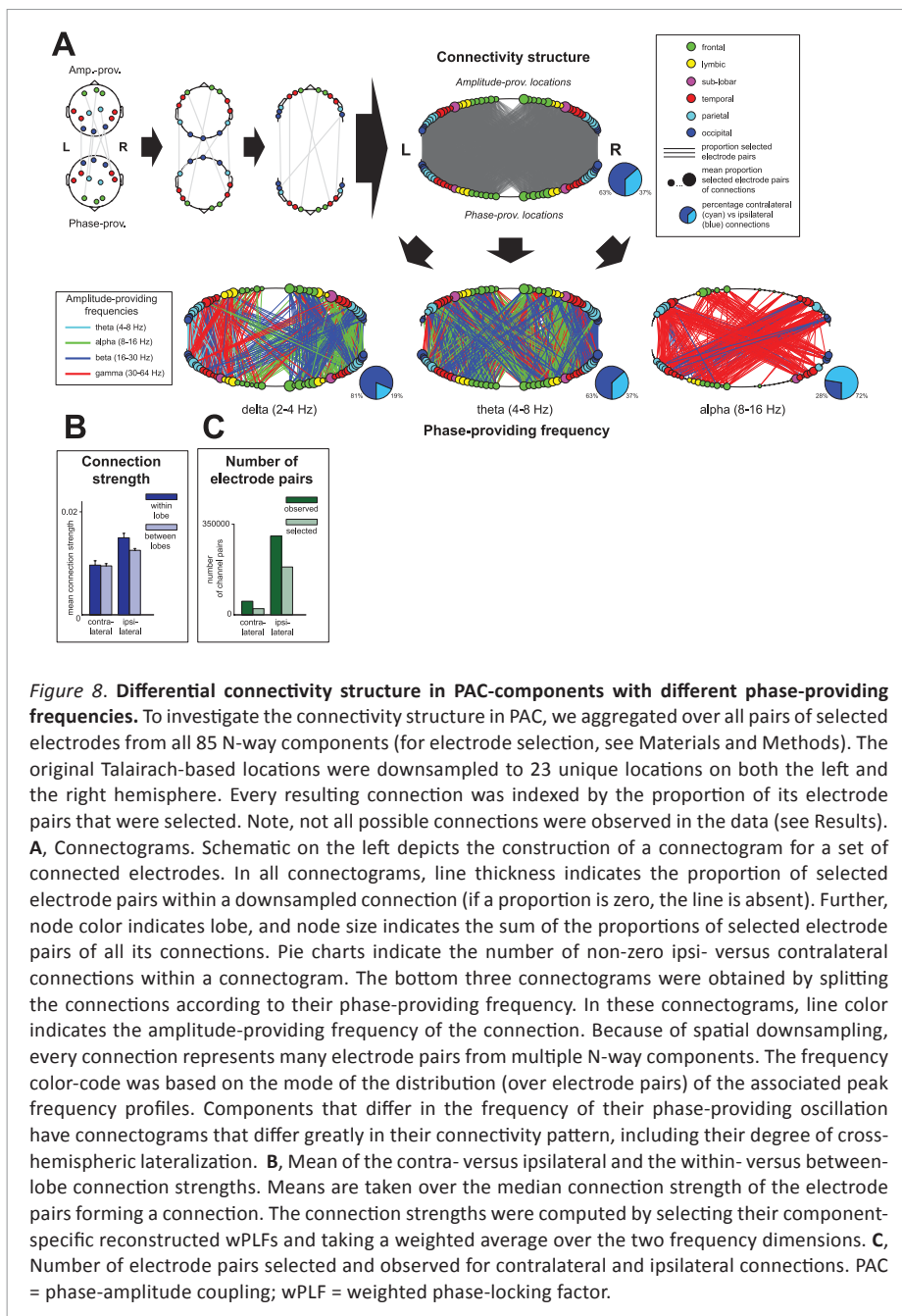
Figure 7. Phase-providing and amplitude-providing spatial maps show different phase configurations. To investigate the phase configurations of both types of spatial maps we computed the phase differences for all possible pairs of electrodes selected from a spatial map. **A**, Density of electrode pairs of each spatial map as a function of their magnitude and their phase differences for the amplitude-providing spatial map. Phase differences cluster around 0. **B**, Same as in A, but for the phase-providing spatial map. Phase differences are mostly around 0, and around $+/-\pi$. **C, D, E, F**, To investigate the reliability of the phase differences, we evaluated the split-half reliability of our decomposition results (see Results and Materials and Methods). **C**, Density of amplitude-providing spatial map phase differences from the first versus those of the second set. **D**, Same information as in C, but for phase-providing spatial maps. Between-set phase differences are highly similar for both spatial maps, showing they are highly reliable. **E**, Phase histograms and mean resultant vector of the amplitude-providing spatial map between-set phase differences for the intervals from $-2\pi/3$ to $-\pi/3$ (green box) and from $\pi/3$ to $2\pi/3$ (red box). **F**, Same as in E, but for the phase-providing spatial maps. For both types of spatial maps, between-set phase differences cluster around 0, indicating reliability of the between-electrode phase differences in this narrow range. For a description of the reliability coefficient r see Results. For selection of electrodes see Materials and Methods. wPLF = weighted phase-locking factor.

holds for both spatial maps. Thus, phase differences in the decomposition reflect true phase differences. As an additional quantification, we calculated differences between the two sets of phase differences (Fig. 7E and 7F). We selected phase differences between $-2\pi/3$ to $-\pi/3$ and $\pi/3$ to $2\pi/3$, as estimated using the first set of trials. For both types of spatial maps, between-set phase differences cluster around 0 (Fig. 7E and 7F). This indicates that, even for this narrow range, the phase differences reflect true phase differences. To support this quantitatively we computed a reliability coefficient, ranging from 0 to 1 (see Materials and Methods). For both spatial maps the coefficient r was high for both intervals (Fig. 7E and 7F).

DIFFERENT CONNECTIVITY STRUCTURE FOR COMPONENTS WITH DIFFERENT PHASE-PROVIDING FREQUENCIES

To reveal the connectivity structure of PAC in our 85 extracted components we aggregated over all pairs of selected electrodes (Fig. 8). As before, we selected electrodes based on the component-specific reconstructed wPLFs (see Materials and Methods). In order to visualize the connectivity structure, we downsampled the anatomical locations of electrodes (using Talairach-coordinates) to 23 locations on the left and 23 locations on the right hemisphere. We did not observe all possible connections based on these downsampled locations: out of the 2116 possible connections, we observed 1698 (80.3%) in our data. However, as will become clear, our quantifications and subsequent comparisons were not biased by this incompleteness. For every observed connection, we calculated the proportion selected electrode pairs within a downsampled connection. This proportion estimates the probability that PAC is found between the downsampled locations. The number of electrode pairs over which this proportion was calculated differed greatly across location pairs. This was especially the case for the small number of contralateral vs the large number of ipsilateral electrode pairs (Fig. 8C).

We use connectograms to show the connectivity structure of PAC (Fig. 8A). Whereas no clear structure is revealed by the connectogram for all components together (top connectogram in Fig. 8A), much structure is revealed when separate connectograms are made for components with different phase-providing frequencies (three bottom connectograms in Fig. 8A). In these connectograms, line color indicates the amplitude-providing frequency of each connection; pie charts show the percentage of non-zero contralateral and ipsilateral connections. Because of spatial downsampling, every connection consists of many electrode pairs from multiple components. The frequencies used for the connectograms were obtained by taking the mode over the peaks of all their frequency profiles. Components that differ in their phase-providing frequency differ greatly in their connectivity pattern, including their degree of cross-hemispheric lateral connections. We



observe that, (1) delta oscillations show mostly ipsilateral connections, (2) theta oscillations show both ipsi- and contralateral connections, and (3) alpha oscillations show predominantly contralateral connections. The imbalance of contralateral vs ipsilateral connections in the top connectogram is partly the result of the relatively small number of patients with bilateral recordings sites (11 out of 27). This source of the imbalance also affects the bottom three connectograms, whose combination forms the top connectogram. Importantly, because this source of imbalance affects all bottom three connectograms to the same extent, their number of contralateral connections can be safely compared to each other.

Our findings were obtained by investigating the number of connections that exist between downsampled locations. We also investigated the coupling strength between these locations, calculated as the median connection strength over all electrode pairs belonging to that connection. For each electrode pair, connection strength was calculated by selecting their component-specific reconstructed wPLFs and taking a weighted average over the two frequency dimensions. We now report on this, with separate averaging over (1) contralateral and ipsilateral, and (2) within- and between-lobe connections (Fig. 8B). We observe that, (1) there is only a small difference in connection strength between lobes compared to within lobes, and (2) the contralateral and ipsilateral connection strengths did not differ greatly: the average strength of the contralateral connections was 69.7% of the average strength of the ipsilateral connections (Fig. 8B). We also investigated the above patterns separately for each of the three phase-providing frequencies (delta, theta and alpha), but we found no substantial differences (figure not shown).

DISCUSSION

We provided evidence for three key properties that could allow PAC to flexibly and selectively route information through distributed neuronal networks. (1) We showed that PAC was widely spatially distributed. From our analyses of significant wPLFs we found that PAC occurred at distances over 10 cm. Using a decomposition based on the PARAFAC model, we showed that this PAC was generated by spatially distributed phase- and amplitude-providing oscillations, of which the phase-providing oscillations were more spread out. The spatial distribution of PAC is required to be able to route information through distributed networks. (2) We showed that over these spatially distributed networks there was great phase diversity. The phase diversity we observed was mainly explained by phase diversity in the phase-providing oscillation, showing phase differences over space, across the whole circle. This phase diversity can determine the flexibility of PAC in selecting

neuronal populations for interaction. (3) We showed that PAC occurred between oscillations of many different frequencies (He et al., 2010; Miller et al., 2010b; Maris et al., 2011). Amplitude-providing frequencies ranged from theta to gamma, and phase-providing frequencies ranged from delta to alpha. This frequency diversity can determine the flexibility of PAC in separating neuronal networks operating in parallel.

Besides providing evidence for these three key properties, we also made a first step towards identifying different roles for phase-providing oscillations at different frequencies. We showed that delta oscillations establish mostly ipsilateral connections, theta oscillations establish both ipsi- and contralateral connections, and alpha oscillations establish predominantly contralateral connections.

Whilst we find PAC that is widely spatially distributed, most reports so far have shown local PAC (Chrobak and Buzsaki, 1998; Lakatos et al., 2005; Mormann et al., 2005; Canolty et al., 2006; Cohen, 2008; Lakatos et al., 2008; Osipova et al., 2008; Penny et al., 2008; Axmacher et al., 2010; He et al., 2010; Miller et al., 2010b; Voytek et al., 2010). The evidence for cross-area PAC is much less abundant (Sirota et al., 2008; Tort et al., 2008; Maris et al., 2011). This is surprising given that, at least for theta, oscillations are measurable over broad regions (von Stein and Sarnthein, 2000; He et al., 2008).

PAC is a form of oscillatory synchronization that involves two different frequencies. A more familiar form of oscillatory synchronization involves only a single frequency: phase consistency between oscillations. This type of oscillatory synchronization was originally put forward as a mechanism to bind different features of an object, encoded in different neuronal populations, and was confined to gamma (Singer and Gray, 1995; Singer, 1999). More recently, it has been proposed as a mechanism of communication between neuronal groups (Fries, 2005). Central to this proposal is that neurons preferably fire in a specific phase of the gamma cycle, implying a temporal relation between spikes of coherently oscillating neurons. This allows neurons to synchronize their periods of maximum excitability and communicate effectively. An expanded mechanism, involving PAC, would be that the phase-providing oscillation modulates when neuronal populations engage in oscillatory phase synchronization. Such a mechanism would require phase consistency during high frequency bursts. Though we did not investigate this, long range phase consistency at high frequencies has been reported (Gregoriou et al., 2009). If it is indeed the case that phase-providing oscillations select neuronal populations for communication, then such cross-frequency interaction could provide dynamic gating of information (Vogels and Abbott, 2009; Akam and Kullmann, 2010). The phase-providing oscillation as a selector would also greatly benefit from a process that creates substantial phase diversity across sites, which we have observed, where

site-specific phases could function as a selection variable. Besides the separation of neuronal activity via phase diversity (i.e. phase ‘multiplexing’), the separation of multiple networks operating in parallel could also be supported by frequency diversity (i.e. frequency ‘multiplexing’).

Though we provide evidence for three key properties that make PAC a likely candidate for routing for information, we do not have a mechanistic neurophysiological model to explain our observations, and providing such an explanation is a crucial challenge for future research. Obviously, neuronal spiking is the signal for targeted communication between neurons. Therefore, we face the challenge to link our findings using ECoG to neuronal signals with a very different spatial specificity. Inevitably, any attempt to provide such a link will involve some speculation. However, it is justified to the extent that it can be related to relevant findings in the literature. We hypothesize that PAC may reflect an interaction between slow and fast rhythmic synaptic input streams, and that the efficacy of this interaction can be modulated by adjusting the timing between these rhythms. Furthermore, we hypothesize that the slow rhythm, the phase-providing oscillation, can be used to segregate information streams by variations in its phase over space. These hypotheses have links with the substantial literature on Up and Down states ([Steriade et al., 1993; Destexhe et al., 2003; Cash et al., 2009; Haider and McCormick, 2009](#)).

Up and Down states are brain states that can be characterized at many levels, ranging from intracellular recordings to macroscopic electroencephalography ([Steriade et al., 2001; Destexhe et al., 2003; Volgushev et al., 2006](#)). Up and Down states are most easily identified during slow wave sleep and anesthesia, when they alternate rhythmically ([Ho and Destexhe, 2000; Sanchez-Vives and McCormick, 2000; Shu et al., 2003; Hasenstaub et al., 2005; Haider et al., 2006](#)). This typically occurs at a frequency below 1 Hz, producing the so-called cortical slow oscillation. During wakefulness and shallow sleep, isolated Down states called K-complexes occur in a non-rhythmic fashion, sometimes preceded by an Up state ([Amzica and Steriade, 1997; Cash et al., 2009](#)). In both rhythmic and non-rhythmic cases, Up and Down states are spatially distributed ([Volgushev et al., 2006](#)). Furthermore, recordings in animals ([Sanchez-Vives and McCormick, 2000; Volgushev et al., 2006](#)) and humans ([Massimini et al., 2004](#)), have shown that the cortical slow oscillation is phase diverse over space. In ECoG recordings, Up and Down states can be identified as positive and negative deflections ([Cash et al., 2009](#)). These originate from a source-sink configuration, with a source in layer II/III and a sink in layer I ([Cash et al., 2009](#)). The neocortical Up state is a network phenomenon, characterized by a balance in excitatory and inhibitory input ([Haider et al., 2006](#)). During an Up state, neurons have an increased membrane potential, bringing them closer to their firing threshold ([Haider et al., 2007](#)). Animal studies have shown that, during an Up state,

there is an increase in spiking activity and high frequency (30-100 Hz) local field potential (LFP) fluctuations (Nowak et al., 1997; Haider and McCormick, 2009). A Down state provides the opposite: the membrane potential is hyperpolarized, and there is a strong decrease in spiking and high frequency LFP fluctuations.

The rhythmic alternation of Up and Down states has similarities to our PAC results: (1) it involves a slow oscillation with high frequency oscillations occurring at specific phases, (2) the slow oscillation is spatially distributed, and (3) the slow oscillation is phase diverse over space. Based on these similarities, we propose that phase-providing oscillations of PAC could affect neuronal populations in a similar way. The phase-providing oscillation could, like the cortical slow oscillation, modulate the basal membrane potentials of neuronal groups, which could provide joint windows of communication during certain phases. This could allow neuronal groups to exchange information during bursts of high frequency LFP fluctuations. This information exchange could involve coherent oscillations. Importantly, there are a number of differences between Up and Down states and our PAC results complicating this comparison. First, slow cortical oscillations are typically <1 Hz, whereas we identified phase-providing oscillations between 2-16 Hz (lower boundary is restricted by epoch length). Second, the phase diversity we observed across space is much larger than the phase diversity in the slow oscillation. Third and last, high frequency LFP fluctuations during Up states are locked to the peak of the slow oscillation, whereas we report strong diversity in preferred coupling phases of PAC. The reported phase of the slow oscillation however, depends on where in the neuropil the signal is recorded: because the Up and Down states are characterized by a source-sink configuration between layer I and layer II/III (Cash et al., 2009), the polarity of the slow oscillation would reverse if one would record from layer II/III. Assuming that the brain's neurophysiological makeup allows for different source-sink configurations across layers, it should be possible to generate PAC with diverse phases as measured on the brain's surface.

More evidence is needed to show that spatially distributed PAC in ECoG signals reflect a neurophysiological mechanism which also modulates spiking activity. At least part of the evidence must come from in-vivo experiments involving simultaneous recordings from multiple sites in the neuropil. The present study can guide the analysis of these recordings. We have demonstrated that PAC is a pervasive phenomenon that has a wide spatial distribution, a strong diversity in preferred coupling phases and involves oscillations at many frequencies. With these properties, PAC is a plausible candidate for supporting selective neuronal communication.

Chapter 3

Uncovering phase-coupled oscillatory networks in electrophysiological data

ABSTRACT

Phase consistent neuronal oscillations are ubiquitous in electrophysiological recordings, and they may reflect networks of phase-coupled neuronal populations oscillating at different frequencies. Because neuronal oscillations may reflect rhythmic modulations of neuronal excitability, phase-coupled oscillatory networks could be the functional building block for routing information through the brain. Current techniques are not suited for directly characterizing such networks. To be able to extract phase-coupled oscillatory networks we developed a new method, which characterizes networks by phase coupling between sites. Importantly, this method respects the fact that neuronal oscillations have energy in a range of frequencies. As a consequence, we characterize these networks by between-site phase relations that vary as a function of frequency, such as those that result from between-site temporal delays. Using human electrocorticographic (ECOG) recordings we show that our method can uncover phase-coupled oscillatory networks that show interesting patterns in their between-site phase relations, such as travelling waves. We validate our method by demonstrating it can accurately recover simulated networks from a realistic noisy environment. By extracting phase-coupled oscillatory networks and investigating patterns in their between-site phase relations we can further elucidate the role of oscillations in neuronal communication.

Adapted from:

van der Meij R, Jacobs J, Maris E (2015). *Uncovering phase-coupled oscillatory networks in electrophysiological data*. Human Brain Mapping.

INTRODUCTION

Oscillations are a prominent feature of neuronal signals (Buzsaki and Draguhn, 2004). When measured at multiple sites, these site-specific signals are very often phase consistent. As these sites may measure multiple sources, they can reflect phase-coupled oscillatory networks. Because oscillations may reflect rhythmic modulations of neuronal excitability (Fries, 2005; Buzsaki et al., 2012), phase-coupled oscillatory networks could be the functional building block for routing of information in the brain (for reviews see Schnitzler and Gross, 2005; Palva and Palva, 2012; Siegel et al., 2012). These networks will overlap at least partially in space, frequency and time, forming a complex structure in which the routing of information depends on phase relations at multiple frequencies (Canolty et al., 2010; Canolty and Knight, 2010; Schyns et al., 2011; Miller et al., 2012a; van der Meij et al., 2012; Akam and Kullmann, 2014).

Networks of functionally connected brain regions have been studied for more than a decade using the hemodynamic response measured by functional magnetic resonance imaging (fMRI; for a review see Deco and Corbetta, 2011). Networks of coupled sites have also been found using electrophysiological signals, on the basis of correlations between envelopes of oscillatory amplitudes at different frequencies (de Pasquale et al., 2010; Brookes et al., 2011; Hipp et al., 2012). Crucially, between-site amplitude envelope correlations do not reflect between-site phase consistency, and therefore cannot be interpreted in terms of phase-coupled fluctuations of neuronal excitability.

Characterizing coupling between sites using fluctuations in neuronal excitability with existing methods is a tremendous challenge if there are no strong hypotheses about which neuronal populations are likely to interact. This is because existing methodology is based on pair-wise measures, such as coherence (Rosenberg et al., 1998), Granger-causality (Bernasconi and Konig, 1999), phase-locking value (Lachaux et al., 1999), and others. Such measures quantify the strength and/or direction of phase coupling at the level of site-pairs, and therefore do not reveal the spatial distribution of phase-coupled networks, at least not without prior information about a seed region and the frequency band in which this phase-coupling occurs.

To investigate phase-coupled oscillatory networks it is crucial to appreciate the fact that brain rhythms have energy in a range of frequencies. This has important implications for the between-site phase relations. For instance, networks with consistent between-site time delays have between-site phase relations that are a linear function of frequency. We developed a new method that is capable of extracting such networks from electrophysiological data.

In the following, we present, apply and validate a method that extracts phase-coupled oscillatory networks. This method is grounded in a plausible model of a neurobiological rhythm: a spatially distributed oscillation with energy in a range of frequencies and involving between-site phase relations that vary as a function of frequency. The method is useful because electrophysiological data almost always involve multiple networks, overlapping in both space and frequency. Our method separates these networks and characterizes them in a neurobiologically informative way. To demonstrate that our method works we apply it real data, and validate it using simulations. Using ECoG recordings we show that it is capable of uncovering networks and characterizing them in an informative way. Using simulated data we show that it is capable of uncovering ground truth networks in the context of neurobiologically realistic noise.

MATERIALS AND METHODS

EXTRACTING PHASE-COUPLED OSCILLATORY NETWORKS USING SPACE

To extract phase-coupled oscillatory networks we developed a new decomposition technique, denoted as SPACE (for Spatially distributed PhAse Coupling Extraction). It is inspired by complex-valued PARAFAC ([Carrol and Chang, 1970](#); [Harshman, 1970](#); [Bro, 1998](#); [Sidiropoulos et al., 2000](#)). In this section, we provide a brief introduction into the method. A full description of the method and the underlying algorithm is provided in the Appendix.

We extract phase-coupled oscillatory networks using two models: the time delay model and the FSP model (for Frequency-Specific Phases). Both models follow our characterization of phase-coupled oscillatory networks presented in the Results section and extract networks that consist of a *frequency profile*, a *spatial amplitude map*, an *epoch profile*, and an array of *phase offsets*. The time delay model (SPACE-time) describes phase relations between sites by temporal delays between sites, in a *spatial time-delay map*. The FSP model (SPACE-FSP) describes these phase relations by *frequency-specific phases*, in *spatial phase maps*. Below, we present both models in more detail. The two models are complementary. The time delay model is capable of directly revealing the temporal structure of, for example, traveling waves, and is therefore suited for targeted analyses of temporal dynamics. The FSP model can extract networks with any kind of phase structure, and is therefore most useful in explorative analyses. Both models extract networks from a 3-way array of Fourier coefficients X_{jkl} , with dimensionality sites (J), frequencies (K), and epochs (L), obtained from a spectral analysis of electrophysiological recordings. Phase-coupled oscillatory networks can partially overlap in their spatial configuration,

spectral content, and temporal pattern. Our method separates such networks by their different structure over the spatial, spectral and temporal dimensions of the input array, that is, on the basis of their different spatial maps, frequency profiles, and epoch profiles.

The time delay model (Fig 1A; see Appendix) is formulated as follows in element-wise notation:

$$\text{SPACE-time: } X_{jkl} = \sum_{f=1}^F a_{jf} \cdot \exp(i2\pi\varphi_k\sigma_{jf}) \cdot b_{kf} \cdot c_{lf} \cdot \exp(i2\pi\tau_{klf}) + \varepsilon_{jkl}$$

The Fourier coefficient X_{jkl} is described as a sum over F network-specific complex-valued numbers. The amplitude of each network-specific complex-valued number is the product of a_{jf}, b_{kf} and c_{lf} , which refer to, respectively, the spatial amplitude map, the frequency profile and the epoch profile. The phase of each network-specific complex-valued number is the product of an element of the spatial time-delay map and a phase offset: $\exp(i2\pi\varphi_k\sigma_{jf})$ and $\exp(i2\pi\tau_{klf})$. Here, $\exp(i2\pi\varphi_k\sigma_{jf})$ describes the site-, frequency-, and network-specific phases, in which φ denotes the k -th frequency (in Hz) and σ_{jf} denotes the site- and frequency-specific time delay. $2\pi\tau_{klf}$ describes the frequency-, epoch-, and network-specific phase offset. The time delay model is based on the assumption that between-site phase differences are the result of between-site time delays. To make this concrete, let σ be the time delay between two sites and let φ be frequency. Then, the between-site phase difference is $\varphi \cdot \sigma$, which increases linearly with frequency. In the FSP model (Fig 1B; see Appendix), the spatial phase maps replace the spatial time-delay maps. For this model, the phase of each network-specific complex-valued number is the product of an element of the spatial phase maps and a phase offset: $\exp(i2\pi\lambda_{jkf})$ and $\exp(i2\pi\tau_{klf})$. The FSP model is formulated as follows in element-wise notation:

$$\text{SPACE-FSP: } X_{jkl} = \sum_{f=1}^F a_{jf} \cdot \exp(i2\pi\lambda_{jkf}) \cdot b_{kf} \cdot c_{lf} \cdot \exp(i2\pi\tau_{klf}) + \varepsilon_{jkl}$$

Except for the site-, frequency- and network-specific phases λ_{jkf} , this model has the same parameters as the time delay model. In contrast to the time delay model, no constraints are imposed on the between-site phase differences as a function of frequency. The parameters of both models can be estimated using an alternating least squares (ALS) algorithm, which monotonically decreases a least squares loss function. For this algorithm, new optimization techniques were developed which are fully described in the Appendix.

In order to be estimable, all parameters of the two models have to be normalized (see Appendix). Because of this normalization, the individual amplitudes a_{jf}, b_{kf} and c_{lf} , and the individual phases/time delays $\lambda_{jkf}, \sigma_{jf}$, are not meaningful. Crucially

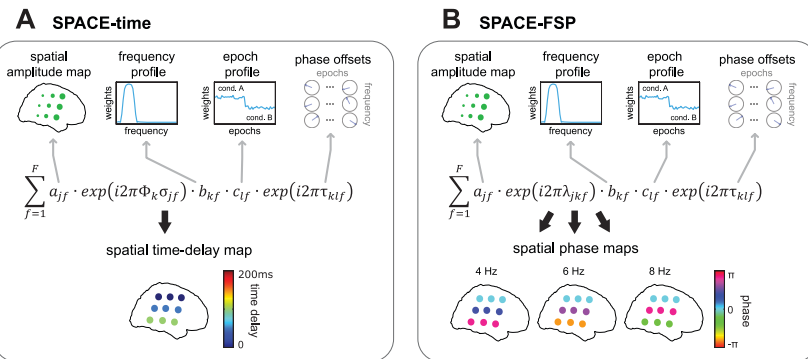


Figure 1. SPACE: describing phase-coupled oscillatory networks by frequency-specific phases and time delays. We developed a new decomposition technique that extracts phase-coupled oscillatory networks, SPACE. Networks are extracted using two models, the time delay model and the FSP model (for Frequency-Specific Phase). The time delay model (SPACE-time) describes phase relations between sites by temporal delays between sites, in a *spatial time-delay map*. The FSP model (SPACE-FSP) describes these phase relations by *frequency-specific phases*, in *spatial phase maps*. **A**, the time delay model describes networks by a *spatial amplitude map*, a *frequency profile*, a *spatial time-delay map*, an *epoch profile*, and *phase offsets*. The equation in A is the element-wise formulation of the time delay model, and it shows how each Fourier coefficients X_{jkl} of site j , frequency k , and epoch l is described. The example shows the same network as in Fig 3. The time-delay maps describe all phase differences by site-specific time delays. In the example, each site row has a time delay of 50ms from top to bottom. These 50ms steps produce the same phases as shown in B, and match the time delays in Fig 3A. **B**, the FSP model describes networks by a *spatial amplitude map*, a *frequency profile*, an *epoch profile*, *phase offsets*, and frequency-specific *spatial phase maps*. The *spatial phase maps* describe all phase differences between sites, matching those in Fig 3A. No constraint is placed on phases over frequencies, in contrast to the time delay model. For a detailed description see Materials and Methods and Results section 1.

however, amplitude *ratios*, and time delay *differences* and phase *differences* between sites, frequencies, and epochs, are not affected by these normalizations, and reveal important characteristics of the extracted phase-coupled oscillatory networks.

In the 3-way array of Fourier coefficients, every epoch is described by a single Fourier coefficient per site and frequency. However, it is often desired to control the frequency resolution by means of multitaper estimation. When using multitaper estimation, every epoch has multiple tapers, and each of these tapers produces one Fourier coefficient. These taper-specific Fourier coefficients are organized in an additional dimension, turning the 3-way array into a 4-way array of Fourier coefficients. However, because frequencies and epochs can differ in their number of tapers, this 4-way array may be partially empty, and the 3-way formulation of the models cannot accommodate this aspect of the data array. Fortunately, we can make use of the cross-product formulation of our models to deal with this. This is the formulation of the models that is used in the remainder of the paper, and it is fully described in the Appendix. Crucially, the cross-product formulation does not affect the spatial amplitude maps, the frequency profiles, the epoch profiles,

nor the spatial phase maps or spatial time-delay maps, as described above and in the Results section. The phase offsets, however, are parameterized differently (see Appendix). An important difference with the models for the 3- and 4-way arrays of Fourier coefficients, is that in the cross-product formulation of these models, between-network coherence is explicitly modeled. Although this can be of great benefit, it also has an undesirable consequence: if the between-network coherences are treated as estimable parameters, then a distributed phase-coupled oscillatory network can be described by an arbitrary number of coherent sub-networks. To avoid this, we force between-network coherence to be zero (see Appendix).

The number of networks F that are extracted needs to be estimated. The number of networks that should be extracted cannot be determined analytically. To find the optimal F , we can make use of an index of the reliability with which the networks can be estimated from the data, as described by Maris et al. (2011). The number of networks that are extracted can be increased incrementally until this reliability index drops below a preset level. A conservative approach is to split the data into two halves, extract networks from both halves, and stop increasing the number of networks when they start to differ between halves. We use this approach for analyzing the ECoG data, and it is described in detail below. Other methods of estimating the optimal F are also possible (see Bro, 1998, for examples from the perspective of PARAFAC/2).

EXPERIMENTAL PARADIGM AND PREPROCESSING OF ECOG RECORDINGS

Three pharmaco-resistant epilepsy patients (1 male, 2 female) were implanted with subdural grid and strip electrodes prior to undergoing resective surgery. Informed consent was obtained from the patients or their guardians if they were underage. The research protocol was approved by the appropriate institutional review boards at the Children's Hospital (Philadelphia, PA) and the University Clinic (Freiburg, Germany). Some of the datasets have been analyzed before (see e.g. Rizzuto et al., 2003; Raghavachari et al., 2006; Jacobs and Kahana, 2009; van Vugt et al., 2010; Maris et al., 2011; van der Meij et al., 2012). Patients performed a Sternberg working memory task (Sternberg, 1966) while ECoG recordings were obtained. Patients were presented with a series of letters (with variable length from 1 to 6) on a computer screen, and they were instructed to remember these. The trial started with the presentation of a fixation cross, followed by a letter for 700ms and by 275-350ms (uniformly distributed) of blank screen. Every additional letter was presented for 700ms and followed by 275-350ms of blank screen, except for the last letter which was followed by a retention interval of 425-575ms (uniformly distributed as well). After the retention interval, a probe letter was presented. Patients were required to indicate by means of key press whether the probe letter was part of the previously

presented letter series. We analyzed the period between the fixation cross and the onset of the probe letter, a period during which the patients were actively engaged in the task. We did not distinguish between the cognitive operations encoding and retrieval, which occur in this period. The main purpose of the current analyses was to demonstrate that plausible phase-coupled oscillatory networks can be extracted.

ECOG recordings were sampled at 256 Hz and rereferenced to the common average. Artifact rejection was performed by visual inspection. All trials and/or electrodes contaminated by epileptiform activity were removed. The data was band-stop filtered with 1 Hz windows at 50 and 60 Hz (depending on continent) and at other frequencies containing line noise. Recordings were additionally band-pass filtered between 0.01 and 100 Hz. All filters were 4th order Butterworth. Subsequently, the mean and the linear trend were removed from each trial. To suppress the $1/f^x$ pattern in the power spectrum, the data was prewhitened by taking the first temporal derivative. Electrode locations were determined by co-registering a postoperative computed tomography scan with a higher resolution preoperative magnetic resonance image. Patients' brains were normalized to Talairach space ([Talairach and Tournoux, 1988](#)). All preprocessing and spectral analysis was performed using custom analyses scripts and the FieldTrip open-source MATLAB toolbox ([Oostenveld et al., 2011](#)).

EXTRACTING PHASE-COUPLED OSCILLATORY NETWORKS FROM ECOG RECORDINGS

Spectral analysis was performed for 2-30 Hz with equally spaced 0.5 Hz bins and a Welch multitapering approach ([Welch, 1967](#)) to control frequency resolution. First, each trial was cut into several 2 second segments, such that each next segment would have a temporal overlap of 75% with the previous segment (incomplete segments at the end of a trial were not used). Each of the 2 second segments was multiplied with a Hanning window, followed by a DFT. These multiple 2 second segments of each trial are the separate Welch tapers. Each epoch used in the analyses corresponds to three consecutive trials and we combined the Fourier coefficients obtained from these trials. This resulted in 30 epochs out of 92 trials for patient 1, 54 epochs out of 163 trials for patient 2, and 89 epochs out of 270 trials from patient 3. Combining tapers of multiple trials was necessary because our method requires that the smallest number of tapers per epoch is larger than the number of networks extracted. Because we wanted to estimate the number of networks using a high frequency resolution, this sometimes lead to a larger number of networks than tapers when defining each trial as an epoch.

The same preprocessing procedure was used for displaying single trials at the peak frequency of the example networks (see Results section). The resulting

time series were then convolved with a complex-valued wavelet at the selected frequencies. This wavelet was constructed by an element-wise multiplication of a three-cycle complex exponential and a Hanning taper of equal length. The real part of the resulting complex-valued time series was then used for display.

Fourier coefficients resulting from spectral analysis were arranged to form a 4-way array and decomposed using the cross-product formulation of both SPACE-time and SPACE-FSP (see Appendix). To avoid local minima, each algorithm was randomly initialized 20 times, and the solution with the highest explained variance was selected (explained variance over initializations is shown in Fig S1). To avoid degenerate decompositions from unfortunate initializations, all decompositions were run with an orthogonality constraint ($D_k = I$; see Appendix). The number of networks to extract (four, two, and four for patient 1, 2, and 3 respectively) was determined on the basis of a split-half approach using the output of SPACE-time. In this procedure, the number of networks was increased until the networks extracted from the odd numbered trials were no longer similar enough to the networks extracted from the even numbered trials. As such, the number of networks that is extracted depends on the networks that are consistently activated by the task. Similarity was evaluated on the basis of a number of split-half reliability coefficients. One coefficient was calculated for each of the parameter sets.

This split-half reliability coefficient was computed for the spatial amplitude map and the frequency profiles as the normalized network-specific inner-product. For the spatial time-delay maps, the split-half reliability coefficient was constructed in two steps:

$$\text{split-half coefficient: } \frac{\sum_{k=1}^K \left(\left| \langle A^1 \cdot \exp(i2\pi\varphi_k\sigma^1), A^2 \cdot \exp(i2\pi\varphi_k\sigma^2) \rangle \right| \cdot \frac{B_k^1 + B_k^2}{2} \right)}{\sum_{k=1}^K \left(\frac{B_k^1 + B_k^2}{2} \right)} \quad (3)$$

First, per split-half s and frequency k , a complex-valued spatial time-delay map $\exp(i2\pi\varphi_k\sigma^s)$ was computed and weighted with the split-half specific spatial amplitude map A^s . Then, the normalized inner-product $\langle \cdot, \cdot \rangle$ was taken between both halves. The final reliability coefficient for the spatial time-delay maps was then constructed by computing the average over frequencies of the absolute value (denoted by $|\cdot|$) of this inner-product, weighted by the average of the frequency profiles B_k^s of both split-halves. For the spatial phase maps, the reliability coefficient was constructed by replacing $\varphi_k\sigma^s$ by λ_k^s in the above equation. When either this coefficient or that of the spatial amplitude map or the frequency profile fell below 0.7, the procedure was stopped, and the previous number of networks was set as the final number of networks. As $D_k = I$, it was not part of the split-half reliability

coefficient.

We additionally computed a similarity coefficient that was used to compare networks extracted using the time delay model to networks extracted using the FSP model. This coefficient was similar to the split-half coefficient described above. For the spatial amplitude map, the frequency profiles, and the epoch profile the coefficient was computed as the normalized inner-product. For the spatial time-delay map and the spatial phase maps the coefficient was constructed as in Eq. 3, except that the spatial time-delay map of the second network $\exp(i2\pi\varphi_k\sigma^2)$ was replaced by the spatial phase maps $\exp(i2\pi\lambda_k^2)$. The similarity coefficient for the whole network was then obtained as the average of the coefficients for spatial amplitude map, the spatial phase map, the frequency profile, and the epoch profile.

SIMULATING PHASE-COUPLED OSCILLATORY NETWORKS

To show that both our method is capable of extracting networks from noisy data we simulated three phase-coupled oscillatory networks travelling over a 5x5 sites grid. Each network had a spatial amplitude map that was nonzero for a selected set of sites, with overlap between the networks. There was one network in the theta range (4-8 Hz), one in the alpha range (8-12 Hz), and one in the beta range (10-25 Hz). Every network was present in 15 out of 25 epochs, with overlap between the epochs. Per epoch, we generated a signal that propagated over the involved sites with a fixed time delay, thus forming a travelling wave. The time delay step size (i.e., the time delay between two adjacent sites) was systematically varied over the values 5, 25, 50 and 100ms. We additionally varied the signal-to-noise ratio (SNR) and the spatial noise correlation, as described below.

The signal was generated as follows. First, 1.5 (theta) or 1 seconds (alpha and beta) of white noise was generated using MATLAB's pseudorandom number generator. Then, after taking the Discrete Fourier Transform (DFT), all Fourier coefficients not belonging to the network's frequency band were set to zero. Subsequently, the signal was transformed back to the time domain using the inverse DFT, and the resulting signal was multiplied with a Hanning window of equal length and padded out to 3 seconds. This resulted in an oscillatory signal within the specified frequency band. Then, again using a DFT, the amplitudes of the Fourier coefficients were scaled such the amplitude spectrum was proportional to $1/f$, giving the power spectrum a $1/f^2$ shape (Miller et al., 2009). The resulting signal was then transformed back to the time domain using the inverse DFT. The site-specific signals were obtained by shifting this time domain signal in accordance with the order of the site in travelling wave and the time delay step size. To every site, we added 3 seconds of noise. These noise signals were generated in the same way as the source signals but without

the removal of particular frequencies, and independently for each site. We varied the amount of spatial noise correlation by generating new site-specific noise signals as a weighted average of the initial noise signals. These weights were proportional to a bivariate Gaussian of which the full-width half maximum (the width of the Gaussian at the point where its magnitude is at the half of its maximum; FWHM) was systematically varied over the values 0, 10, 20, and 40mm (simulated sites were spaced 10mm apart). This results in a FWHM that encompassed 0, 3, 5 and 9 sites, respectively. We also systematically varied noise strength. This was achieved in a final step by setting the SNR of the time series at each site to be 4, 0.16, 0.04 or 0.01.

ANALYZING THE SIMULATED DATA

Except for artifact removal, the simulated data were preprocessed in the same way as the ECoG data. First, the mean and the linear trend were removed from each epoch. Next, to suppress the $1/f^x$ shape of the power spectrum, the data was prewhitened by taking the first temporal derivative.

Spectral analysis was performed for 2-30Hz with equally spaced 1 Hz bins. First, each 3 second epoch was cut into several 1 second segments, such that each next segment would have a temporal overlap of 75% with the previous segment. For 2-16 Hz, each of the 1 second segments was multiplied with a Hanning window, followed by a DFT. For 17-30Hz, each segment of each epoch was multiplied several times with different tapers prior to taking the DFT. These tapers were the first 3 tapers of the Slepian sequence ([Percival and Walden, 1993](#)) of order 4, resulting in a frequency resolution of approximately 2Hz.

The Fourier coefficients of all segments were then collected per epoch, and arranged in a 4-way array. This array consisted of 25 sites, 29 frequencies, 25 epochs, and 57 tapers for every simulation run. Each 4-way array of Fourier coefficients resulting from one simulation run was decomposed using the cross-product formulations of both SPACE-time and SPACE-FSP. To avoid local minima, each algorithm was randomly initialized 10 times, of which the solution with the highest explained variance was retained (explained variance over initializations is shown in Fig S1). As for the analyses of the ECoG data, all decompositions were run with an orthogonality constraint ($D_k = I$; see above). All preprocessing and spectral analysis was performed using custom analyses scripts and the FieldTrip open-source MATLAB toolbox ([Oostenveld et al., 2011](#)).

COEFFICIENTS FOR EVALUATING THE GOODNESS-OF-RECOVERY OF THE SIMULATED NETWORKS

We calculated a number of coefficients to assess the goodness-of-recovery of the simulated networks. We use four different coefficients: (1) one for the spatial

amplitude maps, frequency profiles and epoch profiles, (2) one for the spatial phase maps, (3) one for the spatial time-delay maps, and (4) one for the temporal order of the time delays. The first coefficient is the Pearson correlation coefficient, which ranges from -1 to 1. The other three coefficients were constructed for the purpose of this study, and will be described in more detail in the following. Each of the four coefficients was computed per network and per simulation run and subsequently averaged.

The recovery coefficient for a network-specific spatial time-delay map was calculated as follows:

$$\text{recovery} : \frac{\sum_{k=1}^K \left(\frac{\langle A^{sim} \cdot \exp(i2\pi\varphi_k\sigma), A^{sim} \cdot \exp(i2\pi\varphi_k\sigma^{sim}) \rangle}{\|A^{sim}\|^2} \right) \cdot B_k^{sim}}{\sum_{k=1}^K B_k^{sim}}$$

First, the inner-product \langle , \rangle is taken between the spatial time-delay map of the extracted network and its simulated counterpart, weighted by the simulated spatial amplitude map. The coefficient is then constructed as the sum over frequencies of the absolute value of this inner-product, weighted by the simulated frequency profile. Here, A^{sim} denotes the simulated spatial amplitude map, $\varphi_k\sigma$ the loading vector containing the spatial time-delay map of an extracted network σ multiplied by frequency φ_k in Hz, $\varphi_k\sigma^{sim}$ its simulated counterpart, and B_k^{sim} the frequency-specific loading of the simulated frequency profile of the same network. This coefficient is sensitive to the similarity between the extracted spatial time-delay map and its simulated counterpart, with a weighing that amplifies the contribution of the sites and the frequencies that are strongly involved in the simulated network. It is similar to the coefficient described in the split-half procedure, except that only the simulated spatial amplitude map and simulated frequency profile are used for weighting.

The recovery coefficient for the spatial phase maps is constructed similarly as for the spatial time-delay maps, except $\varphi_k\sigma$ is replaced by λ_k , and $\varphi_k\sigma^{sim}$ by λ_k^{sim} . Here, λ_k denotes the frequency-specific spatial phase map, and λ_k^{sim} its simulated counterpart. This coefficient is sensitive to the similarity between frequency-specific phases generated by the extracted phases and their simulated counterparts, again with a weighing that amplifies the contribution of the sites and the frequencies that are strongly involved in the simulated network.

The recovery coefficient for the temporal order of the spatial time-delay map is calculated as the proportion of site-pairs that are in agreement with respect to their estimated and simulated temporal order:

$$\text{recovery} : \frac{\sum_{j_1=1}^{J^{\text{sim}}-1} \sum_{j_2=j_1}^{J^{\text{sim}}} \left[(\omega_{j_1} - \omega_{j_2}) == (\omega_{j_1}^{\text{sim}} - \omega_{j_2}^{\text{sim}}) \right]}{\frac{J^{\text{sim}} \cdot (J^{\text{sim}} - 1)}{2}}$$

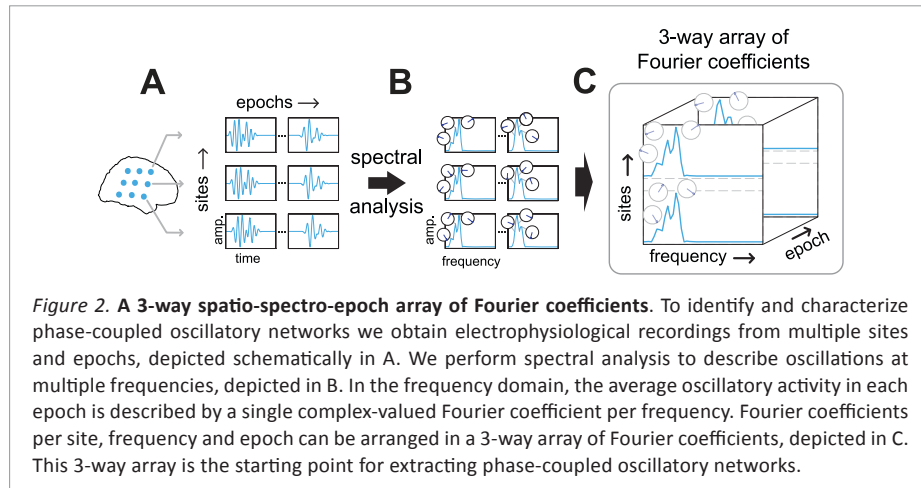
Here, ω_j denotes the position of the j -th site in the ordered set of time delays from an extracted network, and ω_j^{sim} denotes its simulated counterpart. Only sites were used that were part of the simulated network, as defined by the sites that have nonzero simulated values: J^{sim} refers to the total number of involved sites. The numerator of this coefficient is the sum of the site-pairs that have identical ordinal distances between the estimated site-pairs ($\omega_{j_1} - \omega_{j_2}$) and their simulated counterparts ($\omega_{j_1}^{\text{sim}} - \omega_{j_2}^{\text{sim}}$). This sum is then divided by the total number of possible agreements, such that the coefficient expresses agreement as a proportion relative to perfect agreement.

RESULTS

1. CHARACTERIZING PHASE-COUPLED OSCILLATORY NETWORKS IN TERMS OF FREQUENCY PROFILES, SPATIAL MAPS, AND EPOCH PROFILES

Neuronal oscillations are ubiquitous in electrophysiological recordings, and their phase is very often consistent between sites. A phase-coupled oscillatory network is said to be present when this phase coupling is spatially distributed, and its phase relations are stable over multiple cycles of this oscillation. This network is not required to be present throughout a recording; it may be present in some epochs and absent in others. An epoch refers to a temporal segment such as an experimental trial or part of a resting-state recording, and a site refers to any location at which neuronal signals are recorded. To identify these networks, we obtain electrophysiological measurements from multiple sites and multiple epochs (Fig 2A), and perform a spectral analysis on these data. In the frequency domain, the average oscillatory activity in each epoch is described by a single complex-valued Fourier coefficient per frequency (Fig 2B). Because we analyze signals from multiple sites, using multiple frequencies, and from multiple epochs, we obtain Fourier coefficients that can be arranged in a 3-way array, with a spatial, spectral, and epoch dimension (Fig 2C). This 3-way array captures the average oscillatory activity in each epoch, and is the starting point for extracting phase-coupled oscillatory networks.

The 3-way array of Fourier coefficients describes variation over sites, frequencies and epochs in the amplitudes and phases of oscillations generated in the underlying neural tissue. Phase consistency between sites in this 3-way array allows us to extract phase-coupled oscillatory networks (Fig 3). Because the 3-way array describes the



average oscillatory activity in each epoch, these networks describe the average network activity in each epoch. We characterize a phase-coupled oscillatory network using the following parameters: a frequency profile, a spatial amplitude map, a spatial time-delay map (or frequency-specific spatial phase maps), an epoch profile, and epoch-specific phase offsets per frequency (Fig 3B-G). All these parameters will be described below in detail. Importantly, this characterization follows from the assumption that oscillatory networks can be conceived as spatially distributed neuronal sources measured at a number of sites. The sources induce phase-consistent oscillations measurable at different sites, within the frequencies that characterize the network. The phases of the frequency-specific Fourier coefficients can vary both over sites and epochs but, because we assume phase-consistency, the between-site phase relations are identical for all epochs (Fig 3A). Crucially, we characterize a network by multiple frequencies, which is in line with the general observation that neuronal oscillations always have energy in a *band* of frequencies. These frequencies can form a narrow range, e.g. 4-8Hz (the theta band), or a very broad range, e.g. 30-60Hz (the gamma band). Which frequencies are involved in a network is specified in the frequency profile.

A *frequency profile* (Fig 3B) specifies the degree to which different frequencies are involved in the network. It is described by a vector of positive real numbers, which are high for frequencies that are strongly involved, and close to zero for those that are weakly involved. A *spatial amplitude map* (Fig 3C) specifies the degree to which the different sites reflect the network, and is also described by a vector of positive real numbers. An *epoch profile* (Fig 3D) specifies the degree to which the different epochs reflect the network, also described by a vector of positive real numbers. The *frequency profile*, the *spatial amplitude map*, and the *epoch profile* (Fig 3B-D) together describe the degree to which the network is determined by each of the 3

dimensions of the 3-way array of Fourier coefficients. All phase characteristics of the network are described by the *spatial time-delay map* (Fig 3E; or *spatial phase maps*, Fig 3F), and the *phase offsets* (Fig 3G). The latter of these, the *phase offsets* (Fig 3G), capture the temporal offset of the network within each epoch. These phase offsets are frequency-specific. The *spatial time-delay map* (Fig 3E; or frequency-specific *spatial phase maps*, Fig 3F) specifies the consistent between-site phase relations. Importantly, we present a model for coupled oscillatory networks in which any two interacting sites is characterized by phase differences that may vary as a function of frequency (within the frequency band that characterizes this network). The way these phase differences vary over frequencies can provide important insights into how two sites interact. For instance, if there would be a consistent time delay between two interacting sites, then this would result in phase differences that increase linearly with frequency. These phase differences are jointly characterized by the spatial time-delay map (Fig 3E). A spatial time-delay map is the map from which the time delay between any pair of sites can be obtained by taking the difference between the corresponding coefficients in the map. By multiplying this time delay with the frequency of interest, we obtain the between-site phase difference for that frequency. The spatial phase maps (Fig 3F) specify the between-site phase differences more directly, without the constraint of a linear relation with frequency. These maps are frequency-specific spatial maps from which the consistent between-site phase differences can be obtained by simple subtraction between the sites. Because the spatial phase maps do not enforce a particular pattern on the between-site phase differences (e.g., a linear relation with frequency), they are most useful in explorative studies. The spatial time-delay maps are more useful for a targeted investigation of temporal dynamics. Importantly, although phase coupling at the level of site *pairs* can be reconstructed from both types of spatial maps, the maps themselves describe phase coupling at the level of individual sites. This is useful, because it can directly reveal the spatial structure of the network.

Together, the *frequency profile*, the *spatial amplitude map*, the *epoch profile*, the *spatial time-delay maps* or *spatial phase maps*, and the *phase offsets*, characterize a phase-coupled oscillatory network. That is, they describe that part of the 3-way array of Fourier coefficients that originates from a particular phase-coupled oscillatory network. To extract and characterize these networks, we developed a new method, denoted as SPACE (for Spatially distributed PhAse Coupling Extraction). This method is briefly described in the Materials and Methods section, and a full description of the method and the underlying algorithm is provided in the Appendix. The method is based on two models: the time delay model (SPACE-time), that characterizes networks using spatial time-delay maps, and the FSP model (for Frequency-Specific Phases; SPACE-FSP), that characterizes networks using spatial phase maps. In the

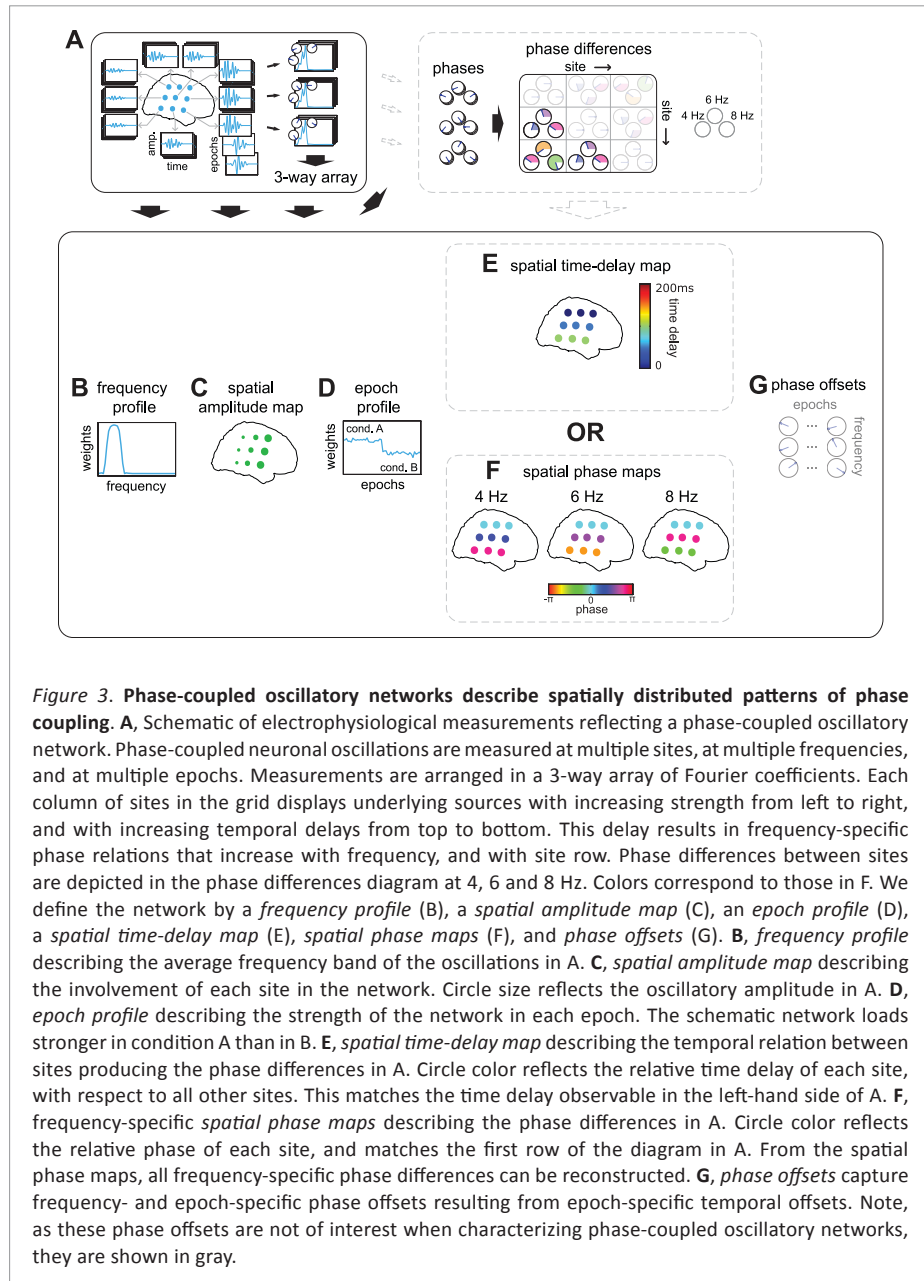


Figure 3. Phase-coupled oscillatory networks describe spatially distributed patterns of phase coupling. **A**, Schematic of electrophysiological measurements reflecting a phase-coupled oscillatory network. Phase-coupled neuronal oscillations are measured at multiple sites, at multiple frequencies, and at multiple epochs. Measurements are arranged in a 3-way array of Fourier coefficients. Each column of sites in the grid displays underlying sources with increasing strength from left to right, and with increasing temporal delays from top to bottom. This delay results in frequency-specific phase relations that increase with frequency, and with site row. Phase differences between sites are depicted in the phase differences diagram at 4, 6 and 8 Hz. Colors correspond to those in F. We define the network by a *frequency profile* (B), a *spatial amplitude map* (C), an *epoch profile* (D), a *spatial time-delay map* (E), *spatial phase maps* (F), and *phase offsets* (G). **B**, *frequency profile* describing the average frequency band of the oscillations in A. **C**, *spatial amplitude map* describing the involvement of each site in the network. Circle size reflects the oscillatory amplitude in A. **D**, *epoch profile* describing the strength of the network in each epoch. The schematic network loads stronger in condition A than in B. **E**, *spatial time-delay map* describing the temporal relation between sites producing the phase differences in A. Circle color reflects the relative time delay of each site, with respect to all other sites. This matches the time delay observable in the left-hand side of A. **F**, frequency-specific *spatial phase maps* describing the phase differences in A. Circle color reflects the relative phase of each site, and matches the first row of the diagram in A. From the spatial phase maps, all frequency-specific phase differences can be reconstructed. **G**, *phase offsets* capture frequency- and epoch-specific phase offsets resulting from epoch-specific temporal offsets. Note, as these phase offsets are not of interest when characterizing phase-coupled oscillatory networks, they are shown in gray.

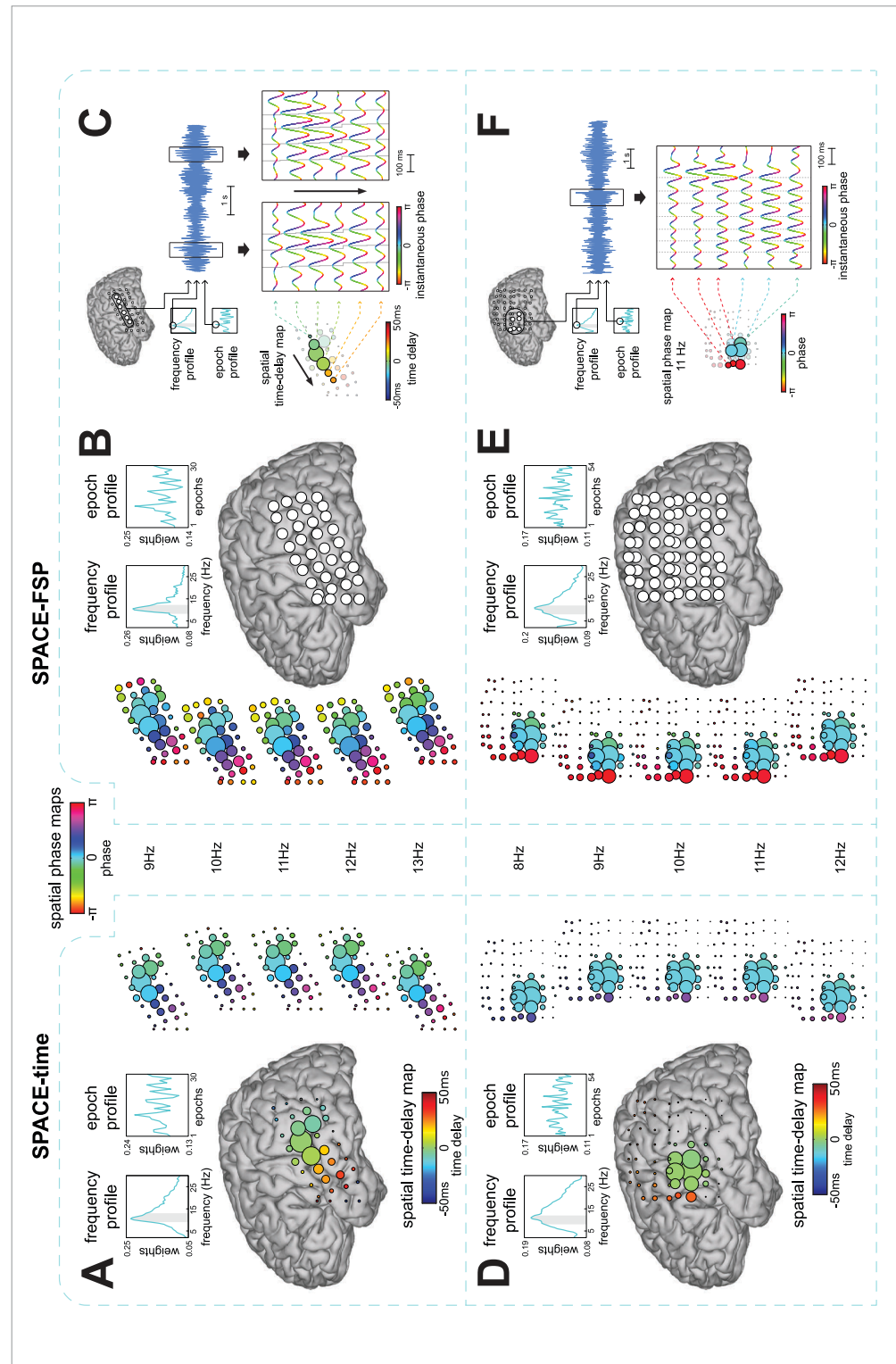
following, we first describe example networks extracted from ECoG recordings. Next, we provide evidence for the robustness of the method, by recovering simulated networks from realistic noisy data. In each section, both models are used and their results compared.

2. SPACE EXTRACTS PHASE-COUPLED OSCILLATORY NETWORKS FROM HUMAN ECoG RECORDINGS

We now present three example networks extracted from ECoG recordings of three epilepsy patients while they were performing a Sternberg working memory task (see Materials and Methods; Fig 4). We analyzed the task period during which the patients were engaged in the task. We did not distinguish between the cognitive operations encoding and retrieval occurring in this period, as the main purpose of the current analyses was to demonstrate that plausible phase-coupled oscillatory networks could be extracted.

Fourier coefficients of each of the three datasets were obtained by using a Welch tapering approach with multiple overlapping 2 second windows per trial, yielding a 4-way array of Fourier coefficients with a 0.5 Hz frequency resolution and a taper dimension (in contrast to the 3-way array introduced above, see Materials and Methods). Each of the three datasets was analyzed using both SPACE-time and SPACE-FSP. Because the 4-way arrays of Fourier coefficients were obtained using multitaper estimation, we used the cross-product formulation of both models (see Materials and Methods and Appendix). Because we wanted to estimate the number of networks using a high frequency resolution (0.5 Hz), each epoch was constructed by combining the tapers of three consecutive trials (see Materials and Methods). The number of extracted networks was determined on the basis of their reliability as evaluated by a split-half procedure (see Materials and Methods). This involves that only networks were extracted that could be identified in two independent datasets, obtained by randomly splitting the trials in two halves. This resulted in four, two, and four extracted networks from the recordings of patient 1, 2, and 3, respectively. We selected one network of each patient and show its description by the time delay and the FSP model (Fig 4), all other networks are presented in Supplementary Figures S2-4. We quantitatively compare both descriptions by a similarity coefficient (see Materials and Methods), which ranges from 0 to 1. The networks shown were selected because they reflect neurophysiologically interesting patterns, such as travelling waves. The three, one, and three non-selected networks showed many different patterns, such as spatial amplitude/phase maps dominated by a few electrodes with little phase diversity and spatial amplitude/phase maps with multiple groups of electrodes exhibiting phase diversity both within and between groups.

From patient 1, we extracted a network that shows a travelling alpha wave over parieto-temporal electrodes (Fig 4A-C). The network extracted using the time delay model (Fig 4A) closely corresponds to the one extracted using the FSP model (Fig 4B): (1) the frequency profile and the epoch profile of the two networks are very similar (similarity coefficient = 0.91), (2) the progression of phases over electrodes and over



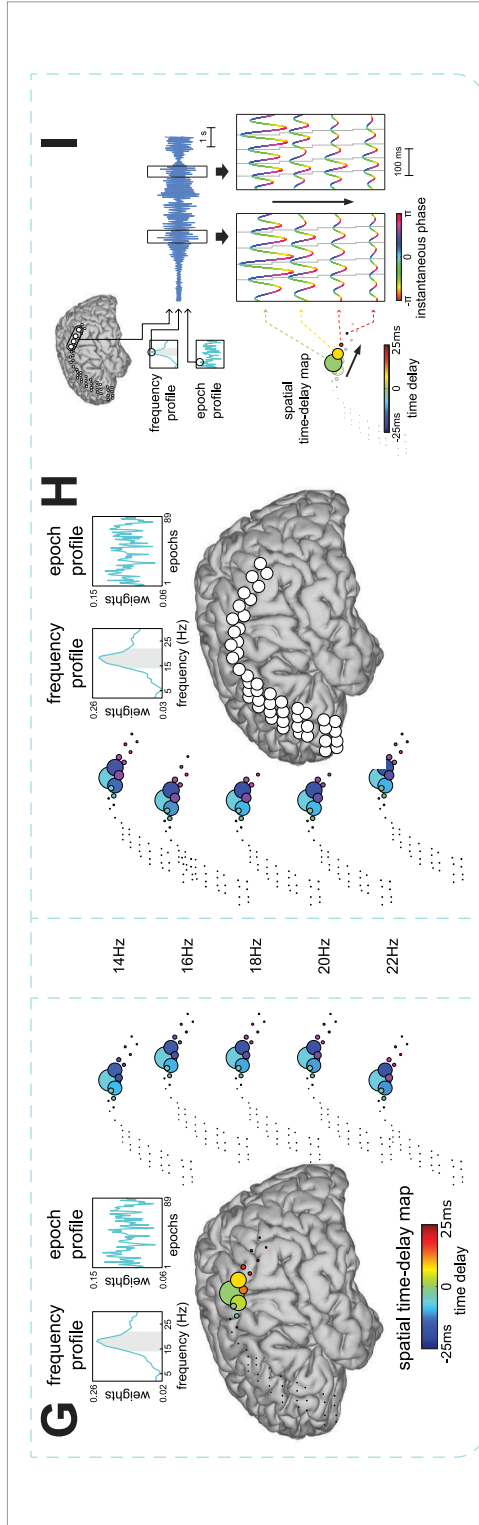


Figure 4. Example phase-coupled oscillatory networks from human ECoG recordings. We show 3 phase-coupled oscillatory networks from ECoG recordings during a Sternberg working memory task from 3 epilepsy patients (see Materials and Methods). Networks are displayed on a Talairach template brain. The first network shows travelling alpha wave over parieto-temporal electrodes (A,B,C). The second network shows an alpha network with phase relations dominated by 0 or π over fronto-parietal electrodes (D,E,F). The third network shows a travelling beta wave over parieto-frontal electrodes (G,H,I). Each dataset was analyzed using the cross-product formulation of SPACE-time (A,D,G) and SPACE-FSP (B,E,F) and the extracted networks were compared (see Materials and Methods). The Fourier coefficients were obtained from Welch-tapered signals of 2 seconds, and therefore had a frequency resolution of 0.5 Hz. We also show single trial observations of the networks (C,F,I). Only those grids/strips with high amplitudes in the spatial amplitude map are shown. **A**, travelling alpha wave described by the time delay model. Frequency and epoch profiles are shown in the top left. The full grid is shown in the center on a Talairach template. The spatial time-delay map is shown on the right side. Electrode size reflects the spatial amplitude map. Electrode color reflects the time delay relative to the strongest electrode. The displayed frequencies are selected from the gray band in the frequency profile. Spatial phase maps are shown on the left to compare phases resulting from the time delay model to those of the FSP model. These maps were generated by multiplying each time delay by $2\pi\varphi_k$, where φ_k reflects the k -th frequency, **B**, travelling alpha wave corresponding to the one in A described by the FSP model. Frequency and epoch profiles are shown on the top left. The spatial phase maps are displayed in the center. Electrode size reflects the spatial amplitude map. Electrode color reflects the phase relative to the strongest electrode in A. **C**, single trial oscillations displaying the travelling alpha wave at the peak frequency (≈ 11 Hz) in the strongest trial. The top panel displays the selected trial, frequency, and electrodes. The bottom panel shows excerpts from this trial. Instantaneous amplitude is colored by instantaneous phase. The gray solid line reflects the time delay between electrodes. Oscillations matching the time delays cross this gray line at their peaks. Black arrows denote the direction of the travelling wave. **D**, **E**, same as A,B but for a dipolar alpha network with 0 or π phase relations. **F**, same as in C but for the dipolar alpha network shown in D and E (≈ 11 Hz), using the estimates for the FSP model. The dashed gray line is now straight. Oscillations matching the spatial phase maps cross this line at their troughs for the top three electrodes and at their peaks for the bottom three electrodes. **G**, **H**, same as A,B but now for a travelling beta wave. **I**, same as C but now for the travelling beta wave (≈ 19 Hz) shown in G and H.

frequencies generated from the time delay network follows the spatial phase maps of the FSP network, with the time delay and the FSP network both showing the alpha wave travelling in the posterior to anterior direction. The only clear difference is that the spatial amplitude map of the FSP network includes more electrodes than the one of the time delay network. We also show the travelling wave in the trial with the highest amplitude at the peak frequency of the network (≈ 11 Hz). We do this for a selection of electrodes that lie in the direction of the travelling wave (Fig 4C). This example shows that, at the level of a single trial, there is a close match between the time delays extracted using the time delay model (calculated over all trials) and these single trial time delays. We additionally computed the speed of the travelling wave using the network from the time delay model. This was done by computing the distances between all electrode-pairs (using Talairach coordinates), dividing these distances by the between-electrode time delays, and subsequently averaging the resulting speeds. (We calculated a weighted average with the weights being the product of the spatial amplitude map loadings of all electrode-pairs.) This resulted in an average speed over electrode-pairs for this travelling alpha wave of 4.38 m/s. This is similar to speeds reported by Massimini et al. (2004) in extracranial human recordings, but is much faster than those reported by Rubino et al. (2006) in ECoG recordings of monkey motor cortex. The direction of the wave is given by the temporal order of the time delays, provided that none of the between-site time differences exceeds 2s (a critical time delay that depends on the frequency resolution, which is 0.5 Hz for our analysis; see Appendix).

From patient 2, we extracted a dipolar alpha network over fronto-parietal electrodes of which the spatial phase maps are dominated by phase relations that are either 0 or π (Fig 4D-F). The network extracted using the time delay model (Fig 4D) closely corresponds to the one extracted using the FSP model (Fig 4E; similarity coefficient = 0.96), except for the spatial time-delay maps. The phase differences that are implied by the spatial time-delay maps are much smaller than the phase relations that were estimated under the FSP model. We also show phase relations in the trial with the highest amplitude at the peak frequency of the network (≈ 11 Hz) for a selection of electrodes from the two clusters (Fig 4F). The single trial phase differences between the two clusters of electrodes closely match the dipolar phase relations estimated under the FSP model.

From patient 3, we extracted a network that shows a travelling beta wave over fronto-parietal electrodes (Fig 4G-I). For all parameters, the network extracted using the time delay model (Fig 4G) closely corresponds to the one extracted using the FSP model (Fig 4H; similarity coefficient = 0.99). Importantly, the progression of phases over electrodes and over frequencies generated from the time delay network follows the spatial phase maps of the FSP network, with the time delay and

the FSP network both showing the beta wave travelling in the anterior to posterior direction. We also show the phase relations in the trial with the highest amplitude at the peak frequency (≈ 19 Hz) for a selection of electrodes that lie in the direction of the travelling wave (Fig 4I). The average speed over electrode-pairs of this travelling beta wave was 5.19 m/s.

3. SPACE RECOVERS PHASE-COUPLED OSCILLATORY NETWORKS FROM REALISTIC NOISY SIGNALS

We performed simulations to test the ability of our method to recover phase-coupled networks from noisy signals. To accurately recover simulated networks, our method needs to fulfill two important requirements: (1) its solutions need to be unique, and (2) it needs to be robust against biologically realistic noise. Although we cannot provide a theoretical proof of uniqueness, in the Appendix, we show the results of a simulation study that strongly suggest uniqueness. To investigate the second requirement, we conducted simulations using realistic noisy signals. These signals were obtained by adding spatially correlated noise to time-domain signals that were generated under the time delay model. This spatially correlated noise reflects scattered neuronal sources without a consistent oscillatory phase coupling structure in some frequency range. These scattered sources distort the structure that is induced by the simulated networks because they cannot be fitted parsimoniously by our models. By increasing noise strength and spatial correlation, we create an environment where it becomes increasingly difficult to distinguish the networks of interest from the background activity. The importance of spatial correlation of the noise became very obvious when we performed pilot simulation studies with uncorrelated noise. We observed that it was trivially easy to accurately and uniquely recover networks in this situation. For instance, we simulated data in the frequency domain by directly generating the 3-way (and 4-way) array of Fourier coefficients using the parameters of both models. Adding large amounts of uncorrelated complex-valued noise had a very weak effect on the recovery of the networks. To test our method under more challenging and more realistic conditions, we generated data in which we controlled both the amount and the spatial correlation of the noise.

We simulated phase-coupled oscillatory networks with varying noise strength, spatial noise correlation, and time delays across a 5x5 sites grid (Fig 5,6,7; for a detailed description see Materials and Methods). Using these simulations, we investigated (1) how network recovery varies as a function of noise strength and correlation, and (2) how recovery varies as a function of the time delays. To this end we performed two sets of simulations: (1) fixed between-site time delays but varying noise strength and spatial noise correlation, and (2) varying time delays, varying noise strength but fixed spatial noise correlation. The signal-to-noise ratio (SNR) was

varied over 4 levels: 4, 0.16, 0.04 and 0.01. Spatial noise correlation was determined by the full-width half-maximum (FWHM) of a bivariate Gaussian distribution at 0, 10, 20, or 40mm. These distances are evaluated relative to the inter-site distances of our 5x5 grid, which had a 10mm spacing. Finally, between-site time delays were varied over the following 4 levels: 5, 25, 50, and 100ms. In the following, we first briefly describe how we simulated phase-coupled oscillatory networks, and how we assessed the similarity between the extracted and simulated networks. Next, we present the results of the two parts of our simulation study.

We simulated three phase-coupled oscillatory networks travelling on a 5x5 sites grid, which were partially repeated over 25 epochs (Fig 5). The three networks had different but partially overlapping frequency profiles: one in the theta, one in the alpha, and one in the beta band (Fig 5B). Each network was further characterized by a spatial amplitude map specifying which sites showed the oscillatory signal and a spatial time-delay map specifying the time and phase relations between these sites (Fig 5A). Spatial amplitude maps were partially overlapping. Per network and epoch, a 1-1.5 second source signal was randomly generated as band-pass filtered brown-noise (see Materials and Methods), which was subsequently mapped to the sensor level (the 5x5 sites grid) according to the spatial amplitude and the spatial time-delay map for that network. Per network, the frequency profile to-be-recovered was set as the average amplitude spectrum (over all epochs; Fig 5B). Epochs varied with respect to whether or not a particular network was involved, and this was specified by the network's epoch profile (Fig 5B). Each network was present in 15 out of 25 epochs. Noisy 3 second signals were created by adding randomly generated brown noise to the model signals that were generated as phase-coupled oscillatory networks (after zero padding the 1-1.5 s model signals to 3 s). In Fig 5C, we show a set of example epochs with varying noise strength. For each of the simulation parameter combinations (4 SNR levels, 4 noise correlation levels and 4 time delays), we generated 100 data sets; each of these simulations will be denoted as a run. Per run, Fourier coefficients were obtained by using a Welch tapering approach with multiple overlapping 1 second windows per epoch. This yielded a 4-way array of Fourier coefficients with a taper dimension and a 1 Hz frequency resolution for frequencies below 17 Hz and, using additional tapering, 2 Hz for frequencies of 17 Hz and above (see Materials and Methods). These 4-way arrays were subsequently analyzed using both SPACE-time and SPACE-FSP. Because the 4-way arrays of Fourier coefficients were obtained using multitaper estimation, we used the cross-product formulation of both models. We computed recovery coefficients, expressing how well the extracted FSP and time delay model parameters recovered the simulated values (see Materials and Methods). These coefficients were computed per network per run. For the spatial amplitude maps, the frequency profiles, and the epoch profile

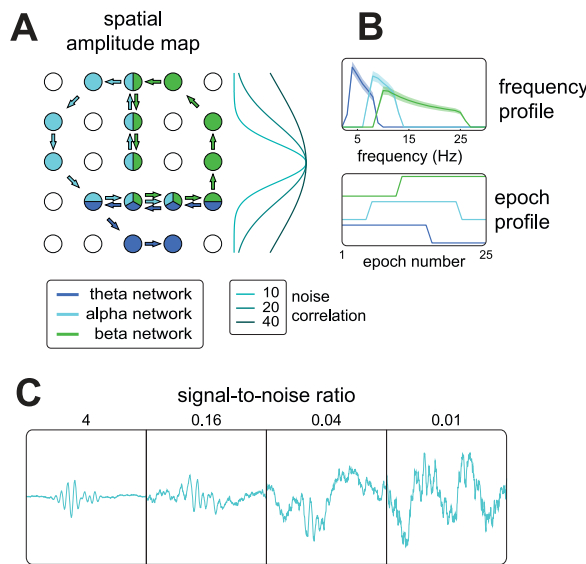


Figure 5. Simulation of phase-coupled oscillatory networks in a realistic noisy environment. To show that SPACE is able to recover networks surrounded by noise, we simulated a theta, alpha, and beta phase-coupled oscillatory network on a 5x5 site grid with variable noise strength and spatial correlation (see Materials and Methods). Each network consisted of an oscillatory signal that progressed over sites with a time delay in a fixed order, and with partially overlapping sites. Signals were generated in three frequency bands, theta (4-8), alpha (8-12), and beta (10-25), and were present in 15 out of 25 epochs of 3 seconds. Each signal was constructed as band-passed randomly generated brown noise per epoch, and lasted 1-1.5 seconds. Randomly generated brown noise was added to the signal. Both signal and noise had a $1/f^2$ shaped power spectrum. **A**, 5x5 site grid with 10mm spacing showing simulated network progression and spatial correlation profile. The spatial amplitude maps had equal nonzero values for a subset of the sites. Amount of spatial correlation (right hand side of grid) was determined by a bivariate Gaussian with a full-width half-maximum of 0, 10, 20, and 40mm. **B**, frequency profile and epoch profile of simulated networks showing partial overlap. The frequency profile shows the average amplitude spectrum (shaded area = std-dev) over epochs, over simulations. Colors indicate network identity and correspond to those in A. **C**, example epochs at various noise levels of a site displaying the theta network.

of SPACE-time/FSP, this coefficient ranges from -1 to 1. For the spatial phase maps and the spatial time-delay maps, this coefficient ranges from 0 to 1. The recovery of the temporal order of the time delays (i.e., disregarding the quantitative differences) extracted by the time delay model was indexed by a coefficient that ranges from 0 to 1.

To investigate the effect of noise on the recovery of the networks, we simulated networks with a 25ms time delay between adjacent sites and varying levels of noise strength and noise correlation (Fig 6). This 25ms time delay resulted in a delay of 125ms, 225ms, and 225ms between the first and the last site for the theta, alpha and the beta network respectively. Recovery coefficients were calculated per network per run, and averaged over the three networks per run. Subsequently, the average

and standard deviation over runs was calculated. We show these results, separately for SPACE-time (Fig 6A) and SPACE-FSP (Fig 6B). We observe that (1) without spatial noise correlation, recovery is highly accurate even for very high noise levels, (2) recovery decreases with noise strength, (3) this decrease is stronger with higher noise correlation, and (4) overall, SPACE-FSP model performs better than SPACE-time. To also give a visual impression of the goodness-of-recovery, we show the extracted frequency profiles for different levels of noise strength and noise correlation (Fig 6A,B). Note that the recovery of the frequency profiles does not approach a perfect fit, both when using the time delay and the FSP model. This is because we obtained the frequency profile to-be-recovered indirectly by averaging the frequency spectra of the simulated time domain signals, instead of directly specifying the frequency profile and inserting it in the model equation (formulated in the frequency domain). Therefore, when evaluating the goodness-of-recovery, we do not compare the estimated profiles to the ground truth.

On the basis of these simulation results, we can formulate some guidelines for applications of SPACE to real data. For that, we consider a goodness-of-recovery coefficient of 0.75 to be sufficient for the label acceptable. Then, for an acceptable network recovery using the FSP model, it is sufficient to have an SNR of 0.16. The spatial noise correlation can then correspond to a noise FWHM covering 9 recording sites (i.e. 40 mm FWHM in the above). If the SNR is only 0.04, an acceptable network recovery requires that the noise FWHM covers at most 5 recording sites (a 20 mm FWHM in the above). For an acceptable network recovery using the time delay model, the spatial noise correlation has to be less: with an SNR of 0.16 or 0.04, the noise FWHM must cover at most 5 or 3 recording sites respectively.

To investigate the effect of the between-site time delays on network recovery, we varied the time delay step size together with noise strength at a fixed spatial noise correlation (20mm FWHM). We simulated networks with a 5, 25, 50, 100ms delay between adjacent sites (Fig 7. In this simulation study, we did not average the recovery coefficients over networks, as the frequency content of the different networks could have an influence on the ability to extract them. We show the recovery results for SPACE-time (Fig 7A) and SPACE-FSP (Fig 7B), separately for every network. For the purpose of presentation, we averaged the recovery coefficients for the spatial amplitude map, the frequency profile, and the epoch profile, and did this for each network in each run. We observe that (1) SPACE-FSP is much less affected by the between-site time delays than SPACE-time, (2) goodness-of-recovery decreases with between-site time delay and this decrease is much stronger when using the time delay model, and (3) between-site time delay and network frequency have interacting effects on goodness-of-recovery when using the time delay model: with increasing time delays, goodness-of-recovery for the alpha network decreases

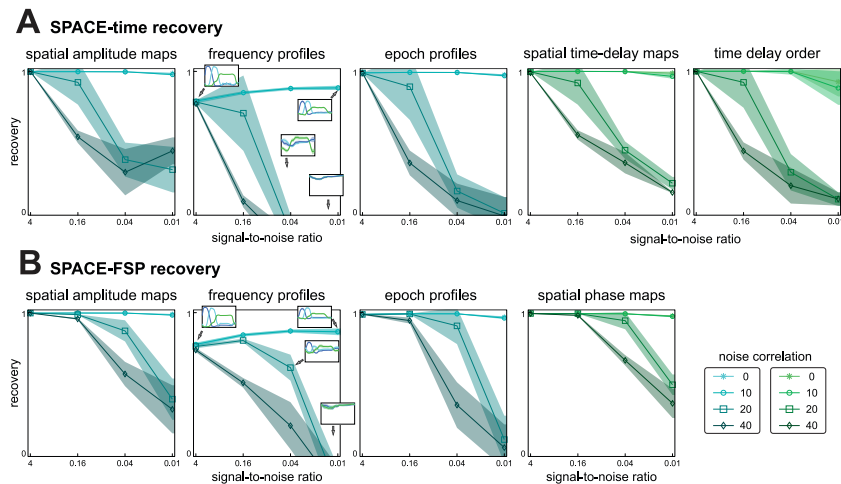
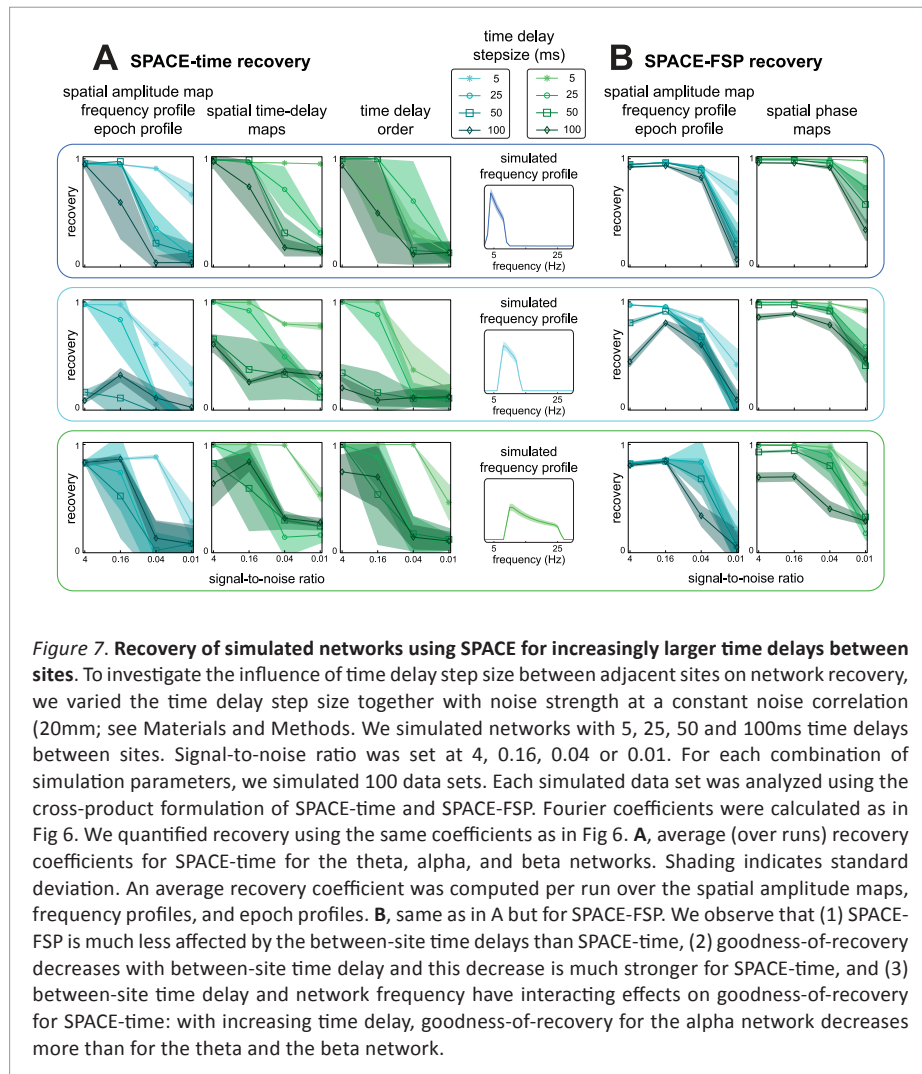


Figure 6. SPACE recovers simulated networks under noisy conditions. To investigate the effect of noise on the recovery of the simulated networks, we simulated networks with 25ms time delay between adjacent sites, with variable noise strength, and spatial noise correlation (see Materials and Methods). Signal-to-noise ratio (SNR) was systematically varied over 4, 0.16, 0.04 and 0.01. Spatial noise correlation was determined by a Gaussian with a full-width half-maximum at 0, 10, 20 or 40mm. For each combination of simulation parameters, we simulated 100 data sets. Each simulated data set was analyzed using the cross-product formulation of SPACE-time and SPACE-FSP. The Fourier coefficients were obtained from Welch-tapered signals of 1 second, and using additional Slepian tapering had a frequency resolution of 1 or 2 Hz (see Materials and Methods). We computed several coefficients reflecting the accuracy of recovery of the simulated networks. These range from -1 to 1 for spatial amplitude maps, frequency profiles, and epoch profiles. For spatial phase maps and spatial time-delay maps, these range from 0 to 1. We additionally analyzed recovery of temporal order of time delays, with a coefficient ranging from 0 to 1. All coefficients were averaged over the three networks, per run. **A**, average (over runs) recovery coefficients for SPACE-time. Shading indicates standard-deviation. Inserts in frequency profiles show the average extracted frequency profile. **B**, same as in A but for SPACE-FSP. **A,B**, the graphs show that (1) recovery is very accurate when noise is uncorrelated even when noise strength is high, (2) recovery decreases with noise correlation, (3) this decrease is stronger with higher noise strength, and (4) overall, SPACE-FSP performs better than SPACE-time. Note, the recovery of the frequency profiles does not approach a perfect fit. This is because we obtained the frequency profile to-be-recovered from a frequency analysis of the simulated time domain signals (band-pass filtered brown noise).

more than for the theta and the beta network. We therefore conclude that, when expected time delays are large, using the FSP model is preferred over the time delay model.

In sum, we have shown that SPACE can recover networks from signals that contain spatially correlated noise. For the FSP model, an SNR of 0.16 suffices to produce an acceptable recovery even when the spatial noise correlation encompasses 9 recording sites. If the SNR is only 0.04, an acceptable network recovery requires that the spatial noise correlation encompasses at most 5 recording sites. For an acceptable network recovery using the time delay model, the spatial noise correlation has to be substantially less. Additionally, when the expected time delays of a phase-coupled

oscillatory network are large relative to cycle length of the network oscillation, then SPACE-FSP can more accurately recover the between-site phase relations generated from the time delays.



DISCUSSION

We developed a method capable of extracting phase-coupled oscillatory networks. Our contribution involves four key elements. First, we provide a precise definition of a phase-coupled oscillatory network in terms of six parameters: a frequency profile, a spatial amplitude map, spatial phase maps or a spatial time-delay map, an epoch profile, and phase offsets (or an equivalent parameter in case of the cross-product formulation). Crucially, this definition respects the fact that brain rhythms involve a range of frequencies, and cannot be characterized by line spectra. Second, we developed a method that extracts these networks from electrophysiological data. Third, we demonstrate that this method is able to extract networks with a revealing phase structure from ECoG data. And fourth, using a simulation study, we quantify the robustness of this method against violations of the phase-coupling structure imposed by the model. This demonstrates the method's usefulness in practical applications.

Neuronal networks realize the many processes that underlie cognitive functions: selecting and routing information, keeping the information in working memory, storing and retrieving information from a more permanent store, etc. All these processes involve interactions between anatomically distinct but connected brain regions. This is the prime motivation for the development of methods that extract these networks from neurobiological data.

Compared to electrophysiology, the functional magnetic resonance imaging (fMRI) community has a long tradition in identifying functional networks. Networks of co-activated brain regions can be found using the spontaneous co-variation of the blood oxygenation level dependent (BOLD) signal measured at rest, that is, in absence of stimulation or a task (Biswal et al., 1997; Raichle et al., 2001; Fox et al., 2005; Honey et al., 2009; Smith et al., 2009; Deco and Corbetta, 2011). These networks are usually referred to as resting state networks (RSNs; Beckmann et al., 2005). An important observation constraining the possible functional role of these fMRI-derived RSNs is that they also exist in the absence of consciousness during anesthesia and sleep (Vincent et al., 2007).

Recently, RSNs have begun to be investigated using magnetoencephalography (MEG) recordings (de Pasquale et al., 2010; Brookes et al., 2011). This is important progress, because MEG directly measures electrophysiological brain activity, bypassing the indirect hemodynamic response. Crucially, the RSNs that were identified did not depend on oscillatory phase coupling. As a part of the analyses, MEG recordings were transformed into time series of band-limited power (BLP) in several frequency bands. These BLP time series were then correlated using a seed-based approach (de Pasquale et al., 2010) or decomposed using independent

component analysis (Brookes et al., 2011). With this approach, it was shown that RSNs could be extracted using BLP time series (especially in the beta band; 15-25 Hz) that were highly similar to those found in fMRI signals (de Pasquale et al., 2010; Brookes et al., 2011).

Another recent method to identify networks is based on phase-amplitude coupling (Maris et al., 2011; van der Meij et al., 2012). Contrary to a correlation between BLP time series, phase-amplitude coupling does depend on oscillatory phase coupling: it indexes the preference for amplitude envelopes at a certain frequency (equivalent to a BLP time series) to have high values at a certain phase of a slower phase-providing oscillation. Most reports focus on the coupling between amplitude-providing and phase-providing oscillations obtained from the same site (Chrobak and Buzsaki, 1998; Schack et al., 2002; Bruns and Eckhorn, 2004; Mormann et al., 2005; Canolty et al., 2006; Cohen et al., 2009). However, focusing on between-site phase-amplitude coupling inspired the development of methods with which networks could be identified (Maris et al., 2011; van der Meij et al., 2012). With these methods, revealing differences between amplitude-providing and phase-providing networks could be identified.

The method presented in this paper allows for an identification of networks using phase coupling between oscillations alone. Crucially, this method respects the fact that brain rhythms have energy in a range of frequencies, and therefore allows between-site phase differences to vary over frequencies. As we have illustrated in the Results section, this property allows us to distinguish different network configurations. One such example is a travelling wave (e.g. the networks in Fig 4A,G, and the simulated networks in Fig 5-7). This wave could be generated by a distributed oscillatory source in which the many subpopulations interact with a temporal delay. The signals generated by such a distributed source can be described by our time delay model. A second example, which can be described by our FSP model, involves a source that is small relative to its distance from the sensors, as is often the case in macroscopic measurements like MEG and EEG, but is also present in more local measurements such as ECoG (see Results section). Such a distant source generates a dipolar potential distribution (two groups of sites whose potentials have opposite signs) over sites that are at the same distance from this source (e.g. the network in Fig 4E, network 2 in Fig S2B, network 1 Fig S3B). The phase differences between these sites are either 0 (synchrony) or π (antiphase) and, importantly, do not vary as a function of frequency. This example shows that the spatial phase maps can depend on the recording technique. The dependence of the spatial distribution of the measurements on the recording technique has been put forward by other authors, starting from the spatial filtering characteristics of the measurement technique (Nunez et al., 2001). A third example is a network driven

by thalamo-cortical interactions (Suffczynski et al., 2001), which has elements of the above two examples. A possible scenario involves multiple cortical populations that are driven by a common thalamic pacemaker. The timing of the input to these cortical populations will differ as a function of the delay in the axonal connection with this thalamic pacemaker. As a result, the phase relations between these cortical populations will be larger than the phase relations within them (which are 0 in the idealized scenario of no within-population differences in axonal delay). The essential difference with this example configuration and the previous dipolar configuration is that between-site phase differences are not only 0 or π , but can take any value in between (as determined by the difference in thalamo-cortical delay). Such a network can be described by both of our models.

Between-site phase relations in electrophysiological recordings may be of crucial importance for the understanding of neuronal communication. Electrophysiological recordings of neural activity (LFPs, ECoG, EEG, MEG) reflect synchronized membrane potential fluctuations. Importantly, membrane potential fluctuations reflect fluctuations in neuronal excitability. This implies that oscillations may reflect rhythmic fluctuations in neuronal excitability. It has therefore been proposed that effective communication between two neuronal populations depends on whether or not the spike input from the sending population arrives at an excitable phase of the receiving population (Fries, 2005; Borgers and Kopell, 2008; Tiesinga et al., 2008). This idea can easily be generalized to motifs that involve more than two neuronal populations, of which some pairs can effectively communicate and others cannot, depending on their phase relations (Fries, 2005). Thus, neuronal populations forming networks by phase-coupled oscillations could be a key mechanism for inter-areal communication and selective routing of information through the brain. In line with this hypothesis, it has been shown that local field potentials at one site coordinate spikes in task-relevant neurons at a remote site (Canolty et al., 2010; Canolty et al., 2012a).

From a methodological point of view, it is important to distinguish our multivariate approach from the more common bivariate approach, in which oscillatory phase coupling is evaluated by pair-wise measures such as coherence (Mormann et al., 2000), imaginary coherence (Nolte et al., 2004), phase-locking value (Lachaux et al., 1999), pair-wise phase consistency (Vinck et al., 2010), the phase-slope index (Nolte et al., 2008), and Granger causality (Bernasconi and Konig, 1999; Kaminski et al., 2001). Some methods can make use of a full multivariate description of the data, but nevertheless only provide a quantification at the level of site-pairs, using the multivariate description to partial out for the contribution of other sites. This holds for phase coupling estimation (Canolty et al., 2012b), partial coherence (Rosenberg et al., 1998), Granger causality (Bernasconi and Konig, 1999; Kaminski et al., 2001),

Transfer Entropy ([Schreiber, 2000](#)), and Phase Transfer Entropy ([Lobier et al., 2014](#)). This quantification at the level of site-pairs is unfortunate, as pair-wise measures do not directly reveal the spatial distribution of phase-coupled networks, unless there is prior information about a seed region via which the other nodes of the network can be identified.

A method that shares several aspects with the method presented in this paper is shifted CP ([SCP; Morup et al., 2008](#)). This method builds on earlier work in which PARAFAC ([Carrol and Chang, 1970](#); [Harshman, 1970](#)) was used to decompose spatio-spectro-temporal electrophysiological data ([Miwakeichi et al., 2004](#); [Morup et al., 2006](#)). Importantly, in these earlier studies, PARAFAC was only applied to the amplitudes of the Fourier coefficients; the phase information was ignored. The novel method, SCP, decomposes the complex-valued raw Fourier coefficients over sites, frequencies and epochs into multiple components. Each SCP component is described by a real-valued spatial map, a complex-valued frequency profile, and a real-valued epoch profile. Importantly, each component is additionally described by a set of epoch-specific time-shifts, which allows the method to model between-epoch differences in the temporal onset of a network. However, as between-site phase relations are not explicitly modeled, only networks with between-site phase differences of 0 and $\pm\pi$ are extracted (by allowing for negative values in the spatial maps). Though this makes SCP suitable for extracting dipolar potential distributions, other types of phase-coupled oscillatory networks cannot be accurately described.

What holds for the comparison with shifted CP, also holds for the comparison with other decompositions, such as ICA ([Bell and Sejnowski, 1995](#)) and regular PARAFAC for complex-valued data ([Sidiropoulos et al., 2000](#)): our method improves on these alternatives because it is grounded in a plausible model of a neurobiological rhythm, a spatially distributed signal with energy in a limited range of frequencies and involving between-site phase relations that vary as a function of frequency. For example, we could apply complex-valued PARAFAC to a 3-way array of raw Fourier coefficients obtained from electrophysiological data. To our knowledge, this has not been reported yet, but there is nothing that prevents it. However, when applying this model, it imposes the restriction that the between-site phase relations in a network are identical for all frequencies. In contrast, our method extracts phase-coupled oscillatory networks that are characterized by a single spatial amplitude map and multiple frequency-specific spatial phase maps, as is required for modeling brain rhythms whose between-site phase relations depend on frequency.

Our method estimates spatial maps and frequency profiles without applying constraints on the shape of the spatial or spectral distribution. This is not necessarily optimal, and future improvement of our method could involve such constraints. Especially smoothness constraints could turn out to be beneficial, and improve the

interpretability of the extracted spatial structure and spectral content of networks. Such constraints have been applied successfully before in source reconstruction methods, such as LORETA ([Pascualmarqui et al., 1994](#)).

It is useful to compare our approach to the more theory-driven approach of computational neuroscientists that build networks of spiking model neurons, often with the objective of explaining correlated neuronal activity (e.g., [Kopell et al., 2000](#); [Whittington et al., 2000](#); [Borgers and Kopell, 2003](#)). These networks of spiking model neurons serve as the neurobiological motivation for network models at a coarser level of description, typically involving weakly coupled Kuramoto oscillators ([Kuramoto, 1984](#); [Ermentrout and Kopell, 1990](#); [Hoppensteadt and Izhikevich, 1997](#); [Kuramoto, 1997](#); [Brown et al., 2004](#)). Networks of Kuramoto oscillators are characterized by their phase interaction function (PIF), which specifies how the oscillators affect each other's phase velocity. These networks describe dynamics in phase relations and therefore can be used to model non-stationary processes. SPACE can also be applied to non-stationary processes, but can accommodate non-stationarity only by adding networks, because every network can only model a stationary pattern of phase relations.

Ideally, we would be able to motivate our method by establishing the relation between the parameters of the uncovered networks and a set of PIFs that may underlie these parameters. This would ground the output of our method in the well-developed mathematical theory of Kuramoto models. Unfortunately, it is unclear what the relation is between, on the one hand, the phase configurations induced by a Kuramoto model (e.g., different types of travelling waves), and on the other hand, Fourier coefficients (the raw frequency domain observations when actual data are collected). This state of affairs limits the application of Kuramoto models to a comparison between observed and simulated/fitted phase configurations, as is possible for instance using Bayesian model comparison (see [Penny et al., 2009](#), for an example of this approach). This differs from our approach in which we estimate the full networks from the raw Fourier coefficients.

In conclusion, our work starts from a precise definition of a phase-coupled oscillatory network that is in agreement with the fact that brain rhythms have energy in a range of frequencies. Crucially, this definition and the associated method allow for between-site phase relations that vary as a function of frequency. This allows us to distinguish different network configurations. Our method identifies networks on the basis of between-site phase coupling. This is an important contribution because (1) the existing bivariate methods can only indirectly reveal networks (using a seed region approach), and (2) the existing multivariate methods can only identify networks using amplitude envelope correlations. When identifying networks of oscillatory brain activity, it is crucial to take into account between-site

phase relations. Because oscillations may reflect rhythmic fluctuations in neuronal excitability, phase-coupled oscillatory networks could be the functional building block for inter-areal communication and selective routing of information throughout the brain.

APPENDIX

SPACE: AN ALTERNATING LEAST SQUARES ALGORITHM FOR EXTRACTING PHASE-COUPLED OSCILLATORY NETWORKS

We developed a method for extracting phase-coupled oscillatory networks from a 3- or a 4-way array of Fourier coefficients. This algorithm is denoted as SPACE (for Spatially distributed PhAse Coupling Extraction). It is inspired by complex-valued PARAFAC ([Carrol and Chang, 1970](#); [Harshman, 1970](#); [Bro, 1998](#); [Sidiropoulos et al., 2000](#)), an N-way decomposition technique. PARAFAC describes the structure in an N-way array by sets of loading vectors (one vector per dimension), which are jointly denoted as components. These components are extracted without requiring statistical constraints like orthogonality or independence, and are unique up to trivial indeterminacies. PARAFAC formed the base from which our new method was built, and it inherits many of its aspects.

SPACE uses two models to extract phase-coupled networks, which are described below (see the Materials and Methods and Results sections for a concise graphical introduction to the method). Extracting phase-coupled oscillatory networks starts with electrophysiological measurements $V_{jl}(t)$ (electrical potentials or magnetic field strength) as a function of time t , at multiple sites j , and in multiple epochs l . Then, by performing a spectral analysis on $V_{jl}(t)$ we can describe the average (over the epoch) oscillatory activity at site j and in epoch l by a complex-valued Fourier coefficient X_{jkl} , per frequency k . These Fourier coefficients can then be arranged in a 3-way array, with dimensions sites (J), frequencies (K), and epochs (L). This 3-way array of Fourier coefficients is the starting point for our method to extract phase-coupled oscillatory networks. These networks describe spatially distributed patterns of phase-coupling, by a spatial amplitude map, a frequency profile, an epoch profile, a spatial phase map per frequency, and a set of phase offsets.

SPACE uses two models to extract networks: SPACE-time and SPACE-FSP (for Frequency Specific Phase), which differ in how they describe the between-site phase relations per frequency. SPACE-time describes all phase differences (which vary as a function of frequency) by site-specific time delays, forming a spatial time-delay map. SPACE-FSP describes the between-site phase differences by site- and frequency-

specific phases, forming a spatial phase map per frequency. Importantly, the phase differences at the level of the site-pairs are calculated from the spatial time-delay map and spatial phase maps (representations at the level of the sites, instead of site-pairs). The element-wise formulations of these two models are as follows:

$$\text{SPACE-time: } X_{jkl} = \sum_{f=1}^F a_{jf} \cdot \exp(i2\pi\varphi_k\sigma_{jf}) \cdot b_{kf} \cdot c_{lf} \cdot \exp(i2\pi\tau_{klf}) + \varepsilon_{jkl}$$

$$\text{SPACE-FSP: } X_{jkl} = \sum_{f=1}^F a_{jf} \cdot \exp(i2\pi\lambda_{jkf}) \cdot b_{kf} \cdot c_{lf} \cdot \exp(i2\pi\tau_{klf}) + \varepsilon_{jkl}$$

The Fourier coefficient X_{jkl} is described as a sum over F network-specific complex-valued numbers. For both models, the amplitude of each network-specific complex-valued number is the product of a_{jf}, b_{kf} and c_{lf} , which refer to, respectively, the spatial amplitude map, the frequency profile and the epoch profile. For the time delay model the phase of each network-specific complex-valued number is the product of an element of the spatial time-delay map and a phase offset: $\exp(i2\pi\varphi_k\sigma_{jf})$ and $\exp(i2\pi\tau_{klf})$. Here, $2\pi\varphi_k\sigma_{jf}$ describes the site-, frequency-, and network-specific phases, in which φ_k denotes the k -th frequency (in Hz) and σ_{jf} denotes the site- and frequency-specific time delay. $2\pi\tau_{klf}$ describes the frequency-, epoch-, and network-specific phase offset. For the FSP model, the phase of each network-specific complex-valued number is the product of an element of the spatial phase maps and a phase offset: $\exp(i2\pi\lambda_{jkf})$ and $\exp(i2\pi\tau_{klf})$. Compared to the time delay model, $\varphi_k\sigma_{jf}$ is replaced by λ_{jkf} . Using the above parameterization of phase-coupled oscillatory networks our model sparsely describes an array of $2JKL$ elements (with the 2 reflecting the complex-valued nature of the input data) by sets of $2J + K + L + KL$ (SPACE-time) or $J + JK + K + L + KL$ (SPACE-FSP) elements.

All parameters are estimated using an alternating least squares (ALS) algorithm. Within each ALS iteration, we alternate over the five parameter sets characterizing the networks, obtaining a new least squares (LS) estimate of each, while keeping the other four parameter sets fixed. After all parameters are updated, a single iteration is completed. This process continues until a predetermined convergence criterion is reached.

We now describe the calculations within a single ALS iteration. Whereas the estimation of the spatial amplitude maps, the frequency and the epoch profiles uses known equations, the estimation of the time delays, frequency-specific phases, and phase offsets requires new algorithms, and these are described in a separate paragraph below.

All parameters are initialized by random starting values. Importantly, like PARAFAC, the algorithm can converge to a local minimum of the least squares

loss function. These suboptimal decompositions can be avoided by starting the algorithm multiple times. When the algorithm repeatedly converges to the same optimal solution starting from multiple random starting points, it can be assumed that the global minimum is reached. Besides local minima, as a consequence of an unfortunate starting point, the algorithm may also get trapped in a degenerate solution, in which networks become highly correlated, and the model estimates become arbitrarily large. This is a well-known problem in PARAFAC (see [Bro, 1998](#), and the references therein) and can be dealt with using multiple random starts. Another strategy to avoid degeneracy is presented below in the section describing the cross-product formulation of both models.

The algorithm(s) described below will be made available in a public GitHub (www.github.com) repository termed *nwaydecomp*. Additionally, it will be made available through the FieldTrip open-source MATLAB toolbox ([Oostenveld et al., 2011](#)).

OBTAINING THE LEAST SQUARES ESTIMATES OF THE SPATIAL AMPLITUDE MAPS, THE FREQUENCY AND THE EPOCH PROFILES

The LS estimation of the spatial amplitude maps (a_{if}), frequency profiles (b_{kf}) and epoch profiles (c_{lf}) resembles an ALS step in PARAFAC, however with two important differences. First, these maps and profiles are real-valued parameters in a complex-valued least squares minimization problem. As will be described in more detail in the next paragraph, this requires that the real and imaginary parts of some complex-valued matrices are concatenated, resulting in an expanded real-valued matrix. Second, we cannot make use of the regular Khatri-Rao product formulation, which plays a central role in the ALS algorithm for PARAFAC. This is due to the fact that the phases resulting from the time delays, the spatial phase maps and the epoch-specific phase offsets are frequency-specific. As a consequence, the least squares estimates of the spatial amplitude maps (a_{if}), frequency profiles (b_{kf}) and epoch profiles (c_{lf}) are obtained separately for every site, frequency, and epoch. We first describe the estimation of the spatial amplitude maps; the estimation of the frequency and the epoch profiles has exactly the same structure. The least squares estimate of the parameters of the j -th site are obtained as follows:

$$A_j = X_j^{cat} \cdot Z^{cat} \cdot (Z^{catT} \cdot Z^{cat})^{-1} \quad (1)$$

A_j is a vector of size $1 \times F$, T denotes the regular transpose and $^{-1}$ denotes the inverse. Here, Z^{cat} and X_j^{cat} refer to $[Real(Z), Imag(Z)]$ and $[Real(X_j), Imag(X_j)]$, which are the row-wise and column-wise concatenation of the real and imaginary parts of Z and X_j respectively. Matrix X_j is the unfolded matrix of Fourier

coefficients for site j , with unfolding over the frequency and epoch dimensions. This results in a matrix with dimensions $1 \times KL$ (with K and L being the number of frequencies and epochs respectively). Matrix Z is a complex-valued matrix formed in two steps. In the first step, the amplitude of the elements of Z are calculated, and in the second step, their phase. The amplitude of Z is given by $C| \otimes |B$, the Khatri-Rao product of the epoch and frequency profiles, C and B . The matrices C and B contain as their columns, respectively, the frequency and the epoch profiles of the different networks. The Khatri-Rao product $| \otimes |$ is defined as follows:

$$C| \otimes |B = \left[c_1 \otimes b_1 \ c_2 \otimes b_2 \dots c_F \otimes b_F \right]$$

This applies to any matrix C and B with an equal number of columns F . The Khatri-Rao product is defined as the concatenation of the Kronecker tensor products \otimes of column 1 to F of C and B . The phases of the elements of Z are calculated as element-wise products of the spatial phase maps (for the time delay model obtained from the spatial time-delay maps) and the phase offsets. These products are calculated in such a way that the indices of the frequencies and the epochs correspond to the amplitudes as calculated by the Khatri-Rao product.

The least squares estimate of the frequency and epoch profiles are calculated similarly to the spatial amplitude maps. For the frequency profile X_j^{cat} is replaced by X_k^{cat} . X is now a matrix unfolded over the site and epoch dimensions, having dimensions $1 \times JL$ (with J being the number of sites). The amplitude of matrix Z is now calculated as $C| \otimes |A$, with A containing in its columns the spatial amplitude maps. The phases of Z are again calculated as a product of the phase parameters described above, with the indices corresponding to the Khatri-Rao product. For the epoch profiles, X_j^{cat} is replaced by X_l^{cat} , and the Khatri-Rao product for the amplitude of Z by $B| \otimes |A$. The procedure for the phases of Z is adjusted accordingly.

OBTAINING THE LEAST SQUARES ESTIMATES OF TIME DELAYS AND FREQUENCY-SPECIFIC PHASES

The time delays and frequency-specific phases are estimated using a method that starts from a rewriting of the LS loss function as a sum of trigonometric functions. This sum can be minimized using a combination of a steepest descent and a modified Newton-Raphson algorithm. The entire procedure is described below for a 3-way array. It is straightforward to adjust this procedure to a 4-way array with a taper dimension.

First, the LS loss function is rewritten as a linear combination of trigonometric functions, with σ or λ , and τ as parameters. We now show how this can be done:

$$\text{Loss function for } \sigma : \|\varepsilon_{jkl}\|^2 = \left\| X_{jkl} - \sum_{f=1}^F a_{jf} \cdot b_{kf} \cdot c_{lf} \cdot \exp(i2\pi\varphi_k \sigma_{jf} + i2\pi\tau_{kif}) \right\|^2$$

$$\text{Loss function for } \lambda : \|\varepsilon_{jkl}\|^2 = \left\| X_{jkl} - \sum_{f=1}^F a_{jf} \cdot b_{kf} \cdot c_{lf} \cdot \exp(i2\pi\lambda_{jkf} + i2\pi\tau_{kif}) \right\|^2$$

Here, $\| \cdot \|$ denotes the norm. By substituting $2\pi\varphi_k \sigma_{jf}$ with Φ_{jkf} and $2\pi\lambda_{jkf}$ with Φ_{jkf} , both equations can be described jointly by:

$$\|\varepsilon_{jkl}\|^2 = \left\| Z_{jkl} \cdot \exp(i\Psi_{jkl}) - \sum_{f=1}^F \hat{Z}_{jkf} \cdot \exp(i\Phi_{jkf} + iT_{kif}) \right\|^2$$

Where T_{kif} denotes $2\pi\tau_{kif}$, \hat{Z}_{jkf} denotes $a_{jf} \cdot b_{kf} \cdot c_{lf}$, and $Z_{jkl} \cdot \exp(i\Psi_{jkl})$ denotes X_{jkl} . Then, using Euler's formula, and substituting $\Phi_{jkf} + T_{kif}$ with $\hat{\Psi}_{jkl}$, this becomes:

$$\|\varepsilon_{jkl}\|^2 = \left\| \left[Z_{jkl} \cdot \cos \Psi_{jkl} \right] - \sum_{f=1}^F \left[\hat{Z}_{jkf} \cdot \cos \hat{\Psi}_{jkl} \right] + i \left(\left[Z_{jkl} \cdot \sin \Psi_{jkl} \right] - \sum_{f=1}^F \left[\hat{Z}_{jkf} \cdot \sin \hat{\Psi}_{jkl} \right] \right) \right\|^2$$

Replacing the squared norm by a sum of squares, we get:

$$\|\varepsilon_{jkl}\|^2 = \left(\left[Z_{jkl} \cdot \cos \Psi_{jkl} \right] - \sum_{f=1}^F \left[\hat{Z}_{jkf} \cdot \cos \hat{\Psi}_{jkl} \right] \right)^2 + \left(\left[Z_{jkl} \cdot \sin \Psi_{jkl} \right] - \sum_{f=1}^F \left[\hat{Z}_{jkf} \cdot \sin \hat{\Psi}_{jkl} \right] \right)^2$$

In the next step, we complete the square and simplify the resulting equation. Then, using the angle addition identity, the Pythagorean identity, replacing $\hat{\Psi}_{jkl}$ by $\Phi_{jkf} + T_{kif}$, and using trigonometric symmetry, we get:

$$\|\varepsilon_{jkl}\|^2 = Z_{jkl}^2 + \hat{Z}_{jkf}^2 + \sum_{f=1}^F 2Z_{jkl} \hat{Z}_{jkf} \cos(\Phi_{jkf} + (T_{kif} - \Psi_{jkl} + \pi)) + \sum_{f=1}^{F-1} \sum_{n=f+1}^F 2\hat{Z}_{jkf} \hat{Z}_{jkn} \cos(\Phi_{jkf} - \Phi_{jkn} + (T_{kif} - T_{kln}))$$

The least squared error of Φ_{jkf} is computed by summing over k, l . Applying the sum, and using the harmonic addition identity, the equation reaches its final form used for optimization:

$$\sum_{k=1}^K \sum_{l=1}^L \|\varepsilon_{jkl}\|^2 = \alpha_j + \sum_{k=1}^K \sum_{f=1}^F [\beta_{jkf} \cos(\Phi_{jkf} + \zeta_{jkf})] + \sum_{k=1}^K \sum_{f=1}^{F-1} \sum_{n=f+1}^F [\gamma_{jkfn} \cos(\Phi_{jkf} - \Phi_{jkn} + \eta_{jkfn})] \quad (2)$$

The parts of the above equation are as follows:

$$\alpha_j = \sum_{k=1}^K \sum_{l=1}^L \left[Z_{jkl}^2 + \sum_{f=1}^F \hat{Z}_{jklf}^2 \right]$$

$$\beta_{jkf} = \sqrt{\left(\sum_{l=1}^L 2Z_{jkl} \hat{Z}_{jklf} \cos(T_{klf} - \Psi_{jkl} + \pi) \right)^2 + \left(\sum_{l=1}^L 2Z_{jkl} \hat{Z}_{jklf} \sin(T_{klf} - \Psi_{jkl} + \pi) \right)^2}$$

$$\zeta_{jkf} = \text{atan2} \left(\frac{\sum_{l=1}^L 2Z_{jkl} \hat{Z}_{jklf} \sin(T_{klf} - \Psi_{jkl} + \pi)}{\sum_{l=1}^L 2Z_{jkl} \hat{Z}_{jklf} \cos(T_{klf} - \Psi_{jkl} + \pi)} \right)$$

$$\gamma_{jkfn} = \sqrt{\left(\sum_{l=1}^L 2\hat{Z}_{jklf} \hat{Z}_{jkln} \cos(T_{klf} - T_{kln}) \right)^2 + \left(\sum_{l=1}^L 2\hat{Z}_{jklf} \hat{Z}_{jkln} \sin(T_{klf} - T_{kln}) \right)^2}$$

$$\eta_{jkfn} = \text{atan2} \left(\frac{\sum_{l=1}^L 2\hat{Z}_{jklf} \hat{Z}_{jkln} \sin(T_{klf} - T_{kln})}{\sum_{l=1}^L 2\hat{Z}_{jklf} \hat{Z}_{jkln} \cos(T_{klf} - T_{kln})} \right)$$

In the last equation, *atan2* refers to the 4-quadrant arctangent and Φ_{jkf} , denotes either $2\pi\varphi_k\sigma_{jf}$ or $2\pi\lambda_{jkf}$.

By minimizing the function in Eq. 2 with respect to σ_{jf} (time delay model) or λ_{jkf} (FSP model) we obtain their LS estimates. We use different nonlinear optimization procedures for the FSP and the time delay model. For every site-frequency pair (j, k) in the FSP model, we perform an F -dimensional minimization with respect to the λ_{jkf} of all F networks. First, we decrease the LS loss function by means of steepest descent until the Hessian matrix of this function becomes positive definite. Subsequently, we minimize the loss function using modified Newton-Raphson. The step size used in steepest-descent and modified Newton-Raphson is determined such that the loss function decreases with every step.

For the time delay model, we perform a one dimensional minimization with respect to σ_{jf} for every site-network pair (j, k). As for the FSP model, this minimization is performed using a combination of steepest descent and modified Newton-Raphson. Importantly, the loss function for the σ_{jf} parameter is rhythmic, and contains many local minima. Therefore, to find the global minimum, an initial estimate has to be found which is in the same cycle that also contains the global minimum. This initial estimate is found by an informed sparse grid search. The sparse grid search is informed by the cycle length of the term in Eq. 2 with the highest frequency, which is the term with the fastest rhythmic component of the LS loss function. The resolution of the grid involves a trade-off between computation time and the probability of finding the global minimum. In practice, a resolution of 16 steps inside a cycle of the fastest rhythmic component is sufficient and the global minimum is almost always found.

OBTAINING THE LEAST SQUARES ESTIMATES OF THE PHASE OFFSETS

The phase offsets capture the arbitrary temporal offset of the phase-coupled oscillatory network relative to the start of each epoch. The LS estimates of these offsets are found in a procedure nearly identical to the one for the frequency-specific phases of the FSP model. Eq. 2 shows how a site- and frequency-specific phase ($2\pi\varphi_{kjf}$ or $2\pi\lambda_{jkf}$) is a function of the data and all the other parameters. An equation of identical form as Eq. 2 can be derived for the phase offsets $2\pi\tau_{kif}$ simply by swapping Φ_{jkf} and T_{kif} in the derivation. Then, the LS estimates of the phase offsets are found by a procedure analogous to finding the frequency-specific phases of the FSP model: for each epoch, the frequency-specific phase offsets are found by a combination of steepest descent and modified Newton-Raphson.

EXTRACTING NETWORKS FROM A 4-WAY ARRAY OF FOURIER COEFFICIENTS USING THE CROSS-PRODUCT FORMULATION OF SPACE

Using multiple tapers (e.g. Welch ([Welch, 1967](#)) or Slepian ([Percival and Walden, 1993](#))) in a spectral analysis allows for controlling the frequency resolution. Using multiple tapers adds a fourth dimension to the array of Fourier coefficients. It is straightforward to extend SPACE from 3-way arrays to 4-way arrays: include an epoch-specific taper profile and phase offsets that are also taper-dependent. However, there are two reasons for considering an alternative. First, because tapers are not a dimension of interest in electrophysiological studies, it is not necessary to estimate taper-specific phases and amplitudes. Second, the 4-way spatial-spectral-epoch-taper array is not always complete: higher frequencies often have more tapers than lower frequencies. We therefore formulated an FSP and a time delay model for cross-products of the 2-dimensional sites-by-tapers slices from the 4-way array of Fourier coefficients. In these cross-products, the tapers are the inner dimension and therefore the taper-specific parameters disappear from the model. This approach is inspired by PARAFAC2 ([Harshman, 1972; Kiers et al., 1999](#)). The cross-product formulation, similar to PARAFAC2, also estimates between-network coherences using an additional parameter set. However, as we describe below, these coherences are set to zero to avoid splitting up networks into an arbitrary number of sub-networks. In the following, we will first describe the models for the cross-products and then describe how we can find the LS estimates of their parameters.

The cross-products are obtained from 2-dimensional sites-by-tapers slices X_{kl} (of size $J \times M$, with M denoting the number of tapers) taken from the 4-way array of Fourier coefficients. The cross-product is $X_{kl} \cdot X_{kl}^*$, with $*$ denoting the complex conjugate transpose, and its two models are the following:

$$\text{SPACE-time: } X_{kl} \cdot X_{kl}^* = AS_k \cdot \text{diag}B_k \cdot \text{diag}C_l \cdot D_k \cdot D_k^* \cdot \text{diag}C_l \cdot \text{diag}B_k \cdot AS_k^* + E_{kl}$$

$$\text{SPACE-FSP: } X_{kl} \cdot X_{kl}^* = AL_k \cdot \text{diag}B_k \cdot \text{diag}C_l \cdot D_k \cdot D_k^* \cdot \text{diag}C_l \cdot \text{diag}B_k \cdot AL_k^* + E_{kl}$$

For the time delay model, AS_k denotes the complex-valued matrix formed by $A \circ \exp(i2\pi\varphi_k \Sigma)$, with A being the spatial amplitude map, Σ a matrix with time delays σ as columns, and \circ denoting the dot-product. Similarly, for the FSP model, AL_k denotes the complex-valued matrix formed by $A \circ \exp(i2\pi\Lambda_k)$, with A being the spatial amplitude map, Λ_k a matrix with spatial phase maps λ_k of the k -th frequency as columns. The frequency- and epoch-specific loadings appear in the equations as, respectively, the diagonal matrices $\text{diag}B_k$ and $\text{diag}C_l$. In the center of the equations, there is the matrix product $D_k \cdot D_k^*$. This matrix product, having size $F \times F$, is the frequency-specific between-network coherency matrix. It captures interactions between networks. When all networks have different frequency profiles, they cannot interact. In this case, $D_k \cdot D_k^*$ equals an identity matrix, i.e. the networks are incoherent. There are also other situations in which it is worthwhile to constrain networks to be incoherent. Consider the case of a distributed network, which can by definition be described by an arbitrary set of coherent sub-networks. Without the constraint that the extracted networks must be incoherent, this distributed network would be split into these smaller networks when the number of networks increases. Their coherence is then captured by $D_k \cdot D_k^*$. By enforcing that $D_k \cdot D_k^* = I$, this split up can be prevented. An additional useful property of this constraint is that degenerate solutions resulting from unfortunate initializations can no longer occur.

It is important to note that the cross-product models and the regular models have many parameters in common. However, they also have some unique parameters. The regular models involve epoch- and frequency-specific phase offsets (which would be taper-, epoch- and frequency-specific when using multitapering). The cross-product models do not involve phase-offsets. Instead, they describe the *average* between-site phase relations, and these do not depend on the phase offsets. Additionally, the between-network coherence is explicitly modeled by the coherency matrix $D_k \cdot D_k^*$. In the regular models, this is not explicitly modeled, although it can be calculated from the phase offsets.

We now describe how to find the LS estimates of the parameters of the cross-product models. It can be shown that these LS estimates can be obtained in an indirect way, by estimating a model for the Fourier coefficients X_{kl} (rather than directly estimating the model for their cross-products; see [Kiers et al., 1999](#), for a proof for PARAFAC2). The following models for X_{kl} are estimated:

$$\text{SPACE-time: } X_{kl} = AS_k \cdot \text{diag}B_k \cdot \text{diag}C_l \cdot D_k \cdot P_{kl}^* + E_{kl}$$

$$\text{SPACE-FSP: } X_{kl} = AL_k \cdot \text{diag}B_k \cdot \text{diag}C_l \cdot D_k \cdot P_{kl}^* + E_{kl}$$

In these equations, there is a crucial role for the matrices P_{kl} , which are constrained to be orthonormal (Kiers et al., 1999). P_{kl} has size $F \times M$, and it contains information about the phase and amplitude of the unobserved network-level signal in each frequency and epoch. Given the matrices P_{kl} , the LS estimates of the cross-product model can be found using a straightforward extension of the algorithm for 3-way arrays of Fourier coefficients. In the next paragraph, we will show how this can be done. Thereafter, we will describe how the matrices P_{kl} can be estimated.

Assuming the matrices P_{kl} to be known, we can construct a 4-way array Y of size $J \times K \times L \times F$ from the 4-way array X of size $J \times K \times L \times M$. Array Y is constructed by replacing every matrix X_{kl} by $X_{kl} \cdot P_{kl}$. Here, X_{kl} has dimensions $J \times M$, and P_{kl} has dimensions $M \times F$. Importantly, array Y does not have empty cells, regardless of whether X has partially empty due to a frequency-specific number of tapers. The parameters of the cross-product models can now be obtained from this 4-way array Y using a straightforward extension of the algorithm for 3-way arrays. In this extension, when estimating the spatial amplitude map, the amplitude of matrix Z in Eq. 1 is now of the form $D \otimes C \otimes B$. However, because matrix D is frequency-specific, a different D_k needs to be used for each B_k , which cannot be achieved using the Khatri-Rao product. As such, a matrix of the same form is constructed with the appropriate indices. The phases of this matrix are constructed similarly. For the estimation of the frequency and epoch profiles, similar adjustments have to be made. The spatial time-delay maps and spatial phase maps can be estimated using the algorithm described previously. However, it is applied to slightly different quantities, resulting from the fact that the LS loss function now also involves a sum over the levels of the fourth dimension (corresponding to the matrix D_k). Matrix D_k is either held at $D_k = I$, or is estimated as a complex-valued frequency-specific matrix of the same size. In the latter case, D_k is estimated using regular complex-valued LS.

The matrices P_{kl} have to be estimated from the data, and we do this as a part of the same ALS algorithm that we use to estimate the parameters of the cross-product model. That is, we estimate P_{kl} on the basis of the data (the matrices X_{kl} of Fourier coefficients) and the current parameters of the cross-product model. Following Kiers et al. (1999), the LS estimate of P_{kl} is the following:

$$P_{kl} = U \cdot V^*$$

Here, U, V denote the left and right singular vectors obtained from the following singular value decomposition:

$$\begin{aligned} \text{SPACE-time: } & U, S, V = \text{svd}\left(X_{kl}^* \cdot A S_k \cdot \text{diag}B_k \cdot \text{diag}C_l \cdot D_k\right) \\ \text{SPACE-FSP: } & U, S, V = \text{svd}\left(X_{kl}^* \cdot A L_k \cdot \text{diag}B_k \cdot \text{diag}C_l \cdot D_k\right) \end{aligned}$$

After calculating new estimates of the P_{kl} matrices, in a new ALS iteration, new estimates of model parameters calculated from a new matrix Y . Note, the input to this SVD should be of full column rank. As such, the number of tapers cannot be lower than the number of networks.

UNIQUENESS OF EXTRACTED NETWORKS

SPACE, like PARAFAC, has a permutation and scaling indeterminacy. This means that there is an ambiguity in the order of the extracted networks, in the scaling of their parameters, and in their phases. For the interpretation, these indeterminacies are of little consequence, and by placing certain constraints on the parameters, a unique LS solution can be found. The permutation indeterminacy is resolved by sorting the networks by their explained variance. To resolve the scaling indeterminacy, we must impose constraints at level of the parameter sets, and these will be described below. The scaling indeterminacy involves that the model fit is not affected when a parameter of a network (e.g. the spatial amplitude map) is multiplied by a single real-valued number, as long as another parameter of the same network is multiplied with its inverse. This indeterminacy is resolved by scaling the spatial amplitude map and the frequency profile such that their norm equals 1 and their mean is positive. The epoch profile is estimated without any constraint and its squared norm reflects the amount of variance explained by the corresponding network. As such, this norm can be used to express the strength of a network relative to the other networks. For display purposes however, the epoch profile is always normalized.

Our spatial amplitude maps, frequency profiles and epoch profiles can have both positive and negative elements, which leads to a phase ambiguity. We resolve this ambiguity by restricting all amplitudes to be positive. For the spatial amplitude maps of the FSP model, this involves that the signs of all negative amplitudes are reversed and the corresponding phases in the spatial phase maps are shifted by 180 degrees. For the frequency and the epoch profiles, the way the ambiguity is resolved depends on whether a 3-way or 4-way array is decomposed. For a 3-way array, the ambiguity is again resolved by reversing the signs of all negative amplitudes, but now phase-shifting by 180 degrees is performed on the frequency- and epoch-specific phase-offsets that correspond to the frequencies and epochs whose sign is reversed. For a 4-way array, the resolution of the ambiguity depends on how matrix D_k is formulated. When D_k is the identity matrix, the 180 degrees phase shifts are applied to the appropriate frequency- and epoch-specific matrices P_{kl} . When D_k is complex-valued, the ambiguity only involves the frequency profile, and the 180 degree phase shifts are applied to the appropriate frequency-specific D_k .

The spatial time-delay maps, spatial phase maps, and phase offsets suffer from

a phase indeterminacy. This results in two ambiguities, which are the result of (1) phase being circular, and (2) a trade-off between the spatial time-delay maps (or spatial phase maps) and the phase offsets. For SPACE-time, increasing all time delays with the same amount results in a phase shift for all frequencies, and this can be compensated by appropriate opposite phase shifts in the phase offsets. For the FSP model, each spatial phase map can be phase-shifted if the corresponding phase offsets are shifted in the other direction. To resolve this phase indeterminacy, a harmless constraint is imposed on the spatial time-delay maps and the spatial phase maps. These constraints are harmless, because they do not affect the between-site phase differences or time delay differences. For the spatial phase maps, there are two possible convenient constraints: (1) the phases are rotated such that the average phase (weighted by the spatial amplitude map) is 0 for each frequency, or (2) such that the strongest site in the spatial amplitude map has a phase of 0. For the spatial time-delay maps, the constraint is related to the notion of a *circularity point*. Because time delays determine circular phases, they are circular as well. Their cycle length depends on the frequencies that are used in their estimation. When using frequencies that are all integer multiples of some number then, for a certain time delay, the spatial phase maps for all frequencies are 0. The smallest non-zero time delay with this property is equal to 1 over the greatest common divisor of all frequencies, and it will be denoted as the circularity point. For example, when the frequencies used are 2 to 30 Hz in 2 Hz bins the greatest common divisor is 2 Hz, and the circularity point is 0.5s. Given this circularity point, there are two possible convenient constraints for the spatial time-delay maps: (1) the time delays are rotated such that the average time delay (weighted by the spatial amplitude map) is halfway between 0 and this circularity point, or (2) the time delays are rotated such that the strongest site in the spatial amplitude map has a time delay of 0. The circularity point is also involved in an ambiguity with respect to the temporal order of the time delays. If the time delay difference between any two sites is larger than the circularity point, then their order is undetermined. For example, given a circularity point of 0.5s, the time delays 0.3s and 0.1s generate identical phases (for all frequencies) as the time delays 0.3s and 0.6s, of which the order is reversed. The same holds for 0.3s and 1.1s, and so on. The consequence of this ambiguity is that the order of the time delays in the spatial time-delay map can only be interpreted under the assumption that none of the time delay differences exceeds the circularity point.

There is currently no proof showing that the solutions of our method are unique. Uniqueness implies that, for a given least-squares optimization problem (i.e., a given dataset), our method produces only a single solution. To assess uniqueness empirically we performed a set of simulations. We randomly generated 10.000

small parameter sets for a three-network time delay and FSP model for 4-way arrays (with $D_k = I$). Each parameter set is denoted as a run. Parameters were generated between 0 and 1 except for the time delays, which were generated between 0.125 and 0.375. This resulted in 10.000 4-way arrays of Fourier coefficients for each model, consisting of 6 sites, 5 frequencies, 4 epochs and 3 tapers (frequencies equally spaced between 2 and 10 Hz). We then decomposed these 4-way arrays using both models, randomly initiating each algorithm five times and then selecting the solution with the highest explained variance. The average explained variance over 10.000 runs was >99.99% (SD = 0.137%) for the time delay model and >99.99% (SD = 0.037%) for the FSP model. This shows that our method is able to find at least one solution of the least-squares optimization problem. We then computed the average absolute difference between the simulated and recovered parameters, with averaging over sites, frequencies, epochs and networks. The average absolute deviation was 1.86×10^{-4} (SD = 2.35×10^{-3}) for the time delay model, and 4.16×10^{-4} (SD = 1.83×10^{-3}) for the FSP model. This small average absolute deviation shows that the solution of our method is most likely unique. Additional evidence for uniqueness is provided by the results of our recovery study (see Results and below).

SUPPLEMENTARY MATERIAL

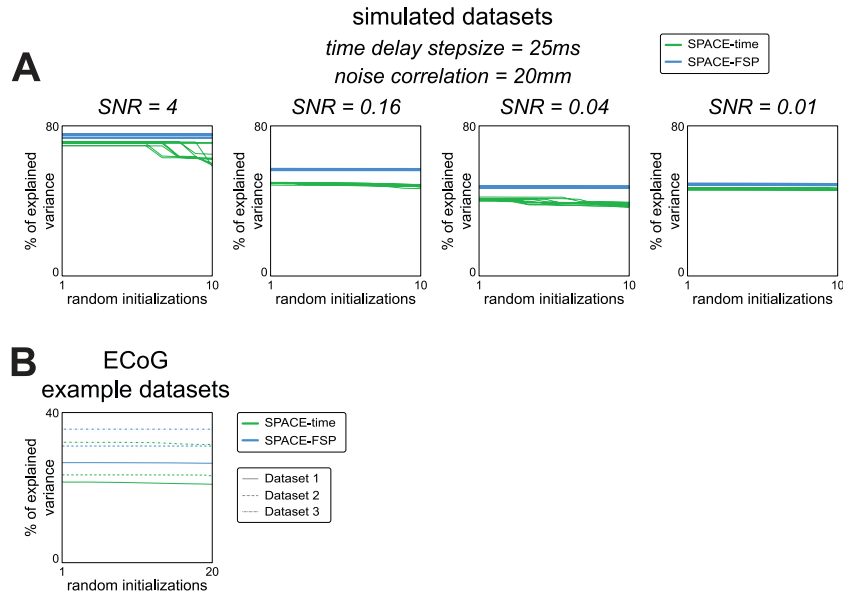
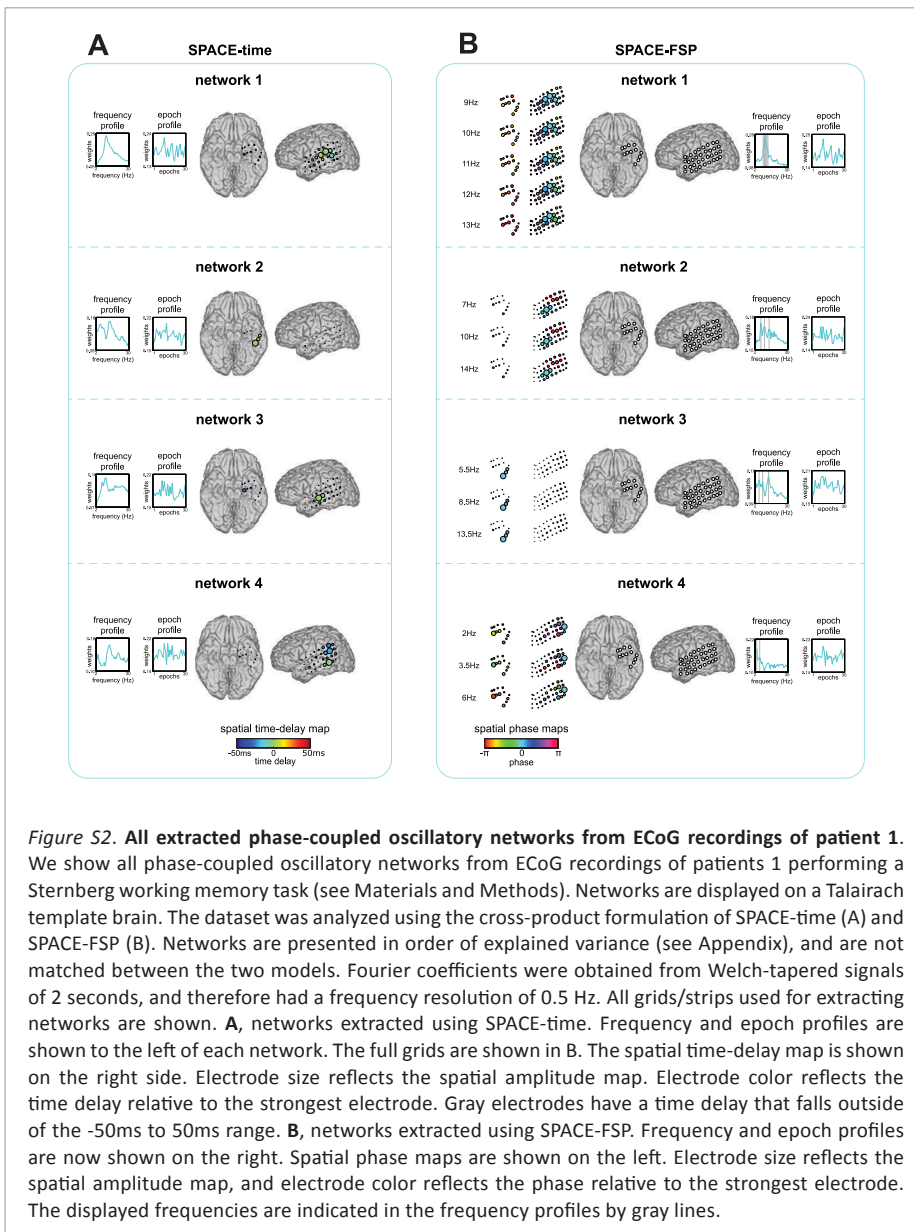
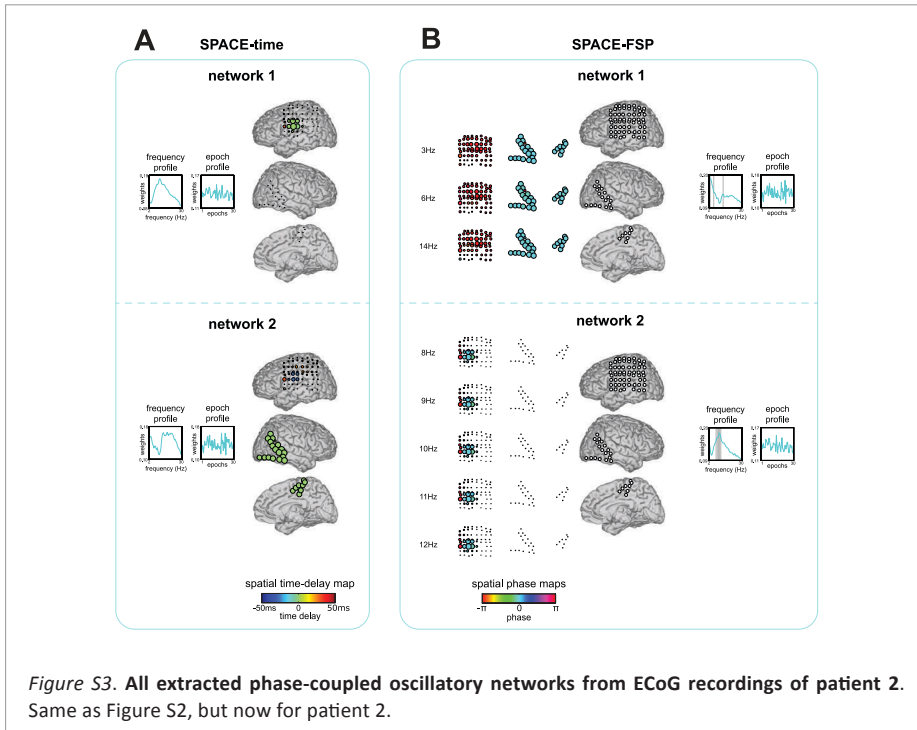
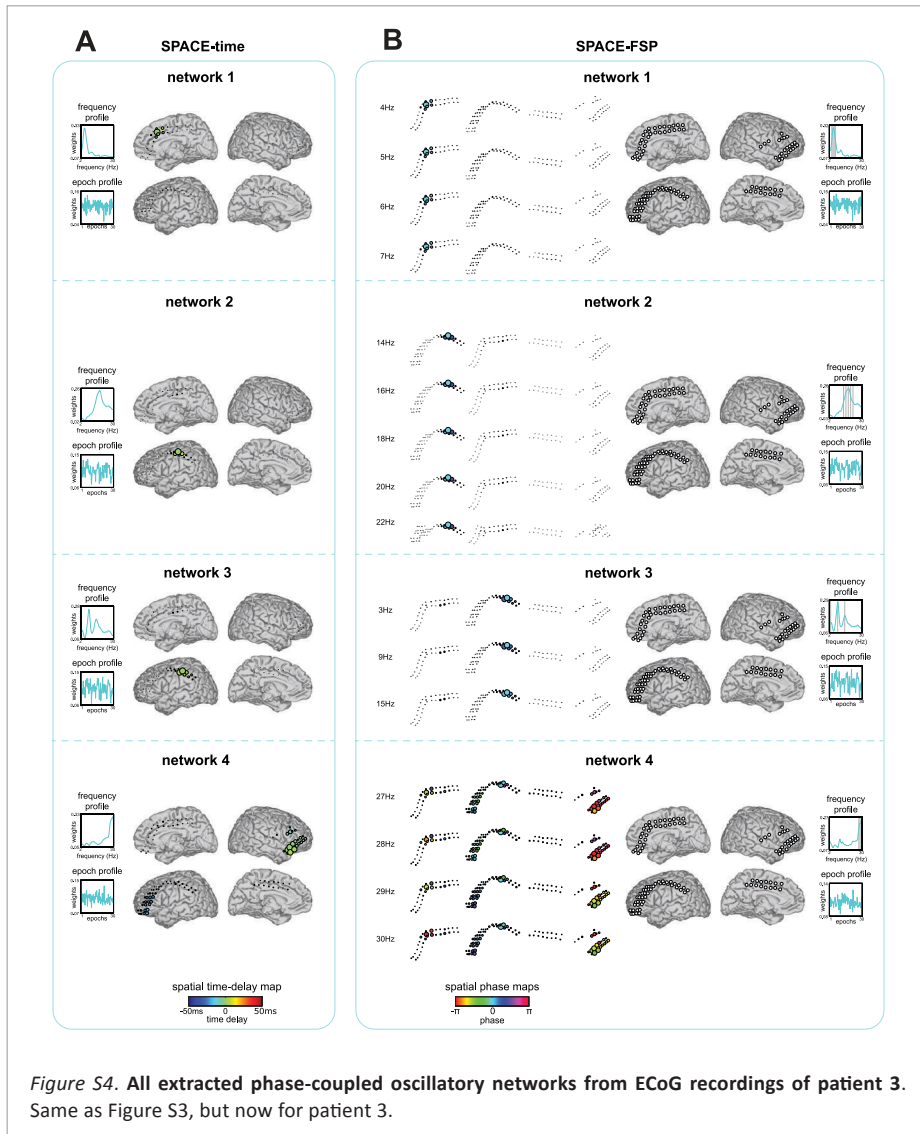


Figure S1. Model fit of random initializations of the simulated data and the example ECoG datasets.

All networks parameters are initialized randomly, and to avoid local minima of the least squares (LS) loss function the algorithm is started multiple times. When the algorithm repeatedly converges to the same solution it can be assumed the global minimum has been reached. We illustrate this by showing the model fit in terms of percentage explained variance of each random initialization. **A**, model fit for random initializations of the simulated data for SPACE-time (blue) and SPACE-FSP (green) separately. Each line reflects the 10 random initializations of a single simulation run, which are sorted by explained variance. The best solution of each run was chosen for recovery analyses of the simulated networks. We show 10 out 100 runs (randomly selected), for all four levels of the signal-to-noise ratio (SNR). Time delay between electrodes was 25ms, and spatial correlation of noise was determined using a Gaussian with a full-width half-maximum at 20mm. The selected simulations vary from near perfect recovery of the simulated networks (highest SNR) to very poor recovery of the networks (lowest SNR; see Fig 6). SPACE-time needed more random initializations to reach the global minimum of the LS loss function than SPACE-FSP, as indicated by the number of initializations at the plateau of explained variance. Additionally, SPACE-FSP explained a higher percentage of variance than SPACE-time in all four levels of SNR. This coincides with SPACE-FSP more accurately recovering the simulated networks than SPACE-time (see Fig 6-7). **B**, same as A but for the three example datasets of which we show networks in Fig 4. In this case the algorithm was randomly initialized 20 times. There were only minimal differences in explained variance over random initializations compared to the simulations in A, and the global minimum was reached in less initializations.







Chapter 4

Rhythmic components in
extracranial brain signals
reveal multifaceted
task modulations of
overlapping phase-
coupled oscillatory
networks

ABSTRACT

Oscillatory neuronal activity is implicated in many cognitive functions, and its phase coupling between sensors may reflect networks of communicating neuronal populations. Oscillatory activity is often studied using extracranial recordings and compared between experimental conditions. This is challenging because there is overlap between sensor-level activity generated by different sources, and this can obscure differential experimental modulations of these sources. Additionally, in extracranial data, sensor-level phase coupling not only reflects communicating populations, but can also be generated by a current dipole, whose sensor-level phase coupling does not reflect source-level interactions. We present a novel method, which is capable of separating and characterizing sources on the basis of their phase coupling patterns as a function of space, frequency and time (trials). Importantly, this method depends on a plausible model of a neurobiological rhythm. We present this model and an accompanying analysis pipeline. Next, we demonstrate our approach by extracting rhythmic components from magnetoencephalographic (MEG) recordings during a cued tactile detection task. We show that the extracted components have overlapping spatial maps and frequency content, which are difficult to resolve using conventional measures. Because our decomposition also provided trial loadings, components could be readily contrasted between experimental conditions. We identified many alpha and beta sources whose activity was suppressed or enhanced as a function of attention and performance, both in task relevant and irrelevant regions. Many components described phase-coupled oscillatory networks, and we show that alpha and beta networks, and their task modulations, are common and widespread in the MEG recordings.

Adapted from:

van der Meij R, Van Ede E, Maris E (under review). *Rhythmic components in extracranial brain signals reveal multifaceted task modulations of overlapping phase-coupled oscillatory networks.*

INTRODUCTION

Neuronal signals contain oscillations at many frequencies (Buzsaki and Draguhn, 2004), and these have been shown to be implicated in many cognitive functions (for a review see Wang, 2010). It is commonly thought that oscillations reflect fluctuations of neuronal excitability (Buzsaki et al., 2012), whose phase coupling may be used for the dynamic communication between neuronal populations (Fries, 2005; Schnitzler and Gross, 2005). Accordingly, neuronal oscillations are of interest to a large scientific community, and phase coupling is a core component in many interpretations of experimental modulations of neuronal oscillations. A large share of this community studies oscillatory activity on the basis of extracranial recordings, such as electroencephalography (EEG) and magnetoencephalography (MEG).

CHALLENGES IN THE STUDY OF OSCILLATORY NEURONAL ACTIVITY IN EXTRACRANIAL RECORDINGS

Investigating oscillatory activity in extracranial recordings (EEG/MEG) is challenging for several reasons. First, interpreting sensor-level activity is strongly hindered by the fact that the underlying sources cannot be uniquely identified. In practice, multiple sources produce overlapping spatial patterns at the sensor-level, and it is unclear how these can be separated. This is especially problematic if the measured signals are compared between experimental conditions: different sources may be differentially affected by the experimental conditions, and it can be very difficult to trace the resulting sensor-level modulation back to the source-level. As such, it may appear that sensor-level activity is either suppressed or enhanced by an experimental manipulation, whereas different underlying sources are each modulated differently (e.g. with some sources being suppressed, while others are enhanced; as we will show later).

Investigating neuronal activity in extracranial brain signals is further hampered by the fact that sensor-level phase coupling not only reflects communicating neuronal populations, but can also reflect activity that is best described by a current dipole, which is produced a point source. Especially when the distance between sources and sensors is large, as for EEG/MEG, it is likely to observe sensor-level phase coupling that can be described by a current dipole.

One way to overcome these challenges is by methods that extract patterns of activity which are more informative of the underlying source activity. In this paper, we present a method that achieves this. It separates the activity patterns of sources whose spatial and spectral profiles strongly overlap, and allows for investigating their individual task modulations. Additionally, it allows for distinguishing between point

sources, whose sensor-level phase coupling does not reveal interactions between neuronal subpopulations, and other sources, for which this *is* the case.

There are existing methods whose objective is also to separate activity from (overlapping) sources, and we will now briefly review these methods. Because we focus on oscillatory activity, we only consider methods for the frequency-domain representation of the signals (i.e., Fourier coefficients). Afterwards, we highlight three key benefits of our method.

EXISTING METHODS FOR SEPARATING OVERLAPPING SOURCES

It is useful to distinguish between methods that only operate on the amplitude of Fourier coefficients, and methods that also take their phase into account. Considering the first, we must further distinguish between methods that can only be applied to amplitudes in a single frequency band (also denoted as *frequency*), and methods that can be applied to amplitudes at multiple frequencies simultaneously. Considering the former, the best-known methods are Independent and Principal Component Analysis (ICA, PCA; [Bell and Sejnowski, 1995](#); [Chapman and McCrary, 1995](#); [Makeig et al., 1997](#); [Debener et al., 2005](#); [Brookes et al., 2011](#)). With these methods, one can describe the structure in a matrix of frequency-band-specific amplitude time-series collected at multiple sensors. More specifically, they decompose this matrix in a number of components with a fixed (time-invariant) spatial pattern and a fixed (spatially invariant) amplitude time course. Importantly, the components are identified using statistical constraints (orthogonality, maximum variance, statistical independence), which do not necessarily follow the neurophysiology of the phenomena under investigation.

Next, we consider a method that can be applied to Fourier amplitudes at multiple frequencies simultaneously: PARAllel FACtor analysis (PARAFAC; [Carrol and Chang, 1970](#); [Harshman, 1970](#); [Miwakeichi et al., 2004](#); [Morup et al., 2006](#)). PARAFAC operates on 3-way arrays of sensors-by-frequencies-by-time-points. It decomposes these arrays into components with a fixed (frequency- and time-invariant) spatial map, a fixed (space- and time-invariant) frequency profile, and a fixed (space- and frequency-invariant) amplitude time course. Crucially, these components are identified without additional statistical constraints.

Some methods also take the phase of Fourier coefficients into account. Many pair-wise measures exist that index a particular aspect of the between-sensor phase relations, in some cases weighted by amplitude. Several of these pair-wise measures can distinguish between direct and indirect phase coupling. This holds for partial coherence ([Rosenberg et al., 1998](#)), Granger causality ([Barnasconi and Konig, 1999](#)), Phase Coupling Estimation ([Canolty et al., 2012b](#)) and (Phase) Transfer

Entropy (Schreiber, 2000; Lobier et al., 2014). Though useful, pair-wise phase coupling between large numbers of sensors is difficult to interpret without a priori hypotheses about which sensors are likely to interact.

Two methods have been proposed for extracting patterns from arrays of Fourier coefficients involving a spatial, a spectral and a temporal dimension: complex-valued ICA (Anemuller et al., 2003; Hyvärinen et al., 2010) and complex-valued PARAFAC (Sidiropoulos et al., 2000). Both methods have not yet been widely applied to neuroscience data. As for the real-valued case, different algorithms exist for complex-valued ICA, and they all identify components using a statistical constraint. Complex-valued PARAFAC does not require a statistical constraint, but instead assumes that the components are characterized by a fixed spatial map, a fixed frequency profile, and a fixed time course. From a neurobiological perspective, an important limitation of complex-valued PARAFAC is that a component's complex-valued sensor loadings describe the between-sensor phase relations by a single set of phases. This results in between-sensor phase relations that are constant over frequencies. This is useful to describe for instance oscillating point sources, but not for source configurations whose phase relations vary over frequencies. Shifted CP is an improvement upon complex-valued PARAFAC (Morup et al., 2008), but can also only describe the phase relations of point sources.

THREE BENEFITS OF OUR PROPOSED APPROACH FOR ANALYZING OSCILLATORY NEURONAL ACTIVITY

In this paper, we present a novel approach for analyzing oscillatory neuronal activity, which uses a model-based method that separates and characterizes sources by their patterns of between-sensor phase coupling. It is a decomposition method that provides a parsimonious description of the structure in oscillatory neuronal activity. The method was first presented in (van der Meij et al., 2015). Unlike existing decomposition methods, it uses a plausible model of a neurobiological rhythm: a spatially distributed oscillation with energy in a range of frequencies and involving between-sensor phase relations that can vary over frequencies. Because the model is formulated for rhythmic neuronal activity, we denote the extracted patterns as rhythmic components. These rhythmic components describe the sources that produce the sensor-level measurements.

Analyzing oscillatory activity using rhythmic components has three key benefits. First, it allows for a separation of sources with overlapping spatial and spectral patterns, and therefore can reveal sources which are difficult to isolate in conventional analyses. Secondly, the strength of a component is quantified for each trial by a single number (denoted as a *trial loading*). These trial loadings allow for a straightforward way of investigating task modulations of oscillatory activity at

the level of the extracted components. Thirdly, identifying rhythmic components is a first step in the analysis of phase-coupled oscillatory networks, because they provide a parsimonious description of the interacting neuronal populations that have produced the pattern of phase-coupling at the sensor-level.

OVERVIEW

In the following, we first present the model underlying the method and an analysis pipeline with the method as its central ingredient. We then show that rhythmic components can reveal a spatial and spectral diversity of overlapping sources that is difficult to realize using conventional analyses. Next, we show how these components reveal task modulations of the sources' activity. Both results are based on an analysis of MEG recordings that were obtained during a cued tactile detection task ([van Ede et al., 2012](#)). Finally, we show that rhythmic components can reveal phase-coupled oscillatory networks, and that these networks are common and widespread in MEG recordings.

MATERIALS AND METHODS

1. A MODEL-BASED METHOD FOR CHARACTERIZING BETWEEN-SENSOR PHASE COUPLING BY RHYTHMIC COMPONENTS

Electrophysiological recordings reflect neuronal oscillations and the phase of these oscillations is often consistent between recording sites (sensors). We proposed a decomposition method based on a model that parsimoniously describes patterns of between-sensor phase coupling by rhythmic components. Importantly, this model is a neurobiologically inspired source model, and therefore describes patterns of between-sensor phase coupling in a way that is informative for this community. This model-based method has been presented previously ([van der Meij et al., 2015](#)), and was denoted as SPACE (Spatially distributed PhAse Coupling Extraction).

To extract components we start with electrophysiological measurements $V_{jl}(t)$ (potential differences or magnetic field strength) measured over time t , obtained from sensor j (total number J) and trial l (total number L). Oscillatory activity in these recordings is described by Fourier coefficients, which we obtain from a spectral analysis involving multitapering (e.g. Welch ([Welch, 1967](#)) or Slepian ([Percival and Walden, 1993](#)) tapering; multitapering is optimal, but not necessary). The obtained Fourier coefficients X_{jklm} describe the average amplitude and the phase of oscillations in each tapered part m of trial l , at frequency k , and at sensor j . The model underlying our method describes the systematic variability of

amplitudes and phases of X_{jklm} by multiple components, each consisting of four parameter sets. The frequency profile describes which frequencies are involved in between-sensor phase coupling. The spatial amplitude map describes which sensors are phase-coupled, at the frequencies in the frequency profile. The spatial phase maps describe, per frequency, the consistent between-sensor phase relations. The trial profile quantifies how strongly each component is present in each trial, and can be viewed as a measure of activity of the neuronal source that is reflected by this component. The spatial amplitude map and the spatial phase maps describe phase coupling by maps at the level of individual sensors, and not at the level of sensor-pairs. This is important, because phase coupling at the level of sensor-pairs does not reveal the networks of coupled sensors in a straightforward way, at least not without *a priori* hypotheses about the (sensor, frequency)-pairs that are involved in these networks.

The model describes the structure in the frequency- and trial-specific cross-spectral density (CSD) matrices, which are obtained from the cross-product of the sensor-by-taper ($J \times M$) matrices of Fourier coefficients X_{kl} , as the average over tapers $(X_{kl} \cdot X_{kl}^*) / M$ ($*$ denotes the complex conjugate transpose). A CSD reflects both the power in the different sensors and the between-sensor phase consistency. The model for these CSDs is discussed conceptually and depicted schematically in Results section 1, and formulated in an equation as follows:

$$X_{kl} \cdot X_{kl}^* = AL_k \cdot \text{diag}B_k \cdot \text{diag}C_l \cdot D_k \cdot \text{diag}C_l \cdot \text{diag}B_k \cdot AL_k^* + E_{kl}$$

The CSDs $X_{kl} \cdot X_{kl}^*$ are modeled as a product of four matrices, of which three appear twice (AL_k , $\text{diag}B_k$ and $\text{diag}C_l$) and one appears only once (D_k). The difference between the model and the observed CSD is the error term E_{kl} . The matrix AL_k ($J \times F$) is complex-valued, and is formed by the spatial amplitude map (specifying the amplitudes of the complex numbers) and the frequency-specific spatial phase map (specifying the phases of the complex numbers) of each component. Matrix $\text{diag}B_k$ ($F \times F$) is diagonal and real-valued, and contains a weighting of components at frequency k . When concatenated over frequencies, the diagonals form the matrix of frequency profiles B . Matrix $\text{diag}C_l$ ($F \times F$) is also diagonal and real-valued, and contains the weighting of components in a trial l . When concatenated over trials, the diagonals form the matrix of trial profiles C . Contrary to the matrices that describe components (AL_k , $\text{diag}B_k$ and $\text{diag}C_l$), matrix D_k ($F \times F$) describes relations between components. Matrix D_k is complex-valued and conjugate symmetric, and describes the phase coupling between components at frequency k . Matrix D_k is denoted as a between-component coherency matrix. In the Results section, we will use the term between-component coherence to denote the absolute value of between-component coherency.

At this point, it is useful to make a technical statement related to our decomposition method as described in van der Meij et al. (2015). Although the underlying model is for the frequency- and trial-specific CSDs, the decomposition method takes as its input the square-root of these CSDs. The square-root CSD is equivalent to the sensor-by-taper matrix of Fourier coefficients, and the latter matrix is the starting-point of the method developed in van der Meij et al. (2015). In this paper, we do not have this equivalence because we have estimated the CSDs in a way that better reflects rhythmic sources (as compared to their usual estimate; see Materials and Methods section 2). Therefore, the square-root of our CSD estimate is not equivalent to the sensor-by-taper matrix of Fourier coefficients.

The model underlying our method has a number of trivial indeterminacies which are resolved by normalizations that do not affect the interpretation of the components. These indeterminacies are similar to the permutation and scaling indeterminacies of PARAFAC/2 (Bro, 1998; Kiers et al., 1999) and result in ambiguities with respect the absolute amplitude, sign, and absolute phase of the parameters. These ambiguities have been described previously (van der Meij et al., 2015), and here we only describe the required normalizations. The absolute value of all real-valued parameter sets is undetermined, and therefore the spatial amplitude maps, the frequency profiles, and the trial profiles, are normalized to have a vector norm of 1. Additionally, the between-component coherency matrices are normalized to have ones on their diagonal. That is, they are constrained to be coherency matrices. The signs of the spatial amplitude maps, frequency profiles, and trial profiles, are undetermined as well, and this indeterminacy is resolved by restricting them to be positive. The absolute phase of the spatial phase maps is also undetermined, and they are normalized per frequency such that the strongest sensor in the spatial amplitude map has a phase of 0. Because of the above normalizations, a component-specific scaling parameter is extracted, which will be denoted as *component strength*, but which does not play a role in the interpretation of the individual components. Because of the different normalizations, the absolute amplitudes and absolutes phases are not meaningful. Crucially however, amplitude *ratios* between sensors, frequencies and trials, and phase *differences* between sensors are not affected by these normalizations, and they therefore reveal important characteristics of the sources that are reflected by the components.

The decomposition method is an iterative algorithm that starts from a random initialization of the parameter values. Importantly, the algorithm can converge to a local minimum of the least squares loss function if the random initialization was unfortunate. Such suboptimal decompositions can be avoided by using multiple random initializations. Then, when the algorithm repeatedly finds the same optimal solution from different random initializations, it can be assumed that the global

minimum has been found.

The decomposition method will be publically available in a GitHub (www.github.com) repository termed *nwaydecomp*. Additionally, it will be made available through the FieldTrip open-source MATLAB toolbox ([Oostenveld et al., 2011](#)), together with a tutorial on its use.

2. ESTIMATING CSDs WITH GREATER SENSITIVITY TO RHYTHMIC SOURCES

We extract components from frequency- and trial-specific CSDs. Typically, these CSDs are estimated as the cross-product of the sensor-by-taper matrices of Fourier coefficients, divided by the number of tapers. Here, we propose an alternative estimator, which produces CSDs that are more strongly affected by rhythmic sources. This alternative estimator capitalizes on the fact that the phase of rhythmic activity is predictable from one cycle to the next. This phase predictability is gradual, and this alternative CSD estimator reflects neuronal activity in proportion to its degree of phase predictability. This also applies to phase coupling *between* neuronal sources: our CSD estimator reflects coupling between neuronal sources in proportion to the degree of predictability of their *phase differences*.

The calculation of the alternative CSD estimator involves a number of steps. In the first step, for a given frequency k , the l -th trial is cut into M non-overlapping segments, which have a length of three cycles of the frequency of interest. Next, each of these M segments is tapered with a Hanning window and the Fourier coefficients are calculated for the frequencies of interest (using a Hanning-tapered three-cycle complex exponential). This results in M column vectors X_{klm} , each having as many elements as the number of sensors J . The regular CSD estimator for frequency k and trial l involves taking the average of the cross-products $X_{klm} \cdot X_{klm}^*$ over the M segments (tapers). Now, our alternative CSD estimator is based on the cross-products between vectors of Fourier coefficients obtained from adjacent non-overlapping segments:

$$\frac{1}{M-1} \sum_{m=2}^M X_{klm} \cdot X_{kl(m-1)}^*$$

Because the cross-product is taken between vectors of Fourier coefficients that are based on segments involving a time lag (such that they are non-overlapping), this estimator is denoted as the *lagged CSD* estimator. The crucial advantage of the lagged CSD over the regular estimator based on the cross-products $X_{klm} \cdot X_{klm}^*$, is that the former depends on the phase consistency between the adjacent segments, that is, on its phase predictability. In fact, the higher the phase predictability of oscillatory activity, the more this activity is reflected in the lagged CSD. Conversely,

the smaller its phase predictability, the less it will be reflected in the lagged CSD.

The above describes the simplest version of the lagged CSD. For our analyses, we calculated a slightly more complicated version, which is based on the same intuition, but makes more efficient use of the data. In its simplest version, the lagged CSD involves non-overlapping segments tapered with Hanning windows, which doesn't optimally use the segment's edges. To compensate for this, we cut the trials in segments that have a 75% overlap, and from these segments we selected all segment-pairs whose members were adjacent and non-overlapping. The lagged CSD was then calculated by averaging the cross-product over these segment-pairs. Because each of the multiple segments per trial is multiplied with a single taper, this approach is equivalent to a Welch multitapering approach ([Welch, 1967](#)). Although not applied in the present study, one can in principle also multiply each segment with *multiple* tapers (e.g. using Slepian tapers; [Percival and Walden, 1993](#)). In this case, the above cross-products are computed only between adjacent non-overlapping segments that were multiplied with the same taper.

Unlike the regular CSD, the lagged CSD is in general not conjugate symmetric and positive semi-definite, although in practice the difference can be small. This is relevant, because our decomposition algorithm requires the CSDs to have these properties. To deal with this, we approximated every lagged CSD by another matrix that does have the required properties. This approximation involves three steps. In the first step, we pre-multiply every lagged CSD by a diagonal matrix that shifts the phases of the rows such that the diagonal elements (which correspond to power in a regular CSD) are real-valued. In the second step, we make the matrix (denoted by Z) conjugate symmetric by means of the following transform: $Z = (Z + Z^*) / 2$. Finally, in the third step, we make this matrix positive semi-definite by performing an eigen decomposition and replacing all negative eigenvalues by zeros. The resulting matrix is conjugate symmetric and positive semi-definite, and will be referred to as the CSD in the remainder. Importantly, compared to the regular CSD, this CSD better reflects sources that are highly rhythmic, as indexed by their phase predictability.

3. DETERMINING THE NUMBER OF COMPONENTS TO EXTRACT

The number of components in the data cannot be determined analytically and needs to be determined empirically, as is also the case for methods such as PARAFAC and ICA. Rather than attempting to estimate the true number of components, we estimate the number of *reliable* components. For this, we need a reliability index for each of the extracted components. We use a reliability index that is based on an odd-even split-half of the trials. More precisely, after splitting the trials in two halves, we extract components from both halves, and evaluate their between-half

similarity. The number of components is increased until the components start to differ between the two halves.

For the analyses presented in this paper we evaluated component reliability by means of split-half similarity coefficients for the spatial amplitude maps, the spatial phase maps and the frequency profiles. These coefficients range between 0 and 1, and we considered component reliability to be acceptable if these coefficients exceeded 0.5 for all three parameter sets. Because multiple components were extracted from both halves, components had to be matched between halves. This was done using the same similarity coefficients.

The split-half similarity coefficients were different for the three parameter sets. For the spatial amplitude maps and the frequency profiles, split-half similarity was calculated as the inner product of, respectively, the normalized spatial amplitude maps and the normalized frequency profiles. For the spatial phase maps, we calculated a split-half similarity coefficient that involves weighting by the spatial amplitude maps and the frequency profiles. This weighting scheme ensures that the similarity coefficient is mainly determined by the most reliable phase estimates, which are obtained from the (sensor, frequency) pairs with the highest amplitudes. This split-half similarity coefficient was calculated as follows:

$$\text{split-half similarity: } \frac{\sum_{k=1}^K \left(\left| \frac{\langle A^1 \cdot \exp(i\lambda_k^1), A^2 \cdot \exp(i\lambda_k^2) \rangle}{\|A^1\| \cdot \|A^2\|} \right| \cdot B_k^1 * B_k^2 \right)}{\sum_{k=1}^K (B_k^1 * B_k^2)}$$

The calculation involves two steps. First, we compute the normalized frequency-specific inner product ($\langle \cdot, \cdot \rangle$) between the amplitude-weighted spatial phase maps $\exp(i\lambda_k^s)$ of both split-halves ($s = 1, 2$ denotes the two halves of the split-half). In the second step, we take the weighted average of the absolute values of these inner products, where the weights are derived from the frequency profiles B^s .

Determining the number of reliable components can be performed using the data at different levels of aggregation. For reasons of computational efficiency, we determined the number of reliable components using data at a higher level of aggregation than the data used for extracting the final components. That is, we determined the number of components on the basis of the trial-averaged CSDs, whereas the final analysis was based on the trial-specific CSDs.

4. EXPERIMENTAL PARADIGM AND ANALYSIS OF MEG RECORDINGS

We analyzed MEG recordings of 11 subjects (4 male; aged 22-49 years) that were obtained and analyzed previously (van Ede et al., 2012). Each subject participated

in two consecutive sessions, resulting in 22 recordings. The study was conducted in accordance with the Declaration of Helsinki, was approved by the local ethics committee (CMO Regio Arnhem-Nijmegen), and all subjects provided informed written consent.

Subjects performed a cued tactile detection task in which the target stimulus was either cued or uncued. The central event in each trial was an auditory stimulus (50ms, white noise) that was paired with a tactile stimulus in half of the trials (0.5ms electric pulse around threshold intensity). The tactile stimulus was delivered to the left or right thumb, and its location was cued by an auditory stimulus (150 ms) on a third of the trials. This auditory cue always preceded the tactile stimulus by 1.5s, and indicated location by pitch (500/1000Hz, counterbalanced over subjects). Subjects indicated on each trial whether a tactile stimulus was present or absent by pressing a button with their index-finger after they had received a lateralized auditory response cue. This cue always arrived 1s after the auditory stimulus, and was presented either to the left or the right ear (alternating over trials; 150ms at 1000Hz). To indicate the presence of a tactile stimulus, subjects responded with their ipsilateral index-finger, and to indicate its absence they responded with their contralateral index-finger. Subjects received auditory feedback indicating accurate detection or not (50ms up-going or down-going frequency sweeps resp.). Cued and uncued trials were randomly interleaved, and subjects completed ~500 trials per recording session. Inter-trial intervals ranged between 2.5 and 12s (mean 3.5s) and were drawn from a truncated negative exponential distribution. For additional details, see [van Ede et al. \(2012\)](#).

For the purpose of the current analyses, we split each trial into three periods. As we had 2 recording sessions from each of the 11 subjects, this resulted in 66 datasets that were analyzed separately. The first period is called *prestimulus*, lasts from t=-1.5s (cue onset) to t=0s (stimulus), and reflects preparation for the possible arrival of the tactile stimulus. The second period is called *stimulus*, lasts from t=0s (stimulus) to t=1s (response cue), and reflects the processing of the stimulus (which may or may not be presented). The third period is called *response*, lasts from t=1s (response cue) to the response button press, and reflects preparation and execution of the response. The duration of this period varied from trial to trial, but was at least 1s long. The average median reaction time over datasets was 1699ms (SD = 255ms) (2 trials were discarded from one dataset because the reaction time was less than 1000ms).

Recordings were obtained from an MEG system with 275 axial gradiometers (CTF MEG; MISL, Coquitlam, British Columbia, Canada), which was housed in a magnetically shielded room. All recordings were low-pass filtered with a 300Hz cutoff and sampled at 1200Hz. Trials containing artifacts were removed using a

semi-automatic detection procedure. Power line noise was removed with a discrete Fourier transform filter. Prior to spectral analysis, we removed the mean and the linear trend from each trial. Next, to suppress the $1/f^x$ shape of the power spectrum, the data was prewhitened by taking the first temporal derivative. All preprocessing and spectral analysis (described below) was performed using custom analyses software and the FieldTrip open-source MATLAB toolbox ([Oostenveld et al., 2011](#)).

To extract components we followed the analysis pipeline described in Results section 2. CSDs were estimated for frequencies between 6 and 40Hz in equally spaced 1Hz bins. We used the approach described in Materials and Methods section 2, involving Welch multitapering. We determined the number of components using the approach described in Materials and Methods section 3. In this procedure, the algorithm was randomly initialized three times. The final components were extracted from the trial-specific CSDs using five random initializations.

5. CHARACTERIZING THE SPATIAL AND SPECTRAL CONTENT OF COMPONENTS

To characterize the spatial and spectral content of the extracted components, we performed several analyses on the spatial amplitude maps and the frequency profiles. These analyses involved classifying components based on their frequency profile and their spatial amplitude maps .We now describe these analyses in more detail.

We classified components as either alpha, beta, and gamma components on the basis of the peak frequency of their frequency profile (with a range between 6 and 40 Hz). Alpha components had a peak frequency between 8 and 16Hz, beta components had a peak frequency between 16Hz and 30Hz, and gamma components had a peak frequency above 30Hz. Eight components from eight different datasets of four different subjects had a peak frequency <8Hz or had a frequency profile that was not uni-modal. These components were discarded, and the remaining 783 components were used for further analyses.

To characterize the spatial diversity of components we categorized them on the basis of their spatial amplitude maps. Every component was assigned to one of the following categories: posterior, left and right sensorimotor, anterior, bilateral, and a rest category. Categorization was based on three measures that each reflect a particular aspect of the component's location on the MEG helmet. These measures make use of a 2-dimensional sensor layout that was constructed from the 3-dimensional sensor positions (identical for all datasets). The first measure is sensitive to the difference between the right and left side of the MEG helmet, and is calculated as follows:

$$\frac{\sum j \in \mathfrak{R}(A_j) - \sum j \in \mathfrak{L}(A_j)}{\sum j \in \mathfrak{R}(A_j) + \sum j \in \mathfrak{L}(A_j)}$$

Here, A is the spatial amplitude map and \mathfrak{R} and \mathfrak{L} are index sets for the right and the left sensors respectively (132 and 131 sensors resp., remaining sensors were discarded). This measure ranges from -1 (only left sensors contributed to the spatial amplitude map) to 1 (only right sensors contributed). The second measure was constructed in the same manner, but is sensitive to differences between anterior and posterior sensors. For this anterior-posterior measure, we used a sensor in the middle of the helmet to split all sensors in an anterior and a posterior set (125 and 148 sensors resp.). The third measure was also constructed in the same manner, but was sensitive to the difference between sensors close to the anterior-posterior midline (medial sensors) and sensors on the lateral sides of the helmet. Sensors were considered to be medial (146 sensors) when they were located in between two marker sensors, of which one was on the left side and the other was on the right side of the helmet; sensors were considered to be lateral when they were located to the lateral side of these marker sensors (126 sensors). These three measures were used to spatially categorize the components. Boundary values for these measures were determined by visual inspection. Components were categorized as posterior when they had an anterior-posterior value between -1 and -0.3. Left sensorimotor components had a left-right value between -1 and -0.2, a medial-lateral value between -0.25 and 0.25, and an anterior-posterior value between -0.2 and 0.4. Right sensorimotor components were defined similarly, but had a left-right value between 0.2 and 1. Anterior components had a left-right value between -0.2 and 0.2, and medial-lateral and anterior-posterior values between 0 and 1. Lastly, bilateral components had a left-right value between -0.2 and 0.2, a medial-lateral value between -1 and -0.1, and an anterior-posterior value between -0.3 and 0.3.

To show representative examples from each category, we selected the 15 components with the most typical spatial amplitude map, also denoted as canonical spatial maps. These components were selected in a stepwise procedure, in which we selected the component that had the highest summed partial correlation with the other spatial amplitude maps (summed over components). The stepwise nature of this procedure follows from the fact that the variance of the already selected spatial amplitude maps was partialled out when calculating the partial correlations. This stepwise selection procedure was continued until 15 components were selected.

6. STATISTICALLY TESTING CORRELATIONS BETWEEN CONTRASTS OVER CLUSTERED OBSERVATIONS

In Results section 4, we report a statistical test involving a correlation over

components between two contrasts: cued versus uncued and hit versus miss. These contrasts are calculated at the level of the extracted components. Crucially, multiple components were extracted from the same dataset and therefore cannot be considered independent observations. Instead, these components exhibit a form of statistical dependence that is typically denoted as clustered observations (clustering within a dataset). We solved this problem by performing the statistical test at the so-called *second level*, the level of the dataset (also called the *random effects* approach). More specifically, we first calculated the correlations between the two contrasts, separately for each of the datasets (i.e. over the components extracted from this dataset). We then performed a one-sample t-test of the null hypothesis that the average correlation (obtained by averaging over the datasets) was equal to zero.

7. IDENTIFYING PEAKS IN SPATIAL AMPLITUDE MAPS

To investigate phase-coupled oscillatory networks (PCNs) we identified peaks in the spatial amplitude maps. These peaks were identified in two steps. In the first step, we identified sensors that were a local maximum in the mini-map defined by this sensor plus its neighboring sensors, and which had an amplitude of at least 30% of the maximum within the whole map. In the second step, we pruned these local maxima such that sensors identified as peaks did not share neighboring sensors. In other words, no sensor identified as a peak shared a neighbor with another peak sensor. When peak sensors shared neighbors, only the peak sensor with the highest amplitude was kept. It has to be admitted that this procedure was not grounded in a biophysical rationale. Rather, it was chosen because it was both intuitively plausible and because it performed well in separating dipolar from non-dipolar spatial maps. Representative examples of detected peaks are shown in Results section 7.

8. BETWEEN-COMPONENT COHERENCE CAN BE ACCURATELY RECONSTRUCTED IN A TWO-STEP ESTIMATION PROCEDURE

To prevent components from splitting up into an arbitrary number of sub-components, we estimated the component-specific parameters under the constraint that the between-component coherency matrices are identity matrices. Then, in a second step, the between-component coherency matrices were estimated while keeping the component-specific parameters fixed. The identity matrix constraint unavoidably leads to some degradation of the component-specific parameters. As such, this two-step strategy is only valid under two assumptions: (1) the resulting component-specific parameter degradation is minimal, and (2) the between-component coherency matrices can be estimated reasonably well from these

(degraded) parameters.

We evaluated the robustness of this two-step strategy in a simulation study in which we generated spatially overlapping MEG components with different levels of source-level coherence. From the simulated data, we extracted two components using the pipeline described above, and evaluated how well these components recovered the true parameter values (the component-specific parameters and the between-component coherency matrices). More specifically, we simulated two oscillatory neuronal sources with peak frequency at 10Hz and dipolar MEG sensor-level representations. We varied the sources' coherence by linearly mixing the source signals using three different degrees of mixing. This resulted in two source signals with a coherence of approximately 0.1, 0.5, and 0.9. The signals from the second source had a delay of 25ms relative to the first source (a quarter cycle at 10Hz). The two source signals were created from white noise to which the following operations were applied: (1) scaling of the amplitudes of its Fourier coefficients such that the amplitude spectrum was proportional to $1/f$, giving the power spectrum a $1/f^2$ shape ([Miller et al., 2009](#)), and (2) band-pass filtering the resulting time domain signals between 8 and 12 Hz, using a 6th order Butterworth filter. The source signals were then projected to the sensor-level using lead fields that were obtained as follows. We started from a single-shell volume conduction model ([Nolte, 2003](#)), calculated from a T1-weighted MR image of the representative subject. Next, the two source locations and their source strengths in the x, y, z directions were chosen such that their lead fields were most similar to the spatial amplitude map and the spatial phase map of two components of the representative subject (see Results section 3; #6 and #8. Finally, these lead fields were scaled with trial profile loadings, as described in the following. The trial profile loadings were either 0.25, 0.50, or 0.75, and pairs of loadings (one loading for every component) were always non-identical. Each unique pair of coefficients was used equally often. To vary the signal-to-noise ratio (SNR), different amounts of spatially uncorrelated sensor-level noise (with a $1/f^2$ power spectrum) was added. However, as SNR did not substantially influence recovery, we only present the simulations with the lowest SNR (0.01). For each level of source mixing, we simulated 100 datasets, also denoted as *runs*. Each of these datasets consisted of 12 trials of 100s each.

The simulated datasets were analyzed in the same way as the real MEG recordings except that we only obtained CSDs for frequencies from 6 to 20Hz instead of from 6 to 40Hz. After extracting two components from each dataset, we investigated their recovery of the simulated parameters. The simulated spatial amplitude and spatial phase maps were obtained from the lead fields, and the simulated frequency profiles and between-component coherency matrices were obtained from a spectral analysis of the source signals. This spectral analysis was identical to the one used for

calculating the sensor-level CSDs. The simulated trial profiles are described above. The to-be-recovered parameters are shown in Figure 1A. Recovery was quantified by coefficients that range from 0 to 1. These coefficients are described in Materials and Methods section 9.

We show the recovery of the simulated spatial amplitude maps and spatial phase maps in Figure 1B, the simulated frequency profiles in Figure 1C, the simulated trial profiles in Figure 1D, and the simulated between-component coherency in Figure 1E. Recovery is shown as a function of source signal coherence. The main findings are the following: (1) spatial amplitude maps, spatial phase maps, frequency profiles, and trial profiles show near perfect recovery with low source signal coherence, (2) with increasing source signal coherence, recovery of the spatial phase maps and trial profiles diminishes slightly, (3) estimated between-component coherence increases with source signal coherence but systematically underestimates it, and (4) the average phase relation between the source signals are poorly recovered by the phase of between-component coherency.

In sum, we have shown that the component-specific parameters of phase-coupled components can be recovered well under the constraint of zero between-component coherence. Differences in source signal coherence are reflected in the estimated between-component coherence, although the source signal coherence itself is underestimated. The average phase relations between the source signals are estimated very poorly, and should therefore not be interpreted.

9. COEFFICIENTS FOR ASSESSING THE RECOVERY OF THE SIMULATED PARAMETERS

We calculated a number of coefficients to assess the recovery of the simulated parameters by the extracted components. We use three different coefficients: (1) one for the spatial amplitude maps, the frequency profiles, and the trial profiles, (2) one for the spatial phase maps, and, (3) one for the phase of the between-component coherence. Each coefficient had ranged from 0 to 1, with 1 reflecting perfect recovery. The first recovery coefficient was constructed as the component-specific inner product between the normalized extracted parameter vector (spatial amplitude map, frequency profile, trial profile) and its simulated counterpart. The recovery coefficient for the spatial phase maps, which is more complicated, is calculated as follows:

$$\text{split-half coefficient: } \frac{\sum_{k=1}^K \left(\left| \text{sum} \left[\left[\left(A^s \circ \exp(i\lambda_k) \right) \cdot \left(A^s \circ \exp(i\lambda_k) \right)^* \right] \circ \overline{\left[\left(A^s \circ \exp(i\lambda_k^s) \right) \cdot \left(A^s \circ \exp(i\lambda_k^s) \right)^* \right]} \right] \cdot B_k^s \right)}{\sum_{k=1}^K B_k^s}$$

The calculation involves four steps. In the first step, we compute the frequency-specific between-sensor phase relations on the basis of the extracted phases $\exp(i\lambda_k)$ and

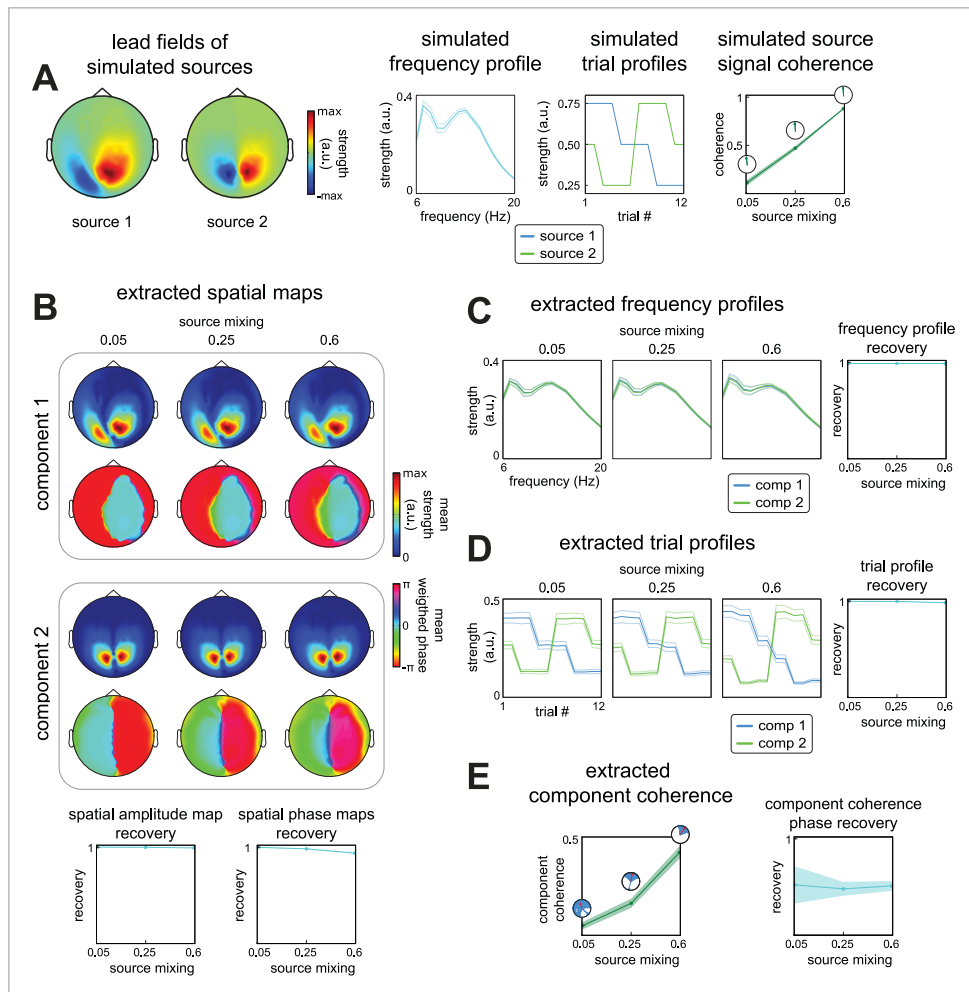


Figure 1. Simulations show phase-coupled components can be accurately extracted. Weak PCNs can be formed by multiple phase-coupled components and are revealed by between-component coherence. However, components are extracted under a zero coherence constraint, and coherence is computed afterwards. This is to prevent a split-up of components into arbitrary numbers of subcomponents. This strategy is only valid if: (1) the resulting component-specific parameter degradation is minimal, and (2) between-component coherence can be estimated reasonably from these (degraded) parameters. Here we present simulations to test this strategy (for details see Materials and Methods section 8, 9). We simulated MEG recordings of two sources and systematically varied their coherence (source mixing of 0.05, 0.25, and 0.6). We generated 100 datasets per level of source mixing. Sensor-level measurements were generated by projecting the source signals through lead fields from the representative subject. Source signals were generated as band-passed noise with a $1/f^2$ shaped power spectrum and consisted of 12 trials of 100s weighted by the trial profile. Spatially uncorrelated noise with a $1/f^2$ shaped power spectrum was added after projecting source signals to the sensor-level. We only show results for the worst signal-to-noise ratio (0.01). Components were extracted from each of 3x100 datasets using the same analysis pipeline as for the real MEG recordings, and we evaluated whether these components accurately recovered the simulated sources. **A**, source lead fields, frequency profiles, trial profiles, and source signal coherence. Frequency profiles shown are the average of the two simulated components, averaged over runs. Source signal coherence shown is the average over runs of the sum of coherence over frequencies, weighted by the product of both frequency profiles. The phase of coherence shown in polar plots was constructed as the mean resultant vector over runs, of the run-specific average phase over frequencies, which was weighted by the product of both frequency profiles. Thin lines in the frequency profiles and shaded area of the source signal coherences reflects the SD. **B**, recovery of the simulated spatial amplitude map and spatial phase maps (constructed from the lead fields). Spatial amplitude maps shown are averaged over runs. Spatial phase maps shown are also averaged over runs, weighted by the simulated frequency profiles. Recovery coefficients reflect average recovery accuracy over runs (shaded areas reflects SD), averaged over both components and range from 0 to 1 (perfect recovery). **C**, same as B but for the frequency profiles. Thick lines display the average frequency profiles, thin lines the SD. **D**, identical to C but for the trial profiles. **E**, recovery of source coherence by between-component coherence. Between-component coherence shown is averaged over runs (shaded area reflects SD), and was constructed as the sum over frequencies per run, weighted by the product of the simulated frequency profiles. Polar plots show the run-specific average phase, weighted in the same way (red arrow reflects mean resultant vector over runs). The results show that the spatial amplitude maps, spatial phase maps, frequency profiles, and trial profiles are minimally impacted by the zero coherence constraint. Between-component coherence was estimated reasonably well, but its phase relations were not. As such, our analysis strategy is valid as long as phase relations between components are not interpreted.

weight these by the normalized simulated spatial amplitude map, A^s . The results of this operation are stored in the square matrix $(A^s \circ \exp(i\lambda_k)) \cdot (A^s \circ \exp(i\lambda_k))^*$, in which $\exp(i\lambda_k)$ is a column vector, \cdot denotes the matrix product, and \circ the element-wise product. The weighting with the normalized simulated spatial amplitude map A^s ensures that the recovery coefficient is mostly determined by the sensors that are strongly affected by the simulated sources. In the second step, we calculate the simulated counterpart of the first matrix (using the simulated phases $\exp(i\lambda_k^s)$), take its conjugate (denoted by the horizontal bar $\bar{}$), and perform an element-wise multiplication of the two matrices. This operation produces large values for sensor pairs whose extracted phase relation differs strongly from the simulated one. In the third step, we summed these phase differences over all sensor-pairs, and take its absolute value, such that we obtain a frequency-specific recovery coefficient that has a range of 0 to 1. (To keep the formula simple, we define $\text{sum}[\]$ to be the sum over all sensor-pairs, which are organized in a matrix.) In the fourth step, we compute their weighted average over frequencies, with the weights obtained from the simulated frequency profile B^s . The resulting coefficient is sensitive to differences between the extracted and simulated spatial phase maps, and is determined most strongly by frequencies and sensors that are strongly affected by the simulated sources.

The recovery coefficient for the phase of between-component coherence was constructed as follows:

$$\left| \frac{\sum_{k=1}^K \left[(\exp(i\varphi_k) \cdot \overline{\exp(i\varphi_k^s)}) \cdot B_k^{s1} \cdot B_k^{s2} \right]}{\sum_{k=1}^K (B_k^{s1} \cdot B_k^{s2})} \right|$$

Computing this coefficient involves two steps. In the first step, we compute the frequency-specific phase difference between the phase of the extracted between-component coherency $\exp(i\varphi_k)$ and the phase of its simulated counterpart $\exp(i\varphi_k^s)$. In the second step, we compute the weighted average of these phase differences over frequencies, where the weights are obtained from the simulated frequency profiles of both components (B_k^{s1} , and B_k^{s2}). The resulting coefficient is sensitive to the phase of between-component coherency, with a weighting that ensures that it is mostly determined by frequencies that dominate the simulated sources.

RESULTS

Measured oscillatory neuronal activity (i.e., at the sensor-level) reflects its underlying sources. We present a model-based method that can distinguish between sources on the basis of their different patterns of between-sensor phase coupling, and their spectral and temporal structure. The method is especially useful when sensors measure neuronal activity that originates from multiple sources, such as with recordings of electrophysiological activity (e.g., ECoG, EEG, MEG). In fact, because of the field spread that is inherent to electrical potentials and magnetic fields (volume conduction in EEG/MEG and common pickup in MEG), there can be a substantial overlap between the spatial distributions of between-sensor phase coupling generated by different sources. Our method separates such sources by their distinct spatial, spectral, and temporal profiles.

Our method is a form of blind source separation and, in contrast to other source separation methods (e.g. ICA/PARAFAC), it is based on a biologically inspired source model. In line with the terminology in this field, we will use the terms sources and components interchangeably. Because our model pertains to a neurobiological rhythm, we denote our components as rhythmic components. Importantly, in contrast to source *localization* (for an overview, see Michel et al., 2004), source *separation* methods do not estimate the sources' location.

An essential feature of the model underlying our method is that it not only provides a parsimonious description of patterns of between-sensor phase coupling, but also describes their variation over frequencies and trials. When analyzing recordings obtained from an experiment, especially the latter is useful: the method quantifies how strongly a component is present in each trial, and this allows us to investigate task modulations of these components. We will demonstrate this in Results section 4.

Components can reflect sources with different spatial extent, ranging from oscillating point sources to spatially distributed sources, such as traveling waves. Oscillating point sources can be identified on the basis of their dipolar pattern at the sensor-level and the induced between-sensor phase relations of either 0 or π . Distributed sources and multiple phase-coupled point sources will be jointly denoted as *phase-coupled oscillatory networks* (PCNs). A PCN differs from a point source by its non-dipolar sensor-level representation. In our initial presentation of the method (van der Meij et al., 2015), we focused on a type of PCN that reflects a distributed source with perfect phase consistency between its subpopulations. As we will show, this type of PCN will be reflected in a single component. Besides this single-component PCN, we will also consider PCNs that consist of multiple weakly coupled components. For this type of weak PCNs, we additionally model and estimate the

between-component phase coupling.

In the following, we present a data analysis strategy that uses our method, and we will illustrate it using MEG recordings from a cued tactile detection task ([van Ede et al., 2012](#)). We first introduce the model underlying our method, and present a data analysis pipeline that depends on it. Subsequently, we present components that are extracted from the MEG recordings. Using these components, we highlight (1) that our approach reveals more than conventional power or coherence analyses, and (2) that the trial-level quantifications are a useful tool to investigate task modulations of neuronal activity. Following this, we focus on the different types networks that these components reflect, and we that these networks are common in MEG recordings.

1. A MODEL FOR CHARACTERIZING PHASE COUPLING IN MULTI-SENSOR ELECTROPHYSIOLOGICAL DATA

Our method is based on a model that describes phase-coupling between oscillations in multi-sensor electrophysiological data, obtained in multiple trials. The amplitude and phase of these oscillations are described by Fourier coefficients. For this, we use a spectral analysis that is based on multiple tapers per trial and frequency, which results in a sensor-by-taper matrix of Fourier coefficients, for every frequency and trial. (Multiple tapers are optimal, but not necessary for the method that will be presented.) We describe the structure in these Fourier coefficients by components, where each component consists of four parameter sets (Fig 2). The *frequency profile* (Fig 2A) describes which frequencies are involved in the phase coupling. The *spatial amplitude map* (Fig 2B) describes the degree to which the different sensors reflect the source that is described by the component. The *spatial phase maps* (Fig 2C) describe, per frequency, the between-sensor phase relations that are induced by this source. Finally, the *trial profile* (Fig 2D) contains the component strength in each trial, which can be used to compare conditions. Importantly, the spatial amplitude map and the frequency-specific spatial phase maps express phase coupling by maps at the level of individual sensors, and not at the level of sensor-pairs. This is important, because phase coupling at the level of sensors-pairs does not directly reveal the network of phase-coupled sensors, because this network is at the level of individual sensors.

The model is presented schematically in Figure 3A (for a mathematical formulation, see Materials and Methods section 1). The observed matrices of Fourier coefficients are frequency- and trial-specific, and they are modeled as the product of four matrices containing the model parameters. The first matrix (cyan) is complex-valued, and is formed by the spatial amplitude map (specifying the amplitudes of the complex numbers) and the frequency-specific spatial phase map (specifying the phases of the complex numbers) of each component. The second (yellow) and third

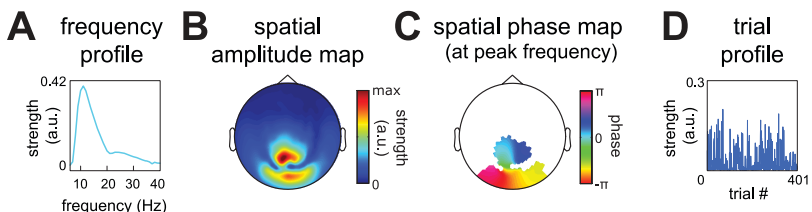


Figure 2. An example rhythmic component reflecting a posterior alpha source. Our decomposition method describes patterns of between-sensor phase coupling over frequencies and over trials by rhythmic components. These components are extracted from Fourier coefficients of electrophysiological recordings, which are obtained by a spectral analysis using multitapering. Components describe the systematic structure of Fourier coefficients over sensors, tapers, frequencies and trials and consist of four parameters sets. The frequency profile (A) describes the frequencies at which there is between-sensor phase coupling. The spatial amplitude map (B) describes which sensors have consistent between-sensor phase relations. The spatial phase maps (C) describe, per frequency, the between-sensor phase relations. The trial profile (D) describes how strongly a component is present in each trial by a single number. The trial profile provides a convenient way to compare conditions at the component-level, by comparing trial-level quantifications of the activity of the source reflected by the component. Importantly, the spatial amplitude map and the spatial phase maps describe phase coupling at the level of sensor-pairs, by maps at the level of individual sensors. This is important, because phase coupling at the level of sensor-pairs cannot reveal networks of coupled sensors without *a priori* hypotheses about which sensor-pairs are likely to interact. The component depicted reflects an posterior alpha source, and is one of 15 components extracted from a representative dataset in Fig 5.

(red) matrices are real-valued diagonal matrices, and they contain the frequency- and trial-specific weighting of each component. The fourth matrix (blue) is complex-valued, and contains the taper-specific amplitudes and phases of each component. These taper-specific amplitudes and phases are also frequency- and trial- specific. The diagonals of the middle two matrices, containing the frequency- and trial- specific weighting of the components, can be concatenated over frequencies and trials, respectively. The columns of the resulting matrices (referred to as loading matrices) contain the frequency and trial profiles of each component.

The model describes a component's between-sensor phase relations by frequency-specific spatial phase maps. This is important, because neurobiological rhythms have energy in a range of frequencies. As such, between-sensor phase coupling induced by such a rhythm must be described by phase relations that may differ across the frequencies involved. This allows our model to characterize sources whose phase relations vary over frequencies. This is the case for a source whose sub-populations interact with a time delay, which results in phase differences that increase linearly with frequency.

It is crucial to observe that we are not decomposing a *2-way matrix* of Fourier coefficients, but a *4-way array* with the following dimensions: sensors, frequencies, trials, and tapers. This higher dimensionality provides additional structure that can be used for identifying and separating components. The model underlying

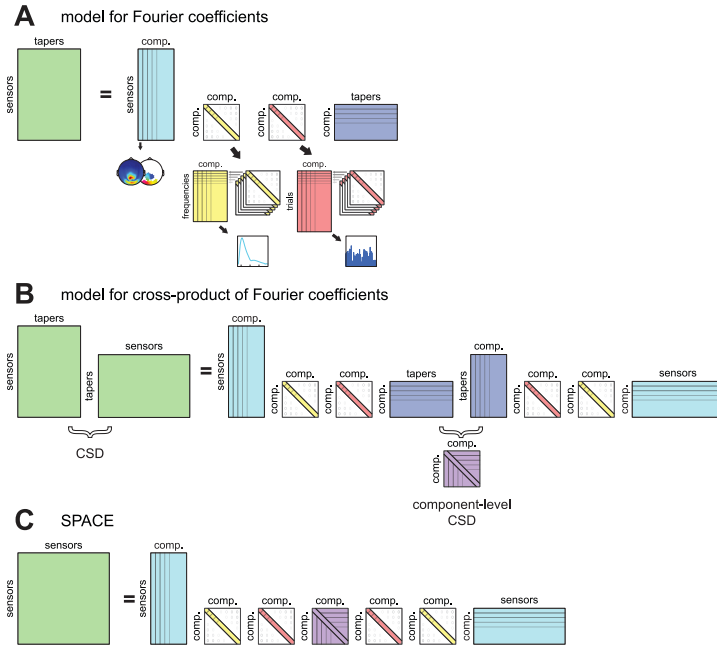


Figure 3. A model for characterizing between-sensor phase coupling by rhythmic components. Our method is based on a model that describes patterns of between-sensor phase coupling of oscillations in electrophysiological recordings. These oscillations are described by Fourier coefficients obtained by a spectral analysis using multitapering, which vary of sensors, tapers, frequencies and trials. Components describe the systematic variability in these Fourier coefficients by a spatial amplitude map, a spatial phase map per frequency, a frequency profile, and a trial profile (Fig 2). Here we present the model schematically. **A.** The model describes the structure in sensor-by-taper matrices of Fourier coefficients (green) per frequency and trial, by the product of four matrices reflecting the four parameter sets. The first (cyan) is complex-valued and contains the spatial amplitude map (Fig 2B) and frequency-specific spatial phase map (Fig 2C) for all components. The second matrix (yellow) is real-valued and diagonal, and contains the frequency-specific weighting of components. When combined over frequencies, it forms the frequency profile (Fig 2A). The third matrix (red) is similar to the second (cyan) but contains the trial-specific loadings, and forms the trial profile (Fig 2D). The fourth matrix (blue) is complex-valued, and contains the frequency- and trial-specific amplitudes and phases of each taper of each component. The middle two matrices are important, as they reflect the fact that we are not decomposing a 2-way matrix, but a 4-way array of Fourier coefficients. Crucially, this is what ensures that our components are unique *without additional statistical constraints* (in contrast to PCA/ICA). **B.** The model in A does not capture between-component coherence. The following model can, and it models the sensor-by-sensor cross-products of the matrices of Fourier coefficients. These cross-products are the cross-spectral density matrices (CSDs), and describe between-sensor phase coupling averaged over tapers. The model for the cross-products is the cross-product of the model in A, and contains the same parameters. In the center there are now the component-by-component cross-products of the matrices (purple) that contained taper-specific parameters. Importantly, these component-by-component cross-products describe the phase coupling between components averaged over tapers, and is the *component-level CSD*. This matrix is explicitly modeled in the final model which we use to extract components. **C.** The final model explicitly models between-component phase coupling by the component-level CSD (purple). Importantly, this is only estimated *per frequency*, and not *per trial and per frequency* (see Materials and Methods section 1 for a mathematical description of the model). Components according to this model can be extracted using a method denoted as SPACE.

our method shares this aspect with other N-way decomposition models such as PARAFAC (Carrol and Chang, 1970; Harshman, 1970). Crucially, this higher number of dimensions ($N > 2$) is what allows for extracting components that are unique *without enforcing statistical constraints*. This contrasts with the widely used ICA and PCA, which require non-biological constraints (statistical independence, orthogonality, maximal variance) to ensure uniqueness.

At this point, the model does not yet contain a parameter that characterizes the between-component phase coupling. However, as will be described later, between-component phase coupling is necessary to describe certain types of PCNs. We now present an extension of the original model which also allows for modeling between-component phase coupling (Fig 3B,C). This is not a model of the sensor-by-taper matrices of Fourier coefficients, but of their cross-products, which are also called cross-spectral density (CSD) matrices. A sensor-by-sensor CSD matrix describes between-sensor phase coupling, averaged over tapers. In the center of the right-hand side of Figure 3B, there is now the cross-product of the matrix containing the taper-specific amplitudes and phases. This component-by-component matrix (purple) is the component-level CSD, which describes the *between-component* phase coupling, averaged over tapers. To arrive at the final model which our method is based upon, we now explicitly model the component-level CSD and replace the cross-product in the center (Fig 3C). Importantly, although the first model (Fig 3A) contains the taper-specific amplitudes and phases *for each frequency and each trial*, the component-level CSD in the final model (Fig 3C, purple) is *only modeled per frequency*. Components according to this model can be extracted using a method denoted as SPACE (for Spatially distributed PhAse Coupling Extraction; van der Meij et al., 2015; see Materials and Methods section 1).

SPACE is inspired by PARAFAC (Carrol and Chang, 1970; Harshman, 1970; Bro, 1998; Kiers et al., 1999; Sidiropoulos et al., 2000). As is the case for PARAFAC, the model underlying our method contains trivial indeterminacies which are solved by various normalizations (see Materials and Methods section 1). One of the consequences of these normalizations is that the component-level CSD is normalized to a between-component coherency matrix per frequency. In the following, we show how components extracted using the proposed method can be used to analyze extracranial brain signals. We first present the analysis pipeline, and then the results that were obtained by applying this pipeline to the data of an MEG experiment.

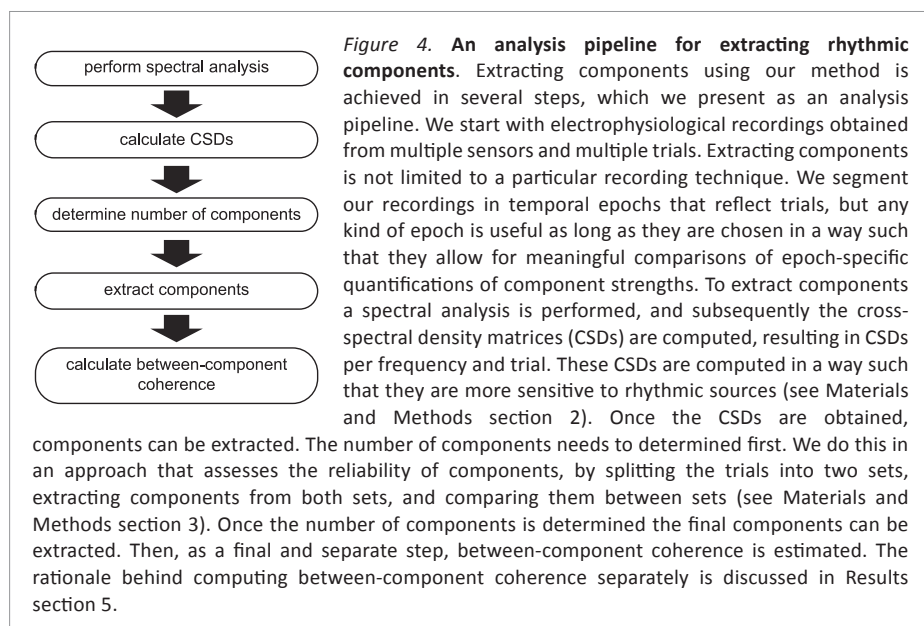
2. AN ANALYSIS PIPELINE FOR EXTRACTING RHYTHMIC COMPONENTS

Extracting components using our method is achieved in several steps, which we present as an analysis pipeline (Fig 4). The input for this pipeline are multi-sensor

electrophysiological recordings obtained in different trials (also called epochs). Although we demonstrate our analysis approach by extracting components from MEG recordings, in principle, any type of multi-sensor electrophysiological recordings can be used. In fact, we initially applied our method to ECoG data ([van der Meij et al., 2015](#)). Additionally, any type of epoch is suitable, as long as they allow for a meaningful comparison of the epoch-specific component strengths.

We start with a spectral analysis and compute a CSD matrix for each frequency and trial. We calculate these CSDs in a way that makes them more sensitive to rhythmic sources than regular CSDs (see Materials and Methods section 2). Using the CSDs as input, we extract components in three steps. First, the number of components to be extracted is determined on the basis of an assessment of the components' reliability. This approach involves splitting the trials in two sets, extracting components from the CSDs of the two sets, and evaluating the components' reliability by comparing them between the two sets (for details see Materials and Methods section 3). In the second step, the component-specific parameters are estimated (spatial amplitude and spatial phase maps, frequency and trial profiles). In the third and last step, we estimate the between-component coherency matrices (the rationale for this is described in Results section 5).

In the following, we apply this pipeline to MEG recordings obtained during a cued tactile detection task ([van Ede et al., 2012](#)). In Results section 3, we present the spatial and spectral content of the extracted components. Next, in Results section 4, we show how the trial-specific component strengths can be used to reveal task



modulations of neuronal activity. Finally, in Results sections 5 and 6, we show that single components can reflect phase-coupled oscillatory networks (PCNs), and in Results section 7, that multiple components can be weakly coupled, forming weak PCNs.

3. RHYTHMIC COMPONENTS IN MEG DATA REVEAL SPATIALLY AND SPECTRALLY DIVERSE SOURCES

To demonstrate the usefulness of our method, we analyzed MEG data recorded in a cued tactile detection task. In the present section, we describe the spatial and spectral diversity in the extracted components and contrast them with the outcome of more conventional analyses.

We present the spatial distribution and spectral content of 783 components that we extracted from 66 extracranial datasets. We first show the components extracted from the data of a representative subject, and then describe all extracted components. In the cued tactile detection task, participants were asked to indicate the presence or absence of a weak electrical stimulus presented to the left or right thumb (for details see Materials and Methods section 4). In 1/3 of the trials, the location of the possible tactile stimulus was cued by an auditory stimulus, allowing subjects to direct their attention to that thumb. On trials without a cue, the tactile stimulus could occur at either thumb. We split the trials from each dataset into three periods. The prestimulus period reflects preparation for the tactile stimulus (1.5 s), the stimulus period reflects stimulus processing (1 s), and the response period reflects response preparation and execution (>1 s). In the first set of analyses, we collapse across these three task periods; their differences will be analyzed in the next two sections. In total, we analyzed 66 datasets (11 subjects * 2 sessions * 3 periods). On average, we extracted 12.0 (SD = 2.0) components per dataset. These components explained on average 50.7% (SD = 6.5%) of the variance in the single-trial CSDs from each dataset.

In Figure 5, we show the components extracted from the prestimulus period data of a representative subject. We extracted 15 components, which reflected 9 alpha sources (Fig 5A; peak within 8 to 16 Hz) and 6 beta sources (Fig 5B; peak within 16 to 30 Hz). These components reflected (1) many overlapping occipital alpha sources, (2) occipital beta sources, (3) an occipito-central/frontal source (#13), and, (4) left and right sensorimotor beta sources. The components differed with respect to the type of sources they reflect. Some of these likely reflect an oscillating point source characterized by a dipolar pattern of between-sensor phase coupling (e.g., #6, 11, 14, 15). This is indicated by their spatial amplitude map having two peaks (local maxima), and by their spatial phase maps at the peak frequency showing phase relations that were mostly 0 and π . There were also components

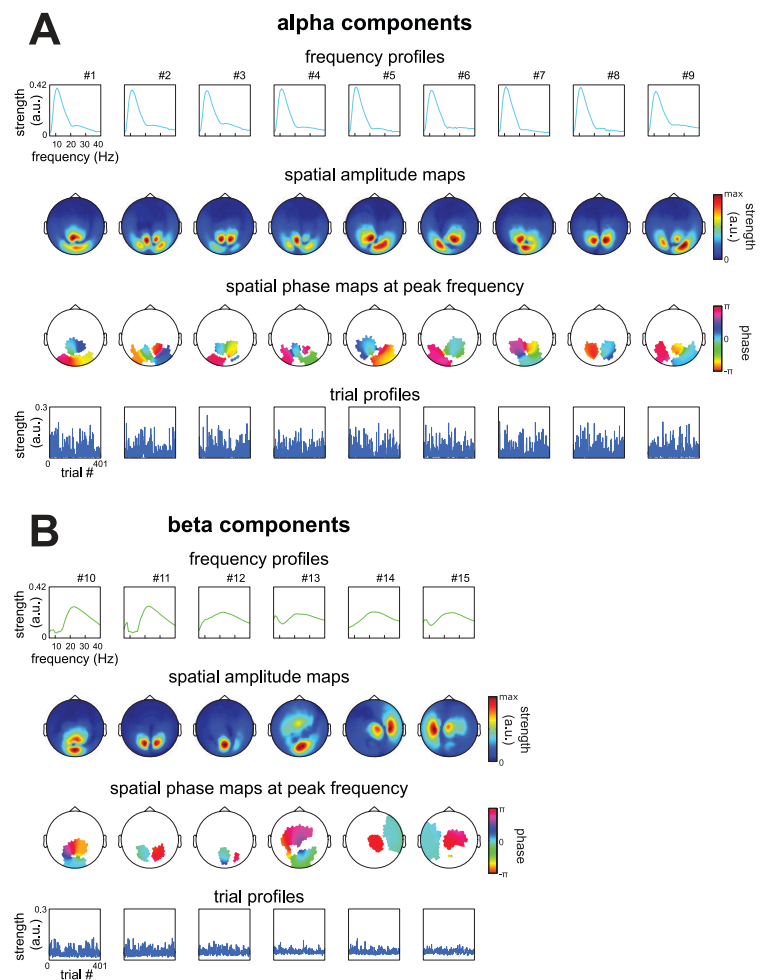


Figure 5. Spatial and spectral structure of sources described by 15 components from a representative subject. We extracted 15 components using the analysis pipeline described in Result section 2 from MEG recordings of a representative subject performing a cued tactile detection task (see Materials and Methods section 4 for task details). This dataset came from the prestimulus period. **A**, frequency profiles, spatial amplitude maps, spatial phase maps at the peak frequency, and trial profiles of components reflecting alpha sources. Phases in the spatial phase maps were masked when amplitudes in the spatial amplitude map fell below 30% of its maximum. **B**, same as A, but for components reflecting beta sources. The components we extracted reflected (1) many overlapping posterior alpha sources, (2) posterior beta sources, an occipito-central/frontal source and (4) left and right sensorimotor beta sources. Components reflected different types of sources. Some components likely reflected point sources (e.g. #6, 11, 14, 15), visible by spatial amplitude map showing two peaks and their spatial phase maps showing phase relations of only 0 and π . Other components with two peaks in their spatial amplitude map showed more phase diversity (e.g. #1, 5, 8, 10, 13), and other had more than two peaks in their spatial amplitude map (e.g. #2, 4, 9). These last two groups likely reflect a distributed source or multiple phase-coupled point sources. These will both be described as phase-coupled oscillatory networks in Results section 5 and 6.

with two peaks in their spatial amplitude maps, but with more phase diversity in their spatial phase maps (e.g., #1, 5, 8, 10, 13; for a discussion of phase diversity, see [van der Meij et al., 2012](#); [Maris et al., 2013](#)). Additionally, several components had more than two peaks in their spatial amplitude map (e.g., #2, 4, 9). These last two groups of components likely reflect a distributed source or multiple phase-coupled point sources. We denote these source configurations as phase-coupled oscillatory networks (PCNs) and describe them in Results section 5 and 6.

We investigated whether the alpha and beta sources revealed by the extracted components were also revealed by conventional analyses involving power and seed-based coherence (Fig 6A,B). Power and coherence were computed using the same CSDs that were used for extracting the components. We observe that (1) the analysis of power suggests only occipital activity, (2) occipital seed-based alpha coherence shows distributed coupling over many occipital sensors, and (3) sensorimotor seed-based beta coherence reveals sensorimotor sources with a monopolar pattern. This contrasts with the extracted components, which revealed (1) that occipital alpha power and coherence originated from many overlapping and separable alpha sources, and (2) that there are clear dipolar beta patterns over sensorimotor cortex, strongly suggesting point sources. The lack of dipolar patterns in sensorimotor seed-based beta coherence and the widespread distribution of occipital seed-based alpha coherence, illustrate an important point: as a result of the overlap between

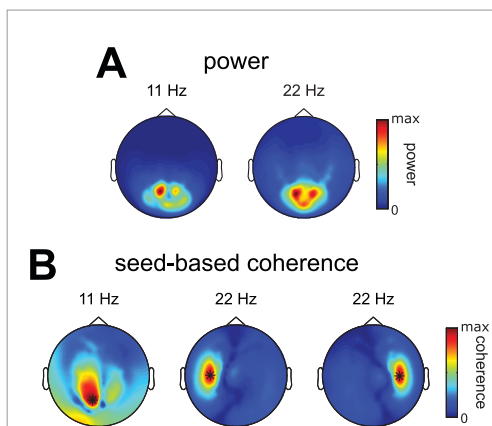


Figure 6. Alpha and beta power and seed-based coherence of the representative subject. To compare the extracted components of our representative subject (Fig 5) to conventional analyses we computed power and coherence using the same CSDs as were used to extract components. **A**, spatial topography of alpha and beta power. **B**, spatial topography of alpha coherence seed from a posterior sensor, and spatial topography of beta coherence seeded from two sensorimotor sensors. Observe that (1) the analysis of power suggests only occipital activity, (2) occipital seed-based alpha coherence shows distributed coupling over many occipital sensors, and (3) sensorimotor sources with a monopolar pattern.

seed-based beta coherence reveals sensorimotor sources with a monopolar pattern. When comparing this to the components extracted using the same CSDs (Fig 5) we observe (1) that occipital alpha power and coherence originated from many overlapping and separable alpha sources, and (2) that there are clear dipolar beta patterns over sensorimotor cortex, strongly suggesting point sources. That these observations cannot be made in power and seed-based coherence illustrates an important point: due to summation of multiple sources sensor-level power and coherence is a very indirect way of studying neuronal activity. Extracting components using our method allows for separating overlapping sources and to analyze them individually.

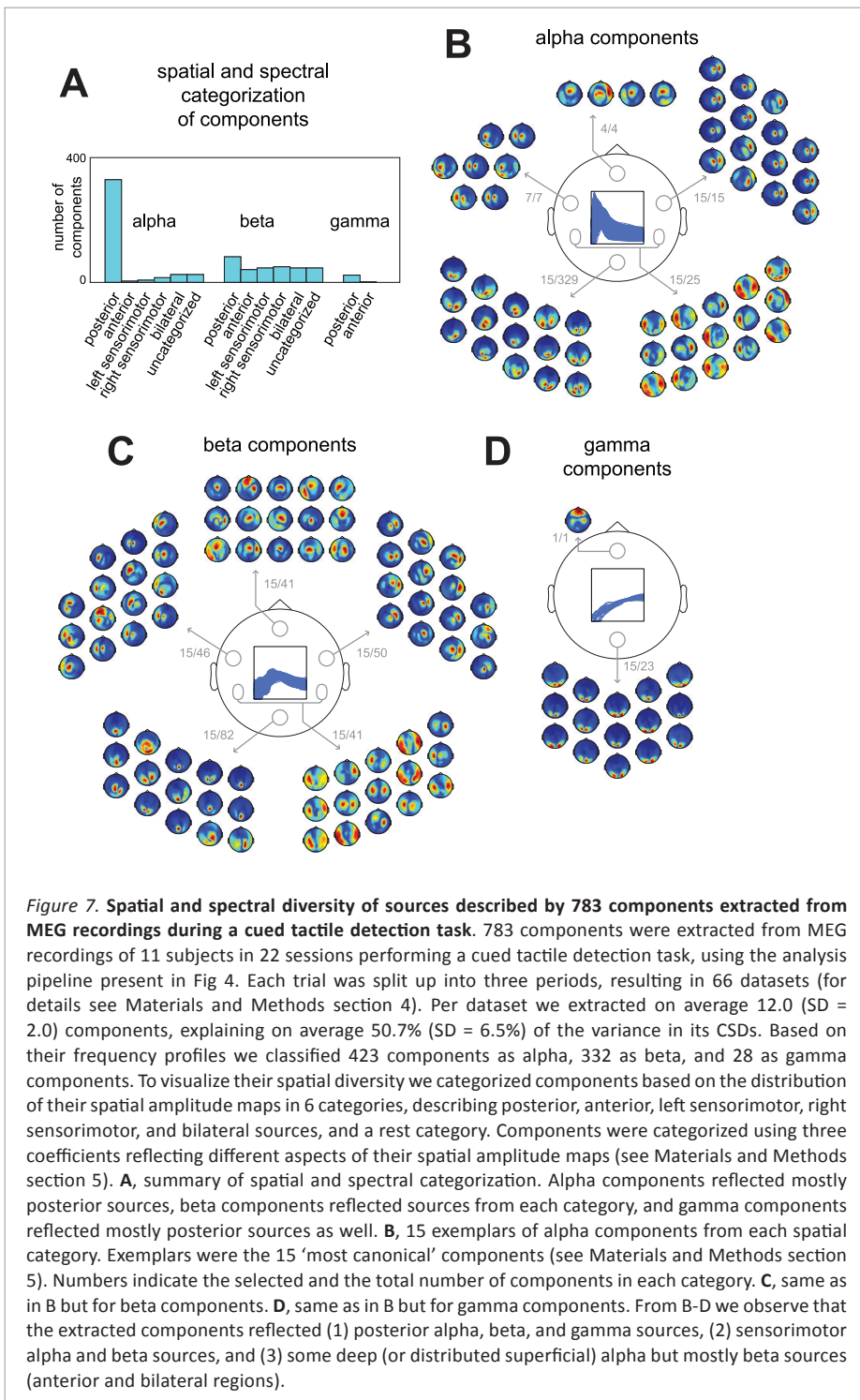
the sensor-level signatures of multiple sources, studying sensor-level coherence is a very indirect way of studying distributed patterns of neuronal activity. In contrast, components extracted using our method allows to separate these overlapping sources and to analyze them individually.

We now present the spatial and spectral content of sources reflected by all 783 components that were extracted. We extracted 423 components reflecting alpha sources, 332 components reflecting beta sources, and 28 components reflecting gamma sources (see Materials and Methods section 5). To investigate their spatial distribution across the brain, we categorized them on the basis of their spatial amplitude maps (Fig 7). We distinguished between six regions: posterior, anterior, left sensorimotor, right sensorimotor, bilateral, plus a rest category for the remaining components. Components were categorized using their values on three coefficients, each of which indexes their relative location over a particular part of the brain: the left versus the right hemisphere, the anterior versus the posterior part of the brain, and the medial versus the lateral part (see Materials and Methods section 5 for details). We first show a summary of this categorization based on location (Fig 7A). This reveals a strong difference between alpha, beta and gamma components. For alpha and gamma components, the spatial amplitude maps mostly covered the posterior region. For beta components, on the other hand, the spatial amplitude maps covered all six regions. To show the diversity in the spatial amplitude maps, for five regions (posterior, anterior, left sensorimotor, right sensorimotor, and bilateral), we show the maps of 15 canonical alpha, beta and gamma components (Fig 7B-D; see Materials and Methods section 5). From the 15 exemplars in each category, we conclude that the components most likely reflected (1) posterior alpha, beta, and gamma sources, (2) sensorimotor alpha and beta sources, and (3) some deep (or distributed superficial) alpha but mostly beta sources (anterior and bilateral regions).

In summary, we have shown that the extracted components reflect spatially and spectrally diverse sources, and that these sources are difficult to identify using conventional power and coherence analyses. The extracted components revealed numerous alpha and beta sources with diverse spatial maps, and showed that the occipital alpha rhythm is generated by many separable sources whose spatial maps overlap at the sensor level. Next, we investigate whether components are modulated by task and behavioral variables, and for this we make use of the components' trial profiles.

4. INVESTIGATING TASK MODULATIONS OF NEURONAL ACTIVITY BY ANALYZING THE COMPONENTS' TRIAL PROFILES

Neuronal activity is often investigated in the context of a task, and the analysis

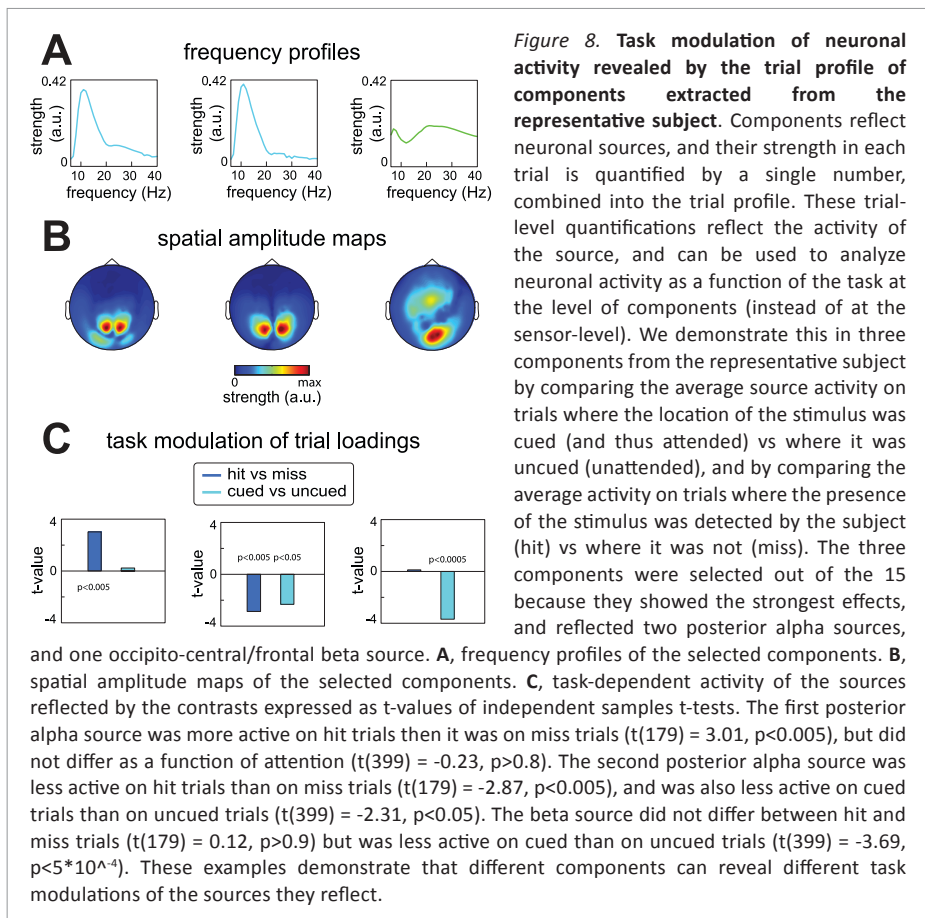


question of interest is usually whether neuronal activity differs as a function of experimental variables and/or the behavior that is elicited (jointly denoted as *task modulations*). This typically involves an analysis at the sensor level, where the relationship between some measure of neuronal activity (e.g. power, coherence) and an independent variable (e.g. conditions, reaction times, performance) is investigated for every sensor or sensor-pair. This is suboptimal for two reasons. First, quantifying the reliability of an effect requires a statistical evaluation for each of the sensors (sensor-pairs), which is problematic without a priori hypotheses about where the effect will occur. Second, when sensor-level representations of neuronal sources overlap due to field spread, then only the sum of their activities can be related to the independent variable. This is problematic if the activity of different, but overlapping, sources is differentially modulated by the task. Our decomposition method provides an alternative: investigating task modulation of neuronal activity at the component-level. This is possible because the underlying model quantifies in a single number how strongly each component is present in a given trial; combined over all trials, these numbers constitute the *trial profile*. Investigating the relationship between an independent variable and the neuronal activity reflected by a component then reduces to relating this trial profile to the independent variable.

We now demonstrate how the components' trial profiles can be used to reveal task modulations of neuronal activity. Specifically, we compare experimental conditions in a cued tactile detection task by comparing condition- and component-specific averages of the trial-level quantifications. Specifically, we investigate whether the activity reflected by a component is modulated by tactile attention and detection performance. The first contrast compares the average source activity on trials where the location of the stimulus was cued and therefore attended, versus those trials in which it was not cued and thus not attended (cued vs uncued). The second contrast compares the average source activity on trials in which the presence of a stimulus was detected with trials in which it was not detected (hit vs miss). We additionally investigate the relationship between the two experimental contrasts as a function the three task periods, and as a function of the spatial and spectral content of the components.

We introduce this task modulation using components obtained from the prestimulus period data of the representative subject (Figure 8). Three components were selected because they showed the largest experimental contrasts of the 15 extracted components (shown in Fig 5). These components reflected two occipital alpha sources and one beta source with a spatial amplitude map over occipital and central regions (Fig 8A,B). The difference in average source activity is expressed by t-values from independent samples t-tests. The first occipital alpha source was more active on hit than on miss trials ($t(179) = 3.01$, $p < 0.005$), but did not differ as a

function of attention ($t(399) = -0.23$, $p>0.8$). In contrast, the second occipital alpha source was less active on hit than on miss trials ($t(179) = -2.87$, $p<0.005$), and was also less active on cued than on uncued trials ($t(399) = -2.31$, $p<0.05$). Finally, the beta source did not differ between hit and miss trials ($t(179) = 0.12$, $p>0.9$) but was less active on cued than on uncued trials ($t(399) = -3.69$, $p<5*10^{-4}$). These examples demonstrate that different components can reveal different task modulations of the sources they reflect.



We now investigate the modulation of source activity by attention and performance for all components (Fig 9). To investigate whether task modulation differed between stimulus preparation, stimulus processing, and response preparation/execution, we show the experimental contrasts separately for the three task periods (Fig 9A). Contrasts are again expressed by t-values. For the stimulation period, both alpha and beta sources showed a positive relation between the two

contrasts in the stimulus period: components whose source activity was weaker on trials in which the stimulus location was cued, also had weaker activity on trials in which the stimulus was detected. Vice versa, components whose source activity was stronger on cued trials also had stronger activity on hit trials. Correlations between the two contrasts in the stimulus period were 0.64 ($p<5*10^{-6}$) and 0.61 ($p<5*10^{-4}$) for alpha and beta components respectively. During the preparation period, beta source activity revealed a similar relation between the two contrasts, with the contrasts having a correlation of 0.39 ($p<0.005$). We did not compute correlations for the gamma components due to the low number of components. As a statistical note, we tested all correlations using a random effects approach (using neuroimaging terminology, *at the second level*), with the components being the first level and the subjects' datasets the second (see Materials and Methods section 6).

In the above, we show that there are alpha and beta sources, whose activity is up- or down-regulated when attention is directed to the location of a possible stimulus, and whose activity is modulated *in the same direction* when a stimulus is correctly detected. This phenomenon has been reported before. First considering down-regulation, knowledge of the location of the stimulus aids in its detection (Posner, 1980), which in task-relevant regions is associated with the suppression of alpha and (in case of somatosensory attention also) beta rhythms. This has been demonstrated both in the visual modality (e.g. Foxe et al., 1998; Thut et al., 2006; Siegel et al., 2008), and the somatosensory modality (e.g. Jones et al., 2010; Haegens et al., 2011; van Ede et al., 2012, with the latter involving an analysis of the same data as the current paper). Next, considering up-regulation, we additionally find alpha and beta sources that show the reverse. That is, the activity of these sources is higher during attention and when stimuli are detected accurately. This has also been reported before, with alpha rhythms being enhanced and thought to suppress task *irrelevant* regions (Jensen et al., 2002; Haegens et al., 2012). Whether our sources show suppressions only in task relevant regions (sensorimotor) and enhancements only in task irrelevant regions (posterior and others) is revealed by their location, which is what we investigate below.

To investigate the location of the sources whose activity was both up-regulated or both down-regulated with attention and performance, we expressed the combined strength of both contrasts as a function of the spatial category of their associated spatial amplitude maps (Fig 9B). These spatial categories were combinations of those described previously (see Results section 3) and describe posterior, sensorimotor (left and right), and deep/distributed sources (anterior and bilateral). We show the combined contrast strength for two selections of components: those whose sources were down-regulated both on trials where the stimulus could be attended and on trials where it was detected, and those whose sources were up-regulated on both types of

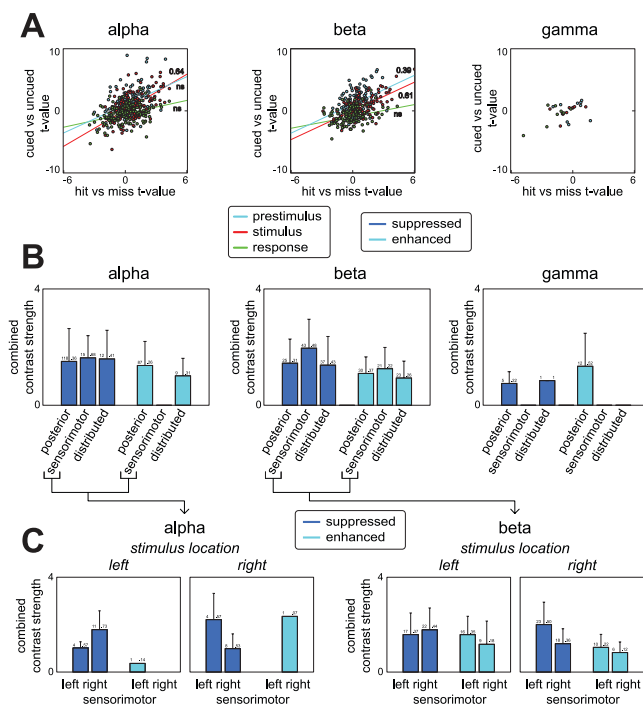


Figure 9. Task modulation of neuronal activity revealed by the trial profiles of all 783 components.

A component's trial profile can be used relate the activity of its source to the task, and provides a more direct way of investigating task modulation of neuronal activity than by analyses at the sensor-level. We demonstrate this by contrasting average source activity as a function of attention, and subject's performance on the task, for all 783 components. Contrasts are the same as in Fig 8. **A**, attention and performance contrasts expressed by t-values as a function of the three task periods to investigate whether activity modulation differed between task stages. Lines are least-squares fit lines. Activity modulations of alpha and beta sources during stimulus processing were positively related: sources that were less active on attended trials (cued) were often also less active on trials where the stimulus was detected (hit), and vice versa. Pearson's correlations were 0.64 ($p<5*10^{-6}$) and 0.61 ($p<5*10^{-4}$) for alpha and beta resp. Beta source activity during stimulus preparation showed a similar relation with a Pearson correlation of 0.39 ($p<0.005$). Correlations for gamma components were not computed due to the low number of components. Statistical testing was performed using a two-level random effects approach (see Materials and Methods section 6). These analyses revealed that there are sources whose activity is 'suppressed' (both less active on cued and hit trials) and 'enhanced' (both more active on cued and hit trials). **B**, combined strength of both contrasts as a function of three spatial categories. Combined contrast strength of a component was constructed by computing the average of the t-values for both contrasts, and subsequently taking its absolute value. Bars indicate SD. The spatial categories describe posterior, sensorimotor ('left/right sensorimotor'), and distributed sources ('anterior' and 'bilateral'; see Materials and Methods section 5 and Fig 7). Alpha and beta components reflecting suppressed and enhanced sources were present in each category. **C**, same as in B, but split up for left and right sensorimotor cortex and for trials in which the stimulus arrived on the left thumb or the right thumb. The results from B and C show that there were sources whose alpha rhythms were suppressed in both task *relevant* regions (sensorimotor) and task *irrelevant* regions (posterior and others), and that there were sources whose beta rhythms were suppressed and enhanced in both task *relevant* regions (sensorimotor) and task *irrelevant* regions (posterior and others). This suggests a complex situation where sources that are located close to each other can be both beneficial and detrimental to the task.

trials (as reflected in, both negative and both positive t-values for the two contrasts resp.). We denote these two types of components as, respectively, suppressed and enhanced. Combined contrast strength of a component was constructed by computing the average of the t-values for both contrasts, and subsequently taking its absolute value. Of the 423 alpha components, 170 were suppressed and 101 were enhanced. For beta components, this was 133 and 87 out of 332. For gamma components this was 7 and 12 out of 28. Suppressed and enhanced components were present in all three spatial categories. The sensorimotor sources can reside in task relevant and irrelevant regions depending on whether the stimulus arrived on the left or right thumb. To investigate the activity of these sources as a function of task relevance, we show combined contrast strength separately for trials in which the stimulus was expected on the left thumb and for trials in which it was expected on the right thumb, and do this for left and right sensorimotor sources (Fig 9C). Left and right sensorimotor suppressed alpha and beta components were present regardless of the side of attention, and this was also the case for enhanced beta components. Only two alpha components showed an enhancement, and it is interesting to note that these occurred only ipsilateral to the attended hand. However, this observation is difficult to interpret due to the low number of sensorimotor alpha components that were extracted (see Fig 7).

With respect to the alpha components, the results from Fig 9B and together show that there are sources whose alpha rhythms are suppressed both in task *relevant* regions (sensorimotor cortices) and task *irrelevant* regions (visual/sensorimotor cortices and others). With respect to the beta components, the results first show that there are both sources whose beta rhythms are *suppressed* and sources whose beta rhythms are *enhanced*. Additionally, both types of sources are observed in task *relevant* as well as task *irrelevant* regions. Together, these findings suggest a complex situation where sources that are located close to each other can be both beneficial and detrimental to the task. Given that these sources often have overlapping sensor-level representations in extracranial recordings, this complexity would be difficult to appreciate when performing analyses at the sensor-level.

In summary, we have shown how task dependent neuronal activity can be analyzed by investigating neuronal activity at the component-level by using the components' trial profiles. We demonstrated this by comparing the average activity of neuronal sources as a function of task and behavior, and showed that there were many alpha and beta sources whose activity systematically varied with tactile attention and performance. Importantly, many of these sources originated from the same regions and reflected either a suppression or enhancement of rhythms in regions both relevant and irrelevant to the task. The signals from these sources often overlapped in our extracranial recordings due to field spread. This demonstrates the

usefulness of our method, which is capable of separating sources when putative sources are located close together.

5. RHYTHMIC COMPONENTS DESCRIBE BOTH STRONGLY AND WEAKLY PHASE-COUPLED OSCILLATORY NETWORKS (PCNs)

A rhythmic component describes the spatial, spectral and temporal structure of phase-coupling that is induced by a neuronal population. Neuronal populations can form phase-coupled oscillatory networks (PCNs) and, using our method, we can distinguish between two types, strong and weak PCNs. A strong PCN is a spatially distributed neuronal population whose subpopulations (not necessarily connected in space) are strongly phase-coupled (in the prototypical case, with a coherence of 1). As we will explain below, a strong PCN is captured by a single component. A weak PCN is a collection of neuronal populations that are only weakly phase-coupled (e.g., only during some parts of an extended period). As we will explain below, a weak PCN is captured by multiple phase-coupled components, each of which reflects one neuronal population. These populations can be point sources or they can also be spatially distributed. In the latter case, this neuronal population is itself a strong PCN. Thus, a weak PCN can be a phase-coupled network of strong PCNs, but may also involve components that reflect point sources.

Strictly speaking, the distinction between distributed and point sources is not biologically realistic. However, it is useful because it allows for making a distinction between components that are strong PCNs (distributed sources) and those that are not (point sources). In practice, we will consider a component to be a point source if its spatial amplitude and spatial phase map closely approximate a current dipole; otherwise, it will be considered a distributed source. Note that a distributed source can be spatially discontinuous, and when the disconnected subpopulations are small, the source's spatial amplitude and spatial phase map can look like a superposition of point sources (e.g., component #2 in Fig 5).

When extracting components, we have to deal with the fact that a single component can be split in any number of components with between-component coherences equal to 1. In terms of the matrices in Figure 3, this splitting of components corresponds to a single spatial map (a column in the leftmost cyan matrix) being replaced by multiple spatial maps, which can be combined into the original one. Importantly, after this split, the corresponding columns of the between-component coherency matrices are equal to each other (and, as a result, the whole matrix is rank-deficient). We prevent such a split-up of components by putting a constraint on the between-component coherencies. Specifically, we constrain these matrices to be identity matrices (zero between-component coherence). Under this constraint, a

PCN that exhibits perfect phase coupling between subpopulations will be captured by a single component. In fact, if this PCN would be split over multiple components then some off-diagonal elements of the between-component coherency matrices will be equal to 1, strongly conflicting with the zero coherence constraint. This constraint also has the consequence that groups of sensors that correspond to weakly phase-coupled neuronal populations, will be split into separate components. After estimating the component-specific parameters under the identity matrix constraint, these weak PCNs are identified by estimating the between-component coherencies while keeping the component-specific parameters fixed.

The zero coherence (identity matrix) constraint unavoidably leads to some degradation of the component-specific parameters of phase-coupled components. As such, our strategy is only valid under two assumptions: (1) the resulting component-specific parameter degradation is minimal, and (2) the between-component coherencies can be estimated reasonably from these parameters. We evaluated the robustness of our strategy by simulating overlapping phase-coupled MEG components, and varying the strength of their coherence. The simulations and their results are described in detail in Materials and Methods section 8. In short, this simulation study showed that (1) the component-specific parameters are only minimally distorted by the constraint, (2) between-component coherence can be recovered well, but (3) the between-component phase relation cannot.

In the following two sections we first describe strong PCNs that are revealed by single components extracted from our MEG recordings. Next, we will describe weak PCNs revealed by their between-component coherencies.

6. STRONG PCNS ARE WIDESPREAD IN MEG RECORDINGS

To identify single-component strong PCNs they need to be distinguished from components that reflect single oscillating point sources. This is achieved by investigating their spatial amplitude and spatial phase maps. A point source has a dipolar pattern at the sensor level: a spatial amplitude map with two peaks, and a between-peak phase relation of π . When a component has more than two peaks and/or it has different between-peak phase relations, it cannot reflect a point source. Instead, such a component reflects a distributed source, or multiple phase-coupled point sources, and thus it reflects a PCN.

We show identified strong PCNs in Figure 10. These PCNs were identified on the basis of the between-peak phase relation, which were obtained from the component's spatial phase map (at the peak frequency of the frequency profile). Spatial peaks were detected by comparing the loadings of the spatial amplitude map between neighboring sensors (see Materials and Methods section 7; peaks of

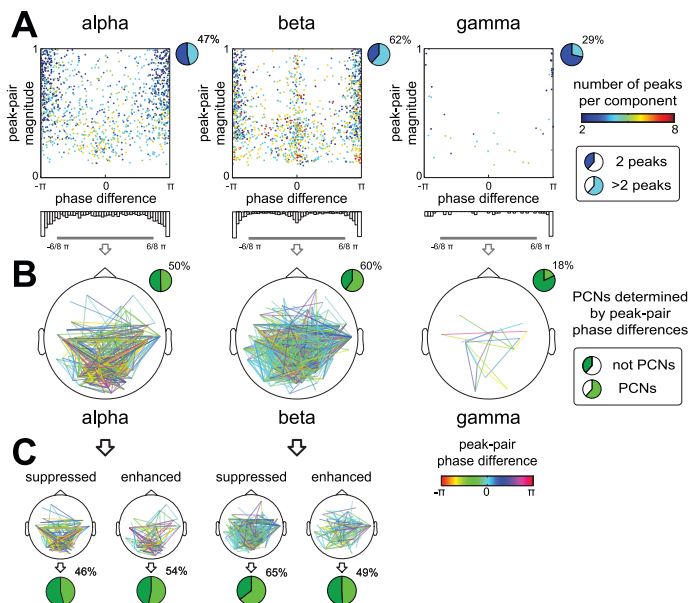


Figure 10. Strongly phase-coupled oscillatory networks (PCNs) are widespread in MEG recordings. Single components that describe distributed sources reflect strong PCNs, and to identify them they need to be distinguished from oscillating point sources. This is achieved by investigating their spatial amplitude and spatial phase maps. A point source has a spatial amplitude map with two peaks (local maxima), and a between-peak phase relation of π . When a component has more than two peaks and/or it has different between-peak phase relations, it cannot reflect a point source. Such a component describes a distributed source (which can include multiple phase-coupled point sources) and thus reflects a strong PCN. Here we present single-component PCNs identified in components from all datasets. **A**, within-component peak-pair phase relations of the spatial phase map at the peak frequency of the frequency profile. Each dot represents a peak-pair within a component, and is color coded w.r.t. to the total number of peaks in the spatial amplitude map of the component. Peak-pair magnitude is determined by the product of the amplitude of the peaks, with the spatial amplitude maps normalized to have a maximum value of 1. Peaks were detected by comparing the loadings of the spatial amplitude map between neighboring sensors (see Materials and Methods section 7; example peaks are shown in Fig 11). Alpha, beta, and gamma all showed (1) components with two spatial peaks and between-peak phase relations of π , and (2) components with more than two peaks and/or between-peak phase relations different from π . **B**, peak-to-peak within-component connections of each component likely reflecting a strong PCN. Line color reflects peak-pair phase difference and line thickness reflects peak-pair magnitude. Components were considered as a PCN when they had at least one peak-to-peak phase relation between $-3/4\pi$ and $3/4\pi$ on the right hand side of the circle. To avoid showing connections between poles of a dipole we only show connections inside this phase interval. Alpha, beta and gamma sources all reflected single-component strong PCNs and were widely spatially distributed. Beta sources described strong PCNs most often (60%), followed by alpha sources, (50%) and gamma sources (18%). Additionally, beta PCNs appeared more widely distributed than alpha strong PCNs. Non-PCN components reflected point sources, being 40%, 50% and 82%. **C**, peak-to-peak within-component connections as in B but for ‘suppressed’ and ‘enhanced’ components separately. Suppressed and enhanced components had either both negative t-values or both positive t-values on the experimental contrasts used in Figure 8 and 9. There were single-component strong PCNs both among the suppressed and enhanced component types, and this was the case for both alpha (resp., 46% and 54%) and beta (resp. 65% and 49%) components. We did not investigate this for gamma components due to their low number. The above results show that (1) single-component strong PCNs are common, (2) are widely distributed, and (3), were common among ‘suppressed’ and ‘enhanced’ components.

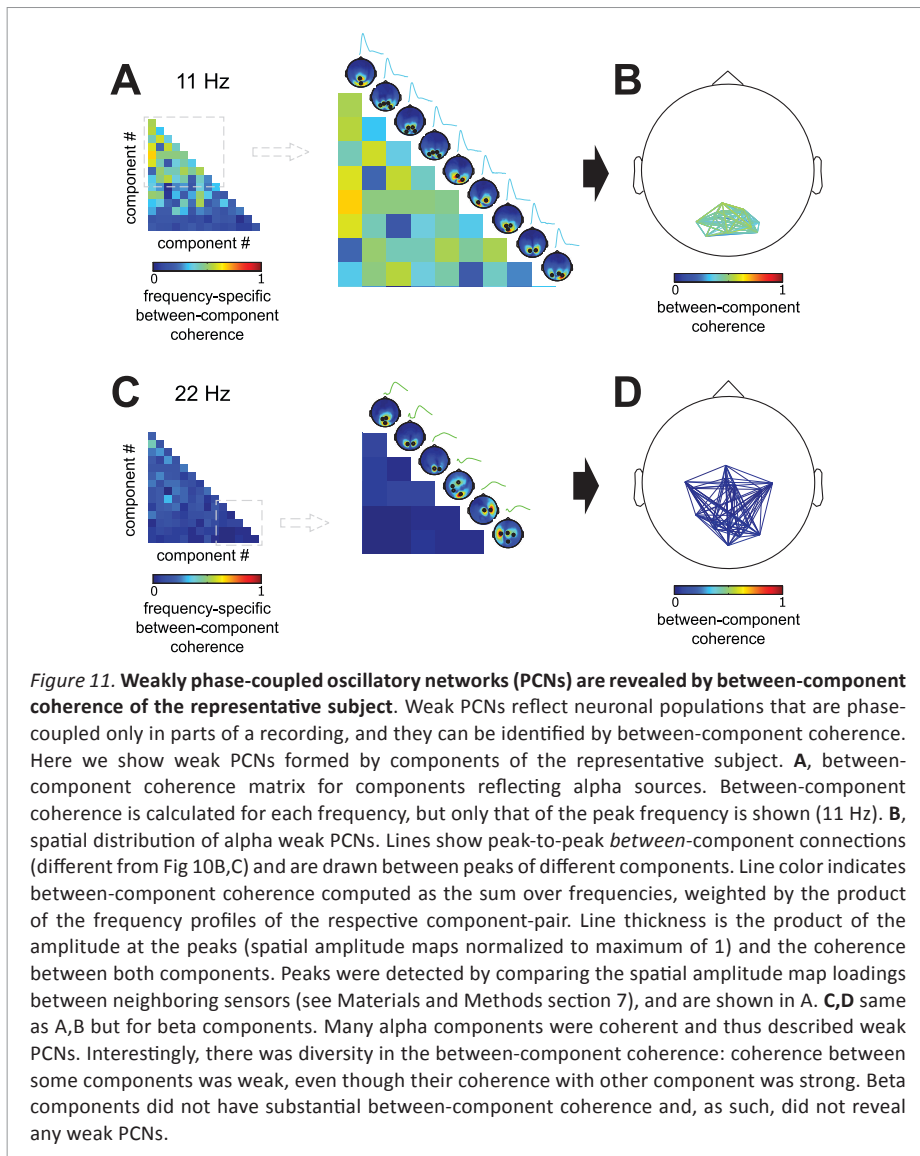
representative subject components are shown in Fig 11). Alpha, beta, and gamma all showed (1) components with two spatial peaks and between-peak phase relations of π , and (2) components with more than two peaks and/or between-peak phase relations different from π (Fig 10A). Components reflecting beta sources most often had more than two peaks (62%), followed by alpha sources (47%). To investigate the spatial distribution of strong PCNs, we show the peak-to-peak within-component connections of each component reflecting a strong PCN (Fig 10B). Strong PCNs were identified on the basis of a strategy that excludes point sources: a component was considered a strong PCN if at least one of the between-peak phase differences fell between $3/4$ and $3/4\pi$ on the right-hand side of the circle (between 135° and 225°). Alpha, beta and gamma sources all reflected widespread strong PCNs. Beta components reflected strong PCNs more often (60%) than alpha components (50%), and gamma components (18%). Additionally, strong PCNs in the beta band appeared more widely distributed than strong PCNs in the alpha band. These numbers also indicate how many components reflected point sources: in the alpha, beta and gamma band, these percentages were, respectively, 40%, 50% and 82%. To investigate whether the emergence of strong PCNs was task-dependent, we also show strong PCNs separately for the suppressed and the enhanced component types (Fig 10C). There were strong PCNs both among the suppressed and enhanced component types, and this was the case for both alpha (46% and 54% resp.) and beta (65% and 49% resp.) components. Because of the low number of components, we did not investigate gamma PCNs. In sum, the above results show that strong PCNs (1) are common, (2) widely distributed, and (3), were common both among suppressed and enhanced component types.

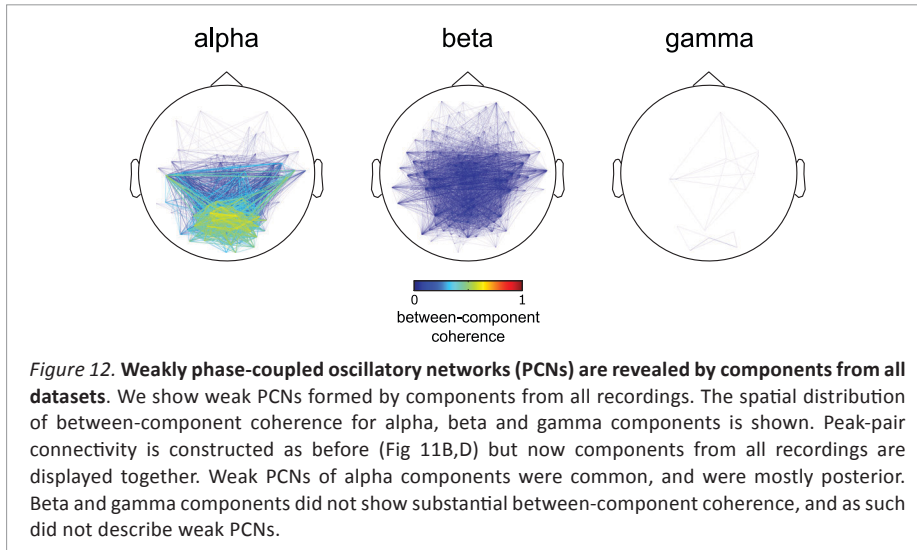
7. WEAK PCNS ARE REVEALED BY BETWEEN-COMPONENT COHERENCE

In Figure 11, we present weak PCNs formed by components of our representative subject. We show the between-component coherence and spatial distribution for the alpha band weak PCNs in panels A and B. The spatial distribution is shown as connecting lines between the peaks of distinct components (which is different from the visualizations in Fig 10B,C, but the peaks were detected in the same way; see Materials and Methods section 7). The colors of the connecting lines reflect the strength of their between-component coherence (obtained by averaging between-component coherence over frequencies, weighted by the frequency profiles). Many of the alpha components were coherent and thus reflected weak PCNs. Interestingly, there was diversity in the between-component coherence: coherence between some components was weak, even though their coherence with other components was strong. Surprisingly, no weak PCNs were found in the beta band (Fig 11C,D).

The weak PCNs that were found in all datasets are shown in Figure 12. Between-

component coherence and its spatial distribution are visualized in the same way as for the representative subject. For alpha components, weak PCNs were common, and were mostly observed over posterior areas. In contrast, beta and gamma components did not show substantial between component coherence, and therefore did not form weak PCNs.





DISCUSSION

We have presented an analysis approach of oscillatory neuronal activity involving rhythmic components that are extracted according to a new decomposition method ([van der Meij et al., 2015](#)). This method characterizes sources in terms of their spatial maps (involving both amplitude and phase information), their frequency profiles, and their trial profiles. The novelty of this approach lies in that this method describes the sensor-level representations of sources in a neurobiologically plausible way: a spatially distributed oscillation with between-sensor phase relations that can vary as a function of frequency. By analyzing MEG recordings during a cued tactile detection task, we demonstrated the following three key benefits of this approach. First, it can separate multiple overlapping sources on the basis of their structure as a function of space (sensors), frequency and time (trials), thereby revealing sources that are very difficult to identify in conventional analyses. Secondly, it allows for a straightforward analysis of task modulations at the component level, by making use of the trial profiles. Lastly, it can reveal phase-coupled oscillatory networks (PCNs).

SEPARATELY CHARACTERIZING THE ACTIVITY OF OVERLAPPING SOURCES

Our method is capable of separating sources using the structure over sensors, frequencies, and trials. Spatially overlapping sources are separated on the basis of their different spectral content and trial structure. Similarly, spectrally and

temporally overlapping sources are separated on the basis of their different spatial maps and, respectively, their different trial structure and spectral content. Separating sources is important because the activity of different sources can be differentially modulated by experimental and behavioral variables. Without separating sources, the activity of overlapping sources is summed, and only their average modulation can be investigated. Moreover, sources differ with respect to the degree with which they are visible at the sensor-level, and this is not only a function of the relevance of a source in an experimental context, but also of unrelated variables such as source depth and the spatial extent of the involved neuronal populations. As a result, the activity of weak sources is hardly visible when these overlap with stronger sources. Using our method, we were able to separate many overlapping sources, such as those that contributed to posterior alpha activity, and we were able to extract sources that were hardly visible at the sensor-level, such as the sensorimotor beta sources (Fig 5,6).

Note that *source separation* methods (SPACE, ICA, PARAFAC) have a different goal than *source reconstruction* methods (e.g. beamforming, minimum norm estimation; for a review see Michel et al., 2004). While the latter are capable of resolving the location of a source, they are unable to separate sources with overlapping spatial distributions.

ANALYZING MODULATIONS OF NEURONAL ACTIVITY AT THE COMPONENT-LEVEL: NOVEL INSIGHTS ON THE ROLE OF ALPHA AND BETA OSCILLATIONS IN ATTENTION, AS STUDIED IN THE SOMATOSENSORY MODALITY

Our method allows for a new way of investigating the relation between neuronal activity, and experimental and behavioral variables. This is normally done by investigating activity at the sensor- and/or source-level, whereas we propose to investigate neuronal activity at the component-level. This is possible, because a component's trial loading is a convenient measure of the trial-specific activity reflected by a component. Using a given component's trial profile, conditions can be compared at the component-level, namely by comparing its loadings for the different conditions. By analyzing neuronal activity at the component-level, we found that there were many alpha and beta sources whose activity was suppressed or enhanced by attention and in relation to behavioral performance. This occurred both in regions relevant (sensorimotor cortex) and irrelevant (e.g. visual cortex) to our somatosensory attention task. However, studies investigating activity at the sensor-level, which describe the *average task modulation of multiple overlapping sources*, only give a partial view on these effects. Studies investigating alpha activity in attention and memory task mostly report alpha being enhanced in regions irrelevant to the tasks (Worden et al., 2000; Jensen et al., 2002; Rihs et al., 2007;

Gould et al., 2011; Haegens et al., 2012), and alpha being suppressed in regions relevant to such tasks (Foxe et al., 1998; Thut et al., 2006; Siegel et al., 2008; Jones et al., 2010; Haegens et al., 2011; van Ede et al., 2011; van Ede et al., 2012). Likewise, studies investigating beta activity in somatosensory and motor tasks mostly report beta being suppressed in regions relevant to these tasks (e.g. Pfurtscheller et al., 1997; Donoghue et al., 1998; Jurkiewicz et al., 2006; Jones et al., 2010; Miller et al., 2010a; van Ede et al., 2010; Haegens et al., 2011; van Ede et al., 2012). The above findings have led to the view that alpha and beta oscillations in visual and somatomotor regions reflects an inhibition of irrelevant neuronal activity. However, we additionally revealed many alpha and beta sources whose activity was *suppressed* in *irrelevant* regions, and those whose activity was *enhanced* in *relevant* regions. Such alpha and beta sources therefore likely do not reflect inhibition of irrelevant information, suggesting that the functional role of alpha and beta activity in such tasks is more complex than is commonly thought. This highlights the usefulness of a method like ours, which can separately characterize the activity of these different sources.

INVESTIGATING PCNS USING RHYTHMIC COMPONENTS: STRONG ALPHA AND BETA NETWORKS AND WEAK ALPHA NETWORKS

Our method estimates phase relations between interacting neuronal populations in two ways: within a component, and between components. These phase relations are the basis for identifying two types of PCNs (weak and strong), and allows for distinguishing them from single point sources. Distinguishing between PCNs and such points sources is important, because the sensor-level phase coupling produced by a point source reflects a single isolated population, whereas the sensor-level phase coupling of PCNs reflects communication between networks of neuronal populations. We additionally distinguish between strong and weak PCNs, which differ in the strength of the phase coupling between the underlying populations. We identified many alpha and beta strong PCNs, which most likely reflect interactions between distributed neuronal populations. Communication between distributed populations by alpha and beta phase coupling is in line with a possible role in top-down control and routing of information (Palva and Palva, 2007; Engel and Fries, 2010; Jensen et al., 2014). Phase coupling between distant areas has been reported before at beta (Brovelli et al., 2004; Gross et al., 2004; Buschman and Miller, 2007; Pesaran et al., 2008; Canolty et al., 2010), and at alpha (von Stein et al., 2000; Halgren et al., 2002; Palva et al., 2005; Pollok et al., 2005) frequencies.

Our approach also allows us to identify weak PCNs. Whereas strong PCNs reflect highly consistent phase coupling between neuronal populations, weak PCNs are the result of weaker phase consistency between populations. Weak PCNs could reflect

temporary networks: networks whose nodes (neuronal populations) interact for shorter periods of time (shorter than the duration of a trial). We only found alpha weak PCNs, and they mostly involved posterior sensors. This suggests a complex picture for the generation of posterior alpha, where nodes of the network may come and go. Temporary networks have been the topic of recent EEG/MEG studies (Breakspear et al., 2004; de Pasquale et al., 2010; Woolrich et al., 2013; Brookes et al., 2014), which show that these networks can form and dissolve at a time-scale as short as several hundred milliseconds. Interestingly, most of these studies find such networks in the beta band, whereas we only found alpha weak PCNs. This could be the result of different task demands, as these studies found either networks in resting state activity (de Pasquale et al., 2010; Woolrich et al., 2013; Brookes et al., 2014) or motor networks during a repetitive motor task (Woolrich et al., 2013). In contrast, our tactile attention paradigm only had minimal motor demands. Alternatively, these different results could also be due to the fact that our networks are defined by phase coupling, whereas the other studies defined networks by correlations between band-limited amplitude envelopes.

RELATION BETWEEN OUR APPROACH AND SEED-BASED APPROACHES

Our method is one of many that have been proposed to identify and characterize networks in electrophysiological signals. We now compare our method to existing ones, which we can group in two categories: (1) seed-based approaches, which we discuss here, and (2) decomposition methods, which we discuss in the next section. For the seed-based approaches, we must further distinguish between methods for identifying networks in resting-state electrophysiological signals (de Pasquale et al., 2010; de Pasquale et al., 2012; Hipp et al., 2012) and methods for identifying networks that are differentially active in different experimental conditions (Hipp et al., 2011). We start with the former. The seed-based approach starts from a pair-wise measure that indexes the coupling between two sensors. Commonly used measures are coherence (Mormann et al., 2000), phase-locking value (Lachaux et al., 1999), and pair-wise phase consistency (Vinck et al., 2010). It is problematic to investigate phase coupling between *all* sensor-pairs because the result cannot be visualized in a way that is easy to interpret. For this reason, one often selects a seed sensor and visualizes the coupling with all other sensors. This approach requires a priori hypotheses about which (sensor, frequency)-pairs are likely to reveal the networks. In contrast, our approach describes coupling at the level of sensor-pairs by spatial maps at the level of individual sensors, which are more straightforward to interpret.

The seed-based approach is further hampered by the fact that extracranial signals suffer from field spread (volume conduction of electrical fields and common pickup of magnetic fields), which results in spatial overlap between signals from

separate sources, as we demonstrate in Figure 5 and 6. In an attempt to deal with this field spread, some authors apply the seed-based approach to signals at the source level (de Pasquale et al., 2010; Hipp et al., 2011; de Pasquale et al., 2012; Hipp et al., 2012). That is, they first use source reconstruction methods, such as the beamformer, to calculate source-level signals, and then characterize coupling between a seed-region and all other regions of interest using pair-wise measures. However, source reconstruction is not sufficient to remove all effects of field spread. Exactly for this reason, Hipp et al. (2012) use a pair-wise measure that is only sensitive to phase coupling that cannot be fully explained by field spread. This measure is based on the idea that average phase relations different from zero cannot be due to field spread (Nolte et al., 2004). In contrast, our method deals with the effects of field spread (1) by separating sources with overlapping sensor-level spatial maps, and (2) by providing spatial phase maps that allow us to distinguish between phase coupling caused by field spread from phase coupling caused by interacting populations.

We now consider a seed-based method for identifying networks that are differentially active in experimental conditions. This method was proposed by Hipp et al. (2011). This method is a statistical method, because it evaluates the statistical significance of differences between conditions. The particular method used by Hipp et al. (2011), cluster-based permutation tests (Maris and Oostenveld, 2007; Maris, 2012), produced contiguous clusters in space, frequency, and time. These clusters were used to identify the networks that were modulated across experimental conditions, as well as the time window in which this modulation occurred. Importantly, because these clusters were defined by a statistical criterion, their size depends on the sensitivity of the statistical test, which in turn depends on the number of observations and its signal-to-noise ratio. Thus, cluster size will increase with, for example, the number of subjects or trials. This is an important constraint on the interpretation of the clusters. In contrast, the spatial extent of our components is determined by how strongly each sensor picks up activity from a source, regardless of the modulation of source strength across experimental conditions.

RELATION BETWEEN OUR APPROACH AND OTHER DECOMPOSITION METHODS

We now consider alternative decomposition methods. It is useful to distinguish between methods that can only decompose arrays of Fourier amplitudes (which are real-valued), and those that can decompose arrays of complex-valued Fourier coefficients. Among the former methods are ICA and PCA (Bell and Sejnowski, 1995; Chapman and McCrary, 1995), and real-valued PARAFAC (Carrol and Chang, 1970; Harshman, 1970; Miwakeichi et al., 2004; Morup et al., 2006). These methods are useful for identifying networks of neuronal populations with correlated amplitude envelopes. However, it is unclear how the correlation between amplitude envelopes

is relevant for the effective communication between neuronal populations. For phase-coupling on the other hand, there are plausible mechanisms arguing for their relevance for this effective communication (Fries, 2005; Siegel et al., 2012; Engel et al., 2013). This is the main motivation for using decomposition methods that characterize networks by their patterns of between-sensor phase coupling in arrays of complex-valued Fourier coefficients.

A few decomposition methods are capable of decomposing complex-valued arrays. These are complex-valued PARAFAC (Sidiropoulos et al., 2000), Shifted CP (Morup et al., 2008), and complex-valued ICA (Anemuller et al., 2003; Hyvärinen et al., 2010). These methods all characterize phase-coupled oscillatory networks, but suffer from a number of shortcomings that do not apply to our method. These methods (1) require constraints that are not neurobiologically motivated (complex ICA), (2) cannot deal with trial- and frequency-specific phase offsets (complex ICA and PARAFAC), (3) cannot make use systematic variability over frequencies to identify networks (complex ICA), and/or, (4) can only describe between-sensor phase relations that are constant over frequencies (Shifted CP and complex PARAFAC). The last of these shortcomings is of particular interest in relation to our method. It limits the implicated methods to describing phase relations of point sources, because other source configurations need not be limited to phase relations that are constant over frequencies. For example, this is the case for a source whose subpopulations communicate with a time delay, which results in phase relations that increase linearly with frequency (e.g. a traveling wave). A model-based method, similar to the one used in this paper, but targeted towards identifying sources whose subpopulations communicate with time delays, has been described in the same original presentation (van der Meij et al., 2015).

CONCLUSIONS

We presented a novel approach for analyzing oscillatory neuronal activity using a decomposition method that can separate overlapping sources by their patterns of between-sensor phase coupling, their spectral content, and their variable presence over trials. Unlike existing decomposition methods, it uses a plausible model of a neurobiological rhythm: a spatially distributed oscillation with energy in a range of frequencies and involving between-sensor phase relations that can vary over frequencies. Using MEG recordings we showed that this approach can separate sources that are difficult to identify using conventional analyses. Our approach also allows for analyzing task modulations of neuronal activity at the level of these separated sources, which is a powerful alternative to analyses at the sensor-level. Furthermore, we showed that our method can reveal phase-coupled oscillatory networks, which may reflect neuronal network communication. These capabilities

make our method a useful tool for investigating the role of oscillatory activity in cognition and behavior, and for untangling the many neuronal interactions that are present in electrophysiological recordings.

Chapter

5

General summary

This thesis concerned the identification, characterization and investigation of neuronal networks formed by the coupling of neuronal oscillations. This type of coupling is interesting, because it is likely to be involved in the communication between neuronal populations. This coupling may also implement the selective aspect of this communication. As such, it could be the key building block for the routing of information through the brain.

In this thesis, I developed and applied decomposition techniques that are capable of uncovering networks formed by coupling of neuronal oscillations from high dimensional arrays of coupling measures, and which allow for an analysis of their properties. Such techniques are necessary, because studying coupling in neuronal networks using existing methods (e.g. the conventional seed-based approach) is a tremendous challenge if there are no a priori hypotheses about which recording sites are likely to interact at which frequencies.

This thesis concerns two types of coupling, and for each of the types a decomposition technique was developed to uncover networks. The first type of coupling is the coupling of high frequency amplitudes to low frequency phases, which is denoted as phase-amplitude coupling (PAC). In this type of coupling, high amplitudes of the fast oscillations occur selectively at a phase of the slow oscillations, called the preferred coupling phase. The second type of coupling is the coupling of the phase of oscillations at the same frequency. I denote networks formed by such coupling as phase-coupled oscillatory networks.

In the sections that follow, I describe the main contributions of this thesis. I first describe the novel data analysis techniques that allowed for uncovering and investigating PAC networks and phase-coupled oscillatory networks. Afterwards I summarize the key results obtained with these techniques.

NOVEL DATA ANALYSIS TECHNIQUES

In **chapter 2** of this thesis I present a new decomposition technique for uncovering networks formed by PAC. This technique is a modification of an existing technique. It is useful, because (1) it is capable of revealing the spatial distribution and frequency content of overlapping PAC networks without a priori hypotheses about which sites and frequencies are involved, (2) it can reveal the origin of diversity in the preferred coupling phase over sites, and, (3) it provides for a convenient analysis of properties of these networks. Networks are extracted from 4-way arrays of PAC measures. Two dimensions of this 4-way array are spatial: one describes which sites show the high frequency amplitudes involved in the coupling (amplitude-providing sites), and the other describes which sites show the low frequency phases to which these amplitudes are coupled (phase-providing sites). The other two

dimensions are spectral: one describes the frequency content of the high frequency amplitudes (amplitude-providing frequency), and the other describes the frequency content of the low frequency phases (phase-providing frequency). Following the dimensions of this 4-way array, the technique characterizes the spatial distribution of networks by an *amplitude-providing spatial map* and a *phase-providing spatial map*, and their frequency content by an *amplitude-providing frequency profile* and a *phase-providing frequency profile*. The two spatial maps describe PAC networks by a network of sites whose low frequency phase modulates the high frequency amplitude at another network of sites. The frequency profiles describe which frequencies are involved in this coupling. An important feature of the technique is that it is capable of explaining diversity in the preferred coupling phase over all pairs of coupled sites, by phase differences in the two spatial maps. Whereas phase differences in the phase-providing spatial map reflect consistent between-site phase differences of the phase-providing oscillation, phase differences in the amplitude-providing spatial map reflects between-site time delays of amplitude bursts of the amplitude-providing oscillation. As such, phase differences in the two spatial maps can reveal temporal characteristics of the PAC networks. For example, it can distinguish between a situation in which the high frequency amplitude bursts are synchronized over sites versus a situation in which they have a temporal offset. The former situation is of interest because it can reflect coordinated windows of communication between neuronal populations that are part of a network.

In **chapter 3** of this thesis I present a new decomposition technique for uncovering phase-coupled oscillatory networks, denoted as SPACE. This technique is useful for three reasons: (1) it is capable of separating networks that overlap in space and frequency, (2) it characterizes these networks in a neurobiologically informative way, and, (3) it allows for a straightforward investigation of task modulations at the network-level. Like the technique for uncovering PAC networks, it also does not require a priori information about which sites and frequencies are likely to interact. The technique is grounded in a plausible model of a neurobiological rhythm: a spatially distributed oscillation involving multiple frequencies and frequency-specific between-site phase differences. Using this model, networks are extracted on the basis of their phase coupling patterns as a function of space, frequency, and time (trials of an experiment). Networks are obtained from a 4-way array of phase coupling measures. Two dimensions of this array are spatial, and they contain information about which sites are part of a network. One dimension is spectral, and it contains information about the frequency of the coupled oscillations. The remaining dimension is temporal, and contains information about how strongly a network is present in each trial. The model characterizes a phase-coupled oscillatory network by four parameters. The *spatial amplitude map* describes the degree to

which the different sites reflect the network. The *spatial phase maps* describe, per frequency, the average phase differences between all sites. The *frequency profile* describes which frequencies are involved in the phase coupling. Finally, the *trial profile* quantifies how strongly a network is present in each trial. The trial profiles are very useful for investigating task modulations at the level of the networks. Contrary to typical investigations of coupling at the level of site-pairs, the spatial amplitude map and the frequency-specific spatial phase maps describe phase coupling by maps at the level of individual sites. This is important, because a quantification of phase coupling at the level of sites-pairs does not directly reveal the spatial distribution of a network. Additionally, because the technique allows for frequency-specific between-site phase differences, it can characterize different network configurations. In fact, the technique characterizes networks using two different models: the *FSP model* (for Frequency Specific Phase; described above) and the *time delay model*. Whereas the FSP model places no constraint on the relationship of phase differences over frequencies, the time delay model describes phase differences over frequencies by a time delay for each site, thus producing a *spatial time-delay map*. The time delay model is a special case of the FSP model, and is most suited for a targeted analysis of networks in which between-site phase differences are the result of time delays. An example of such a network is a travelling wave, in which oscillatory activity propagates over sites. The FSP model is more suitable for exploratory analyses, in which the network configurations are unknown.

EMPIRICAL DEMONSTRATIONS AND NOVEL INSIGHTS

In **chapter 2**, I investigated networks formed by PAC in electrocorticographic (ECoG) recordings from epilepsy patients, and analyzed their spatial distribution, diversity in preferred coupling phase, and frequency diversity. These properties of PAC networks are of interest, because they could determine the flexibility of PAC as a mechanism for routing of information. To investigate these properties, I first collapsed over the dimensions of the 4-way arrays of PAC measures described in the above, and showed that PAC occurred between distant electrodes, had diverse preferred coupling phases, and involved many frequencies. Using the decomposition technique, I was able to extract the underlying networks, and investigate their properties. By doing so, I demonstrated that PAC networks were spatially distributed and widespread, and occurred between many frequencies. Additionally, the spatial distributions of the phase-providing oscillations were more widespread than that of the amplitude-providing oscillations. Importantly, I showed that diversity in the preferred coupling phase of PAC could mostly be attributed to between-electrode phase differences of the phase-providing oscillation. This means that the phase-providing oscillations were coupled at many different phases, and that the high frequency amplitude bursts

at the amplitude-providing electrodes occurred closely together in time. These temporal characteristics, together with the spatial distribution, phase diversity, and frequency diversity of PAC networks, suggest that PAC could be a flexible mechanism for routing information through neuronal networks.

In **chapter 3**, I presented a decomposition technique for uncovering phase-coupled oscillatory networks. To show that the technique is capable of uncovering networks with interesting between-site phase differences, I applied it to ECoG recordings from epilepsy patients, and presented several example networks, of which some described traveling waves. I additionally validated the technique using simulated data, and showed that it was capable of recovering networks in the context of neurobiologically realistic noise. This shows that the technique can be a useful and reliable tool for the characterization and analysis of phase-coupled oscillatory networks.

In **chapter 4**, I demonstrated the usefulness of the decomposition technique for uncovering phase-coupled oscillatory networks as an approach for analyzing extracranial brain signals, and investigating their task modulations. By decomposing magnetoencephalography (MEG) recordings during a cued tactile detection task, I showed that the technique was capable of separating and characterizing the many spatially and spectrally overlapping sensor-level activity patterns generated by different sources. Importantly, using conventional analysis approaches, these activity patterns were very difficult to resolve. The technique separated these overlapping patterns on the basis of their different spatial maps, spectral content, and degree of involvement in the different trials. Among the extracted sensor-level activity patterns were those that were generated by distributed sources, reflecting phase-coupled oscillatory networks, but also those that were more accurately described by point sources, showing dipolar patterns of sensor-level phase coupling. Because the technique quantifies the trial-specific strength of a network or point source in its trial profiles, it was possible to analyze task modulations of their activity. This allowed me to reveal that there were many overlapping alpha and beta networks and point sources, whose activity was suppressed or enhanced with attention and performance on the task, both in task-relevant and task-irrelevant regions. This is interesting, because conventional analyses of alpha and beta activity at these locations describe the average activity of such sources, which are predominantly reported to be only suppressed in relevant regions, and enhanced in irrelevant regions. Using the decomposition technique, I was able to separate the underlying sources, and show that the situation is much more complex. As such, I showed that the technique is not only useful for uncovering and characterizing phase-coupled networks, but also for revealing the different sources that produce extracranial brain signals, and for investigating their task modulation.

CONCLUDING REMARKS

Neuronal networks formed by the coupling of neuronal oscillations are thought to serve a key role in routing information through the brain. Using conventional approaches, it is tremendously difficult to find these networks in the high dimensional arrays that describe this coupling. This thesis provides techniques that identify and characterize such networks, and they do so in a neurobiologically plausible way. The application of such techniques will likely increase in the nearby future, as advances in recording techniques result in an ever increasing number of signals that can be recorded at the same time. Conventional techniques are ill-suited for these high dimensional data, and methodological advances such as the ones in this thesis are essential for their analysis. This thesis also identified several properties of oscillatory networks that makes them suitable for the flexible routing of information. However, much is still unclear about how the brain achieves this, and uncovering the precise mechanisms is an important challenge for future research.

Appendix

Bibliography

Nederlandse samenvatting

Acknowledgements

Publication list

About the author

Donders series

BIBLIOGRAPHY

- Akam T, Kullmann DM (2010) Oscillations and Filtering Networks Support Flexible Routing of Information. *Neuron* 67:308-320.
- Akam T, Kullmann DM (2014) Oscillatory multiplexing of population codes for selective communication in the mammalian brain. *Nat Rev Neurosci* 15:111-122.
- Amzica F, Steriade M (1997) The K-complex: Its slow (<1-Hz) rhythmicity and relation to delta waves. *Neurology* 49:952-959.
- Anemuller J, Sejnowski TJ, Makeig S (2003) Complex independent component analysis of frequency-domain electroencephalographic data. *Neural Netw* 16:1311-1323.
- Axmacher N, Henseler MM, Jensen O, Weinreich I, Elger CE, Fell J (2010) Cross-frequency coupling supports multi-item working memory in the human hippocampus. *Proc Natl Acad Sci U S A* 107:3228-3233.
- Beckmann CF, Smith SM (2005) Tensorial extensions of independent component analysis for multisubject FMRI analysis. *Neuroimage* 25:294-311.
- Beckmann CF, DeLuca M, Devlin JT, Smith SM (2005) Investigations into resting-state connectivity using independent component analysis. *Philos Trans R Soc B-Biol Sci* 360:1001-1013.
- Bell AJ, Sejnowski TJ (1995) AN INFORMATION MAXIMIZATION APPROACH TO BLIND SEPARATION AND BLIND DECONVOLUTION. *Neural Comput* 7:1129-1159.
- Bernasconi C, Konig P (1999) On the directionality of cortical interactions studied by structural analysis of electrophysiological recordings. *Biol Cybern* 81:199-210.
- Bishop GH (1933) Cyclic changes in excitability of the optic pathway of the rabbit. *Am J Physiol* 103:13-224.
- Biswal BB, VanKylen J, Hyde JS (1997) Simultaneous assessment of flow and BOLD signals in resting-state functional connectivity maps. *NMR Biomed* 10:165-170.
- Borgers C, Kopell N (2003) Synchronization in networks of excitatory and inhibitory neurons with sparse, random connectivity. *Neural Comput* 15:509-538.
- Borgers C, Kopell NJ (2008) Gamma oscillations and stimulus selection. *Neural Comput* 20:383-414.
- Breakspear M, Williams LM, Stam CJ (2004) A novel method for the topographic analysis of neural activity reveals formation and dissolution of 'dynamic cell assemblies'. *J Comput Neurosci* 16:49-68.
- Bro R (1998) Multi-way Analysis in the Food Industry. Models, Algorithms, and Applications. In: Universiteit van Amsterdam.
- Brookes MJ, Woolrich M, Luckhoo H, Price D, Hale JR, Stephenson MC, Barnes GR, Smith SM, Morris PG (2011) Investigating the electrophysiological basis of resting state networks using magnetoencephalography. *Proc Natl Acad Sci U S A* 108:16783-16788.
- Brookes MJ, O'Neill GC, Hall EL, Woolrich MW, Baker A, Corner SP, Robson SE, Morris PG, Barnes GR (2014) Measuring temporal, spectral and spatial changes in electrophysiological brain network connectivity. *Neuroimage* 91:282-299.
- Brovelli A, Ding MZ, Ledberg A, Chen YH, Nakamura R, Bressler SL (2004) Beta oscillations in a large-scale sensorimotor cortical network: Directional influences revealed by Granger causality. *Proc Natl Acad Sci U S A* 101:9849-9854.
- Brown E, Moehlis J, Holmes P (2004) On the phase reduction and response dynamics of neural oscillator populations. *Neural Comput* 16:673-715.
- Bruni A, Eckhorn R (2004) Task-related coupling from high-to low-frequency signals among visual cortical areas in human subdural recordings. *Int J Psychophysiol* 51:97-116.
- Burke JF, Zaghloul KA, Jacobs J, Williams RB, Sperling MR, Sharan AD, Kahana MJ (2013) Synchronous and Asynchronous Theta and Gamma Activity during Episodic Memory Formation. *J Neurosci* 33:292-304.
- Buschman TJ, Miller EK (2007) Top-down versus bottom-up control of attention in the prefrontal and posterior parietal cortices. *Science* 315:1860-1862.
- Buzsaki G, Draguhn A (2004) Neuronal oscillations in cortical networks. *Science* 304:1926-1929.
- Buzsaki G, Anastassiou CA, Koch C (2012) The origin of extracellular fields and currents - EEG, ECoG, LFP and spikes. *Nat Rev Neurosci* 13:407-420.
- Cannon J, McCarthy MM, Lee S, Lee J, Borgers C, Whittington MA, Kopell N (2014) Neurosystems: brain rhythms and cognitive processing. *Eur J Neurosci* 39:705-719.
- Canolty RT, Knight RT (2010) The functional role of cross-frequency coupling. *Trends in cognitive sciences* 14:506-515.
- Canolty RT, Ganguly K, Carmen JM (2012a) Task-Dependent Changes in Cross-Level Coupling between Single Neurons and Oscillatory Activity in Multiscale Networks. *PLoS Comput Biol* 8.
- Canolty RT, Cadieu CF, Koepsell K, Ganguly K, Knight RT, Carmen JM (2012b) Detecting event-related changes of multivariate phase coupling in dynamic brain networks. *J Neurophysiol* 107:2020-2031.
- Canolty RT, Ganguly K, Kennerley SW, Cadieu CF, Koepsell K, Wallis JD, Carmen JM (2010) Oscillatory phase coupling coordinates anatomically dispersed functional cell assemblies. *Proc Natl Acad Sci U S A* 107:17356-17361.
- Canolty RT, Edwards E, Dalal SS, Soltani M, Nagarajan SS, Kirsch HE, Berger MS, Barbaro NM, Knight RT

- (2006) High gamma power is phase-locked to theta oscillations in human neocortex. *Science* 313:1626-1628.
- Carrol JD, Chang J (1970) Analysis of individual differences in multidimensional scaling via an N-way generalization of "Eckart-Young" decomposition. *Psychometrika* 35.
- Cash SS, Halgren E, Dehghani N, Rossetti AO, Thesen T, Wang C, Devinsky O, Kuzniecky R, Doyle W, Madsen JR, Bromfield E, Eross L, Halasz P, Karmos G, Cserecsa R, Wittner L, Ulbert I (2009) The Human K-Complex Represents an Isolated Cortical Down-State. *Science* 324:1084-1087.
- Chapman RM, McCrary JW (1995) EP COMPONENT IDENTIFICATION AND MEASUREMENT BY PRINCIPAL COMPONENTS-ANALYSIS. *Brain Cogn* 27:288-310.
- Chrobak JJ, Buzsaki G (1998) Gamma oscillations in the entorhinal cortex of the freely behaving rat. *J Neurosci* 18:388-398.
- Cohen MX (2008) Assessing transient cross-frequency coupling in EEG data. *J Neurosci Methods* 168:494-499.
- Cohen MX, Axmacher N, Lenartz D, Elger CE, Sturm V, Schlaepfer TE (2009) Good Vibrations: Cross-frequency Coupling in the Human Nucleus Accumbens during Reward Processing. *J Cogn Neurosci* 21:875-889.
- de Pasquale F, Della Penna S, Snyder AZ, Marzetti L, Pizzella V, Romani GL, Corbetta M (2012) A Cortical Core for Dynamic Integration of Functional Networks in the Resting Human Brain. *Neuron* 74:753-764.
- de Pasquale F, Della Penna S, Snyder AZ, Lewis C, Mantini D, Marzetti L, Belardinelli P, Ciancetta L, Pizzella V, Romani GL, Corbetta M (2010) Temporal dynamics of spontaneous MEG activity in brain networks. *Proc Natl Acad Sci U S A* 107:6040-6045.
- Debener S, Ullsperger M, Siegel M, Fiehler K, von Cramon DY, Engel AK (2005) Trial-by-trial coupling of concurrent electroencephalogram and functional magnetic resonance imaging identifies the dynamics of performance monitoring. *J Neurosci* 25:11730-11737.
- Deco G, Corbetta M (2011) The Dynamical Balance of the Brain at Rest. *Neuroscientist* 17:107-123.
- Destexhe A, Rudolph M, Pare D (2003) The high-conductance state of neocortical neurons in vivo. *Nat Rev Neurosci* 4:739-751.
- Donoghue JP, Sanes JN, Hatsopoulos NG, Gaal G (1998) Neural discharge and local field potential oscillations in primate motor cortex during voluntary movements. *J Neurophysiol* 79:159-173.
- Engel AK, Fries P (2010) Beta-band oscillations - signalling the status quo? *Curr Opin Neurobiol* 20:156-165.
- Engel AK, Gerloff C, Hilgetag CC, Nolte G (2013) Intrinsic Coupling Modes: Multiscale Interactions in Ongoing Brain Activity. *Neuron* 80:867-886.
- Ermentrout GB, Kopell N (1990) OSCILLATOR DEATH IN SYSTEMS OF COUPLED NEURAL OSCILLATORS. *SIAM J Appl Math* 50:125-146.
- Fox MD, Snyder AZ, Vincent JL, Corbetta M, Van Essen DC, Raichle ME (2005) The human brain is intrinsically organized into dynamic, anticorrelated functional networks. *Proc Natl Acad Sci U S A* 102:9673-9678.
- Foxe JJ, Simpson GV, Ahlfors SP (1998) Parieto-occipital similar to 10 Hz activity reflects anticipatory state of visual attention mechanisms. *Neuroreport* 9:3929-3933.
- Fries P (2005) A mechanism for cognitive dynamics: neuronal communication through neuronal coherence. *Trends Cogn Sci* 9:474-480.
- Fries P (2009) Neuronal Gamma-Band Synchronization as a Fundamental Process in Cortical Computation. In: *Annual Review of Neuroscience*, pp 209-224. Palo Alto: Annual Reviews.
- Gould IC, Rushworth MF, Nobre AC (2011) Indexing the graded allocation of visuospatial attention using anticipatory alpha oscillations. *J Neurophysiol* 105:1318-1326.
- Gregoriou GG, Gotts SJ, Zhou HH, Desimone R (2009) High-Frequency, Long-Range Coupling Between Prefrontal and Visual Cortex During Attention. *Science* 324:1207-1210.
- Gross J, Schmitz F, Schnitzler I, Kessler K, Shapiro K, Hommel B, Schnitzler A (2004) Modulation of long-range neural synchrony reflects temporal limitations of visual attention in humans. *Proc Natl Acad Sci U S A* 101:13050-13055.
- Haegens S, Handel BF, Jensen O (2011) Top-Down Controlled Alpha Band Activity in Somatosensory Areas Determines Behavioral Performance in a Discrimination Task. *J Neurosci* 31:5197-5204.
- Haegens S, Luther L, Jensen O (2012) Somatosensory Anticipatory Alpha Activity Increases to Suppress Distracting Input. *J Cogn Neurosci* 24:677-685.
- Haider B, McCormick DA (2009) Rapid Neocortical Dynamics: Cellular and Network Mechanisms. *Neuron* 62:171-189.
- Haider B, Duque A, Hasenstaub AR, McCormick DA (2006) Neocortical network activity in vivo is generated through a dynamic balance of excitation and inhibition. *J Neurosci* 26:4535-4545.
- Haider B, Duque A, Hasenstaub AR, Yu YG, McCormick DA (2007) Enhancement of visual responsiveness by spontaneous local network activity in vivo. *J Neurophysiol* 97:4186-4202.
- Halgren E, Boujon C, Clarke J, Wang C (2002) Rapid distributed fronto-parieto-occipital processing stages during working memory in humans. *Cereb Cortex* 12:710-728.
- Harshman R (1972) PARAFAC2 - EXTENSIONS OF A PROCEDURE FOR EXPLANATORY FACTOR-ANALYSIS AND MULTIDIMENSIONAL SCALING. *J Acoust Soc Am* 51:111-8.
- Harshman RA (1970) Foundations of the PARAFAC procedure: model and conditions for an 'explanatory' multi-mode factor analysis. UCLA Working Papers in Phonetics 16:1-84.
- Hasenstaub A, Shu YS, Haider B, Kraushaar U, Duque

- A, McCormick DA (2005) Inhibitory postsynaptic potentials carry synchronized frequency information in active cortical networks. *Neuron* 47:423-435.
- He BJ, Zempel JM, Snyder AZ, Raichle ME (2010) The temporal structures and functional significance of scale-free brain activity. *Neuron* 66:353-369.
- He BYJ, Snyder AZ, Zempel JM, Smyth MD, Raichle ME (2008) Electrophysiological correlates of the brain's intrinsic large-scale functional architecture. *Proc Natl Acad Sci U S A* 105:16039-16044.
- Hipp JF, Engel AK, Siegel M (2011) Oscillatory Synchronization in Large-Scale Cortical Networks Predicts Perception. *Neuron* 69:387-396.
- Hipp JF, Hawellek DJ, Corbetta M, Siegel M, Engel AK (2012) Large-scale cortical correlation structure of spontaneous oscillatory activity. *Nat Neurosci* 15:884-U110.
- Ho N, Destexhe A (2000) Synaptic background activity enhances the responsiveness of neocortical pyramidal neurons. *J Neurophysiol* 84:1488-1496.
- Honey CJ, Sporns O, Cammoun L, Gigandet X, Thiran JP, Meuli R, Hagmann P (2009) Predicting human resting-state functional connectivity from structural connectivity. *Proc Natl Acad Sci U S A* 106:2035-2040.
- Hoppensteadt FC, Izhikevich EM (1997) Weakly connected neural networks: Springer New York.
- Hyvarinen A, Ramkumar P, Parkkonen L, Hari R (2010) Independent component analysis of short-time Fourier transforms for spontaneous EEG/MEG analysis. *Neuroimage* 49:257-271.
- Jacobs J, Kahana MJ (2009) Neural representations of individual stimuli in humans revealed by gamma-band electrocorticographic activity. *J Neurosci* 29:10203-10214.
- Jensen O, Colgin LL (2007) Cross-frequency coupling between neuronal oscillations. *Trends Cogn Sci* 11:267-269.
- Jensen O, Mazaheri A (2010) Shaping functional architecture by oscillatory alpha activity: gating by inhibition. *Frontiers in Human Neuroscience* 4:8.
- Jensen O, Gelfand J, Kounios J, Lisman JE (2002) Oscillations in the alpha band (9-12 Hz) increase with memory load during retention in a short-term memory task. *Cereb Cortex* 12:877-882.
- Jensen O, Gips B, Bergmann TO, Bonnefond M (2014) Temporal coding organized by coupled alpha and gamma oscillations prioritize visual processing. *Trends Neurosci* 37:357-369.
- Jones SR, Kerr CE, Wan QA, Pritchett DL, Hamalainen M, Moore CI (2010) Cued Spatial Attention Drives Functionally Relevant Modulation of the Mu Rhythm in Primary Somatosensory Cortex. *J Neurosci* 30:13760-13765.
- Jurkiewicz MT, Gaetz WC, Bostan AC, Cheyne D (2006) Post-movement beta rebound is generated in motor cortex: Evidence from neuromagnetic recordings. *Neuroimage* 32:1281-1289.
- Kaminski M, Ding MZ, Truccolo WA, Bressler SL (2001) Evaluating causal relations in neural systems: Granger causality, directed transfer function and statistical assessment of significance. *Biol Cybern* 85:145-157.
- Kiers HAL, Ten Berge JMF, Bro R (1999) PARAFAC2 - Part I. A direct fitting algorithm for the PARAFAC2 model. *Journal of Chemometrics* 13:275-294.
- Kopell N, Ermentrout GB, Whittington MA, Traub RD (2000) Gamma rhythms and beta rhythms have different synchronization properties. *Proc Natl Acad Sci U S A* 97:1867-1872.
- Kuramoto Y (1984) Chemical oscillations, waves, and turbulence: Springer-Verlag, New York.
- Kuramoto Y (1997) Phase- and center-manifold reductions for large populations of coupled oscillators with application to non-locally coupled systems. *Int J Bifurcation Chaos* 7:789-805.
- Lachaux JP, Rodriguez E, Martinerie J, Varela FJ (1999) Measuring phase synchrony in brain signals. *Hum Brain Mapp* 8:194-208.
- Lakatos P, Karmos G, Mehta AD, Ulbert I, Schroeder CE (2008) Entrainment of neuronal oscillations as a mechanism of attentional selection. *Science* 320:110-113.
- Lakatos P, Shah AS, Knuth KH, Ulbert I, Karmos G, Schroeder CE (2005) An oscillatory hierarchy controlling neuronal excitability and stimulus processing in the auditory cortex. *J Neurophysiol* 94:1904-1911.
- Lisman JE, Jensen O (2013) The Theta-Gamma Neural Code. *Neuron* 77:1002-1016.
- Lobier M, Siebenhuhner F, Palva S, Palva JM (2014) Phase transfer entropy: A novel phase-based measure for directed connectivity in networks coupled by oscillatory interactions. *Neuroimage* 85:853-872.
- Makeig S, Jung TP, Bell AJ, Ghahremani D, Sejnowski TJ (1997) Blind separation of auditory event-related brain responses into independent components. *Proc Natl Acad Sci U S A* 94:10979-10984.
- Maris E (2012) Statistical testing in electrophysiological studies. *Psychophysiology* 49:549-565.
- Maris E, Oostenveld R (2007) Nonparametric statistical testing of EEG- and MEG-data. *J Neurosci Methods* 164:177-190.
- Maris E, van Vugt M, Kahana M (2011) Spatially distributed patterns of oscillatory coupling between high-frequency amplitudes and low-frequency phases in human iEEG. *Neuroimage* 54:836-850.
- Maris E, Womelsdorf T, Desimone R, Fries P (2013) Rhythmic neuronal synchronization in visual cortex entails spatial phase relation diversity that is modulated by stimulation and attention. *Neuroimage* 74:99-116.
- Massimini M, Huber R, Ferrarelli F, Hill S, Tononi G (2004) The sleep slow oscillation as a traveling wave. *J Neurosci* 24:6862-6870.
- Michel CM, Murray MM, Lantz G, Gonzalez S, Spinelli L, de Peralta RG (2004) EEG source imaging. *Clin Neurophysiol* 115:2195-2222.
- Miller KJ, Foster BL, Honey CJ (2012a) Does rhythmic entrainment represent a generalized mechanism for

- organizing computation in the brain? *Front Comput Neurosci* 6.
- Miller KJ, Sorensen LB, Ojemann JG, den Nijs M (2009) Power-Law Scaling in the Brain Surface Electric Potential. *PLoS Comput Biol* 5.
- Miller KJ, Schalk G, Fetz EE, den Nijs M, Ojemann JG, Rao RPN (2010a) Cortical activity during motor execution, motor imagery, and imagery-based online feedback. *Proc Natl Acad Sci U S A* 107:4430-4435.
- Miller KJ, Hermes D, Honey CJ, Hebb AO, Ramsey NF, Knight RT, Ojemann JG, Fetz EE (2012b) Human Motor Cortical Activity Is Selectively Phase-Entrained on Underlying Rhythms. *PLoS Comput Biol* 8.
- Miller KJ, Hermes D, Honey CJ, Sharma M, Rao RP, den Nijs M, Fetz EE, Sejnowski TJ, Hebb AO, Ojemann JG, Makeig S, Leuthardt EC (2010b) Dynamic modulation of local population activity by rhythm phase in human occipital cortex during a visual search task. *Front Hum Neurosci* 4:197.
- Miwakeichi F, Martinez-Montes E, Valdes-Sosa PA, Nishiyama N, Mizuhara H, Yamaguchi Y (2004) Decomposing EEG data into space-time-frequency components using Parallel Factor Analysis. *Neuroimage* 22:1035-1045.
- Mormann F, Lehnertz K, David P, Elger CE (2000) Mean phase coherence as a measure for phase synchronization and its application to the EEG of epilepsy patients. *Physica D* 144:358-369.
- Mormann F, Fell J, Axmacher N, Weber B, Lehnertz K, Elger CE, Fernandez G (2005) Phase/amplitude reset and theta-gamma interaction in the human medial temporal lobe during a continuous word recognition memory task. *Hippocampus* 15:890-900.
- Morup M, Hansen LK, Herrmann CS, Parnas J, Arnfred SM (2006) Parallel Factor Analysis as an exploratory tool for wavelet transformed event-related EEG. *Neuroimage* 29:938-947.
- Morup M, Hansen LK, Arnfred SM, Lim LH, Madsen KH (2008) Shift-invariant multilinear decomposition of neuroimaging data. *Neuroimage* 42:1439-1450.
- Nolte G (2003) The magnetic lead field theorem in the quasi-static approximation and its use for magnetoencephalography forward calculation in realistic volume conductors. *Phys Med Biol* 48:3637-3652.
- Nolte G, Bai O, Wheaton L, Mari Z, Vorbach S, Hallett M (2004) Identifying true brain interaction from EEG data using the imaginary part of coherency. *Clin Neurophysiol* 115:2292-2307.
- Nolte G, Ziehe A, Nikulin VV, Schlogl A, Kramer N, Brismar T, Muller KR (2008) Robustly estimating the flow direction of information in complex physical systems. *Phys Rev Lett* 100.
- Nowak LG, Sanchez-Vives MV, McCormick DA (1997) Influence of low and high frequency inputs on spike timing in visual cortical neurons. *Cereb Cortex* 7:487-501.
- Nunez PL, Wingeier BM, Silberstein RB (2001) Spatial-temporal structures of human alpha rhythms: Theory, microcurrent sources, multiscale measurements, and global binding of local networks. *Hum Brain Mapp* 13:125-164.
- Oostenveld R, Fries P, Maris E, Schoffelen J-M (2011) FieldTrip: Open Source Software for Advanced Analysis of MEG, EEG, and Invasive Electrophysiological Data. *Computational Intelligence and Neuroscience* 2011.
- Osipova D, Hermes D, Jensen O (2008) Gamma Power Is Phase-Locked to Posterior Alpha Activity. *PLoS One* 3.
- Palva JM, Palva S, Kaila K (2005) Phase synchrony among neuronal oscillations in the human cortex. *J Neurosci* 25:3962-3972.
- Palva S, Palva JM (2007) New vistas for alpha-frequency band oscillations. *Trends Neurosci* 30:150-158.
- Palva S, Palva JM (2012) Discovering oscillatory interaction networks with M/EEG: challenges and breakthroughs. *Trends in cognitive sciences* 16:219-230.
- Pascualmarqui RD, Michel CM, Lehmann D (1994) LOW-RESOLUTION ELECTROMAGNETIC TOMOGRAPHY - A NEW METHOD FOR LOCALIZING ELECTRICAL ACTIVITY IN THE BRAIN. *Int J Psychophysiol* 18:49-65.
- Penny WD, Duzel E, Miller KJ, Ojemann JG (2008) Testing for nested oscillation. *J Neurosci Methods* 174:50-61.
- Penny WD, Litvak V, Fuentemilla L, Duzel E, Friston KJ (2009) Dynamic Causal Models for phase coupling. *J Neurosci Methods* 183:19-30.
- Percival D, Walden A (1993) Spectral analysis for physical applications: multitaper and conventional univariate techniques, 583 pp. In: Cambridge Univ. Press, New York.
- Pesaran B, Nelson MJ, Andersen RA (2008) Free choice activates a decision circuit between frontal and parietal cortex. *Nature* 453:406-U461.
- Pfurtscheller G, Neuper C, Andrew C, Edlinger G (1997) Foot and hand area mu rhythms. *Int J Psychophysiol* 26:121-135.
- Pollok B, Gross J, Muller K, Aschersleben G, Schnitzler A (2005) The cerebral oscillatory network associated with auditorily paced finger movements. *Neuroimage* 24:646-655.
- Posner MI (1980) ORIENTING OF ATTENTION. *Quarterly Journal of Experimental Psychology* 32:3-25.
- Raghavachari S, Lisman JE, Tully M, Madsen JR, Bromfield EB, Kahana MJ (2006) Theta oscillations in human cortex during a working-memory task: evidence for local generators. *J Neurophysiol* 95:1630-1638.
- Raichle ME, MacLeod AM, Snyder AZ, Powers WJ, Gusnard DA, Shulman GL (2001) A default mode of brain function. *Proc Natl Acad Sci U S A* 98:676-682.
- Rihs TA, Michel CM, Thut G (2007) Mechanisms of selective inhibition in visual spatial attention are indexed by alpha-band EEG synchronization. *Eur J Neurosci* 25:603-610.

- Rizzuto DS, Madsen JR, Bromfield EB, Schulze-Bonhage A, Seelig D, Aschenbrenner-Scheibe R, Kahana MJ (2003) Reset of human neocortical oscillations during a working memory task. *Proc Natl Acad Sci U S A* 100:7931-7936.
- Rosenberg JR, Halliday DM, Breeze P, Conway BA (1998) Identification of patterns of neuronal connectivity-partial spectra, partial coherence, and neuronal interactions. *J Neurosci Methods* 83:57-72.
- Rubino D, Robbins KA, Hatsopoulos NG (2006) Propagating waves mediate information transfer in the motor cortex. *Nat Neurosci* 9:1549-1557.
- Sanchez-Vives MV, McCormick DA (2000) Cellular and network mechanisms of rhythmic recurrent activity in neocortex. *Nat Neurosci* 3:1027-1034.
- Schack B, Vath N, Petsche H, Geissler HG, Moller E (2002) Phase-coupling of theta-gamma EEG rhythms during short-term memory processing. *Int J Psychophysiol* 44:143-163.
- Schnitzler A, Gross J (2005) Normal and pathological oscillatory communication in the brain. *Nat Rev Neurosci* 6:285-296.
- Schreiber T (2000) Measuring information transfer. *Phys Rev Lett* 85:461-464.
- Schyms PG, Thut G, Gross J (2011) Cracking the Code of Oscillatory Activity. *PLoS Biol* 9:8.
- Shu YS, Hasenstaub A, Badoval M, Bal T, McCormick DA (2003) Barrages of synaptic activity control the gain and sensitivity of cortical neurons. *J Neurosci* 23:10388-10401.
- Sidiropoulos ND, Giannakis GB, Bro R (2000) Blind PARAFAC receivers for DS-CDMA systems. *IEEE T Signal Proces* 48:810-823.
- Siegel M, Donner TH, Engel AK (2012) Spectral fingerprints of large-scale neuronal interactions. *Nat Rev Neurosci* 13:121-134.
- Siegel M, Donner TH, Oostenveld R, Fries P, Engel AK (2008) Neuronal Synchronization along the Dorsal Visual Pathway Reflects the Focus of Spatial Attention. *Neuron* 60:709-719.
- Singer W (1999) Neuronal synchrony: A versatile code for the definition of relations? *Neuron* 24:49-65.
- Singer W, Gray CM (1995) VISUAL FEATURE INTEGRATION AND THE TEMPORAL CORRELATION HYPOTHESIS. *Annu Rev Neurosci* 18:555-586.
- Sirota A, Montgomery S, Fujisawa S, Isomura Y, Zugaro M, Buzsaki G (2008) Entrainment of neocortical neurons and gamma oscillations by the hippocampal theta rhythm. *Neuron* 60:683-697.
- Smith SM, Fox PT, Miller KL, Glahn DC, Fox PM, Mackay CE, Filippini N, Watkins KE, Toro R, Laird AR, Beckmann CF (2009) Correspondence of the brain's functional architecture during activation and rest. *Proc Natl Acad Sci U S A* 106:13040-13045.
- Steriade M, Nuñez A, Amzica F (1993) A novel slow (less-than-1 Hz) oscillation of neocortical neurons in vivo: depolarizing and hyperpolarizing components. *J Neurosci* 13:3252-3265.
- Steriade M, Timofeev I, Grenier F (2001) Natural waking and sleep states: A view from inside neocortical neurons. *J Neurophysiol* 85:1969-1985.
- Sternberg S (1966) High-speed scanning in human memory. *Science* 153:652-654.
- Suffczynski P, Kalitzin S, Pfurtscheller G, da Silva FHL (2001) Computational model of thalamo-cortical networks: dynamical control of alpha rhythms in relation to focal attention. *Int J Psychophysiol* 43:25-40.
- Talairach J, Tournoux P (1988) Co-planar stereotaxic atlas of the human brain : 3-dimensional proportional system : an approach to cerebral imaging. Stuttgart: Georg Thieme.
- Thut G, Nietzel A, Brandt SA, Pascual-Leone A (2006) alpha-Band electroencephalographic activity over occipital cortex indexes visuospatial attention bias and predicts visual target detection. *J Neurosci* 26:9494-9502.
- Tiesinga P, Fellous JM, Sejnowski TJ (2008) Regulation of spike timing in visual cortical circuits. *Nat Rev Neurosci* 9:97-109.
- Tort ABL, Kramer MA, Thorn C, Gibson DJ, Kubota Y, Graybiel AM, Kopell NJ (2008) Dynamic cross-frequency couplings of local field potential oscillations in rat striatum and hippocampus during performance of a T-maze task. *Proc Natl Acad Sci U S A* 105:20517-20522.
- van der Meij R, Kahana M, Maris E (2012) Phase-Amplitude Coupling in Human Electrocorticography Is Spatially Distributed and Phase Diverse. *J Neurosci* 32:111-123.
- van der Meij R, Jacobs J, Maris E (2015) Uncovering Phase-Coupled Oscillatory Networks in Electrophysiological Data. *Hum Brain Mapp*.
- van Ede F, Jensen O, Maris E (2010) Tactile expectation modulates pre-stimulus beta-band oscillations in human sensorimotor cortex. *Neuroimage* 51:867-876.
- van Ede F, Koster M, Maris E (2012) Beyond establishing involvement: quantifying the contribution of anticipatory alpha- and beta-band suppression to perceptual improvement with attention. *J Neurophysiol* 108:2352-2362.
- van Ede F, de Lange F, Jensen O, Maris E (2011) Orienting Attention to an Upcoming Tactile Event Involves a Spatially and Temporally Specific Modulation of Sensorimotor Alpha- and Beta-Band Oscillations. *J Neurosci* 31:2016-2024.
- van Vugt MK, Schulze-Bonhage A, Litt B, Brandt A, Kahana MJ (2010) Hippocampal gamma oscillations increase with memory load. *J Neurosci* 30:2694-2699.
- Vincent JL, Patel GH, Fox MD, Snyder AZ, Baker JT, Van Essen DC, Zempel JM, Snyder LH, Corbetta M, Raichle ME (2007) Intrinsic functional architecture in the anaesthetized monkey brain. *Nature* 447:83-U84.
- Vinck M, van Wingerden M, Womelsdorf T, Fries P, Pennartz CMA (2010) The pairwise phase consistency: A bias-free measure of rhythmic neuronal synchronization. *Neuroimage* 51:112-122.

- Vogels TP, Abbott LF (2009) Gating multiple signals through detailed balance of excitation and inhibition in spiking networks. *Nat Neurosci* 12:483-491.
- Volgushev M, Chauvette S, Mukovski M, Timofeev I (2006) Precise long-range synchronization of activity and silence in neocortical neurons during slow-wave sleep. *J Neurosci* 26:5665-5672.
- von Stein A, Sarnthein J (2000) Different frequencies for different scales of cortical integration: from local gamma to long range alpha/theta synchronization. *Int J Psychophysiol* 38:301-313.
- von Stein A, Chiang C, Konig P (2000) Top-down processing mediated by interareal synchronization. *Proc Natl Acad Sci U S A* 97:14748-14753.
- Voytek B, Canolty RT, Shestyuk A, Crone N, Parvizi J, Knight RT (2010) Shifts in gamma phase-amplitude coupling frequency from theta to alpha over posterior cortex during visual tasks. *Frontiers in Human Neuroscience* 4:12.
- Wang XJ (2010) Neurophysiological and Computational Principles of Cortical Rhythms in Cognition. *Physiol Rev* 90:1195-1268.
- Welch PD (1967) The use of fast Fourier transform for the estimation of power spectra: A method based on time averaging over short, modified periodograms. *Audio and Electroacoustics, IEEE Transactions on* 15:70-73.
- Whittington MA, Traub RD, Kopell N, Ermentrout B, Buhl EH (2000) Inhibition-based rhythms: experimental and mathematical observations on network dynamics. *Int J Psychophysiol* 38:315-336.
- Womelsdorf T, Schöffelen JM, Oostenveld R, Singer W, Desimone R, Engel AK, Fries P (2007) Modulation of neuronal interactions through neuronal synchronization. *Science* 316:1609-1612.
- Woolrich MW, Baker A, Luckhoo H, Mohseni H, Barnes G, Brookes M, Rezek I (2013) Dynamic state allocation for MEG source reconstruction. *Neuroimage* 77:77-92.
- Worden MS, Foxe JJ, Wang N, Simpson GV (2000) Anticipatory biasing of visuospatial attention indexed by retinotopically specific alpha-band electroencephalography increases over occipital cortex. *J Neurosci* 20:art. no.-RC63.

NEDERLANDSE SAMENVATTING

Dit proefschrift betrof de identificatie, karakterisering en het onderzoek van neuronale netwerken die worden gevormd door de koppeling van neuronale oscillaties. Dit type koppeling is interessant, want het speelt waarschijnlijk een rol in de communicatie tussen neuronale populaties. Dit type koppeling zou ook het selectieve aspect van deze communicatie kunnen implementeren. Zodoende zou het een fundamentele bouwsteen kunnen vormen voor het routeren van informatie door het brein.

In dit proefschrift heb ik ontbindingstechnieken ontwikkeld en toegepast die in staat zijn netwerken bloot te leggen die gevormd worden door de koppeling van neuronale oscillaties. Deze technieken zijn in staat dit te doen in hoog dimensionale getalstructuren van koppelingsmaten, en maken het mogelijk om eigenschappen van deze netwerken te analyseren. Dergelijke technieken zijn nodig, omdat het bestuderen van neuronale netwerken met bestaande methoden (bijv. conventionele selectie gebaseerde methodiek) een enorme uitdaging is wanneer er geen *a priori* hypotheses zijn over welke meetlocaties interactueren op welke frequenties.

Dit proefschrift betreft twee typen van koppeling, en voor elk van deze typen heb ik een ontbindingstechniek ontwikkeld om netwerken bloot te leggen. Het eerste type koppeling is een koppeling tussen hoge frequentie amplitudes en lage frequentie fasen, ook wel fase-amplitude koppeling (FAK) genoemd. Bij dit type koppeling komen de hoge amplitudes van de snelle oscillatie selectief voor op een bepaalde fase van de trage oscillaties, ook wel de voorkeursfase genoemd. Het tweede type koppeling is een koppeling tussen de fasen van oscillaties van dezelfde frequentie. Netwerken gevormd door dit type koppeling duid ik aan met fasegekoppelde oscillatoire netwerken.

In de secties die volgen, beschrijf ik de belangrijkste contributies van dit proefschrift. Eerst beschrijf ik de nieuwe data analyse technieken die het mogelijk maken FAK netwerken en fasegekoppelde oscillatoire netwerken bloot te leggen. Daarna vat ik de hoofdbevindingen samen die verkregen zijn met behulp van deze technieken.

Nieuwe data analysetechnieken

In **hoofdstuk 2** van dit proefschrift presenteert ik een nieuwe ontbindingstechniek voor het blootleggen van netwerken gevormd door FAK. Deze techniek is een aanpassing van een bestaande techniek. De techniek is nuttig, want (1) het is in staat de spatiële verdeling en de frequentie inhoud van overlappende FAK netwerken te onthullen zonder *a priori* hypotheses over de betrokken locaties en frequenties, (2)

het kan de oorsprong van diversiteit in de voorkeursfase over locaties onthullen, en, (3) het maakt een gemakkelijke analyse mogelijk van eigenschappen van deze netwerken. Netwerken worden geëxtraheerd uit 4-dimensionele getalstructuren van FAK maten. Twee van deze vier dimensies zijn spatieel: één beschrijft welke locaties de hoge frequentie amplitudes van de koppeling laten zien (de amplitudeleverende locaties), de ander welke locaties de lage frequentie fases laten zien (de faseleverende locaties). De twee andere dimensies zijn spectraal van aard: één beschrijft de frequentie inhoud van de hoge frequentie amplitudes (de amplitudeleverende frequenties), de ander de frequentie inhoud van de lage frequentie fases (de faseleverende frequenties). De techniek volgt deze 4-dimensionele getalstructuur, en karakteriseert de spatiële verdeling van netwerken met een *amplitudeleverende spatiële kaart* en een *faseleverende spatiële kaart*, en de frequentie inhoud van netwerken met een *amplitudeleverende frequentie profiel* en een *faseleverende frequentie profiel*. De twee spatiële kaarten beschrijven FAK netwerken door een netwerk van locaties wiens lage frequentie fase de hoge frequentie amplitude van een ander netwerk van locaties moduleert. De frequentie profielen beschrijven welke frequenties betrokken zijn bij deze koppeling. Een belangrijke eigenschap van de techniek, is dat het in staat is de diversiteit in voorkeursfases van alle paren van locaties, te verklaren door faseverschillen in de twee spatiële kaarten. Faseverschillen in de faseleverende spatiële kaart reflecteren consistentie faseverschillen tussen locaties van de faseleverende oscillatie, faseverschillen in de amplitudeleverende spatiële kaart reflecteren tussenlocatie tijdsverschillen van de amplitude salvo's van de amplitudeleverende oscillatie. Zodoende kunnen faseverschillen in de twee spatiële kaarten temporele eigenschappen van de FAK netwerken aan het licht brengen. Bijvoorbeeld, het kan het onderscheid maken tussen een situatie waarin de hoge frequentie amplitude salvo's gelijktijdig plaatsvinden over locaties, versus een situatie waarin ze er tijdverschillen tussen deze salvo's zijn. Dit laatste voorbeeld is interessant, want het zou gecoördineerde tijdsramen van communicatie tussen neuronale populaties van een netwerk kunnen reflecteren.

In hoofdstuk 3 van dit proefschrift presenteert ik een nieuwe ontbindingstechniek voor het blootleggen van fasegekoppelde oscillatoire netwerken, SPACE genaamd. Deze techniek is nuttig vanwege drie redenen: (1) het is in staat netwerken te scheiden die overlappen in ruimte en frequentie, (2) het karakteriseert deze netwerken op een neurobiologisch informatieve wijze, en, (3), het maakt een voor de hand liggende analyse mogelijk van taakmodulaties op het niveau van de netwerken. Net als de techniek voor het blootleggen van FAK netwerken, heeft deze techniek geen a priori informatie nodig over welke locaties en welke frequenties waarschijnlijk interacteren. De techniek is geïndiceerd in een plausibel model van een neurobiologisch ritme: een spatieel gedistribueerde oscillatie bestaande uit

meerdere frequenties met frequentiespecifieke tussenlocatie faseverschillen. Aan de hand van dit model worden netwerken geëxtraheerd op basis van hun fasekoppelingspatronen als een functie over ruimte, frequentie, en tijd (repetities van een experiment, ook wel ‘trial’ genoemd). Netwerken worden verkregen uit een 4-dimensionale getalstructuur van fasekoppelingsmaten. Twee dimensies zijn spatief en bevatten informatie over welke locaties onderdeel zijn van een netwerk. Eén dimensie is spectraal en bevat informatie over frequenties van de gekoppelde oscillaties. De overblijvende dimensie is temporeel en bevat informatie over hoe sterk een netwerk aanwezig is in elke trial. Het model beschrijft een fasegekoppeld oscillatoir netwerk door vier parameters. De *spatiële amplitude kaart* beschrijft de mate waarin verschillende locaties het netwerk laten zien. De *spatiële fase kaarten* beschrijven, per frequentie, het gemiddelde faseverschil tussen alle locaties. Het *frequentie profiel* beschrijft welke frequenties betrokken zijn bij de fasekoppeling. Als laatste, het *trial profiel* kwantificeert hoe sterk een netwerk aanwezig is in elke trial. De trial profielen zijn erg nuttig voor het onderzoeken van taakmodulaties op het niveau van de netwerken. In tegenstelling tot conventionele analyses van koppeling op het niveau van locatieparen, beschrijven de spatiële amplitude kaart en de frequentiespecifieke spatiële fase kaarten fasekoppeling op het niveau van de individuele locaties. Dit is belangrijk, want een kwantificering van fasekoppeling op het niveau van locatieparen laat niet direct de spatiële verdeling van het netwerk zien. Bijkomend, omdat de techniek frequentiespecifieke faseverschillen toelaat, kan het verschillende netwerkconfiguraties beschrijven. De techniek beschrijft in werkelijkheid dan ook netwerken aan de hand van twee modellen: het *FSF model* (voor FrequentieSpecifiekeFase, hierboven beschreven) en het *tijdsverschil model*. Waar het FSF model geen begrenzing legt op de relatie van faseverschillen over frequenties, beschrijft het tijdsverschil model deze faseverschillen door een tijdsverschil voor elke locatie, in een *spatiële tijdsverschillen kaart*. Het tijdsverschil model is een bijzonder geval van het FSF model, en is het meest geschikt voor een doelgerichte analyse van netwerken met tussenlocatie faseverschillen die het gevolg zijn van tijdsverschillen. Een voorbeeld van een dergelijk netwerk is een reizende golf, waarin oscillatoire activiteit propageert over locaties. Het FSF model is meer geschikt voor exploratieve analyses, waarin de netwerk configuraties onbekend zijn.

Empirische demonstraties en nieuwe inzichten

In **hoofdstuk 2** heb ik netwerken gevormd door FAK onderzocht in electrocorticografische (ECOG) metingen bij epilepsiepatiënten, en analyseerde de spatiële verdeling van deze netwerken, de diversiteit in hun voorkeursfases, en hun frequentie diversiteit. Deze eigenschappen van FAK netwerken zijn interessant, want ze zouden de flexibiliteit van FAK kunnen bepalen als mechanisme voor het routeren

van informatie. Om deze eigenschappen te kunnen onderzoeken, heb ik allereerst de dimensionaliteit van de hierboven beschreven 4-dimensionele getalstructuren terzijde gelegd, en laten zien dat FAK voorkwam tussen ver uit elkaar gelegen elektroden, grote diversiteit had in voorkeursfases, en voorkwam tussen veel frequenties. Gebruik makend van de hierboven beschreven ontbindingstechniek, was ik in staat om de onderliggende netwerken te extraheren, en hun eigenschappen te onderzoeken. Hiermee demonstreerde ik dat FAK netwerken spatieel verdeeld en wijdverspreid waren, en dat deze netwerken veel verschillende frequentieparen betrokken. Daarnaast liet ik zien dat de spatiele verdelingen van de faseleverende oscillaties meer wijdverspreid waren dan die van de amplitudeleverende oscillaties. Belangrijk, ik liet zien dat de diversiteit in de voorkeursfases van FAK grotendeels kon worden toegeschreven aan tussenElektrode faseverschillen van de faseleverende oscillaties. Dit betekent dat de faseleverende oscillaties gekoppeld waren op veel verschillende fases, en dat de hoge frequentie amplitude salvo's op de amplitudeleverende elektrodes gelijktijdig plaatsvonden. Deze temporele karakteristieken, samen met de spatiele verdelingen, fase diversiteit en frequentie diversiteit van FAK netwerken, laten zien dat FAK een flexibel mechanisme zou kunnen zijn voor het routeren van informatie door neuronale netwerken.

In **hoofdstuk 3** presenteerde ik een ontbindingstechniek voor het blootleggen van fasegekoppelde oscillatoire netwerken. Om te laten zien dat deze techniek in staat is om netwerken bloot te leggen met interessante tussenlocatie faseverschillen heb ik deze techniek toegepast op ECoG metingen van epilepsiepatiënten, en liet ik verscheidene voorbeeldnetwerken zien, waarvan sommige reizende golven beschreven. Daarnaast heb ik de techniek gevalideerd gebruik makende van gesimuleerde data, en heb ik laten zien dat deze in staat was om netwerken terug te vinden in de context van neurobiologisch realistische ruis. Dit laat zien dat de techniek een nuttig en bruikbaar middel is voor het beschrijven en analyseren van fasegekoppelde netwerken.

In **hoofdstuk 4** demonstreerde ik de waarde van de ontbindingstechniek voor fasegekoppelde oscillatoire netwerken als een manier om buitenschedelijke hersensignalen te analyseren. Door magnetoencefalografische (MEG) metingen tijdens een tactiele detectie taak te ontbinden, liet ik zien dat de techniek in staat was de vele spatiale en spectrale overlappende sensorniveau activiteits patronen van verschillende bronnen van elkaar te onderscheiden. Belangrijk, deze patronen waren zeer moeilijk te onderscheiden met conventionele analysetechnieken. De techniek scheideerde deze overlappende patronen op basis van hun verschillende spatiale kaarten, spectrale inhoud, en activiteit in de verschillende trials. Onder deze geëxtraheerde sensorniveau activiteits patronen bevonden zich patronen die geproduceerd waren door gedistribueerde bronnen, welke fasegekoppelde

netwerken reflecteren, maar ook bronnen die beter beschreven konden worden als puntbronnen, welke dipolaire sensorniveau fasekoppelingspatronen lieten zien. Omdat de techniek de trialspecifieke sterkte van netwerken of puntbronnen kwantificeert in hun trial profielen was het mogelijk om taakmodulaties van hun activiteit te onderzoeken. Dit maakte het mogelijk voor mij om vele overlappende alfa en bèta netwerken en bronnen te onthullen, wiens activiteit onderdrukt of versterkt werd door aandacht en taakprestatie, zowel in taakrelevante, als taakirrelevante gebieden. Dit is interessant, omdat conventionele analyses van alfa en bèta activiteit op deze locaties de gemiddelde activiteit beschrijven van dergelijke bronnen, en dat overwegend gevonden wordt dat deze bronnen slechts onderdrukt worden in taakrelevante gebieden, en versterkt in taakirrelevante gebieden. Gebruik makend van de ontbindingstechniek, was ik in staat de onderliggende bronnen van elkaar te scheiden, en te laten zien dat de situatie veel complexer is. Zodoende heb ik laten zien dat de techniek niet alleen nuttig is voor het blootleggen en beschrijven van fasegekoppelde netwerken, maar dat deze ook in staat is de verschillende bronnen te openbaren die buitenschedelijke hersensignalen produceren, en om hun taakmodulaties te onderzoeken.

Tot slot

Neuronale netwerken gevormd door de koppeling van neuronale oscillaties worden gezien als een belangrijke mogelijkheid voor het routeren van informatie door het brein. Het vinden van deze netwerken in de hoogdimensionale getalstructuren die ze beschrijven, is echter zeer moeilijk met conventionele analyse benaderingen. Dit proefschrift beschrijft technieken die dergelijke netwerken identificeren en karakteriseren op een neurobiologisch plausibele wijze. De toepassing van dergelijke technieken zal sterk toenemen in de nabije toekomst, gezien de technologische vooruitgang in meettechnieken zal leiden tot een alsmaar toenemend aantal signalen die gelijktijdig kunnen worden gemeten. Conventionele technieken zijn zeer slecht geschikt voor deze hoogdimensionale data, en methodologische vooruitgangen zoals degene in dit proefschrift zijn essentieel voor hun analyse. Dit proefschrift identificeert ook verscheidene eigenschappen van oscillatoire netwerken die hun erg geschikt maken voor het flexibel routeren van informatie. Desniettemin, er is nog steeds erg veel onduidelijk over hoe het brein dit bereikt, en het blootleggen van de precieze mechanismen is een belangrijke uitdaging voor toekomstig onderzoek.

A

ACKNOWLEDGEMENTS

And now, this time has finally come. I'm sitting in the warm San Diego sun, a breeze softly blowing around me, thinking about all the people I have met in these past years. People who I cannot imagine missing from this time period, unforgettably linked to my life during my PhD. Saying thank you to each and every one of you seems like an insurmountable task, and I can only hope I can do so without forgetting anyone. Here goes.

Dear **Eric**, thank you for taking me on for all those years, your guidance, methodological sharpness, and your openness to letting me find my spot in science. I learned an incredible amount from you, and whenever I'm at my sharpest and clearest, you're not far from my mind and my writing. I have yet to meet someone with as clear an understanding of all things analytical and statistical as you. Thank you, especially, for stimulating me to undertake my tour des labs and quest for data in the US. A time I am still thankful for, as it had a profound impact on my life, both professionally and personally. Thank you.

Thank you **Markus**, for willing to be my promotor. Thank you **Ole**, and **Ingrid**, for helping me take those first small steps in research under your wings. There are things you taught me that I still use today. Being a member of the group, was a wonderful, and often hilarious time.

During my lab tour I met so many wonderful people. Thank you **Jeff** for taking me into the lab, and especially **Kai** and **Dora**, for the incredibly friendly welcome, our chats about data and brains, and good time in general. With the theme of 'chariots of fire' in the back of my mind, I remember beer, liquor, running, and data. The last of which still resides under the same name on my hard drive, if you can still remember what you wrote down that one night. And thanks **Kai** as well, for linking me up with **Chris H.** and **Gerwin**, I had a great time meeting you two, and visiting the lab in upstate NY.

Thank you **Chris**, **Ross**, and **Jennifer**, for being such wonderful roommates in Seattle. **Jennifer**, I had a wonderful time those few weeks. A tumultuous time, with so many great memories. That camping trip and that hippy house concert still come to mind every now and then.

Thank you **Mike**, for having me over while working on our collaborative project, your advice in this process, and your advice while looking for a postdoc near the end of my PhD. **John**, **Ashwin**, **Joel**, and the rest, it was great starting 'Roemer' hour. Happy hour again some time? **Josh**, I enjoyed our data chats, and thank you the collaboration on one of my recent projects.

In the same spirit, thank you **Bernhard**, for relaxing together while working on

some coupling things, I still remember the wonderful tips you gave me for NYC, hope to catch another beer soon. **Marijn**, the same to you, I'm sure we will meet again at a conference soon.

Bob, thank you for allowing me to hang around the lab for a while. Without my visit, I would have never met **Brad** (hi!). **Ryan**, glad to meet a kindred data spirit. I think I was at the lab during party season, as I remember many a fun night while hanging out with **Yvonne**, **Maya**, **Brad**, **Ryan**, **Bob**, **Sara** and many others. Say hi to **Vitoria** for me, and pretty soon **Arjen** too! **Yvonne**, thanks for hooking me with that awesome house. **Yvonne**, **Sepideh**, and **Charlotte**, it was great hanging out in SF with you, watching freaky costumes running around, hope to repeat again. **Charlotte**, best time ever jumping out of an airplane.

Back to Nijmegen, where the core of life resided, and which has a special place in my heart. I can barely decide where to begin, the amount of people I want to thank and are dear to me almost seems too much.

First up, FieldTrip. Thank you so much **Robert** and **Jan-Matthijs**, I had such a great time for all those years. So many things I learned from all of our meetings, and much of your advice one-on-one I still think of every now and then. Being part of the team has truly been a blessing. The experience of coding in this big software development project, the workshops, especially the one in Trento, all of our brainstorms and discussions and explanatory sessions during our meetings, it has been very, very, valuable. Thank you **Eelke**, **Jorn**, **Nietzsche**, **Arjen**, **Stephen**, **Diego**, **Ana**, **Johanna**, **Jim**, **Lilla**, **Cristiano**, **Saskia** and many of the others members with whom I shared time on the team, I had a blast. All our meetings, and not to forgot all the bbqs, the drinks, the bowling, the skiing. It was awesome. What a trip indeed.

The DCC, my dear DCC. My home for so many years. My home made from so many people. And so many changes over the years, people coming and going. **Sybrine**, **Loes**, **Celine**, **Pascal**, **Mark**, **Sebo**, **Moniek**, **Maaike**, **Verena** and many others, my time at the DCC started with all of you. Thank you for adopting me into the fun and wild thing that is the DCC. Those first zomerfeesten, every night till at least 4, going to the Fuik so often (?), still warm memories. And funny pre-smartphone-era pictures. So long ago already?

Maaike, **Ivar**, **Herr Prof Dr Markus**, **Sybrine**, **Frank**, **Sasha**, taking that golfing course, mooie broek!, was awesome, scheef! Taking you there in my babe/elderly man magnet, and parking next to proper cars, pretending to be the kitchen help still makes me giggle. **Pascal**, **Mark**, **Frank**, **Sybrine**, thank you for kidnapping said pope mobile and sending me ransom photo's every now and then (also, for leaving the lights on?). **Loes** and **Celine**, that time in NYC was a very special one for me. Thank you so much for being there at the time, for allowing me to crash with you, hanging out, and for letting me meet those that I did. **Loes**, Lucy, thank you, for all

the wonderful times, hanging out, the chats, the beers, the wine. I'm very happy you remained in Nijmegen after Venlo. Good memories. **Maaike** and **Pascal**, our road trip was a fantastic time. Thank you for flying towards me back then, and going through all those beautiful places together. I wish we could have spent more time in each of those. Well, except Vegas. Fond memories, of dessert and snow, lots of big trees, and a funny hat. **Maaike**, I hope my old home will feel like yours as well. See you in SD?

So many more, from the beginning or the years after, **Steffie**, **Matthias**, **Ricky**, **Simon**, **Tjerk**, **Fenny**, **Iris**, **Adjmal**, **Mark**, **Guilio**, **Sanne**, **Claire**, **Sarah**, **Frank**, and so many more, I cannot imagine my life at the DCC without you all. **Steffie**, **Matthias**, **Loes**, I loved our dinners together. Sure, that's totally a peach. Needs more sugar though. And strawberries are not nuts. **Steffie**, thank you, for joining the DCC, informally, and for the time we spent together. Warm memories. **Adjmal**, I'm greatly thankful to have met you, during that time in Washington. It, and many shared moments after, was fantastic. Burgers. Our industry musings. Life. Keep on rising and reaching, mr Jinx. See you in the snow my dear friend. **Sarah**, I miss you. And **Ross**, who got adopted to the DCC so quickly he even signed up for the bata before you. Thank you for all the wonderful times, and for letting me meet so many great friends of yours, many still to come, I'm sure. **Frankie**, krulliebollie, or krolliebullie, my Chinese takeaway half-brother, my all-the-time-during-the-day-so-why-not-fix-electronics-with-a-heatgun-partner, my toilet-paper-fort-friend, my jumping-dance-buddy. I hope there will be many a party where we can jump around happily, and many a drink to drink, and life story to share. See you soon my good friend. **Matthias**, thank you so much for your friendship in the past years. It's very dear to me. You always feel very close. Thank you for all the talks we had, all the beers and food we shared, all the laughs we laughed, and all the life we lived, and relived. Thank you.

Mark, **Giulio**, thank you for finally waking up my love for photography, that was boiling under the surface for so long. Thank you, **Sanne**, **Willem**, and **Linsey** as well, for that awesome photo settimana Senese. **Giulio**, and your family, it was great of you to have us over. And thank you for many a good time, frog-mobile to the tikibad again? **Claire**! And **Hanneke** en **Mieke**, it doesn't fit the timeline that I'm trying to hold together, but screw it, thank you so much for taking me climbing, and teaching me. And for all the nice, incredibly delicious and gezellige dinners. It feels wonderful to have been able to get to know you. **Franc**, **Jeroen**, and others, I had a great deal of online fun with you all, I still remember that special gathering bbq. Fond memories!

Volleyball! **Sara**, **Kors**, **Pascal** and **Pascal**, and of course **Steffie**, **Loes**, **Celine**, **Arjan**, **Verena** and many others, it was great getting to know that sport, even though it was all just for the social time. As a bonus I suck much less at it now. **Verena**, **Matthias**, and not to forgot **Lisa** (the dog one), those new year's parties were

wonderful, thank you for opening up your house for so many great DCC gatherings, and for all the other fun times. I hope to finally meet your new loved ones soon.

The lab, thank you **Freaky Freek**, for sharing that office with a rumor, and for all the occasional beers and chats we had. **George**, you're the best Greek-screaming officemate I could ever wish for. It was great sharing our Harry Potter sized office with you. I wish you all the best with your newly expanded family, in your new UK home. And you as well of course, **Freek** and **Rocio**, your daughter is one of the most adorable little dancing baby girls I have met. **Anne**, **Remco**, and of course of **Malte** and **Lieneke**, it was great to have you there. **Remco**, it was awesome that you joined the DCC, even though I only started to get to know you after my thesis-bubble. Things changed, but I equally hope to see you around nonetheless. **Lieneke**, it's a shame we still didn't get to bake our humongous piece of pepernoten-chocolate. Hopefully we will still get a chance sometime, somewhere.

The bbqs at the Berendonck! What a fantastic way to spend the Dutch summer months. It reminds me of the Hoornse Plas. Thank you all for joining me so often, **Sybrine**, **Loes**, **Matthias**, **Ricky**, **Tjerk**, **Simon**, **Alina**, **Giulio**, **Pascal**, **Mark**, **Dan**, **Remco**, **Rene**, **Tom**, **Iske**, **Ruud**, and many others. When I visit in a little while, let's go for another swim and grill. And equally summery, the sailing weekends! Such as blast. Thank you **Yvonne**, **Gerard**, **Norbert**, and all the rest for organizing and joining. They were awesome.

From the heat to the cold. Dear **Frank**, **Sybrine**, **Mark**, **Moniek**, **Matthias**, that ski-holiday, up in La Plange, it was so so soooo, wonderful. Ein schönsten Zeit in der Welt. Ein bischen skimphoman. Es fängt mir Traumen. Warm memories, warm stories. In Flemmisch. Except Voldemort. The years after, **Anke Marit**, **Jeanette**, **Rene**, **Tjerk**, **Tim**, **Ruud**, **Sasha**, **Lisa**, **Fenny**, **Sanne**, **Willem**. Very happy times. Hope to get a chance to repeat, and head out again.

And with that, the DCCN. **Rene**, **Tom**, **Iske**, **Sean**, **Ruud**, **Anke Marit**, **Alina**, **Jolien**, **Arjen**, **Marlieke**, **Mirjam**, **Miriam**, **Richard**, **Tim**, **Flora**, **Ruben**, **Eelco**, **Verena**, **Winke**, **Susanne**, and many others, it's been great sharing so many drinks, seeing you on conferences, hanging out in general, partying, burgers at Wally's, and overall good times. I'm really happy you all migrated to the CC for the Friday pleasantness years back. **Rene**, it's been great hanging out with you as the last ones on so many parties. It's a shame I had a break for a while, but I plan to get back in the tradition. I'm positive I will see you at a random party in the future. For example, some social faculty party! **Tom**, you're one of the most friendly, enthusiastic, and occasionally joyfully ranting people I know, and musical! Thank you for the good times. Go have another poofie, and make the cat wiser. Hope to catch another beer soon. **Ruud**, same to you! **Anke Marit**, I'm happy to have been able to get to know you. Come over here, and we'll do some surfing! Better and safer than wind surfing, totally.

Ricky, Simon, Tjerk, and every now and then **Lorijn**, I miss you all. Our bad movie nights couldn't have been better, and in ways, couldn't have been worse! I hope Skip gets to be used and abused as often as possible in the coming bbq season. Thank you all, for making my last year, or years, at the DCC so ever more joyful. Warm hugs to you. All the snow-zombie-ninja-biker-nazi-wolves who're gonna steal all your cocaine, zombie-philosopher-stripers, murderous tires, the occasional giant spider, tornado-sharks, incredibly confusing Japanese things, and the IPAs and pizzas. Hope to do another night when I'm back. Death Spa I heard? **Simon**, I'm really happy I got the chance to get to know you better in Nijmegen, than we did in our hold home. Thank you, for the good times. And hopefully many to come. **Tjerk**, likewise, I miss you, and your awesome t-shirts. I hope to see many more obscure references in the future. And hear you make magic come out of guitars. **Ricky**, thank you for an amazing year, filled with so many memories. I'm incredibly happy to have met you. There's a special place in my heart for you.

Dear **Terry**, dear **Reyhan**, and with you of course **Sarah**, and **Eddie!** Thank you so much for all the generous memories, the warm evenings, all the laughs, all the postcards. Aunties? No. My Turkish sisters. **Terry**, my life would be different without you. It's funny to think back at how randomly we met. That dinner at Ankara's, the poker night soon after. Thinking about not having met you, cramps my heart. **Reyhan**, it's been so long since I saw you. I hope to be able to hug you soon, and your cute little Kahlua. If you are in need of a space to crash as an illegal, I will hide you as long as you desire.

Marlene, Florian, Vitoria, Carmen, thank you for all the drinks and parties and gatherings. **Marlene**, and **Dan** of course! Thank you for opening your awesome house to me for a little while, one of my favorites. **Marlene**, you're one of the sweetest people I know. I'm pretty sure your voice creates butterflies. **Dan**, I'm very happy you joined the DCC, you add a great amount of warmth and gezelligheid. **Vitoria**, it's been so long ago since we met, and so many things have changed since then. Yet, you always feel close by. See you, and your dear **Kris**, soon. **Sara, Monique, Ezgi, Jo, Ingar**, and many others, it was great fun. Another drink, very soon. **Anne B!** It's been a long time, but a blast nonetheless. Related, **Lincoln!** Far away now, but let's do a beer soon. Curious about your ventures. **Luc, Bart, Julian**, thanks for all the lunches! Including many of the above of course. **Chayada, Richard, Xuyan, Alessia, Antonella, Samarth, Natasha**, and very recently **Johanna**, and long ago **Wessel**, and **Egbert** the past years, it was great hanging out!

Via the DCC, **Bas**, it was awesome brewing, and drinking, all the beers that we did. Happy to have met you, and that we realized our common interest that one night at the Arsenaal. Thank you for always hosting, it was great fun messing up your house during all the stages. **Joelle**, it's been a while, but our intermezzo's of

beer and saté at Camelot were a wonderful tradition throughout the years. Hope to renew it soon. And **Bas**, Bassie, kerel, it's been so long as well. But nevertheless, it feels like yesterday we last hung out, and the time in between like a breeze. Let's recap soon. **Hans**, thank you for all your advice and mentorship in the past years. My paths would have been very different without it.

Sweet sweet stagekamer. **Lisa**, **Vincent**, **Ivar**, **Lena**, **Miriam**, **Frauke**, **Emily**, and of course **Katie**. It was awesome the past years. The Sinterklaasses, the visits to Oxford, our time pre-Donders, and other s-related activities, I look forward to many more. Next up, San Diego? **Lisa** and **Vincent**, thank you for hosting me for a while in your warm, welcoming, home. It felt like a privilege, it brings a smile upon my face. And I'm still reading OOTS. Hope to come by again soon. **Lena**, thank you for all the good times, our late night talks, our sharings, our secrets. It was great having you as a first visitor. See you all soon, hopefully at **Ivar's** wedding?

Dear **Leander**, dear brother, thank you for being a part of my life. And dear **Mercedes**, thank you for the same. Thank you for creating that sweet cute little bundle of joy, and chaos, during the years of my PhD. Thank you, for making me an uncle. I look forward to the day your new bundle joins you, I can't wait to meet her.

And last, but not least. Thank you, **Sybrine**, my paranympth. I cannot imagine the past years without you. To do so right now breaks my heart. Thank you for your warmth and kindness, you're a sweet soul. Thank you, **Miriam**, my paranympth. Dear Miriam. Almost 8 years ago we met, and I cannot imagine that number not increasing. You hold a very special place in my heart. **Fenny**, sweet Fenny. You touched my life. I want to thank you for so many things. But, that, I will do in person.

And now, I have to make this come to an end, lest this really does become a memoirs of a time gone by. I can only end, with saying this. Thank you. Thank you, thank you, thank you. Thank you? Thank you. And, most of all,

Thank you.

PUBLICATIONS

van der Meij R, Kahana M, and Maris E (2012). *Phase-amplitude coupling in human ECoG is spatially distributed and phase diverse*. Journal of Neuroscience, 32(1), 111-123.

Piai V, Roelofs A, **van der Meij R** (2012). *Event-related potentials and oscillatory brain responses associated with semantic and Stroop-like interference effects in overt naming*. Brain Research, 1450, 87-101.

Van Wingerden M, **van der Meij R**, Kalenscher T, Maris E, Pennartz C (2014). *Phase-amplitude coupling in rat orbitofrontal cortex discriminates between correct and incorrect decisions during associative learning*. Journal of Neuroscience, 34(2), 493-505.

van der Meij R, Jacobs J, and Maris E (2015). *Uncovering phase-coupled oscillatory networks in electrophysiological data*. Human Brain Mapping.

van der Meij R, Van Ede F, and Maris E (under review). *Rhythmic components in extracranial brain signals reveal multifaceted task modulations of overlapping phase-coupled oscillatory networks*.

Staresina B, Bergmann T, Bonnefond M, **van der Meij R**, Jensen O, Deuker L, Elger C, Axmacher N, Fell J (under review). *Hierarchical nesting of slow oscillations, spindles and ripples in the human hippocampus during NREM sleep*.

BOOK CHAPTERS

Van der Meij R, Schoffelen JM, (2014). *Digital Filtering*. In: Jaeger D., Jung R. (Ed.) Encyclopedia of Computational Neuroscience: SpringerReference (www.springerreference.com). Springer-Verlag Berlin Heidelberg, 2013.

ABOUT THE AUTHOR

Roemer van der Meij was born on the 5th of December, 1984, in Groningen, The Netherlands. In 2003, he started his studies in Psychology at the University of Groningen, with a focus on Cognitive Science and Neuropsychology. After obtaining his Bachelor of Science (B.Sc.) degree in 2007, he started a Research Master's program in Cognitive Neuroscience, at the Radboud University, Nijmegen. Here, Roemer started working with intracranial electrophysiology under the supervision of Ingrid Nieuwenhuis and Ole Jensen, studying the effects of sleep on hippocampal memory retrieval. In 2009 he obtained his Master of Science (M.Sc.) degree (cum laude). Still in 2009, Roemer started his PhD project, at the Radboud University, Nijmegen, at the newly formed Donders Institute for Brain, Cognition, and Behaviour. Here, he worked on finding a way to characterize and investigate communicating neuronal networks formed by oscillatory coupling in high dimensional data, under the supervision of Eric Maris in the Neurophysiology of Active Perception group. He collaborated extensively with groups throughout the community, using both intracranial (electrocorticography) and extracranial (magnetoencephalography) recordings to develop several new analysis methods. The results of this work are presented in this thesis. Since early 2015, Roemer works a postdoctoral researcher together with Bradley Voytek, at the University of California, San Diego, United States, where he studies the temporal dynamics of oscillatory neural activity and its impact on ongoing cognitive processes.

DONDERS GRADUATE SCHOOL FOR COGNITIVE NEUROSCIENCE SERIES

1. Van Aalderen-Smeets, S.I. (2007). *Neural dynamics of visual selection*. Maastricht University, Maastricht, the Netherlands.
2. Schoffelen, J.M. (2007). *Neuronal communication through coherence in the human motor system*. Radboud University Nijmegen, Nijmegen, the Netherlands.
3. De Lange, F.P. (2008). *Neural mechanisms of motor imagery*. Radboud University Nijmegen, Nijmegen, the Netherlands.
4. Grol, M.J. (2008). *Parieto-frontal circuitry in visuomotor control*. Utrecht University, Utrecht, the Netherlands.
5. Bauer, M. (2008). *Functional roles of rhythmic neuronal activity in the human visual and somatosensory system*. Radboud University Nijmegen, Nijmegen, the Netherlands.
6. Mazaheri, A. (2008). *The influence of ongoing oscillatory brain activity on evoked responses and behaviour*. Radboud University Nijmegen, Nijmegen, the Netherlands.
7. Hooijmans, C.R. (2008). *Impact of nutritional lipids and vascular factors in Alzheimer's disease*. Radboud University Nijmegen, Nijmegen, the Netherlands.
8. Gaszner, B. (2008). *Plastic responses to stress by the rodent urocortinergic Edinger-Westphal nucleus*. Radboud University Nijmegen, Nijmegen, the Netherlands.
9. Willems, R.M. (2009). *Neural reflections of meaning in gesture, language and action*. Radboud University Nijmegen, Nijmegen, the Netherlands.
10. Van Pelt, S. (2009). *Dynamic neural representations of human visuomotor space*. Radboud University Nijmegen, Nijmegen, the Netherlands.
11. Lommertzen, J. (2009). *Visuomotor coupling at different levels of complexity*. Radboud University Nijmegen, Nijmegen, the Netherlands.
12. Poljac, E. (2009). *Dynamics of cognitive control in task switching: Looking beyond the switch cost*. Radboud University Nijmegen, Nijmegen, the Netherlands.
13. Poser, B.A. (2009). *Techniques for BOLD and blood volume weighted fMRI*. Radboud University Nijmegen, Nijmegen, the Netherlands.
14. Baggio, G. (2009). *Semantics and the electrophysiology of meaning. Tense, aspect, event structure*. Radboud University Nijmegen, Nijmegen, the Netherlands.
15. Van Wingen, G.A. (2009). *Biological determinants of amygdala functioning*. Radboud University Nijmegen Medical Centre, Nijmegen, the Netherlands.
16. Bakker, M. (2009). *Supraspinal control of walking: Lessons from motor imagery*. Radboud University Nijmegen Medical Centre, Nijmegen, the Netherlands.
17. Aarts, E. (2009). *Resisting temptation: The role of the anterior cingulate cortex in adjusting cognitive control*. Radboud University Nijmegen, Nijmegen, the Netherlands.
18. Prinz, S. (2009). *Waterbath stunning of chickens – Effects of electrical parameters on the electroencephalogram and physical reflexes of broilers*. Radboud University Nijmegen, Nijmegen, the Netherlands.
19. Knippenberg, J.M.J. (2009). *The N150 of the Auditory Evoked Potential from the rat amygdala: In search for its functional significance*. Radboud University Nijmegen, Nijmegen, the Netherlands.
20. Dumont, G.J.H. (2009). *Cognitive and physiological effects of 3,4-methylenedioxymethamphetamine (MDMA or 'ecstasy') in combination with alcohol or cannabis in humans*. Radboud University Nijmegen, Nijmegen, the Netherlands.
21. Pijnacker, J. (2010). *Defeasible inference in autism: A behavioral and electrophysiological approach*. Radboud University Nijmegen, Nijmegen, the Netherlands.
22. De Vrijer, M. (2010). *Multisensory integration in spatial orientation*. Radboud University Nijmegen, Nijmegen, the Netherlands.
23. Vergeer, M. (2010). *Perceptual visibility and appearance: Effects of color and form*. Radboud University Nijmegen, Nijmegen, the Netherlands.
24. Levy, J. (2010). *In cerebro unveiling unconscious mechanisms during reading*. Radboud University Nijmegen, Nijmegen, the Netherlands.
25. Treder, M. S. (2010). *Symmetry in (inter)action*. Radboud University Nijmegen, Nijmegen, the Netherlands.
26. Horlings, C.G.C. (2010). *A weak balance: Balance and falls in patients with neuromuscular disorders*. Radboud University Nijmegen, Nijmegen, the Netherlands.
27. Snaphaan, L.J.A.E. (2010). *Epidemiology of post-stroke behavioural consequences*. Radboud University Nijmegen Medical Centre, Nijmegen, the Netherlands.
28. Dado – Van Beek, H.E.A. (2010). *The regulation of cerebral perfusion in patients with Alzheimer's disease*. Radboud University Nijmegen Medical Centre, Nijmegen, the Netherlands.
29. Derkx, N.M. (2010). *The role of the non-preganglionic Edinger-Westphal nucleus in sex-dependent stress adaptation in rodents*. Radboud University Nijmegen, Nijmegen, the Netherlands.
30. Wyczesany, M. (2010). *Covariation of mood and brain activity. Integration of subjective self-report data with quantitative EEG measures*. Radboud University Nijmegen, Nijmegen, the Netherlands.
31. Beurze S.M. (2010). *Cortical mechanisms for reach planning*. Radboud University Nijmegen, Nijmegen, the Netherlands.
32. Van Dijk, J.P. (2010). *On the Number of Motor*

- Units.* Radboud University Nijmegen, Nijmegen, the Netherlands.
33. Lapatki, B.G. (2010). *The Facial Musculature - Characterization at a Motor Unit Level*. Radboud University Nijmegen, Nijmegen, the Netherlands.
 34. Kok, P. (2010). *Word order and verb inflection in agrammatic sentence production*. Radboud University Nijmegen, Nijmegen, the Netherlands.
 35. van Elk, M. (2010). *Action semantics: Functional and neural dynamics*. Radboud University Nijmegen, Nijmegen, the Netherlands.
 36. Majdandzic, J. (2010). *Cerebral mechanisms of processing action goals in self and others*. Radboud University Nijmegen, Nijmegen, the Netherlands.
 37. Snijders, T.M. (2010). *More than words - Neural and genetic dynamics of syntactic unification*. Radboud University Nijmegen, Nijmegen, the Netherlands.
 38. Grootens, K.P. (2010). *Cognitive dysfunction and effects of antipsychotics in schizophrenia and borderline personality disorder*. Radboud University Nijmegen Medical Centre, Nijmegen, the Netherlands.
 39. Nieuwenhuis, I.L.C. (2010). *Memory consolidation: A process of integration – Converging evidence from MEG, fMRI and behavior*. Radboud University Nijmegen Medical Centre, Nijmegen, the Netherlands.
 40. Menenti, L.M.E. (2010). *The right language: Differential hemispheric contributions to language production and comprehension in context*. Radboud University Nijmegen, Nijmegen, the Netherlands.
 41. Van Dijk, H.P. (2010). *The state of the brain, how alpha oscillations shape behaviour and event related responses*. Radboud University Nijmegen, Nijmegen, the Netherlands.
 42. Meulenbroek, O.V. (2010). *Neural correlates of episodic memory in healthy aging and Alzheimer's disease*. Radboud University Nijmegen, Nijmegen, the Netherlands.
 43. Oude Nijhuis, L.B. (2010). *Modulation of human balance reactions*. Radboud University Nijmegen, Nijmegen, the Netherlands.
 44. Qin, S. (2010). *Adaptive memory: Imaging medial temporal and prefrontal memory systems*. Radboud University Nijmegen, Nijmegen, the Netherlands.
 45. Timmer, N.M. (2011). *The interaction of heparan sulfate proteoglycans with the amyloid protein*. Radboud University Nijmegen, Nijmegen, the Netherlands.
 46. Crajé, C. (2011). *(A)typical motor planning and motor imagery*. Radboud University Nijmegen, Nijmegen, the Netherlands.
 47. Van Grootel, T.J. (2011). *On the role of eye and head position in spatial localisation behaviour*. Radboud University Nijmegen, Nijmegen, the Netherlands.
 48. Lamers, M.J.M. (2011). *Levels of selective attention in action planning*. Radboud University Nijmegen, Nijmegen, the Netherlands.
 49. Van der Werf, J. (2011). *Cortical oscillatory activity in human visuomotor integration*. Radboud University Nijmegen, Nijmegen, the Netherlands.
 50. Scheeringa, R. (2011). *On the relation between oscillatory EEG activity and the BOLD signal*.
 51. Bögels, S. (2011). *The role of prosody in language comprehension: When prosodic breaks and pitch accents come into play*. Radboud University Nijmegen, Nijmegen, the Netherlands.
 52. Ossewaarde, L. (2011). *The mood cycle: Hormonal influences on the female brain*. Radboud University Nijmegen, Nijmegen, the Netherlands.
 53. Kuribara, M. (2011). *Environment-induced activation and growth of pituitary melanotrope cells of Xenopus laevis*. Radboud University Nijmegen, Nijmegen, the Netherlands.
 54. Helmich, R.C.G. (2011). *Cerebral reorganization in Parkinson's disease*. Radboud University Nijmegen, Nijmegen, the Netherlands.
 55. Boelen, D. (2011). *Order out of chaos? Assessment and treatment of executive disorders in brain-injured patients*. Radboud University Nijmegen, Nijmegen, the Netherlands.
 56. Koopmans, P.J. (2011). *fMRI of cortical layers*. Radboud University Nijmegen, Nijmegen, the Netherlands.
 57. van der Linden, M.H. (2011). *Experience-based cortical plasticity in object category representation*. Radboud University Nijmegen, Nijmegen, the Netherlands.
 58. Kleine, B.U. (2011). *Motor unit discharges - Physiological and diagnostic studies in ALS*. Radboud University Nijmegen Medical Centre, Nijmegen, the Netherlands.
 59. Paulus, M. (2011). *Development of action perception: Neurocognitive mechanisms underlying children's processing of others' actions*. Radboud University Nijmegen, Nijmegen, the Netherlands.
 60. Tielemans, A.A. (2011). *Myotonic dystrophy type 2. A newly diagnosed disease in the Netherlands*. Radboud University Nijmegen Medical Centre, Nijmegen, the Netherlands.
 61. Van Leeuwen, T.M. (2011). *'How one can see what is not there': Neural mechanisms of grapheme-colour synaesthesia*. Radboud University Nijmegen, Nijmegen, the Netherlands.
 62. Van Tilborg, I.A.D.A. (2011). *Procedural learning in cognitively impaired patients and its application in clinical practice*. Radboud University Nijmegen, Nijmegen, the Netherlands.
 63. Bruinsma, I.B. (2011). *Amyloidogenic proteins in Alzheimer's disease and Parkinson's disease: Interaction with chaperones and inflammation*. Radboud University Nijmegen, Nijmegen, the Netherlands.
 64. Voermans, N. (2011). *Neuromuscular features of Ehlers-Danlos syndrome and Marfan syndrome; expanding the phenotype of inherited connective tissue disorders and investigating the role of the extracellular matrix in muscle*. Radboud University Nijmegen Medical Centre, Nijmegen, the Netherlands.
 65. Reelick, M. (2011). *One step at a time. Disentangling the complexity of preventing falls in frail older persons*. Radboud University Nijmegen Medical Centre, Nijmegen, the Netherlands.

66. Buur, P.F. (2011). *Imaging in motion. Applications of multi-echo fMRI*. Radboud University Nijmegen, Nijmegen, the Netherlands.
67. Schaefer, R.S. (2011). *Measuring the mind's ear: EEG of music imagery*. Radboud University Nijmegen, Nijmegen, the Netherlands.
68. Xu, L. (2011). *The non-preganglionic Edinger-Westphal nucleus: An integration center for energy balance and stress adaptation*. Radboud University Nijmegen, Nijmegen, the Netherlands.
69. Schellekens, A.F.A. (2011). *Gene-environment interaction and intermediate phenotypes in alcohol dependence*. Radboud University Nijmegen, Nijmegen, the Netherlands.
70. Van Marle, H.J.F. (2011). *The amygdala on alert: A neuroimaging investigation into amygdala function during acute stress and its aftermath*. Radboud University Nijmegen, Nijmegen, the Netherlands.
71. De Laat, K.F. (2011). *Motor performance in individuals with cerebral small vessel disease: An MRI study*. Radboud University Nijmegen Medical Centre, Nijmegen, the Netherlands.
72. Mädebach, A. (2011). *Lexical access in speaking: Studies on lexical selection and cascading activation*. Radboud University Nijmegen, Nijmegen, the Netherlands.
73. Poelmans, G.J.V. (2011). *Genes and protein networks for neurodevelopmental disorders*. Radboud University Nijmegen, Nijmegen, the Netherlands.
74. Van Norden, A.G.W. (2011). *Cognitive function in elderly individuals with cerebral small vessel disease. An MRI study*. Radboud University Nijmegen Medical Centre, Nijmegen, the Netherlands.
75. Jansen, E.J.R. (2011). *New insights into V-ATPase functioning: the role of its accessory subunit Ac45 and a novel brain-specific Ac45 paralog*. Radboud University Nijmegen, Nijmegen, the Netherlands.
76. Haaxma, C.A. (2011). *New perspectives on preclinical and early stage Parkinson's disease*. Radboud University Nijmegen Medical Centre, Nijmegen, the Netherlands.
77. Haegens, S. (2012). *On the functional role of oscillatory neuronal activity in the somatosensory system*. Radboud University Nijmegen, Nijmegen, the Netherlands.
78. van Barneveld, D.C.P.B.M. (2012). *Integration of exteroceptive and interoceptive cues in spatial localization*. Radboud University Nijmegen, Nijmegen, the Netherlands.
79. Spies, P.E. (2012). *The reflection of Alzheimer disease in CSF*. Radboud University Nijmegen Medical Centre, Nijmegen, the Netherlands.
80. Helle, M. (2012). *Artery-specific perfusion measurements in the cerebral vasculature by magnetic resonance imaging*. Radboud University Nijmegen, Nijmegen, the Netherlands.
81. Egetemeir, J. (2012). *Neural correlates of real-life joint action*. Radboud University Nijmegen, Nijmegen, the Netherlands.
82. Janssen, L. (2012). *Planning and execution of (bi) manual grasping*. Radboud University Nijmegen, Nijmegen, the Netherlands.
83. Vermeer, S. (2012). *Clinical and genetic characterisation of autosomal recessive cerebellar ataxias*. Radboud University Nijmegen Medical Centre, Nijmegen, the Netherlands.
84. Vrins, S. (2012). *Shaping object boundaries: Contextual effects in infants and adults*. Radboud University Nijmegen, Nijmegen, the Netherlands.
85. Weber, K.M. (2012). *The language learning brain: Evidence from second language and bilingual studies of syntactic processing*. Radboud University Nijmegen, Nijmegen, the Netherlands.
86. Verhagen, L. (2012). *How to grasp a ripe tomato*. Utrecht University, Utrecht, the Netherlands.
87. Nonkes, L.J.P. (2012). *Serotonin transporter gene variance causes individual differences in rat behaviour: For better and for worse*. Radboud University Nijmegen Medical Centre, Nijmegen, the Netherlands.
88. Joosten-Weyn Banningh, L.W.A. (2012). *Learning to live with Mild Cognitive Impairment: development and evaluation of a psychological intervention for patients with Mild Cognitive Impairment and their significant others*. Radboud University Nijmegen Medical Centre, Nijmegen, the Netherlands.
89. Xiang, H.D. (2012). *The language networks of the brain*. Radboud University Nijmegen, Nijmegen, the Netherlands.
90. Snijders, A.H. (2012). *Tackling freezing of gait in Parkinson's disease*. Radboud University Nijmegen Medical Centre, Nijmegen, the Netherlands.
91. Rouwette, T.P.H. (2012). *Neuropathic pain and the brain - Differential involvement of corticotropin-releasing factor and urocortin 1 in acute and chronic pain processing*. Radboud University Nijmegen Medical Centre, Nijmegen, the Netherlands.
92. Van de Meerenkon, N. (2012). *States of indecision in the brain: Electrophysiological and hemodynamic reflections of monitoring in visual language perception*. Radboud University Nijmegen, Nijmegen, the Netherlands.
93. Sterrenburg, A. (2012). *The stress response of forebrain and midbrain regions: Neuropeptides, sex-specificity and epigenetics*. Radboud University Nijmegen, Nijmegen, the Netherlands.
94. Uithol, S. (2012). *Representing action and intention*. Radboud University Nijmegen, Nijmegen, The Netherlands.
95. Van Dam, W.O. (2012). *On the specificity and flexibility of embodied lexical-semantic representations*. Radboud University Nijmegen, Nijmegen, The Netherlands.
96. Slats, D. (2012). *CSF biomarkers of Alzheimer's disease: Serial sampling analysis and the study of circadian rhythmicity*. Radboud University Nijmegen Medical Centre, Nijmegen, the Netherlands.
97. Van Nuenen, B.F.L. (2012). *Cerebral reorganization in premotor parkinsonism*. Radboud University Nijmegen Medical Centre, Nijmegen, the Netherlands.
98. van Schouwenburg, M.R. (2012). *Fronto-striatal mechanisms of attentional control*. Radboud University Nijmegen, Nijmegen, The Netherlands.
99. Azar, M.G. (2012). *On the theory of reinforcement learning: Methods, convergence analysis and*

- sample complexity.* Radboud University Nijmegen, Nijmegen, The Netherlands.
100. Meeuwissen, E.B. (2012). *Cortical oscillatory activity during memory formation.* Radboud University Nijmegen, Nijmegen, The Netherlands.
 101. Arnold, J.F. (2012). *When mood meets memory: Neural and behavioral perspectives on emotional memory in health and depression.* Radboud University Nijmegen, Nijmegen, The Netherlands.
 102. Gons, R.A.R. (2012). *Vascular risk factors in cerebral small vessel disease: A diffusion tensor imaging study.* Radboud University Nijmegen Medical Centre, Nijmegen, The Netherlands.
 103. Wingbermuehle, E. (2012). *Cognition and emotion in adults with Noonan syndrome: A neuropsychological perspective.* Radboud University Nijmegen, Nijmegen, The Netherlands.
 104. Walentowska, W. (2012). *Facing emotional faces. The nature of automaticity of facial emotion processing studied with ERPs.* Radboud University Nijmegen, Nijmegen, The Netherlands.
 105. Hoogman, M. (2012). *Imaging the effects of ADHD risk genes.* Radboud University Nijmegen, Nijmegen, The Netherlands.
 106. Tramper, J. J. (2012). *Feedforward and feedback mechanisms in sensory motor control.* Radboud University Nijmegen, Nijmegen, The Netherlands.
 107. Van Eijndhoven, P. (2012). *State and trait characteristics of early course major depressive disorder.* Radboud University Nijmegen Medical Centre, Nijmegen, The Netherlands.
 108. Visser, E. (2012). *Leaves and forests: Low level sound processing and methods for the large-scale analysis of white matter structure in autism.* Radboud University Nijmegen, Nijmegen, The Netherlands.
 109. Van Tooren-Hoogenboom, N. (2012). *Neuronal communication in the synchronized brain. Investigating the functional role of visually-induced gamma band activity: Lessons from MEG.* Radboud University Nijmegen, Nijmegen, The Netherlands.
 110. Henckens, M.J.A.G. (2012). *Imaging the stressed brain. Elucidating the time- and region-specific effects of stress hormones on brain function: A translational approach.* Radboud University Nijmegen, Nijmegen, The Netherlands.
 111. Van Kesteren, M.T.R. (2012). *Schemas in the brain: Influences of prior knowledge on learning, memory, and education.* Radboud University Nijmegen, Nijmegen, The Netherlands.
 112. Brenders, P. (2012). *Cross-language interactions in beginning second language learners.* Radboud University Nijmegen, Nijmegen, The Netherlands.
 113. Ter Horst, A.C. (2012). *Modulating motor imagery. Contextual, spatial and kinaesthetic influences.* Radboud University Nijmegen, Nijmegen, The Netherlands.
 114. Tesink, C.M.J.Y. (2013). *Neurobiological insights into language comprehension in autism: Context matters.* Radboud University Nijmegen, Nijmegen, The Netherlands.
 115. Böckler, A. (2013). *Looking at the world together. How others' attentional relations to jointly attended scenes shape cognitive processing.* Radboud University Nijmegen, Nijmegen, The Netherlands.
 116. Van Dongen, E.V. (2013). *Sleeping to Remember On the neural and behavioral mechanisms of sleep-dependent memory consolidation.* Radboud University Nijmegen, Nijmegen, The Netherlands.
 117. Volman, I. (2013). *The neural and endocrine regulation of emotional actions.* Radboud University Nijmegen, Nijmegen, The Netherlands.
 118. Buchholz, V. (2013). *Oscillatory activity in tactile remapping.* Radboud University Nijmegen, Nijmegen, The Netherlands.
 119. Van Deurzen, P.A.M. (2013). *Information processing and depressive symptoms in healthy adolescents.* Radboud University Nijmegen, Nijmegen, The Netherlands.
 120. Whitmarsh, S. (2013). *Nonreactivity and metacognition in mindfulness.* Radboud University Nijmegen, Nijmegen, The Netherlands.
 121. Vesper, C. (2013). *Acting together: Mechanisms of intentional coordination.* Radboud University Nijmegen, Nijmegen, The Netherlands.
 122. Lagro, J. (2013). *Cardiovascular and cerebrovascular physiological measurements in clinical practice and prognostics in geriatric patients.* Radboud University Nijmegen Medical Centre, Nijmegen, the Netherlands.
 123. Eskenazi, T.T. (2013). *You, us & them: From motor simulation to ascribed shared intentionality in social perception.* Radboud University Nijmegen, Nijmegen, The Netherlands.
 124. Ondobaka, S. (2013). *On the conceptual and perceptual processing of own and others' behavior.* Radboud University Nijmegen, Nijmegen, The Netherlands.
 125. Overvelde, J.A.A.M. (2013). *Which practice makes perfect? Experimental studies on the acquisition of movement sequences to identify the best learning condition in good and poor writers.* Radboud University Nijmegen, Nijmegen, The Netherlands.
 126. Kalisvaart, J.P. (2013). *Visual ambiguity in perception and action.* Radboud University Nijmegen Medical Centre, Nijmegen, The Netherlands.
 127. Kroes, M. (2013). *Altering memories for emotional experiences.* Radboud University Nijmegen, Nijmegen, The Netherlands.
 128. Duijnhouwer, J. (2013). *Studies on the rotation problem in self-motion perception.* Radboud University Nijmegen, Nijmegen, The Netherlands.
 129. Nijhuis, E.H.J (2013). *Macroscopic networks in the human brain: Mapping connectivity in healthy and damaged brains.* University of Twente, Enschede, The Netherlands
 130. Braakman, M. H. (2013). *Posttraumatic stress disorder with secondary psychotic features. A diagnostic validity study among refugees in the Netherlands.* Radboud University Nijmegen, Nijmegen, The Netherlands.
 131. Zedlitz, A.M.E.E. (2013). *Brittle brain power. Post-stroke fatigue, explorations into assessment and treatment.* Radboud University Nijmegen, Nijmegen, The Netherlands.
 132. Schoon, Y. (2013). *From a gait and falls clinic visit towards self-management of falls in frail elderly.*

- Radboud University Nijmegen Medical Centre, Nijmegen, The Netherlands.
133. Jansen, D. (2013). *The role of nutrition in Alzheimer's disease - A study in transgenic mouse models for Alzheimer's disease and vascular disorders*. Radboud University Nijmegen, Nijmegen, The Netherlands.
 134. Kos, M. (2013). *On the waves of language - Electrophysiological reflections on semantic and syntactic processing*. Radboud University Nijmegen, Nijmegen, The Netherlands.
 135. Severens, M. (2013). *Towards clinical BCI applications: Assistive technology and gait rehabilitation*. Radboud University Nijmegen, Nijmegen, Sint Maartenskliniek, Nijmegen, The Netherlands.
 136. Bergmann, H. (2014). *Two is not always better than one: On the functional and neural (in)dependence of working memory and long-term memory*. Radboud University Nijmegen, Nijmegen, The Netherlands.
 137. Wronka, E. (2013). *Searching for the biological basis of human mental abilities. The relationship between attention and intelligence studied with P3*. Radboud University Nijmegen, Nijmegen, The Netherlands.
 138. Lüttjohann, A.K. (2013). *The role of the cortico-thalamo-cortical system in absence epilepsy*. Radboud University Nijmegen, Nijmegen, The Netherlands.
 139. Brazil, I.A. (2013). *Change doesn't come easy: Dynamics of adaptive behavior in psychopathy*. Radboud University Nijmegen, Nijmegen, The Netherlands.
 140. Zerbi, V. (2013). *Impact of nutrition on brain structure and function. A magnetic resonance imaging approach in Alzheimer mouse models*. Radboud University Nijmegen, Nijmegen, The Netherlands.
 141. Delnooz, C.C.S. (2014). *Unravelling primary focal dystonia. A treatment update and new pathophysiological insights*. Radboud University Nijmegen Medical Centre, Nijmegen, The Netherlands.
 142. Bultena, S.S. (2013). *Bilingual processing of cognates and language switches in sentence context*. Radboud University Nijmegen, Nijmegen, The Netherlands.
 143. Janssen, G. (2014). *Diagnostic assessment of psychiatric patients: A contextual perspective on executive functioning*. Radboud University Nijmegen, Nijmegen, The Netherlands.
 144. Piai, V. Magalhães (2014). *Choosing our words: Lexical competition and the involvement of attention in spoken word production*. Radboud University Nijmegen, Nijmegen, The Netherlands.
 145. Van Ede, F. (2014). *Preparing for perception. On the attentional modulation, perceptual relevance and physiology of oscillatory neural activity*. Radboud University Nijmegen, Nijmegen, The Netherlands.
 146. Brandmeyer, A. (2014). *Auditory perceptual learning via decoded EEG neurofeedback: a novel paradigm*. Radboud University Nijmegen, Nijmegen, The Netherlands.
 147. Radke, S. (2014). *Acting social: Neuroendocrine and clinical modulations of approach and decision behavior*. Radboud University Nijmegen, Nijmegen, The Netherlands.
 148. Simanova, I. (2014). *In search of conceptual representations in the brain: towards mind-reading*. Radboud University Nijmegen, Nijmegen, The Netherlands.
 149. Kok, P. (2014). *On the role of expectation in visual perception: A top-down view of early visual cortex*. Radboud University Nijmegen, Nijmegen, The Netherlands.
 150. Van Geldorp, B. (2014). *The long and the short of memory: Neuropsychological studies on the interaction of working memory and long-term memory formation*. Radboud University Nijmegen, Nijmegen, The Netherlands.
 151. Meyer, M. (2014). *The developing brain in action - Individual and joint action processing*. Radboud University Nijmegen, Nijmegen, The Netherlands.
 152. Wester, A. (2014). *Assessment of everyday memory in patients with alcohol-related cognitive disorders using the Rivermead Behavioural Memory Test*. Radboud University Nijmegen, Nijmegen, The Netherlands.
 153. Koenraadt, K. (2014). *Shedding light on cortical control of movement*. Radboud University Nijmegen, Nijmegen; Sint Maartenskliniek, Nijmegen, The Netherlands.
 154. Rutten-Jacobs, L.C.A. (2014). *Long-term prognosis after stroke in young adults*. Radboud University Nijmegen Medical Centre, Nijmegen, The Netherlands.
 155. Herbert, M.K. (2014). *Facing uncertain diagnosis: the use of CSF biomarkers for the differential diagnosis of neurodegenerative diseases*. Radboud University Nijmegen Medical Centre, Nijmegen, The Netherlands.
 156. Llera Arenas, A. (2014). *Adapting brain computer interfaces for non-stationary changes*. Radboud University Nijmegen, Nijmegen, The Netherlands.
 157. Smulders, K. (2014). *Cognitive control of gait and balance in patients with chronic stroke and Parkinson's disease*. Radboud University Nijmegen Medical Centre, Nijmegen, The Netherlands.
 158. Boyacioglu, R. (2014). *On the application of ultra-fast fMRI and high resolution multiband fMRI at high static field strengths*. Radboud University Nijmegen, Nijmegen, The Netherlands.
 159. Kleinnijenhuis, M. (2014). *Imaging fibres in the brain*. Radboud University Nijmegen, Nijmegen, The Netherlands.
 160. Geuze, J. (2014). *Brain Computer Interfaces for Communication: Moving beyond the visual speller*. Radboud University Nijmegen, Nijmegen, The Netherlands.
 161. Platonov, A. (2014). *Mechanisms of binocular motion rivalry*. Radboud University Nijmegen, Nijmegen, The Netherlands.
 162. Van der Schaaf, M.E. (2014). *Dopaminergic modulation of reward and punishment learning*. Radboud University Nijmegen Medical Centre, Nijmegen, The Netherlands.
 163. Aerts, M.B. (2014). *Improving diagnostic accuracy*

- in parkinsonism.* Radboud University Nijmegen Medical Centre, Nijmegen, The Netherlands.
164. Vlek, R. (2014). *From Beat to BCI: A musical paradigm for, and the ethical aspects of Brain-Computer Interfacing.* Radboud University Nijmegen, Nijmegen, The Netherlands.
 165. Massoudi, R. (2014). *Interaction of task-related and acoustic signals in single neurons of monkey auditory cortex.* Radboud University Nijmegen, Nijmegen, The Netherlands
 166. Stolk, A. (2014). *On the generation of shared symbols.* Radboud University Nijmegen, Nijmegen, The Netherlands.
 167. Krause F. (2014). *Numbers and magnitude in the brain: A sensorimotor grounding of numerical cognition.* Radboud University Nijmegen, Nijmegen, The Netherlands.
 168. Munneke, M.A.M. (2014). *Measuring and modulating the brain with non-invasive stimulation.* Radboud University Nijmegen Medical Centre, Nijmegen, The Netherlands.
 169. Von Borries, K. (2014). *Carrots & Sticks - a neurobehavioral investigation of affective outcome processing in psychopathy.* Radboud University Nijmegen Medical Centre, Nijmegen, The Netherlands.
 170. Meel-van den Abeelen, A.S.S. (2014). *In control. Methodological and clinical aspects of cerebral autoregulation and haemodynamics.* Radboud University Nijmegen Medical Centre, Nijmegen, The Netherlands.
 171. Leoné, F.T.M. (2014). *Mapping sensorimotor space: Parieto-frontal contributions to goal-directed movements.* Radboud University Nijmegen, Nijmegen, The Netherlands.
 172. Van Kessel, M. (2014). *Nothing left? How to keep on the right track - Spatial and non-spatial attention processes in neglect after stroke.* Radboud University, Nijmegen, The Netherlands.
 173. Vulto-van Silfhout, A. T. (2014). *Detailed, standardized and systematic phenotyping for the interpretation of genetic variation.* Radboud University Medical Centre, Nijmegen, The Netherlands.
 174. Arnoldussen, D. (2015). *Cortical topography of self-motion perception.* Radboud University, Nijmegen, The Netherlands.
 175. Meyer, M.C. (2015). *"Inbetween Modalities combined EEG – fMRI".* Radboud University, Nijmegen, The Netherlands.
 176. Bralten, J. (2015). *Genetic factors and the brain in ADHD.* Radboud university medical center, Nijmegen, The Netherlands.
 177. Spaak, E. (2015). *On the role of alpha oscillations in structuring neural information processing.* Radboud University, Nijmegen, The Netherlands.
 178. Van der Doelen, R. (2015). *Translational psychiatry; the twists and turns of early life stress and serotonin transporter gene variation.* Radboud university medical center, Nijmegen, The Netherlands.
 179. Lewis, C. (2015). *The structure and function of intrinsic brain activity.* Radboud University, Nijmegen, The Netherlands.
 180. Huang, Lili. (2015). *The subiculum: a promising new target of deep brain stimulation in temporal lobe epilepsy. Investigation of closed-loop and open-loop high frequency stimulation of the subiculum in seizure and epilepsy models in rats.* Radboud University, Nijmegen, The Netherlands.
 181. Maaijwee, N.A.M.M (2015). *Long-term neuropsychological and social consequences after stroke in young adults.* Radboud university medical center, Nijmegen, The Netherlands.
 182. Meijer, F.J.A. (2015). *Clinical Application of Brain MRI in Parkinsonism: From Basic to Advanced Imaging.* Radboud university medical center, Nijmegen, The Netherlands.
 183. Van der Meij, R. (2015). *On the identification, characterization and investigation of phase dependent coupling in neuronal networks.* Radboud University, Nijmegen, The Netherlands.

This production of this dissertation was sponsored by

